Synthesis and Characterization of Alumina Reinforced Aluminum Syntactic Foam Materials

THESIS

Submitted in partial fulfillment
of the requirements for the degree of

DOCTOR OF PHILOSOPHY

by

MURALI KARTHEEK S S

ID. No. 2018PHXF0450H

Under the Supervision of
Prof. Suresh Kumar Reddy Narala

&

Co-supervision of
Prof. Vincent Shantha Kumar

BIRLA INSTITUTE OF TECHNOLOGY AND SCIENCE, PILANI

2024

BIRLA INSTITUTE OF TECHNOLOGY AND SCIENCE – PILANI

Certificate

This is to certify that the thesis titled "**Synthesis and Characterization of Alumina Reinforced Aluminum Syntactic Foam Materials**," submitted by **Murali Kartheek S S** ID No. **2018PHXF0450H,** for the reward of Ph.D. of the Institute, embodies the original work done by him under the supervision.

Signature of Supervisor	:	
Name of the Supervisor	:	**Dr. Suresh Kumar Reddy Narala**
Designation	:	**Professor & Head** Department of Mechanical Engineering, BITS-Pilani, Hyderabad Campus, Jawahar Nagar, Kapra Mandal, Hyderabad- 500078, Telangana, India
Date	:	

Signature of Co-Supervisor	:	
Name of the Co-Supervisor	:	**Dr. Vincent Shantha Kumar**
Designation	:	**Associate Professor** Department of Mechanical Engineering, BITS-Pilani, Dubai Campus, Dubai International Academic City PO Box: 345055, · Dubai, UAE
Date	:	

Declaration

I hereby declare that the thesis entitled "**Synthesis and Characterization of Alumina Reinforced Aluminum Syntactic Foam Materials**", is conducted under the supervision of Prof. N Suresh Kumar Reddy, Professor, Department of Mechanical Engineering, Birla Institute of Technology and Science - Pilani, Hyderabad Campus and Co-supervision of Prof. Vincent Shantha Kumar, Associate Professor, Department of Mechanical Engineering, Birla Institute of Technology and Science - Pilani, Dubai Campus. I also declare that thesis represents my own work, which has been done after registration for the degree of PhD at Birla Institute of Technology and Science - Pilani, Hyderabad Campus, and has not been previously included in any thesis or dissertation submitted to this or any other institution for degree, diploma or other qualification.

Signature:_____

Name: Murali Kartheek S S

Date: 12th Feb 2024

Place: Hyderabad

Acknowledgments

This thesis represents the joint efforts of several individuals who helped me reach this point. There are no adequate words to express my profound thanks and admiration to Prof. N. Suresh Kumar Reddy and Prof. Vincent Shantha Kumar for their continuous support in carving the thesis and supporting research objectives. I could not have imagined more excellent advisory support for my doctoral studies. Prof. Suresh Kumar Reddy Narala has given me a perfect opportunity to work under his guidance, for which I am incredibly grateful. This study was completed with his exceptional support, immense patience, and invaluable advice during critical instances. I greatly respect the consistent encouragement I received from his end, which enabled me to grow professionally and personally. Also, I thank Prof. Vincent Kumar for co-supervising me and extending his support throughout my Ph.D. tenure at every stage. I highly admire his profound support, encouragement, and availability throughout. I will never forget his crucial input during all the technical discussions and evaluations.

I thank the Doctoral Research Committee (DRC) members for providing valuable support during this research work. I sincerely thank my thesis advisory and examination committee members, Professors S.P Regalla and Dr. Kundan Kumar Singh. They graciously donated their time to provide me with insightful feedback on improving the quality of my work. During the continuous evaluation, their support and comments made me steer my research in the right direction.

Special thanks to the current and former heads of the Department of Mechanical Engineering, BITS Pilani, Hyderabad Campus, Prof. Suresh Kumar Reddy Narala and

Prof. Amit Kumar Gupta, respectively. Their support led to the successful completion of my research. I immensely thank Prof. Vamsi Krishna Venuganti, Associate Dean, AGSRD, and his team for providing guidance and support in seamlessly completing the administrative and research tasks throughout my SRF and Ph.D. tenure. I take this opportunity to thank our Honorable Director, Prof. G Sundar, for his endless support to all the research scholars in the form of research facilities and grants to complete our doctoral studies.

Special thanks must go to the BITS central workshop, central analytical lab(CAL) staff, and those in charge, who always supported me by providing cutting-edge technology and facilities that helped me in synthesis and characterization. I want to thank all the laboratory workers at BITS Pilani, Hyderabad Campus, for their quick assistance and guidance. My heartful thanks go to Mr. P Sreedhar, Mr. B Chandrashekar, Mr. Mahindra Chari, and Mr. Jinu Paul, laboratory staff and technicians of the Department of Mechanical Engineering, for providing me with practical hands-on training and their kind assistance and support during my studies in the central workshop. Also, I wish to thank the CAL staff, Mr. Tirumallaiha and Mr. Suresh, for patiently supporting imaging and characterization. I extend my gratitude towards the resource of knowledge (online and offline) provided by the Central Library. Without their support, exploring the latest literature and accessing research articles and patents may take ages.

Most of the results presented in this dissertation would not have been attainable in the facilities given by some of the laboratories. Current incharge Prof. Sujith. R and Prof. Suresh Kumar Reddy Narala, former faculty incharge of the Central Workshop and Tribology Lab. Prof. Amrita Priyadarshini, former faculty incharge of the Tribology Lab, Dr. P Pavan Kumar, former faculty incharge of the Tribology Lab, and

Dr. Nithin R. Kotkunde, faculty in-charge of the Material Testing Lab, have my most profound appreciation and gratitude. My special thanks to Mr. Bhuwaneswarn for his immense support in executing the material tests, and I remember the technical discussions we had to understand the behavior of novel materials.

I cannot forget the friends who helped me through difficult times, encouraged me, and shared my successes. There is no way to express how much it meant to me to be in a friendly lab environment. These brilliant friends and colleagues inspired me over the years: Dr. Pavan Datta Jadav, Dr. Amar Shelwant, Mr. Chennakesava Sai, Mr. Ahsan, Mr. Gunashekar G, Mr. Sai Kiran, Mr. Abhinav, and all the other current and former scholars that I know.

I wish to thank my parents-in-law, Mr. P. Ramamurthy and Mrs. Visalakashi, for their unwavering emotional and moral support at every stage of this journey. I also appreciate the heartwarming generosity of my sister-in-law, Ms. Pulya Sruthi, to be a cheerful and joyful family member.

Last but the most influential persons in my life whom I cannot thank are my parents, Mr. S. V. S. A. Padmanabham and Mrs. Padma, and my wife, Mrs. Sravani Pulya, and son, Mr. Trivikram Aditya. They are my solid pillars and support by all means.

Murali Kartheek S S

Abstract

The need for advanced materials was the driving force behind the introduction of composite technology. Compared to monolithic materials, composites generally have two or more distinct constituents. When a reinforcement material is added to the metal matrix, it imparts unique features to the resultant in a metal matrix composites (MMCs). Among the wide classification of composite materials, syntactic foams(SFs) are light weight composites with hollow ceramic/glass particles reinforced in a metal matrix such as aluminum, magnesium, titanium, steels and others.

The aluminum matrix syntactic foams (AMSFs) are lightweight composite foams with functional and structural properties such as low relative density and high energy absorbing nature. These qualities made AMSFs a practical alternative to conventional materials desirable for automotive, aerospace, and shipbuilding industries as energy absorbers. Many studies have reported the mechanical aspects of these materials. However, a detailed analysis of energy-absorbing behavior on aluminum matrix syntactic foams is sparse. This work produces alumina-reinforced aluminum syntactic foams using the powder metallurgy route. A systematic study on quasi-static room temperature (RT), elevated temperature (ET), and high strain rate (HSR) studies is conducted to understand the effect of the volume fraction and size of the particle individually. The compressive stress-strain response shows volume fraction and temperature dependency for different particle size ranges. Despite large deformation, the deformation behavior of all the samples has shown no sudden drop in stress-strain response and macroscopic stability.

Further, the energy absorption properties of the AMSFs are discussed extensively, such as energy absorption per unit volume (MJ/m^3), energy absorption

efficiency (%), and ideal energy absorption efficiency (%) of the earlier tests are presented. These energy absorption properties are essential in understanding the material response and the overall energy absorbed by the material concerning the loading condition.

Also, the compressive behavior of alumina hollow spheres reinforced AMSF using experimental, analytical, and numerical methods are attempted. The elastic properties are estimated using ABAQUS's analytical and micromechanical-based numerical homogenization techniques. The feasibility of modeling the elastic and elasto-plastic behavior is studied using the finite element (FE)--based representative volume elements (RVE) model. These RVE models are generated for different volume fractions based on user-defined code to analyze the elastic and elasto-plastic behavior of AMSFs using the FE solver ABAQUS. In addition to the elastic properties, the stress-strain response of the metal matrix syntactic foams is determined using RVE models. The experimental data and FE predictions are compared in this work. These FE models have great potential in studying the ceramic hollow particles reinforced metal matrix syntactic foams and developing new porous composites under compression loading using RVE-based models.

Further, the AMSFs are probed to understand the corrosion behavior under different chemical solutions. These solutions are prepared with different NaCl, NaOH, and HCl concentrations. The corrosive response of the AMSFs is measured based on their size and volume fractions of ceramic hollow particles inside the matrix. All the Al- Al_2O_3 syntactic foam samples displayed enhanced corrosion resistance in all solutions over conventional composites. Due to the high agglomeration percentage of the fine particle distribution, Al-500μm-1.3 exhibited outstanding corrosion resistance. SEM analyses and impedance data parameters corroborate the enhanced

corrosion resistance of Al- Al_2O_3 syntactic foam samples in neutral and alkaline media compared to acidic media.

Finally, novel hybrid syntactic foams are attempted to be produced using the powder metallurgy route by combining two different hollow materials. This investigation reports a novel Al-Al_2O_3-Cenosphere reinforced multi-particle syntactic foam (MPSF). These MPSFs exhibit superior energy absorption properties during the quasi-static and high strain rate (HSR 2700 s^{-1}) loadings. This novel material is studied at different strain rates, such as 1 s^{-1}, 900 s^{-1}, 1600 s^{-1}, and 2700 s^{-1} under compression. The deformation response in HRS studies is monitored using high-speed imaging. The stress-strain response obtained from dynamic loading shows a positive shift in the slope of the plateau region. The energy absorption properties of AMSFs under low and high strain rates have shown a maximum value of 72.34 % and 78.92 %, respectively, showing superior properties under high strain rates. The hardening and deformation behavior of the produced AMSFs is studied to understand the material's response. This study comprises the overall reaction of the AMSFs under different loadings and their failure behavior.

Table of Contents

List of Tables

List of Figures

List of Abbreviations

Abbreviation	Description
Al	Aluminum
AMSF	Aluminum Matrix Syntactic Foams
EAE	Energy Absorption Efficiency
EDM	Electric Discharge Machining
EDX	Energy Dispersive X-Ray Analysis
EIS	Electrochemical Impedance Spectroscopy
FEM	Finite Element Method
LH	Linear Homogenization
MMCs	Metal Matrix Composites
MMSF	Metal Matrix Syntactic foam
PBC	Periodic boundary condition
PDP	Potentiodynamic polarization
PM	Powder Metallurgy
RVE	Representative volume element
SEA	Specific Energy Absorption
SEM	Scanning Electron Microscope
SF	Syntactic Foam

Chapter 1: Introduction

This chapter consists of a brief introduction to cellular materials, foams, and syntactic foams (SFs). First, a brief background and motivation for this work are given to carry out this work. Section 1.2 explains the details of porous materials and their types, emphasizing the syntactic and metal matrix syntactic foams (MMSFs) and their potential applications. Later, a brief outline of the thesis is provided with key highlights of each chapter.

1.1 BACKGROUND AND MOTIVATION

The rapidly developing technology demands advanced material components and structures in engineering applications. This encourages researchers and scientists to shift from conventional metals and materials to advanced composites and hybrid materials to limit weight and size while maintaining quality and durability. Integrating lightweight materials into engineering designs may overcome several manufacturing challenges, such as the structures' overall weight, durability, and mechanical energy absorption[1,2]. Modern lightweight materials are essential in engineering design due to their enhanced properties and adaptability that can be deployed for various engineering applications [1].

The weight of the engineering structure has always a prime concern over decades. The initial attempts were made to produce porous materials to reduce the weight of engineering structures. The primary objective was to progressively increase the structural adaptability of metallic materials while preserving their mechanical and chemical properties. However, the low-dense porous materials failed to withstand dynamic loading conditions during the functioning. Also, attempts are made to

enhance the structural stability through alloying and the addition of whiskers and nanotubes to improve the mechanical response of the materials [3,4]. However, the results are not promising due to their low elastic modulus and low plateau stress (constant stress region under deformation) under large deformations. In this regard, there is a gap in developing lightweight materials with high strength and durability under extreme loading conditions.

The lightweight porous materials are classified based on their design and manufacturing techniques. In materials engineering, where innovation meets versatility, a remarkable class of materials has emerged, captivating the imagination of scientists and engineers alike, called syntactic foams (SFs). These SFs are a class of porous composite materials where a hollow particle is dispersed within a matrix material to reduce the density without significant compromise in the mechanical properties. In contrast to the conventional foams (open pore and close pore foams), porosity is induced through the hollow particles randomly distributed inside the matrix material. The addition of a metallic and non-metallic hollow particle leads to an increase in the density of the SFs. These hollow particles are available in different materials, sizes, and shapes. The porous nature of SF materials yields unique stress-strain behavior and enhanced mechanical and acoustic properties [5–7]. The combination of these properties drew the attention of scientists and manufacturers due to their lightweight properties and superior energy absorption properties essential for various engineering applications.

These extraordinary materials possess a seemingly unique nature, combining the strength and resilience of traditional solids with the lightweight and buoyant properties of foams. A novel fusion of matrix material, such as metal or polymer, with many hollow spheres known as balloons or hollow particles typically of 0.1 mm to 6 mm in

size. These hollow particles are usually made of glass, ceramic, or metals. This intricate combination creates a fascinating interaction, granting syntactic foams with remarkable characteristics and an astonishing range of applications. The integration of a lightweight metal matrix with hollow particles yields a cellular structure with reduced density and enhanced specific strength. This foam-like structures finds practical applications in several industries, including automotive, aerospace, and protective constructions, that necessitate efficient impact absorption capabilities.

In the literature, various studies are proposed to understand syntactic foams' elastic and elasto-plastic properties experimentally and using numerical studies for porous and composite porous materials (also refered as SFs). Gaining a comprehensive understanding of the macroscopic characteristics of these porous composites is of utmost importance in order to effectively design materials to meet the demands of future applications. The microscopic qualities of a system are significantly impacted by the inherent characteristics of its constituent materials. Limited investigations have been conducted on the representative volume element (RVE) based model within the realm of numerical approaches. These mico-size representative models have commonly been termed RVE in the literature. A RVE model typically consists of a micorscale model with macroscopic entities such as particle distribution and grain orientations.

Modeling the macroscopic structure of porous structure involves models with huge memonry and requires significant amount of computational cost due to the anisotropic nature of the structure. The earlier numerical studies on the SFs have shown the elastic properties and macroscopic response of the polymer and metal-based SFs. However, the elasto-plastic response of the SFs is studied using macroscopic scale models and CT-scan models. This may result in a large amount of computational time

and data storage due to the complexity of the model. In this regard, a representative model may be considered an alternative to understanding the elasto-plastic response of porous materials. The homogenization technique yields the model's effective properties that represent the part of the sizeable heterogeneous microstructure [8]. The study of the MMSF's response using 3D models is essential to achieve more accurate prediction in the materials' linear elastic and elasto-plastic response.

Among the various classes of SFs, aluminum syntactic foams typically contain aluminum alloys as matrix and ceramic/glass hollow particles. The interaction of the aluminum matrix with the hollow particles results in unique mechanical and structural properties [1,7]. These hollow particles are typically in the size range of a few micrometers to a few millimeters in diameter. Over a few decades, an increase in research publications on the development of conventional and hybrid SFs has been studied widely. Despite the current availability of literature on SFs, limited studies have focused on the relationship between the effect of hollow particle size and volume fraction on the energy absorption response in various deformation conditions.

Further, the material's static behavior alone is insufficient to implement in structural applications. The dynamic response of the SFs is extensively studied for polymer-based materials. The effect of the size and volume fraction of the alumina-based SFs is seldom studied in the literature. Similarly, understanding the corrosion response of the aluminum matrix syntactic foams (AMSF) is another exciting area to implement the MMSFs commercially. Thus, the motivation behind AMSFs lies in their potential to offer lightweight, strong, and versatile materials for various applications across industries, addressing the growing demand for improved performance, energy efficiency, and sustainability.

1.2 SYNTACTIC FOAM MATERIALS

The research and development into aluminum syntactic foams evolved from the need for lightweight materials with enhanced mechanical properties in various industries. These foams' unique combination of reduced density and enhanced specific strength makes them attractive for various applications. Such materials with enhanced strength and extended life are constantly in demand in many industries, such as aerospace, sports, automotive, and military applications. Significant research is taking place to enhance the properties of conventional metals and alloys to achieve the desired properties. However, the major challenge occurs in improving the strength with a minimum increase in density. The earlier studies on ceramic composites and laminated structures have shown enhanced properties in a specific direction due to the influence of high-strength ceramic/intermetallic particles and intermetallic layers [9,10]. However, there is a negligible drop in the density of these materials. In this regard, the materials and design engineers have attempted to induce porosity into the material, resulting in low density and extended plateau stress in the plastic region. These porous materials are structurally engineered to retain the desired functional integrity with reduced weight suitable for several engineering components. The properties of these materials can be enhanced by optimizing the process parameters, which may give great scope to implement in a wide range of applications.

A porous material (foams) with various novel thermal, mechanical, acoustic, and electrical properties is produced using different metals and polymers. Metal foams are broadly classified into open cell, closed cell, and composite foams. Barnhart et al. comprehensively summarize the various manufacturing methos of metal foam materials and liquid metals [11]. Different types of cellular materials and their classifications are shown in **Figure 1.1**.

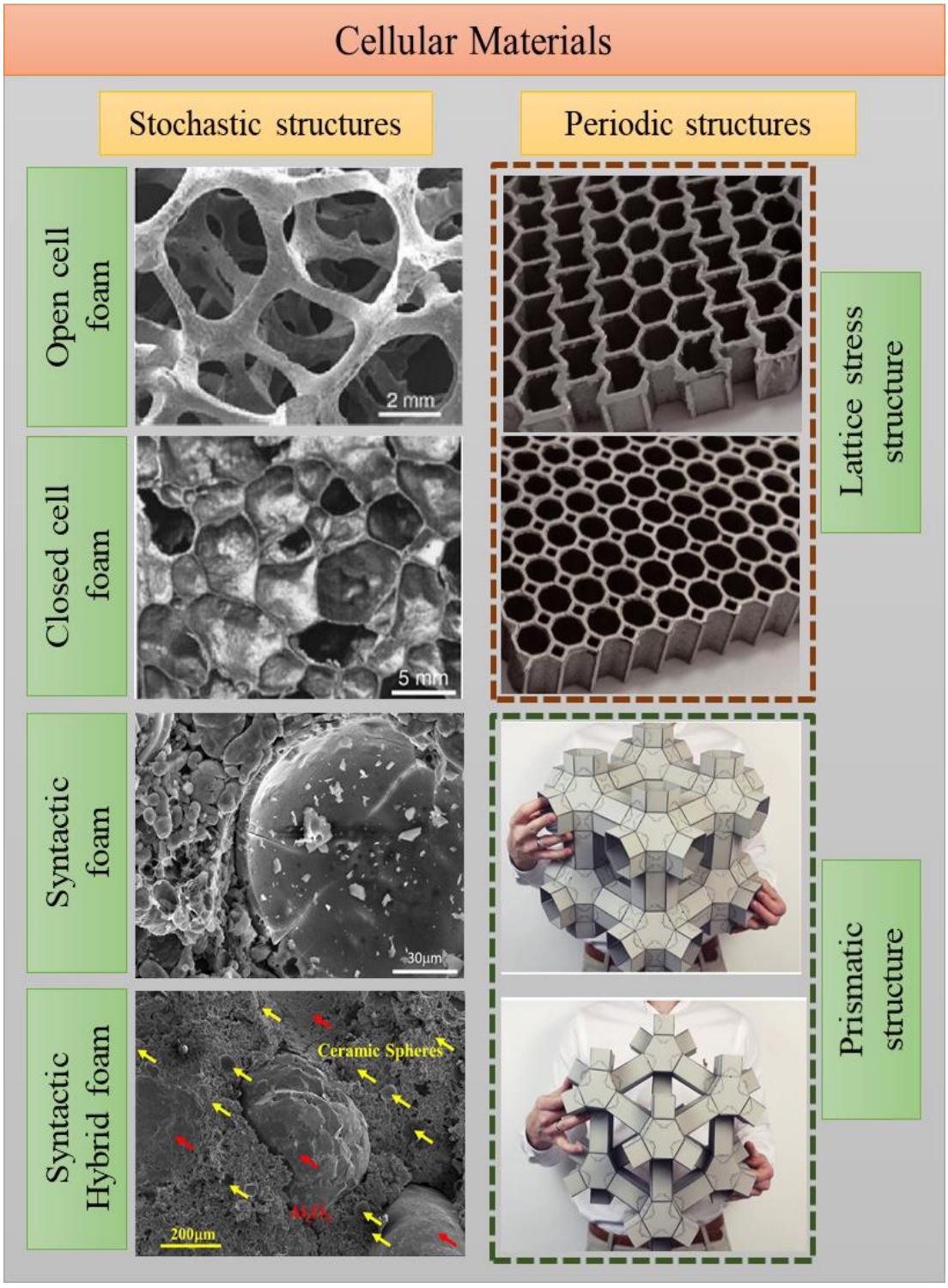

Figure 1.1 : Classification of cellular materials[12,13]

Cellular materials are structures that are characterized by a porous or cellular microstructure. These materials consist of a network of voids or cells separated by solid walls or struts. The arrangement and geometry of these cells can vary, and cellular materials can be found in natural structures like bones, as well as in engineered materials. Key features of cellular materials include low density, high strength-to-weight ratio, and good energy absorption capabilities. They find applications in various industries such as aerospace, automotive, and biomedical engineering.

Cellular materials can be produced using a variety of manufacturing techniques, each suited to specific applications and desired material properties. Here are some common manufacturing techniques for cellular materials:

- Foaming
- Additive Manufacturing (3D Printing).
- Chemical Vapor Deposition (CVD)
- Sol-Gel Processing
- Replication Techniques

Syntactic foams are a specific type of composite material composed of a matrix (polymeric, metallic, or ceramic) and hollow microspheres, typically made of glass or polymer. These microspheres act as reinforcement within the matrix, providing additional strength and stiffness while keeping the overall density low. Syntactic foams are known for their buoyancy, thermal insulation properties, and strength. The common different between cellular materials and syntactic foams with excellent mechanical properties are shown in **Table 1.1**.

Table 1.1: Comparision of the Cellular materials and syntactic foams

Category	Cellular Materials	Syntactic foams
Definition	Structures with a porous or cellular microstructure.	Composite materials with a matrix and hollow microspheres.
Density	Generally low density due to the porous structure.	Low density due to incorporation of hollow microspheres.
Strength	Offers high strength with a good strength-to-weight ratio.	Provides high strength with lightweight characteristics.
Applications	Used in aerospace, automotive, and healthcare industries.	Commonly used in marine, deep-sea, and aerospace applications.
Manufacturing Process	Methods include foaming, sintering, and additive manufacturing.	Manufactured by dispersing microspheres into a liquid resin, followed by curing.
Specific Properties	Variable properties, such as thermal insulation and energy absorption.	Buoyancy, thermal insulation, and tailorable mechanical properties.
Examples	Natural examples include bones. Engineered examples include foams and lattice structures.	Used in marine applications, deep-sea exploration, and aerospace.
Advantages	Low weight, high strength, and good energy absorption.	Lightweight, buoyant, and tailorable mechanical properties.
Challenges	May have limitations in terms of specific applications.	Microsphere-matrix interface and material compatibility challenges.
Recent Advancements	Advances in additive manufacturing techniques for cellular structures.	New formulations for enhanced buoyancy and strength.
Future Prospects	Potential for further customization and application expansion.	Continued exploration in deep-sea environments and aerospace.

The significant difference between open and closed-cell foams under stochastic structures is that the cell walls are interconnected for closed-cell foams. The open-cell foams are suitable for thermal insulation, and closed-cell foams are suitable for acoustic insulation[14]. A network of materials is connected across the volume in the open foam material. The SF material is a separate class of foams where the density of the material is reduced with the help of hollow particles. These hollow particles have

a shell thickness of a few microns and are introduced into the metal matrix to achieve the desired density.

Syntactic foams find extensive utilisation across several applications, encompassing:

Marine applications: Syntactic foams are used as buoyancy foams in lifeboats, buoys, and other marine structures. They are also suitable for core materials in sandwich panels for boat hulls and decks.

Aerospace applications: Syntactic foams are suitable for structural materials in aircraft wings and fuselage sandwich panels. They are also used as buoyancy foams in liferafts and other aerospace structures.

Sports equipment: Syntactic foams are used as cores in golf clubs, tennis rackets, and other sports equipment. They are also used as shock absorbers in helmets and other protective gear.

Industrial applications: Syntactic foams are used as thermal insulation, soundproofing, and vibration-damping materials. They are also used as fillers in plastics and other composites.

Syntactic foams are a highly advanced, versatile material with numerous applications. They are lightweight, robust, buoyant, and resistant to chemicals, making them ideal for a variety of demanding applications. In contrast to open- and closed-cell foams, the primary limitation of SFs is their high relative density owing to ceramic particles. Nonetheless, the SFs have a substantially reduced density than conventional materials, which may decrease the weight of machine structures. Also, these materials are extensively used as core sandwich materials and shell structures in military and

automotive applications, such as energy-absorbing members in critical zones and heat exchangers. Metal foams are typically more difficult to produce than polymer foams. Consequently, substantial research has been conducted on the numerous MMSF manufacturing techniques [1].

The typical MMSFs are produced using SiC, alumina, steel, and cenospheres induced in aluminum, magnesium, titanium, and zinc matrix materials. Different combinations of these materials may be produced using liquid infiltration techniques[15]. Pressure infiltration and dispersion methods are other commonly adopted techniques in the literature to produce syntactic foams[10]. However, a solid-state technique such as powder metallurgy is seldom explored concerning MMSFs [2,18,19].

The experimental investigations on SFs reported in the scientific literature concentrated on density, mechanical response, and energy absorption behavior. Understanding the deformation behaviour in the plateau region of the stress-strain curve was the primary concern. In addition, micromechanical properties of syntactic foams were analysed using analytical methods and finite element (FE) programmes. Different analytical methods are proposed in these studies, and the interaction between the particle and the matrix is considered to measure the elastic properties. However, most of these numerical studies are limited to polymer matrix SFs, and sparse literature is available on the MMSFs.

MMSFs are distinguished by their exceptional compressive properties. To understand these properties, it is necessary to understand how syntactic foam fails under compression and the stress-strain response. During early compression, microspheres close to the foam’s center may collapse. The matching stress is known

as the foam's peak strength. In addition, the stress decreases as the strain increases, and a relatively low constant amount of stress, known as the plateau strength, persists for a specific strain range until the stress begins to climb exponentially as shown in **Figure 1.2**. The matrix shall densify during the stress drop and plateau area, and the remaining microspheres shall collapse until the foam is entirely densified. This strain, known as the densification strain, enables us to identify the beginning of the stress rise. The region of the compression test plot extending up to the densification strain may help us determine the maximum impact energy the foam can absorb.

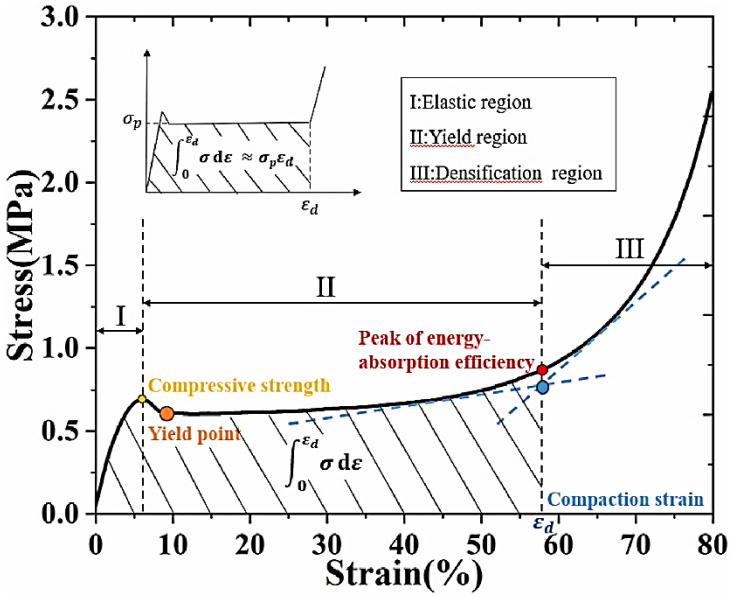

Figure 1.2 : Stress-strain graph of a syntactic foam highlighting the key features [20].

The aerospace and automotive sectors constantly seek lightweight materials to enhance fuel efficiency and reduce carbon emissions. Aluminum syntactic foams can replace traditional materials while maintaining structural integrity and reducing weight, resulting in improved performance and reduced energy consumption. Similarly, materials in marine and offshore environments must withstand harsh conditions, including corrosion and high pressures. Also, the energy-absorbing

properties of syntactic foams make them valuable for impact protection applications. This makes aluminum syntactic foams useful for applications such as crash-worthy structures in transportation, protective packaging, and sports equipment.

Despite undeniable progression in the study of SF materials, there are significant concerns about the effect of manufacturing techniques, raw materials of matrix and reinforcements, particle size effects, electrochemical response of the material, and the effect of the loading rates. Understanding these properties and their failure mechanisms may bridge the gap in producing these porous materials commercially.

1.3 THESIS OUTLINE

The primary emphasis of this work is to develop an alumina-based aluminum matrix syntactic foam using a powder metallurgy route with different volume fractions that match theoretical density. Various experimental investigations are carried out to study the effect of particle size and volume fraction on different materials properties such as density, mechanical strength, corrosion, and derived properties such as energy absorption efficiency of AMSFs. The high temperature and high strain rate compression studies are conducted to understand the influence of strain rate on the deformation behavior of AMSFs. Further, the corrosion studies are probed to examine the material response to different chemical and pH conditions. Finally, novel hybrid syntactic foams are produced to further reduce the density of the aluminum syntactic foams with no significant reduction in the mechanical properties and structural integrity after testing under quasi-static and dynamic loadings. The following table outlines the various topics covered in the thesis:

The thesis outline and different key topics covered in each chapter are as follows:

Chapter 1: Introduction to Syntactic Foam	• Cellular materials: Foams and their types. • Research motivation and background • Thesis outline
Chapter 2: Literature Survey on AMSFs	• A critical review of Syntactic foams materials • Studies on different matrix and filler materials, their synthesis techniques, and characterization tools used • The significant gaps in research and the objectives of the current work are listed.
Chapter 3: Synthesis and characterization of AMSFs	• Synthesis of novel aluminum alumina syntactic foams. • Details of powder metallurgy processing parameters. • Details of the freeze-fracture techniques are discussed.
Chapter 4: Density and mechanical characterization of AMSFs	• The mechanical properties of the Al-Alumina, under different loading conditions. • The effect of the volume fraction and size of the hollow particles on the mechanical properties are discussed. • The compressive responses under high temperatures and dynamic loading conditions are also explained.
Chapter 5: Energy absorption properties of AMSFs	• The energy absorption properties of the syntactic foams. • The ideal energy absorption behavior is discussed in detail.
Chapter 6: Simulation studies to measure the elastic and elasto-plastic properties of SFs	• Analytical model's valuations to predict the elastic properties of the AMSFs. • The modeling of the multi-particle unit cell models to study the elastic and elasto-plastic properties of the syntactic foams models are explained.
Chapter 7: Electrochemical studies on AMSFs	• Influence of chemical solution and its pH concentration on electrochemical response of AMSFs
Chapter 8: Novel hybrid syntactic foams synthesis and characterization	• Novel hybrid syntactic foam materials synthesis and characterization.
Chapter 9: Conclusions	• This summary and conclusions derived from this study are explained. Recommendations for future work are also presented.

Chapter 2: Literature Review

The chapter literature review contains an extensive literature survey on the synthesis and characterization of AMSFs from widely referred research articles. This chapter contains eight sections. Section 2.1 introduces the MMSFs and AMSFs, and their significant characteristics. Later, Sections 2.2 and 2.3 present different types of the matrix and reinforcements studied in the literature. Section 2.4 covers the various processing techniques adopted to produce the MMSFs and AMSFs. The numerical studies conducted on the SFs are discussed in Sections 2.5 and 2.6 discusses the work reported on mechanical properties tested under various loading rates, such as quasi-static and dynamic. Later in Section 2.7, the gaps in the literature and research objectives are presented. Section 2.8 presents an overall summary of the extensive literature survey and its implications.

2.1 INTRODUCTION

SF is a unique porous composite material created by adding hollow spheres to a matrix (often micro-hollow particles) [21]. **Figure 2.1** depicts a 2D solid model of a syntactic foam made of hollow spheres. The matrix materials are typically polymers or lightweight metals, while the reinforcing hollow particles are metal or ceramic [22,23]. Syntactic foam, in general, offers superior mechanical capabilities over typical open-cell and closed-cell foams. Also, these materials are significantly lighter than particulate composite materials. These metal foams are widely studied to meet the requirements of lightweight, high-strength property applications. In general, lightweight materials and metals are selected for the matrix material.

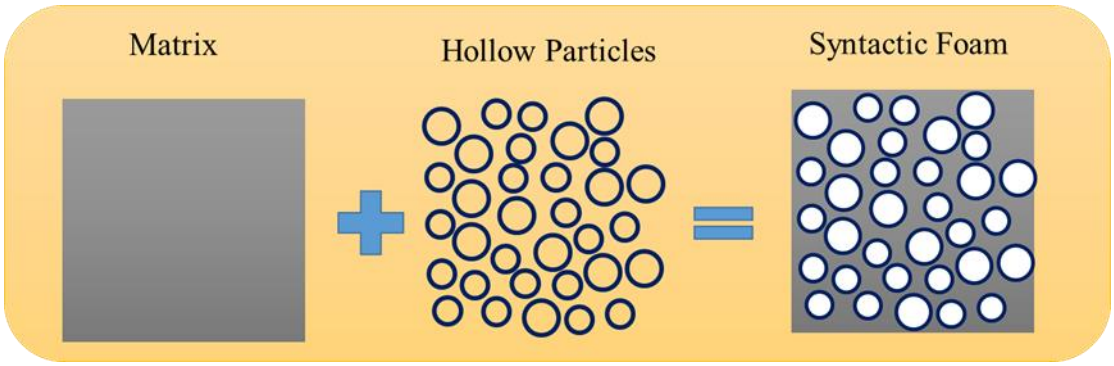

Figure 2.1 : Schematic model of syntactic foams showing hollow particles and matrix material

The lightweight porous materials and structures have enhanced mechanical properties compared to their conventional counterparts [6,24,25]. So, the attention towards such porous and cellular materials has increased in the recent past due to their extended plateau strength and high energy absorbing ability [25]. For example, lightweight construction parts are introduced as sandwich panels of rotorcraft blades and automobile parts [1,26,27]. This section discusses a detailed literature review based on the raw materials, processing techniques, and characterization tools.

2.2 MATRIX MATERIAL

A prime focus in literature is understanding the compressive and mechanical response of the SFs materials. Initially, the studies on SFs have focused on the mechanical properties of various polymer-based materials due to ease of production and applicability [28–30]. Under metallic foams, aluminum and its alloy-based SFs are widely studied as matrix materials along with magnesium[31], steel[32], and titanium[33]. The compressive behavior for different length-to-diameter ratios of aluminum matrix SFs is studied by Orbulov [34]. Later, Maria et al. and Ferguson et al. reported studies on Al-Al_2O_3 SFs [35,36]. The initial part of this work was focused on particle thickness's effect on the mechanical properties of the Al-Al_2O_3 SFs. The

syntactic foam properties adhere to two significant constituents, matrix and hollow particles. The different matrix material types, volume fractions, and structural arrangements of the hollow or porous particles display different mechanical, dielectric, and physical properties. This phenomenon is because the material types, volume fraction, and structural arrangement determine their material properties. Interestingly, many methods have demonstrated that SF characteristics may be controlled based on the selection of materials. It is essential to choose the proper microspheres and core additives and to maintain precise volume fraction, size, and distribution. Metals [22], polymers [30], and ceramics [37] are frequently employed in the production of SFs, while there are alternative matrix materials such as high entropy alloys are expected that gain popularity in this regard [25]. The proper microspheres and core additives should be chosen with precise volume fractions, sizes, and distributions[38]. Metal, ceramic, and polymer matrices are typical types used to make SFs.

A significant amount of work is published on polymer-based materials due to ease of availability and manufacturing. Later, it was observed that ceramic-based SFs have superior properties than polymer SFs; however, they are few studied due to their high production cost and limited scalability [1]. For instance, Jayavardhan et al. [39] investigated SFs constructed from the epoxy matrix with borosilicate glass hollow particles. The experiment demonstrated that the foam was corrosion-resistant and resistant to hostile environments. In a separate investigation by Szlancsik et al. [40], various metal matrix mixtures of aluminum alloys and sets of hollow oxide ceramic spheres were evaluated. The results demonstrated that hollow reinforced ceramic spheres improve resistivity, with larger spheres yielding a more significant increase than smaller spheres due to the smaller sphere’s fragility and shorter fracture propagation distance.

The most commonly studied matrix materials in the literature are aluminum, zinc, magnesium, iron, copper, and titanium [22,31,33,41,42]. Aluminum, magnesium, and zinc are the most widely selected matrix materials among these commercially available materials. These materials possess excellent energy efficiency, corrosion resistance, and superior mechanical properties. Further, aluminum and magnesium are highly competitive structural materials for various industrial applications. Few authors have reported on titanium matrix composites may be due to their high production cost. The iron-based syntactic foams are also explored little. Marx and Rabiei have reported the mechanical response of the stainless steel matrix SFs [6]. This study develops a macroscopic domain of SFs in a finite element package, and the macroscopic stress-strain response is recorded. Such materials have potential applications in armor vehicles and lightweight structures. Also, there are few reports of syntactic foams containing zinc. Broxtermann et al. have reported both quasi-static and dynamic responses of the zinc matrix syntactic foams [41]. In another study, the performance of the zinc-based syntactic foams was studied at elevated temperatures [43].

2.3 HOLLOW PARTICLE

Different types of particles are studied as reinforcements in SFs. These filler materials are used for various reasons, from decreasing the cost of the components to modifying their strength and altering their magnetic, electrical, or fire-retardant qualities, as required by the intended uses. For the fillers of SFs, a few commercially available particles can be chosen, including glass, minerals, metal, ceramic, polymer, and industrial waste particles [44]. Typical filler materials include alumina, silica, hollow and solid glass particles, fly ash, and carbon black. The composite's intended qualities mainly determine the selection of materials. The form of filler particles has a significant impact on influencing the qualities of the SFs. Hence, particles are often

categorized according to shape, size, and shell thickness. Also, these particles have varying surface areas for the same volume, influencing the size of the interfacial zone between the particle and matrix resin. Due to the various corner radius of curvature and aspect ratios of each form, the stress concentration factor would vary for each. Compared to the other categories, spherical particle fillers are more common.

In recent years, using cenospheres, which are hollow spherical particles, has expanded significantly in creating core materials with low density and excellent damage tolerance. These low-density substances are categorized as close-cell foams known as “Syntactic Foams.” By adjusting the substance or density of cenospheres, the density of syntactic foams may be modified across a broad range.

Further, quasi-static in-situ compression studies on fly ash hollow particles reinforced SFs by Zou et al. showed the crack distribution and failure of the hollow particles due to external force [45]. Another study on the effect of heat treatment of Al-alloy and expanded perlite particles produced through counter gravity route has shown up to 80% energy absorption efficiency [46]. Recent studies on the AMSFs have widely discussed the energy absorption efficiency to assess the properties of various combinations of syntactic foams [47–49].

Synthesis of Hollow Particles

The manufacturing of hollow particles used in syntactic foams involves various methods to create spheres with controlled size, wall thickness, and properties. Here are some common manufacturing methods for producing hollow particles. Depnding up on the material and manufacturing methods, the hollow particle size and particle wall thickness can be controlled:

1. Glass Microspheres

Glass microspheres are often manufactured using a process known as glass microballoons or microsphere production. In this method, tiny droplets of molten glass are released into a high-temperature flame. The rapid cooling of these droplets forms hollow glass spheres. The size and wall thickness of the microspheres can be controlled by adjusting parameters such as the flame temperature and the rate of droplet formation.

2. Polymeric Microspheres:

Polymeric microspheres are commonly produced through suspension polymerization or emulsion polymerization. In suspension polymerization, monomers are suspended in a liquid and polymerized to form solid spheres. Subsequently, the removal of the core material leaves behind hollow polymeric microspheres. Emulsion polymerization involves the polymerization of monomers in an emulsion, resulting in the formation of hollow polymer spheres.

3. Phenolic Microspheres:

Phenolic microspheres are often manufactured using a technique called spray drying. In this process, a liquid phenolic resin is atomized into small droplets, and these droplets are rapidly dried in a hot gas stream, forming hollow microspheres. The resulting phenolic microspheres can withstand high temperatures, making them suitable for applications in syntactic foams that require thermal stability.

4. Metallic Microspheres:

Metallic microspheres, such as aluminum microspheres, can be produced through various methods, including atomization and mechanical milling. In

atomization, molten metal is broken into small droplets using high-pressure gas, and these droplets solidify into hollow spheres. Mechanical milling involves the mechanical grinding of bulk material into fine particles, and subsequent treatment can create hollow metallic microspheres.

5. Cenospheres:

Cenospheres are naturally occurring hollow spheres found in fly ash, a waste product from coal combustion. These hollow spheres are separated from fly ash using techniques such as froth flotation or centrifugation. Cenospheres are lightweight and have properties that make them suitable for applications in syntactic foams requiring low density and thermal insulation.

The manufacturing method chosen for hollow particles depends on the desired properties and characteristics required for the specific application of the syntactic foam. Each technique offers a way to control the size, shape, and composition of the hollow particles, allowing engineers to tailor syntactic foams for various applications in industries such as aerospace, marine, and automotive. Ongoing research continues to explore new and improved manufacturing techniques for hollow particles to enhance the performance of syntactic foams.

2.4 PROCESSING TECHNIQUES

The structural strength of the metal foams can be enhanced by introducing hollow particles. These hollow particles are made of metal [22,50], glass [51], and ceramic [52] particles and are introduced into the polymer or metal matrix. The typical syntactic foams materials are widely applicable in sandwich cores to absorb large deformations and impact energy. Based on their potential applications or unique properties, each category of foams offers a variety of manufacturing techniques.

Syntactic foams with unique matrix and hollow particle combinations can be produced using different manufacturing techniques. Therefore, the primary determining factor for the qualities of syntactic foams is the manufacturing procedure used. The stir casting technique is the most common method to create metal matrix syntactic foams (MMSFs).

Initially, the MMSFs are produced using the infiltration technique. In this technique, the hollow particles are filled inside a mold, and the liquid metal can infiltrate the gaps between the individual particles[53]. This technique is later modified into low-pressure and high-pressure infiltration techniques[53,54]. This technique enhanced the mixing of the hollow particles inside the matrix. Also, it reduces the unintended porosity inside the matrix that usually occurs due to the manufacturing techniques and poor interaction between the particles and the matrix. Compared to solid-state manufacturing techniques, liquid-state techniques are more reported effective.

The overall mechanical and thermal properties of the SFs are influenced by the properties of the matrix and hollow particles. A proper understanding of the physical properties and microstructural constituents of the SFs can yield tailored composite foams for specific applications. Pan et al. reported the effect of the solution-aging heat treatment on the strength of the aluminum alloy matrix SF produced through the liquid route[55]. The experimental investigation involves synthesizing foams and analyzing the material properties such as density, plateau stress, peak strength, densification strain and energy absorption. These properties are greatly affected by the matrix material and hollow particle size, and wall thickness. The most common techniques to produce SFs are liquid infiltration [35,53,54] and powder metallurgy [33]. A typical syntactic foam material consists of a matrix and hollow particles such as silica,

alumina, fly ash and metals. These particles are commercially available in a size range of 0.1 to 6 mm in diameter [6,16,52]. The effect of particle wall thickness and the effective density of the hollow particles helps design the material for a specific application on a commercial scale. Newsome et al. reported a relationship between thickness and diameter on the peak strength and toughness [56]. Apart from the hollow particle, the matrix also plays a crucial role in attaining the cumulative effect of strength and toughness. Meng et al. reported that a high entropy alloy as matrix material demonstrated maximum strength of 1220 MPa using the infiltration technique CoCrFeMnNi-based [25].

2.5 MECHANICAL STUDIES

The safety of the passengers during a collision and to prevent deformation beyond the safety limits is the primary concern of automotive sector. It is desired that the structural materials posses superior energy-absorbing property with reduced weight. In metal matrix syntactic foams (MMSF) the high strength hollow particles are randomly distributed within a soft matrix material [57]. These materials are well studied due to various superior properties that include reduced weight and enhanced energy-absorbing efficiency (EAE) [7]. Due to their high strength-to-weight ratio, extended plateau stress region, and sound-dampening capacity, materials with a high EAE are in high demand in industrial sectors such as shipbuilding, aerospace, construction, automobiles, and safety applications. [3,58–61]. The MMSFs using different combinations of matrix materials and hollow spheres, such as zinc alloys-cenosphere [62], Al Alloy- ceramic spheres [51,63], stainless steel - glass microspheres [64], and CoCrFeMnNi- Al_2O_3 [25] and functionally graded zinc alloy [65] have been reported. The mechanical and energy absorption capabilities of these MMSFs can be customised by modifying several parameters related to synthesis and

material selection. The focus of these investigations was on examining the mechanical properties of syntactic foams (SFs) composed of certain matrix and filler components. [7,25,66].

Aluminum is one of the commonly used material in several industries [67–70]. Many works on aluminum matrix syntactic foams (AMSFs) are reported due to its ease of production, affordability, and availability [48,61,71]. The key parameters to customise the properties of MMSFs are the material and size, volume fraction of hollow particles, and synthesis route. Optimizing these parameters enhances syntactic foam materials' properties and performance as structural materials.

The most commonly studied hollow particles are cenospheres [66], glass micro spheres [72], and alumina [73], of different sizes ranging from 0.02 to 8 mm. Su et al. reported the effect of the hollow particle size on the energy absorption capacity (EAC), which is 47 $MJ.m^{-3}$ at 0.9 - 1.6 mm diameters [61]. However, the hollow spheres made only a minimal contribution to the plastic deformation, while cracks were seen at or above a strain of 25%. The reduction in crushing strength of hollow spheres is apparent as their size increases. [51]. The alumina hollow spheres-based SFs of 3 mm diameter are studied by Licitra et al. [52,74]. The reported densities are between 2.11 g. cm^{-3} - 1.62 $g.cm^{-3}$. Sharp densification was observed without a significant plateau region due to the large sphere diameters.

Many findings have shown that the fraction of the reinforcement may directly influence the density of SFs and their mechanical properties [22,38,74]. Su et al. reported 1.78 g. cm^{-3} density at 43.31 % volume fraction using 2 - 3 mm diameter alumina and expanded hollow glass spheres [48]. Similarly, another study using aluminum matrix and alumina spheres (0.2 - 5mm diameter) achieved 1.56 g—cm^{-3}

density with 41.13 % porosity [55]. As the volume fraction increases for a unit volume, the matrix thickness between two adjacent spheres reduces. At higher volume fractions, the plastic flow of the matrix material is restricted under deformation. However, materials need sufficient elasticity for many structural applications, contributing mainly to plastic deformation. The reduction of syntactic foams' matrix fraction reduces hold capacity, causing rapid crack propagation and early failure [38].

The selection of processing conditions is an additional component that contributes to the attainment of high EAC. The production methods for Aluminum Metal Matrix Composites (AMSFs) are commonly categorized into two main approaches: the melt route and powder metallurgy. The processing techniques encompassed in this study consist of pressure infiltration castings [60], stir casting [75], squeeze casting [76], and powder metallurgy [66]. The data for specific energy absorption and absorption capacity exhibits a wide distribution, influenced by several factors such as processing processes, reinforcement material, and volume percentage of hollow spheres [25,60,61,66,77]. Aluminum matrix syntactic foams (AMSFs) produced by the powder metallurgy method offer numerous benefits, including decreased manufacturing expenses and the ability to accommodate various aluminum alloy systems. Nevertheless, limited scholarly research is available on the synthesis of aluminum matrix syntactic foams (AMSFs) employing powder metallurgy as the melt method [66,71].

In **Figure 2.2,** different simplified deformation models and the possible deformation pattern of an MMSF are highlighted. The initial elastic region is similar, whereas a typical cellular material may undergo linear hardening with a slope - E_p (hardening modulus), continuous hardening, non-linear hardening, and softening and hardening mode of deformation in the plastic region [78]. In a recent study on the

constitutive models to predict the deformation response of the SFs [79]. The deformation behavior of metallic foams with a range of densities, demonstrated the relationship between stress vs. EAC and EAE, respectively, by Cheng et al. [7]. The analytical models discussed are widely used in numerical studies.But, the influence of hardening modulus and EAE proparties are not widely discussed in the literature.

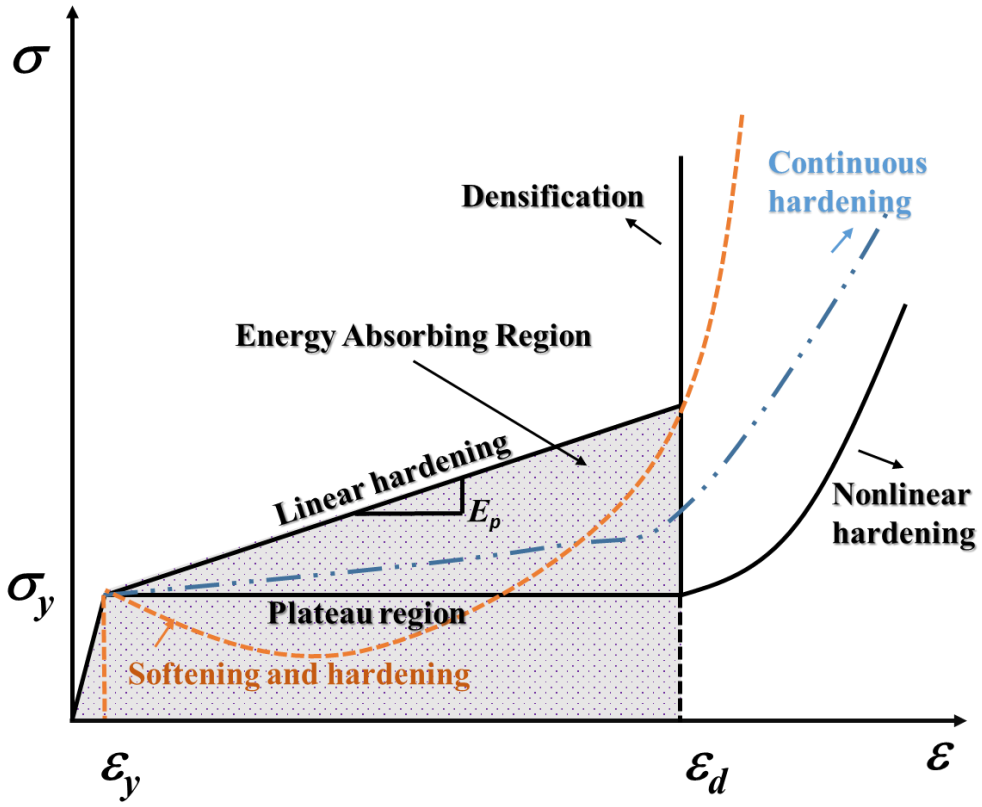

Figure 2.2 : The possible stress-strain models of cellular materials under compression.

Typical aluminum metal foams offer stress values < 15 MPa in contrast to the high elastic properties of syntactic foams and hybrid syntactic foams [80,81]. Developing low-cost advanced syntactic foam materials and understanding the plastic behavior of the AMSF is crucial to fit for several industrial applications.

The high-temperature studies on the cenospheres reinforced aluminum matrix SFs were reported by Mondal et al. up to 200 ºC temperature [82]. An early shift in the plateau stress during the deformation was reported in contrast to room temperature behavior. In another study, expanded perlite-reinforced foams tests have shown a decrease in the mechanical properties with an increase in temperature up to 500 ºC. This trend is similar to open/ closed cell foams due to the thermal softening of the matrix material[83,84]. Also, other aspects that drive the deformation behavior of SFs at elevated temperature is the work softening and transition of brittle to ductile behavior of the constitutive materials [85].

In summary, quasi-static properties may not be sufficient to replace conventional materials in automobiles and aerospace industries using the SFs. Balch et al. performed dynamic compression studies at 2300 s^{-1} on aluminum-ceramic microspheres and reported a peak stress value of 248 MPa. The matrix and reinforcement of the samples are examined under micro-compute tomography, which reviles the pour distribution and particle failure [86]. In another study, silicon carbide hollow particles induced SFs with a density of 1.819 g/cm^3 have shown a maximum compressive strength of 181 MPa [87]. During the dynamic loading, different combinations of matrix and reinforcements yield at least a 10-30% rise in peak stress under dynamic compression[41,52,88].

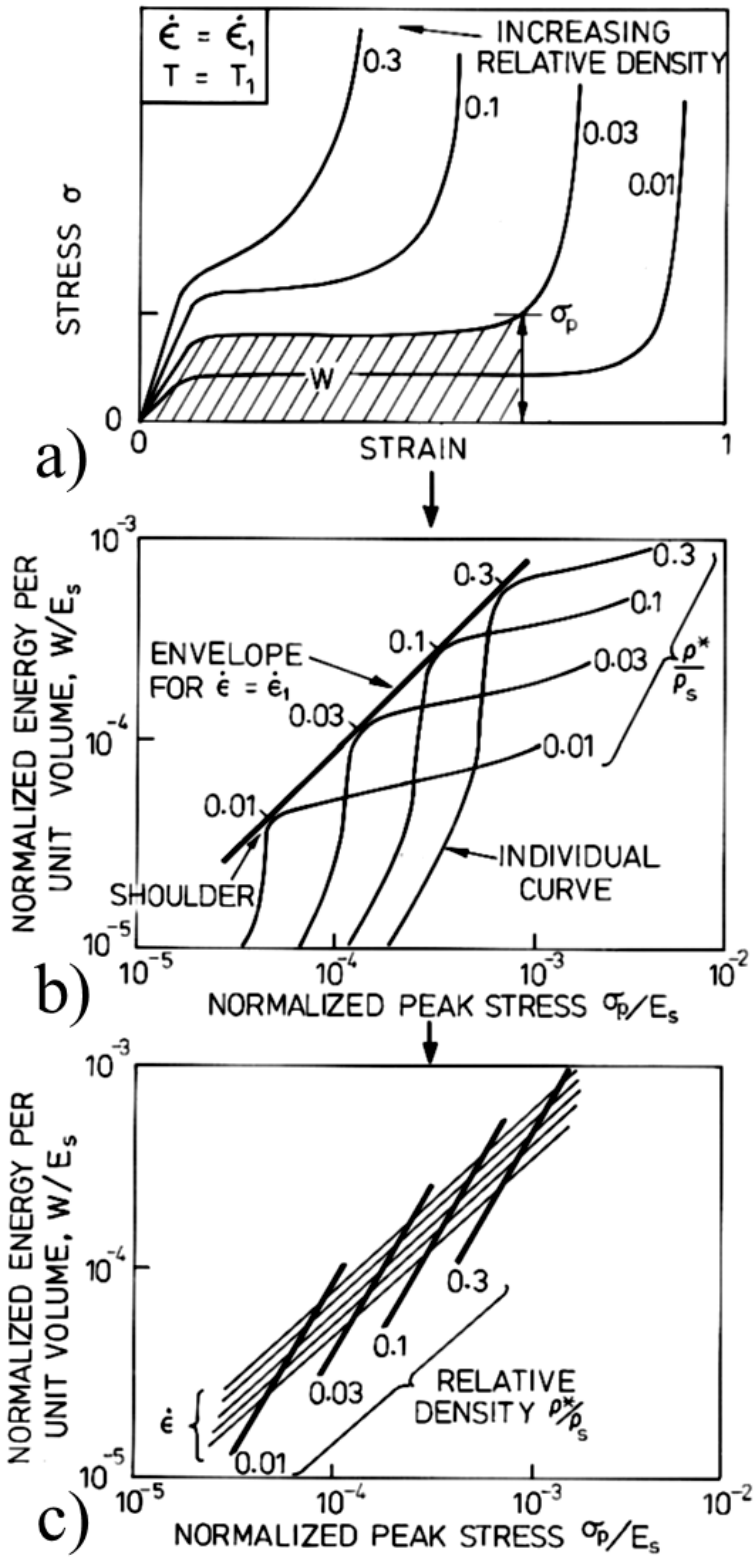

Figure 2.3 : Schematic of energy absorption properties (a) Ideal energy absorption efficiency[89] (b) Energy absorption diagram and (c) Energy absoprtion properties of foams [90].

In the literature, some energy absorption properties on syntactic foams are reported [47,49,89,91]. The energy absorption properties are quantified using three critical parameters. These properties are widely considered within the design framework of energy absorption and weight reduction in cellular materials [89,92]. The energy absorption efficiency, to identify the maximum energy absorbed by the materials during deformation as shown in **Figure 2.3(a)**. Also, the essential quantity, the specific energy, is computed as the maximum amount of energy that can be lost per unit weight of the specimen. Finally, the energy absorption capacity is normalized data of energy absorption vs. stress with the elastic modulus of the matrix. The normalized energy absorption (W^*) vs. stress (σ^*) diagram at different relative densities is shown in **Figure 2.3(b-c)**. The line connects the point's locus at a particular strain value. Usually, these locus points are considered at the densification strain.

Syntactic foams, captivating materials boasting an enticing blend of low density and remarkable mechanical properties, have garnered significant interest across diverse engineering disciplines. Delving into the mechanical behavior of these fascinating materials, both under static and dynamic loading, is crucial to unlocking their full potential and ensuring their safe and effective implementation. Strength and stiffness studies under static compression unveil the inherent strength and stiffness of syntactic foams during crushing. Factors like microsphere volume fraction, shell material, and matrix properties significantly influence these mechanical responses, providing valuable insights for material design and selection.

Energy absorption properties also evaluate the energy absorption capabilities of syntactic foams, essential for applications demanding impact resistance. The crushing

of hollow microspheres and matrix deformation contribute to energy dissipation, making these foams attractive for protective structures.

Under dynamic loading when SFs are subjected to rapid loading, such as impacts these materials exhibit distinct mechanical behavior compared to static conditions. Dynamic testing using Split Hopkinson Pressure Bars (SHPB) probes the high-strain-rate response, revealing increased strength and energy absorption compared to static tests. Dynamic loading can trigger unique failure mechanisms in syntactic foams, including microsphere fracture, matrix yielding, and interfacial debonding. Understanding these mechanisms through microscopy and fractography is vital for optimizing material design and predicting performance under real-world dynamic scenarios.

By meticulously studying the mechanical behavior of syntactic foams under both static and dynamic loading conditions, researchers and engineers gain invaluable knowledge for tailoring these materials to specific applications. This comprehensive understanding unlocks their true potential in areas ranging from lightweight structures and energy absorption systems to protective gear and high-performance composites.

2.6 NUMERICAL STUDIES

Apart from experimental studies, some literature on syntactic foam's micro and macroscopic properties uses analytical and finite element(FE) routes [93–96]. The micromechanics-based models provide few insights into understanding the compressive behavior of the foams. Unlike particulate composite materials, the micromechanical models for SFs require sophisticated methods to estimate the effective elastic modulus. In earlier studies, Lee and Westmann developed a model to identify the upper and lower bounds for shear and bulk modulus values for SFs [93].

Later, in subsequent investigations, a significant amount of work is performed on polymer-based foams [29,30]. The shear and bulk modulus of polyester resin-based foams with a 35% volume fraction of hollow particles is reported by Huang and Gibson [94]. In this model, the particles are considered suspended in a dilute medium. The model results overestimated the effective modulus at high-volume fractions since the displacement due to the particle interactions is not considered. Porfiri and Gupta propose a single inclusion problem-based model to find effective properties even at higher volume fractions that match the experimental data [38]. These micromechanics-based analytical models may estimate the elastic properties of various polymer matrix-based SFs with reasonable accuracy. However, these studies consider the interface between the matrix and the particles as perfectly bonded and provide upper and lower bounds of the predicted data. Also, these models may not consider the composite material's distribution of particles and bond interface properties[95]. In this regard, computational micromechanics models based on representative volume elements (RVE) are developed, which may predict the material properties more accurately.

These FE models of syntactic foams consist of randomly distributed particles with uniform shell thickness inside a matrix. Bardella et al. developed an RVE-based FE model to study the elastic properties of the SFs and compared it using theoretical models such as Mori-Tanaka, and Self-Consistent[97]. In the literature, the RVE-based modeling aimed at predicting the elastic properties. Later, the studies are extended to produce a full-scale model to reproduce the stress-strain response during plastic deformation[6]. Szlancsik et al. studied the micromechanical properties of aluminum alloys and compared them against the numerical and FE element modeling using a full-scale finite element model [40]. Al99.5-GM-O AMSFs-based full-scale models are developed to study the elasto-plastic behavior under free compression [50].

Additionally, few works focused on generating the RVE domain using advanced algorithms and micro-computer tomography scans [98,99]. A mathematical approach to stress-strain behavior is reported by Lorgeril et al. [100]. This study is extended to a continuous approach by Orbulov & Májling to produce the macroscopic behavior of the SFs and the peak function [101].

The emphasis of the RVE models in the literature is to study elastic behavior. Full-scale models are developed to mimic the elasto-plastic behavior of the SF structures. However, applying the RVE models to study the elasto-plastic response needs more attention to reduce the computational cost and ease of analysis. This study examines the elastic and elasto-plastic responses of AMSFs under compression. With the help of a user-defined algorithm, different volume fractions of RVE models are developed and studied. The elastic constants are identified using the analytical and FE-RVE model. Different analytical models are studied and compared against the properties obtained from numerical methods.

Further, the elasto-plastic behavior of Al_2O_3-reinforced aluminum matrix syntactic foam (AMSF) comparisons to the experimental data are discussed. The FE-based stress-strain responses are compared against experimental data. The effectiveness of sensitivity parameters for different models against the RVE is examined.

2.7 CORROSION STUDIES

In the literature, polymer and metal-based syntactic foams are widely studied. Many works on metal matrix syntactic foams (MMSFs) are reported on structural properties such as compression tension [28] under different loading conditions. The reports on electrochemical behavior of MMSFs are limited. The microstructure and

the corrosion properties of Ti-based SFs are reported by Mondal et al. under the influence of NaCl solution. It is observed that there is a significant drop in the corrosion rate with the addition of cenospheres[102]. Qureshi et al. studied the electrochemical response of magnesium reinforced with hollow silica particles under the influence of simulated body fluids. The presence of hollow nanospheres of 1.5% in the magnesium matrix has enhanced corrosion resistance [103]. In another study, the effect of cenospheres-reinforced aluminum SFs is studied produced through the powder metallurgy route. This work demonstrates the influence of volume fraction using the techniques of potentiodynamic polarization and electrochemical impedance spectroscopy [104].

Another study on AZ61 Mg alloy-based SFs in the presence of 3 wt.% NaCl solution has been reported [8]. These microwave-sintered Mg-SFs have shown reduced current densities with increased cenosphere volume fraction [105]. There are few studies on the corrosion behavior of AMSFs. In research on Al-Alloy syntactic foams, including hollow glass particles, the authors indicate that the syntactic foam samples exhibit more excellent corrosion resistance than the base alloy in a 3.5% NaCl solution [9]. This is due to alumina hollow particles, which lower the matrix's surface area.

The studies on MMSFs find their applications in extreme environments such as marine, automotive, aerospace, and defense industries to reduce weight and retain structural stability. In this regard, aluminum matrix syntactic foams (ASFs) are widely suited for lightweight energy absorption applications due to their low relative density, high specific energy, and significant compressive deformations. The effect of alumina hollow particles under compression loading is well studied in the earlier findings [35]. The alumina-reinforced AMSFs have shown maximum yield stress of 350 MPa under

compression. The hard ceramic hollow particles have proven to show excellent mechanical properties. The utilization of alumina hollow particles as support structures leads to enhanced moduli and strengths in ASFs, surpassing those of traditional foams synthesized through the use of gas-releasing chemicals. However, the study of electrochemical properties is still unexplored despite its high reputation for structural properties.

The scope of using syntactic foams in structural applications where they may be subjected to a corrosive environment. There is a gap in verifying their corrosion behavior sufficiently. Thus, more research is necessary to give additional information and understanding of their corrosion behavior, particularly for those manufactured using a powder metallurgy (PM) technique. So, the present work aims to explore the influence of microspheres on the corrosion behavior.

2.8 GAPS IN LITERATURE AND OBJECTIVES

In this direction, the literature study above suggests that a higher volume fraction of hollow spheres may lead to low-density values, but the plastic deformation is greatly affected. Combining high-strength brittle alumina spheres with soft silica-based cenospheres may improve the plasticity during the plateau region of syntactic foam materials. The present investigation aims to study the influence of single and multiple hollow spheres on the overall performance of AMSFs. The material response to the densification strain has been explored without compromising the materials' overall strength.

Alumina particles are known for their high strength and refractory nature. Despite their high density (4 g/cm^3), these materials apply to various industrial needs. Like fly ash cenosphere, the production cost of the alumina hollow particles is

minimal. Using low-cost filler materials such as cenosphere and alumina is economically and commercially beneficial. Earlier studies have indicated that fly ash particles-based SFs are highly explored. Several researchers have also demonstrated the benefits of using treated fly ash in various polymer matrices. However, the alumina hollow particles reinforced SFs are less studied, and their influence on the overall structure concerning their size, volume fraction, and shell thickness needs to be understood.

The primary interest of any material design is to improve its load-bearing capacity, identify the maximum failure stress, and avoid early structural collapse. So, the properties of the materials under different loading conditions provide a better estimate to assess the impact of loading and temperatures on the material. In this context, it is observed that there is a scope to identify and study different loading and temperature conditions and their energy absorption behavior of the AMSF system.

The emphasis of the RVE models in the literature is to study the elastic behavior, and macroscopic models are developed to mimic the elasto-plastic behavior of the SF structures. However, applying the RVE models to study the elasto-plastic response needs more attention to reduce the computational cost and ease of analysis.

In the literature, a few corrosion studies on ASFs have been reported, leaving a gap in understanding the effect of volume fraction and particle size on the corrosion behavior of the ASFs. This work aims to bridge the gaps in understanding the electrochemical response of the aluminum-reinforced aluminum matrix syntactic foams under different pH conditions. To the best of the authors' knowledge, a comprehensive analysis of the ASFs produced using powder metallurgy route exposed to three different chemical combinations is reported for the first time. The corrosion

behavior of three different volume fractions and three particle sizes is studied using potentiodynamic polarization and electron impedance spectroscopy.

2.9 SUMMARY AND IMPLICATIONS

Metal matrix syntactic foams are an essential category of lightweight cellular materials applicable in various industrial applications, such as the aerospace, automotive, and marine sectors. The literature review focuses on the most popular matrix metal, synthesis techniques, influence on physical and mechanical behavior, industrial uses, challenges, and future possibilities. The summary of the literature review is as follows:

- The initial studies are dedicated to polymer-based SFs. However, the MMSFs showed promising properties under different loading conditions over conventional foams and polymer-based SFs.

- Aluminum and magnesium are commonly explored in the literature under the lightweight materials category. However, there is a scope to understand the various other properties that can make these materials commercially viable.

- Among the processing techniques, stir casting and infiltration techniques (gravity, pressure, gas assisted, negative pressure, and mechanical stirring) routes are the most reported technique to produce MMSFs foam.

- The literature uses hollow particles such as cenosphere, hollow glass spheres, lightweight expanded clay aggregates, alumina, expanded glass, hollow iron particles, and ceramic particles to develop MMSFs.

- It is observed that the failure behavior of the hollow particles remained a challenge in metallic syntactic foams. This phenomenon is due to other driving factors such as processing techniques, matrix particles interface properties, particle size, and wall thickness. A detailed study of processing techniques, particle size, and volume fraction may address this issue.

- Due to the broad applicability of aluminum, MMSFs are prominently focused on the aluminum matrix syntactic foams.

- The energy absorption characteristics of the SFs are significantly influenced by various factors, including manufacturing techniques, particle percentage inside the matrix, size of the hollow spheres, material, and the heat treatment methods employed.

- The electrochemical aspects of the AMSFs and MMSFs are seldom studied in the literature, leaving a gap in understanding the effect of various aqueous media and particle size on solutions on the electrochemical response of the AMSFs.

- To achieve a reduced densities in the MMSFs multiple hollow particles with different densities may be added. This hybrid combination may contribute to enhancing the mechanical properties and reduce the weight of the strcture.

Based on the detailed research survey and the gaps identified. The following objectives are formulated and presented based on the preceding considerations in the following chapters. Also, a work plan based on the proposed objectives is shown in **Figure 2.4.**

The proposed research objectives are as follows:

1.	To produce AMSFs using the powder metallurgy route.
2.	To study the microstructure of AMSFs and the density of the SFs.
3.	Study the mechanical properties of AMSFs under different loading conditions and temperatures. Understanding the corrosion properties under different pH conditions is essential.
4.	Draw the relation between microstructural and mechanical properties of AMSFs and understand the failure behavior of AMSFs.
5.	To develop computational models of AMSF and to simulate the same to evaluate the energy-absorbing applications using experimental data.

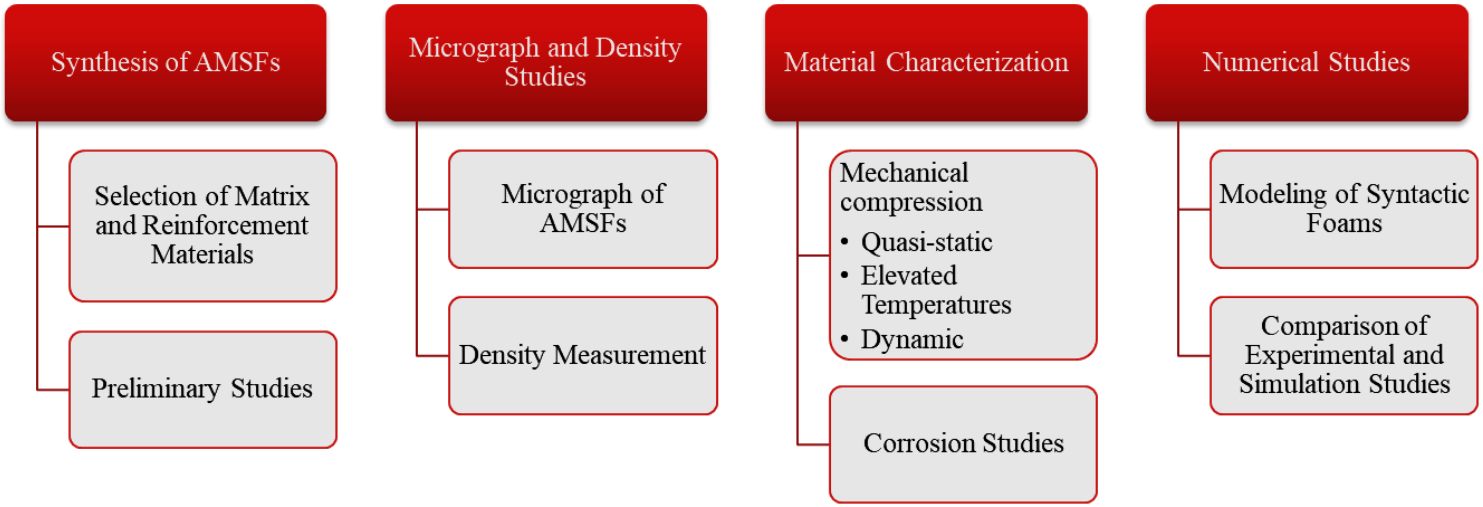

Figure 2.4 : Research work plan based on the objectives proposed

Chapter 3: Development and Characterization of AMSFs

This chapter details the selection of raw materials, processing parameters, and manufacturing techniques adopted to produce aluminum matrix syntactic foams (AMSF). It also includes techniques to be adopted to produce the metal matrix syntactic foams successfully using the powder metallurgy route. Later in this chapter, the characterization techniques and evaluation schemes are explained to assess the properties of the syntactic foams, such as density, mechanical studies, and corrosion response of the materials under different loading rates and temperatures.

3.1 INTRODUCTION

Metal matrix syntactic foam is a unique material that finds several applications where weight reduction and structural strength are of significant interest. It is observed that multiple attempts are made to produce such structures using both polymer and metal matrix-based syntactic foams. Among these materials, aluminum is of significant interest due to its versatile applications, ease of manufacturing, and machining properties. In this study, aluminum is selected as a matrix material to capture the effect of particle size and the volume fraction of the ceramic hollow particles. Several studies have discussed the behavior of glass-based and cenosphere-reinforced SFs. Sparse literature is available on alumina-based Sfs and its mechanical response. However, a comparative study is made among the alumina and cenosphere-based SFs.

The liquid route is the widely used fabrication technique for aluminum matrix syntactic foams. In this route, alternative techniques such as gravity infiltration, low-

pressure, and high-pressure infiltration techniques also propose elsewhere [32,53,54]. Despite the various advantages of the liquid route proposed in the literature, this technique has a few limitations. The infiltration pressure and temperatures must be considered to mix the particles uniformly (Orbulov and Dobránszky 2008). The hollow particles tend to float on the top surface of the liquid layers due to the buoyancy effect. In liquid routes, the temperatures are significantly high, so only particles that can withstand high temperatures can be used in this technique[81]. For example, hollow glass particles soften at 600 ^{o}C, and thus it is relatively challenging to obtain SFs using the liquid route [108].

Due to several advantages, the powder metallurgy (PM) route is widely applicable in conventional composite materials. This technique offers excessive control over the volume fraction and particle distribution, eventually leading to tailored microstructure, material, and mechanical properties. The application of the PM route to syntactic foams was discussed earlier [66,108] for a matrix with high melting points. However, there is a scope to apply the PM to soft materials such as aluminum and magnesium to reduce manufacturing costs and production time. This technique also provides the versatility to produce different sizes and shapes of components and the scope to design the materials according to the industry's needs.

3.2 RESEARCH METHODOLOGY AND EXPERIMENT DESIGN

3.2.1 Fabrication of Al_2O_3-reinforced syntactic foams

The AMSFs reinforced with hollow alumina particles are prepared using the powder metallurgy process. A pure aluminum powder of <50 μm particle size and the Al_2O_3 hollow particles of different sizes are selected for processing. Aluminum powder and alumina hollow particles are procured from the Sisco Research

Laboratories Pvt. Ltd. and Kaifeng Datong Refractories Co. Ltd., respectively. As received, the chemical compositions of the raw materials are shown in **Table 3.1**. The hollow particles are segregated according to the three sizes using the sieve sizes **1**- 0.45-0.6 mm, **2**- 0.85- 1.2 mm, and **3**- 1.7 mm by carefully sieving using the vibratory sieving machine. The distribution of the particle's wall thickness and diameters for each batch selected while synthesizing the syntactic foams is shown in **Figure 3.1(a-b)**. It is observed from the literature that the structural stability is questionable for high-volume fractions (above 40%) of hollow particles with an average diameter above 4 mm under room temperature conditions[51,53]. In this regard, it may be interesting to understand the response of the hollow particles under low-volume fractions with smaller diameters.

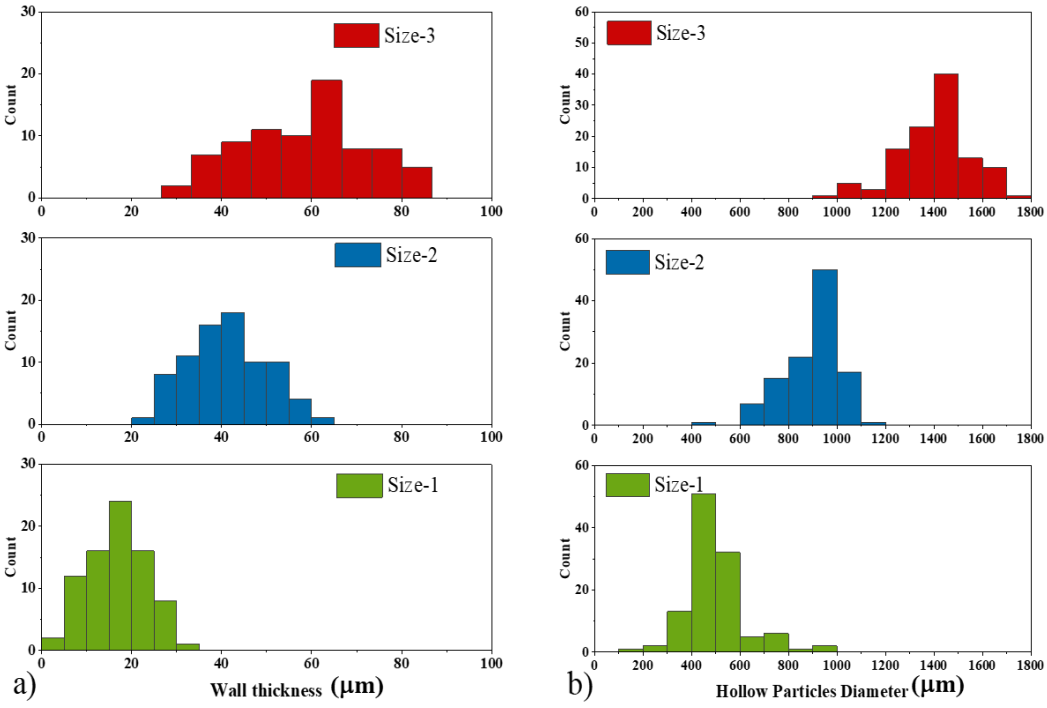

Figure 3.1 : Size distribution of hollow particles selected for the study (a) Wall-thickness, (b) Diameter

Table 3. 1 : Chemical composition of the raw materials.

Material	Chemical composition (weight percentage)
Aluminum	99.988%
Alumina Hollow particles	$Al_2O_3 \geq 99$, $SiO_2 \leq 0.18$, $Na_2O \leq 0.15$, $Fe_2O_3 \leq 0.15$

After segregating the particles based on size, wall thickness and the diameter of a sample group from each size are collected using optical and FE-SEM images to measure the particle's thickness-to-diameter ratio (t/D). The representative micrographs are shown in **Figure 3.2(a-c)** using the scanning electron microscopy (SEM) of FEI make and Apreo LoVac model. An earlier study on alumina-based SFs shows that a high volume fraction of the hollow particles leads to structural failure. Thus, three different volume fractions (V_f - 10%, 20% & 30%) of hollow particles are selected as per the weight ratio. As shown in **Figure 3.3**, each particle size was allowed to mix uniformly with matrix powder particles using a vibratory ball mill in the absence of the balls to avoid the fracture of the hollow particles. During this step, 5-10 ml methanol is added for every batch of powder hollow particles mixture. This may enhance a uniform powder coating on the shell walls and avoid overheating.

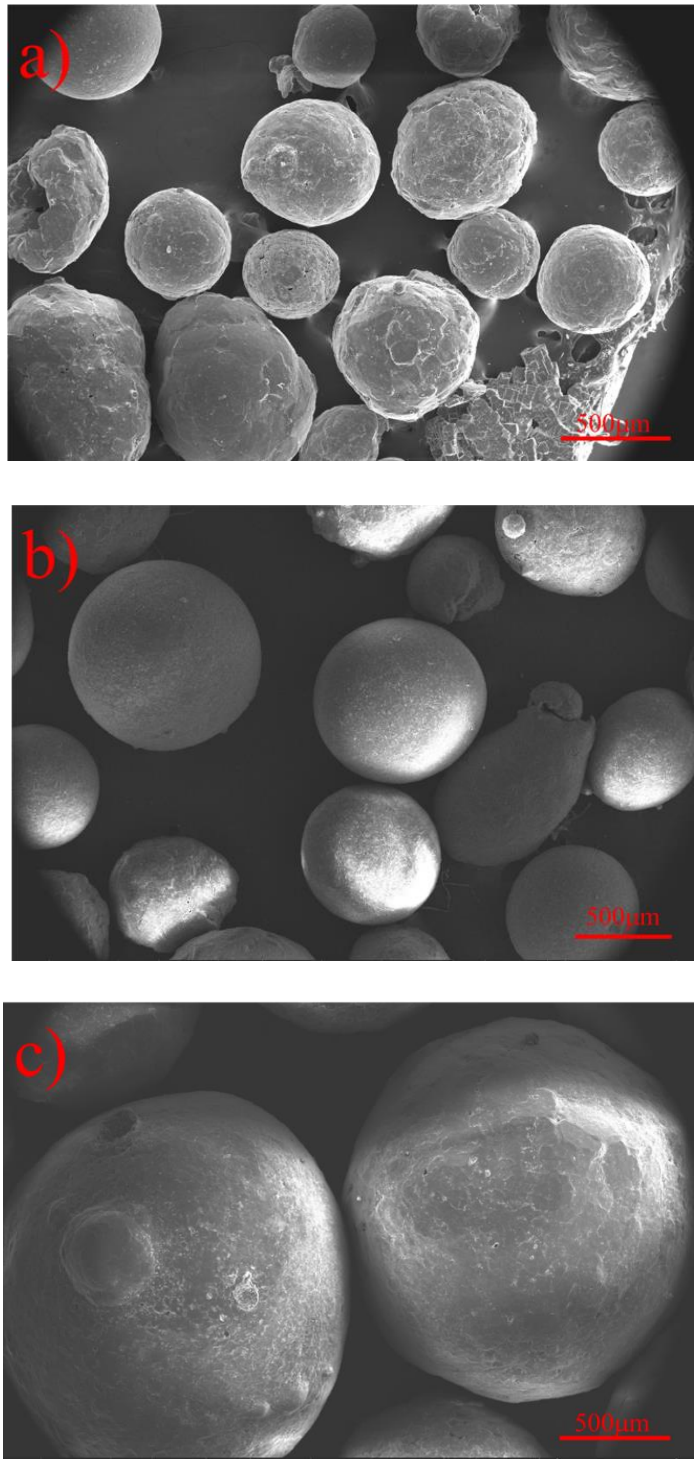

Figure 3.2 : Micrographs of Al_2O_3 hollow particles of different sizes (a) 500 µm, (b) 1000 µm, (c) 1500 µm obtained using SEM of FEI make and Apreo LoVac model.

Further, for each volume fraction, the powder plus hollow particles mixture is cold compacted uniaxially to a size of 13 mm diameter and 10 mm height samples. The H/D ratio of all the samples tested in this study is close to 0.75. These samples are sintered at $0.8T_m$ of matrix material for 4 hours in an inert atmosphere without external pressure. The initial studies made during the synthesis of aluminum matrix syntactic foams showed reduced densities compared to the theoretical values. With the increase in sintering temperature, the density of the syntactic foams improved close to the theoretical density. At 0.8 Tm and above, no change in the measured density is observed. So the sintering temperature is considered as 0.8 Tm of the matrix material. A detailed schematic of the synthesis process and the density optimization curve for different sintering temperature are shown in **Figure 3.3(a) & (b)**. Cho et al. and Mondal et al. explained the solid phase process to produce metal matrix syntactic foams (MMSFs) [33,108].

The microstructure of the processed SFs is studied using a freeze-fracture technique by immersing the samples in liquid nitrogen solution for 5 min and breaking it along the cross-section using a hammer to see the fractured surface of the SFs. This technique was discussed in some earlier studies [108]. The surface of the samples and particles are examined using an FEI-supplied Field Emission Scanning Electron Microscopy (FE-SEM). To study the distribution of the hollow particles cross the area of the samples.

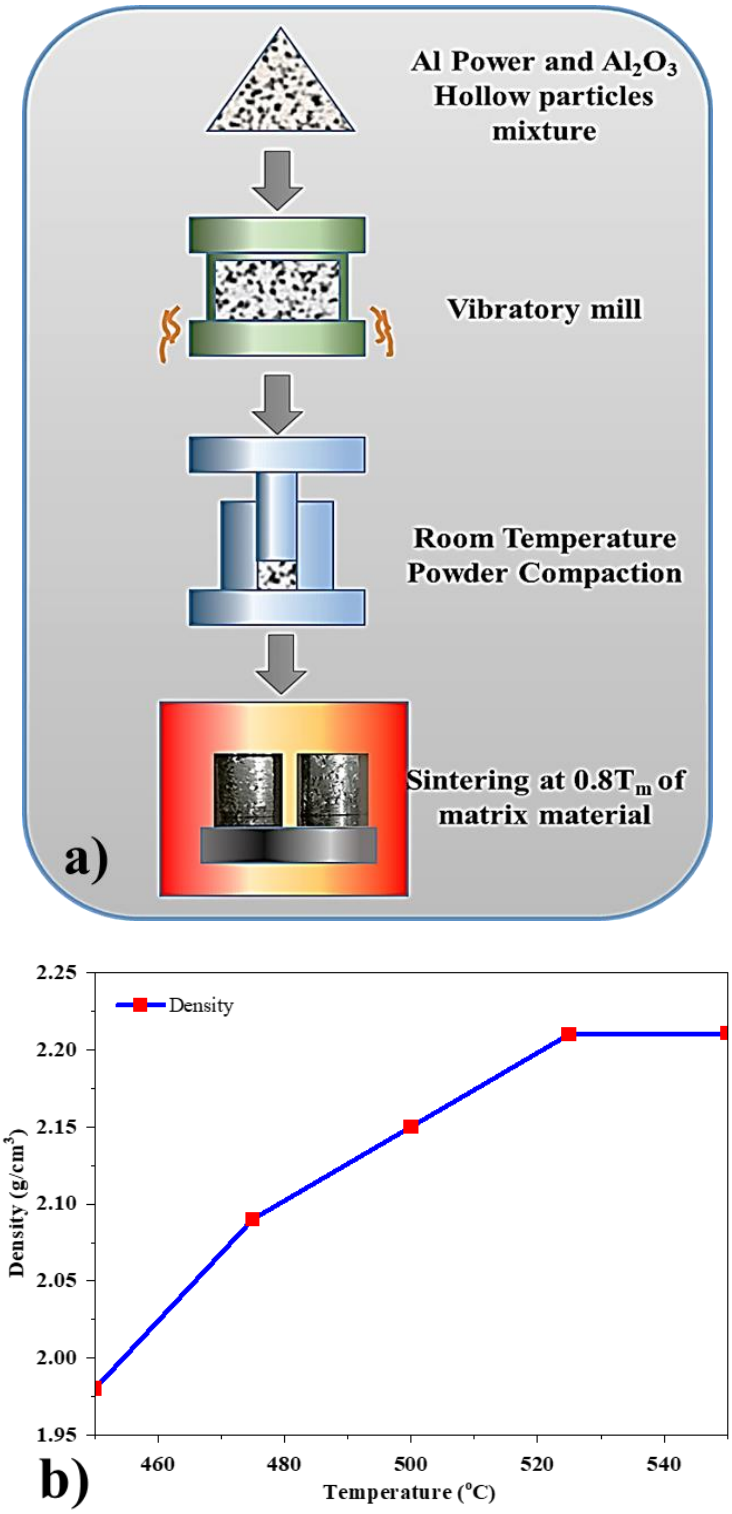

Figure 3.3 : (a) Schematic of powder metallurgy route to produce AMSF material and (b) Sintering Temperature optimization to produce syntactic foams.

3.2.2 Density measurement

The theoretical density of the hollow particles is measured by considering the outer diameter of the hollow particles and cell wall thickness measured using the SEM images for a large sample group. In this study, the density of the alumina without pores is considered from the literature [109]. Further, the theoretical density of the composite is measured using equation (2):

$$\frac{t}{D} = 0.5\left[1 - \left(1 - \frac{\rho_{HP}}{\rho_{Al_2O_3}}\right)^{1/3}\right] \tag{3.1}$$

$$\rho_{SF} = \left(\rho_{HP} \times \left(V_f\right)_{HP}\right) + \left(\rho_m \times \left(1 - \left(V_f\right)_m\right)\right) \tag{3.2}$$

Where the ρ is the density and V_f is the volume fraction. The subscript *SF*, *HP*, and *m* represent syntactic foam, hollow particles, and matrix. Also, t- wall thicknes, D- diameter of hollow particles. The bulk density of the alumina is considered in the literature as 3.9 g/cm^3 [109].

The experimental density of the samples was measured using the Mettler Toledo density kit. These experimental densities reported in this work are the average data obtained from at least three samples.

The sintered samples received from the furnace are cleaned with alcohol, and the weight of the specimens is measured using an analytical balance of up to 10^{-4} grams precision. Respective dimensions are measured using a digital micrometer. The experimental density (mass/volume) has been measured for all samples. Five samples are measured for each condition to get the average density value. The equation 3.3 is used to measure the experimental density of the composite using mass of the material and its volume. Whereas the equation 3.2 is used to calculate the theoretical density of

the composite using the actual density of the hollow particles and matrix materials. The actual density of the hollow particle is measured from the equation 3.1.

Theoretical density:

$$\rho_c = \frac{1}{\sum(W_k/\rho_k)} \tag{3.3}$$

3.3 MECHANICAL TESTINGS

3.3.1 Quasi-Static Room-Temperature

A representative image of samples, compression testing setup, and deformation of samples before and after compression tests are shown in **Figure 3.4**. At least three samples are tested for each sample condition. The material properties measured are the average values of at least three specimen data for each condition. The top and bottom faces of the cylindrical pieces are ground using standard metallurgical techniques to achieve a flat surface. The compression tests are conducted at a strain rate of 10^{-3} $s^{-1,}$ and the data is obtained using the cross-head displacement (resolution- 0.1 μm). Young's modulus is measured using a standard measuring technique. The elastic properties from the stress-strain curves were measured separately for all the samples, and the respective volume fraction's average values were reported.

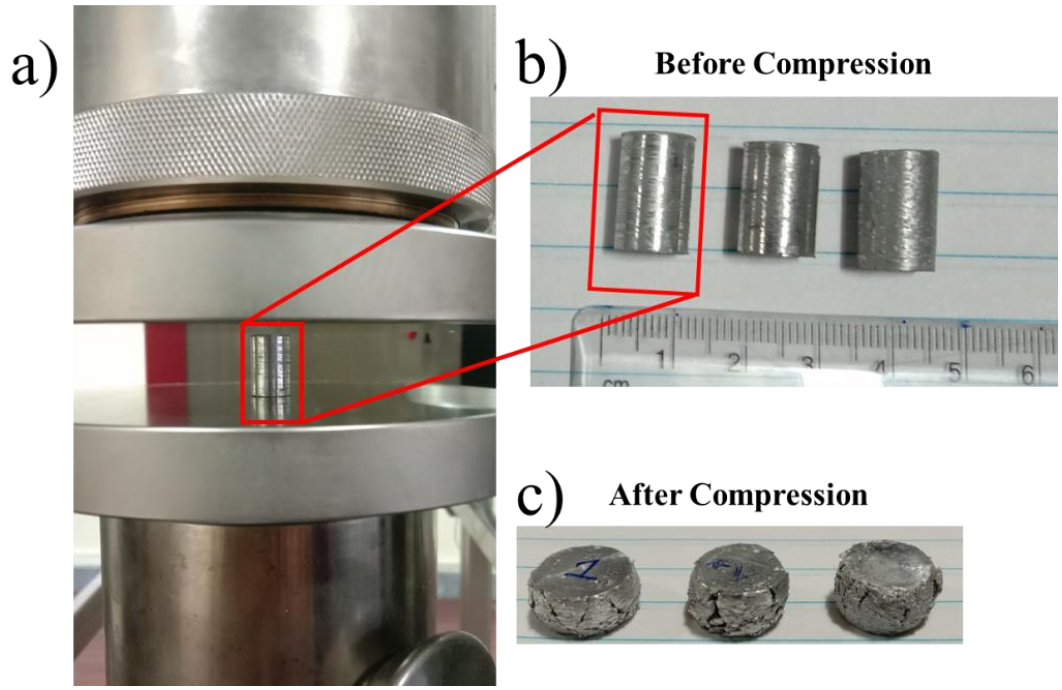

Figure 3.4 : Representative digital image of the (a) Compression testing arrangement, (b) Samples before testing (10%, 20%, 30% volume fraction), and (c) Samples after testing under uniaxial compression.

3.3.2 Quai-Static High-Temperature

Syntactic foams are known for their energy absorption ability under compression. To probe this behavior and to understand the role of radius ratio on the mechanical properties of SFs, compression studies are performed on nine different samples at different temperatures and strain rate settings. The mechanical studies are conducted at different temperatures (100, 175, and 250 ºC) under quasi-static (0.001 s^{-1} strain rate) mode using Zwick Roell Z100 of load cell capacity 5kN with a temperature chamber up to 250 ºC as shown in **Figure 3.5**. Before testing the samples, the initial height and diameter of the pieces are recorded, and stress vs. strain data is measured based on the respective dimensions. The typical sample dimensions are 13 mm in diameter and 8 mm in height for all the test conditions.

Figure 3.5 : Compression testing setup used to perform quasi-static room temperature and high-temperature tests

3.3.3 Dynamic Testing

The design and construction of an split hopkinson's pressure bar (SHPB) test rig are known for dynamic testing of diverse materials under compression/tension at strain rates significantly more than a few hundred times per second. The Hopkinson Pressure Bar has mainly been used to evaluate a material's transient response to dynamic stress. It comprises a high-pressure air-filled loading apparatus with a pressure chamber, a cannon barrel, and a release mechanism. Additional components include incident, transmission, and a striker bar supported by Teflon bearings. The striker, incident, and transmitted bars' lengths are 152, 1220, and 1220 mm, respectively, while the diameter of the bars is 21 mm. Al7075 hardened aluminum alloy with high yield strengths (450 MPa) to endure very high impact velocities in the material is used for striker bars and

pressure bars. On a rigid beam, these pressure bars are placed. The SFs specimens are sandwiched between the two pressure bars with an aspect ratio of 0.75 and an average sample diameter of 13 mm. The radial expansion of the specimen during loading creates a frictional limitation at the pressure bar-specimen contact. When the specimen is at rest, when frictional effects are at their peak, the specimen may deform unevenly. These frictional limitations have been alleviated by applying a thin lubricant coating at the interfaces. Therefore, molybdenum disulfide lubricant is used in the current investigation.

Figure 3.6 displays a digital photograph of the SHPB setup. In these trials, the striker bar's axial contact on the input bar's free end, accelerated by a long cannon barrel, starts the loading pulse. Regulators manage the air pressure to set the striking bar's velocity at the required velocity. Strain gauges are placed at a distance of 18.5 cm from the junction ends of the incident and transmitter pressure bars. These gauges have a resistance of 350 Ohms and a gauge factor of 2.10 at room temperature.

Figure 3.6 : Image of the SHPB setup used to test the SF samples.

The digital processing oscilloscope setup amplifies and records the strain gauge signal. Following the striker bar's impact, the input pressure bar experiences an elastic compression wave with a constant amplitude and finite duration. Since the pulse in the incidence bar is twice as long as the striker bar, the incident pulse wavelength may be changed by utilizing striker bars of various lengths. To reduce wave dispersion and achieve the ideal waveform, the SHPB is additionally modified using pulse shapers. The striker bar's impact velocity and pulse amplitude are both inversely correlated. When the compressive loading pulse from the incidence pressure bar reaches the specimen, some pulses are reflected off the contact between the specimen and the input bar. At the same time, the remaining portion is transmitted to the transmitted bar. The magnitudes of these transmitted and reflected pulses can determine the specimen's physical characteristics. In order to reduce the effects of longitudinal and lateral inertia and wave dispersion inside the specimen, the total specimen dimensions must be minimal. Due to the loading pulse's length relative to the specimen's wave transit time, the short specimen experiences many internal reflections throughout the loading pulse. The specimen's stress distribution is homogeneous due to the reflections.

SHPB Calculations:

The SHPB calculations to calculate the stress-strain response obtained from the wave data received from the strain gage. Consider the stress in the bar [110].

$$\sigma_x = \sqrt{E.\rho}.v = \rho.C_0.v \qquad (3.4)$$

The stress wave velocity C_0 is, of course, the speed at which the wave passes along the bar in x direction:

$$C_0 = \frac{dx}{dt} \tag{3.5}$$

$$\sigma = \frac{E}{C_0}.v = \frac{E}{C_0}.\frac{du}{dt} \tag{3.6}$$

and since

$$\varepsilon = \frac{\sigma}{E}$$

$$\varepsilon = \frac{1}{C_0}.\frac{du}{dt} \tag{3.7, 3.8}$$

$$\therefore u = C_0 \int \varepsilon dt$$

The total displacement of the ends of the bars at time T after the start of the pulses

$$u_1 = C_0 \int_0^T \varepsilon_I dt + (-C_0) \int_0^T \varepsilon_R dt = C_0 \int_0^T (\varepsilon_I - \varepsilon_R) dt$$

$$u_2 = C_0 \int_0^T \varepsilon_T dt \tag{3.9(a-b))}$$

Average Axial Strain in Specimen at time T

$$\varepsilon_s = \frac{u_1 - u_2}{L_0} = \frac{C_0}{L_0} \int_0^T (\varepsilon_I - \varepsilon_R - \varepsilon_T) dt \tag{3.10}$$

Strain Rate in Specimen

$$\dot{\varepsilon}_s = \frac{du_s}{dt} = \frac{C_0}{L_0}(\varepsilon_I - \varepsilon_R - \varepsilon_T) \tag{3.11}$$

Average Axial Stress in Specimen:

Load on face 1 of specimen: $P_1 = EA(\varepsilon_I + \varepsilon_R)$

(3.12(a-b))

Load on face 2: $P_2 = EA\varepsilon_T$

The terms E and A are Young's Modulus and the cross-sectional area of the bars.

$$\therefore \sigma_s = \frac{P_1 + P_2}{2} \cdot \frac{1}{A} = \frac{E}{2}(\varepsilon_I + \varepsilon_R + \varepsilon_T) \tag{3.13}$$

Where, $\varepsilon_I, \varepsilon_R, and\ \varepsilon_T$ are the strains due to the incident, reflection and transmission waves.

Thus we can construct a stress/strain curve for the specific strain rate since we have a systematic record of the stress and strain the sample undergoes during the test.

The specimen's diameter and length must not be excessive. The length should be decreased to adequately justify the assumption of force equilibrium along the specimen. Also, the radial self-confinement can be minimized by keeping the radius minimum. Therefore, in addition to any actual strength gained by dynamic effects, it would seem like an increase in the dynamic material strength [110].

3.4 ELECTROCHEMICAL CHARACTERIZATION

The solutions used in the present research were to study the corrosion behavior of the AMSF in aqueous environment solutions. These solutions are prepared for different molar concentrations (0.01M, 0.1 M, and 1 M) in three different pH levels. The corrosion behavior of the AMSFs is studied at three solutions selected with different pH values, such as acidic (HCl), neutral (NaCl), and base/alkaline solutions (NaOH).

The essential factors to be considered for developing composite materials are based on their applicability. The electrochemical response of the material is essential, along with the microstructure and mechanical response. In this process, understanding the corrosion mechanisms is essential to assess the degree of damage the material may

undergo during the operation. Also, the electrochemical behavior of a material in aqueous solutions helps to comprehend the chemical stability of the composite for structural applications.

The electrolytes were produced using purified water and analytical reagent-grade chemicals. The corrosion behavior of AMSFs in aqueous environments was investigated by conducting electrochemical tests using potentiodynamic polarization (PDP) and Electrochemical Impedance Spectroscopy (EIS). These tests were performed for three distinct volume fractions of AMSFs.

3.4.1 Potentiodynamic polarization (PDP)

The corrosion studies on AMSFs were performed using Metrohm Autolab 204 Potentiostat, as shown in **Figure 3.7**. All the tests were conducted at room temperature conditions using three-electrode cells: Platinum wire as a counter electrode (CE), Saturated calomel electrode (SCE, USCE = 241 mv) as reference electrode (RE), and test sample AMSFs as a working electrode (WE). The scanning rate of the tests performed is maintained as 0.000167 v/sec with 100ml of newly prepared electrolyte solution used for every test. The exposed sample area to the electrolyte was $1cm^2$, and the remaining area was covered with Teflon tape to prevent an additional reaction. The open circuit potential for each sample (working electrode) was obtained by immersing it in an electrolyte solution for~20 mins. The polarization curves were obtained at least three times to ensure the reproducibility of the data.

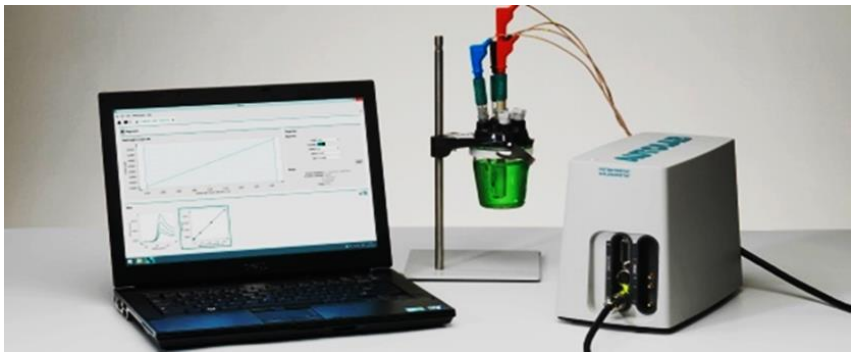

Figure 3.7 : Image showing the Metrohm Autolab 204 Potentiostat setup

3.4.2 Electrochemical impedance spectroscopy (EIS)

The EIS is conducted similar to the PDP test to obtain Nyquist and Bode plots for each electrolyte solution. VersaSTAT 3 potentiostat, shown in **Figure 3.8,** was used to run EIS experiments. A fresh sample and 100 ml chemical solution were used for every impedance test. For the purpose of evaluating impedance qualities, a frequency range of 10000 Hz to 10 Hz is used for the alternating current (AC) signal. The excitation signal used is a sine wave with a peak-to-peak amplitude of 0.01 V. The impedance spectra were analyzed using EC-Lab software. The impedance spectra were converted into an equivalent circuit for the purpose of analysis.

Further, the Nyquist plot for each AMSF condition was fitted into an equivalent circuit, measured by its Chi-squared ($\chi 2$) values, and translated into an equivalent circuit with the help of the EC-Lab software. Subsequently, a suitable comparable circuit was chosen to accurately model the optimal curve. Typically, a circuit is comprised of a pair of resistors denoted as R1 and R2. The interface between the reference and counter electrodes is characterized by a parameter known as resistance (R1, measured in Ohms). The charge transfer resistance (R2, Ω) represents the interface between the metal substrate and the surrounding solution.

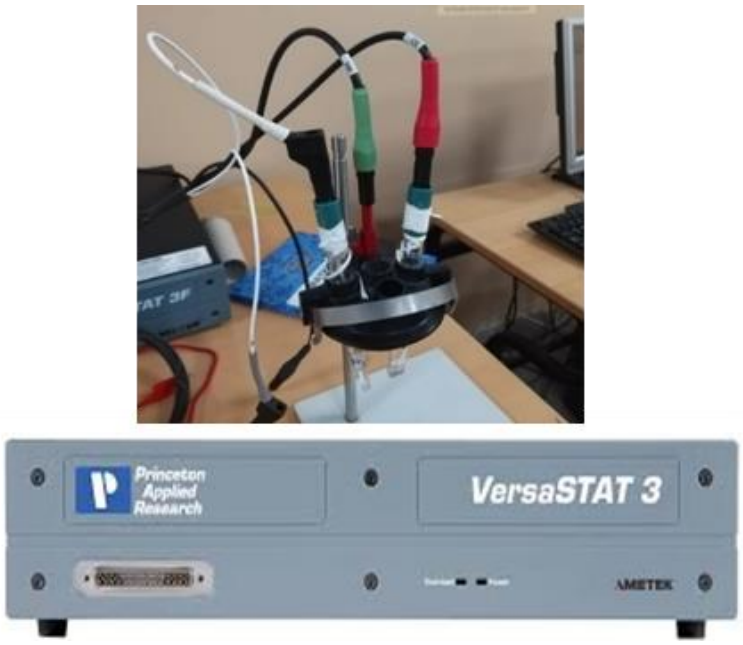

Figure 3.8 : Photograph of VersaSTAT 3 potentiostat

Similarly, the Capacitance (C)/ Double-layer capacitance (C1, µFarads) is the electrolyte and metal interface. Due to the inhomogeneities in the microstructure, surface roughness, and composition of the material's surface, the Constant Phase Element (CPE) acts as a imperfect capacitor. Continuous phase element exponential (n) provides information about the Warburg impedance (Z_w) and coating capacitance. The equation for the infinite Warburg impedance (Z_w) is:

Warburg impedance (Z_w) = $(\sigma\omega)^{-1/2}$ (1-j)

Where σ is the Warburg coefficient (Ω cm^2 s$^{-1/2}$) and $\omega=2\pi f$ (rad s^{-1}).

Here $(\sigma\omega)^{-1/2}$ is the frequency impedance real part, and $(\sigma\omega)^{-1/2}$ (-j) is the imaginary part. These parameters are used to study the corrosion process kinetics.

The CPE is dependent on the value of 'n.' The value of 'n' varies between 0 to 1, and it has the following significance:

Case 1: When n=1, CPE acts as an ideal capacitor, and the phase angle (θ) is 90^o.

Case 2: When n=0, CPE acts as an ideal resistor, and the phase angle (θ) is 0^{o}.

Case 3: When n=0.5, CPE acts as a Warburg impedance with diffusion characteristics.

Case 4: When 0.5<n<1, CPE describes a frequency dispersion of time constant.

Case 5: When n= 1, CPE has inductance characteristics.

3.5 SUMMARY

A detailed synthesis and characterization techniques of the AMSFs are provided. The processing techniques include powder mixture, green compacts, and sintering process to produce different volume fractions of the foams are discussed. Further, the details to calculate the theoretical and practical densities of the AMSFs are discussed. The freeze-fracture technique is adopted to understand the particle distribution in the matrix. The mechanical characterization techniques to understand the mechanical response of the SFs at different loading conditions are mentioned. A detailed theory about the Split Hopkinson's Pressure Bar is also provided. At last, the experimental scheme to probe the corrosion behavior of the produced AMSFs using the potentiodynamic polarization technique and electrochemical impedance spectroscopy is also provided. All the tests are repeated at least 3 times for each sample condition to check for repeatability and scatter. Thus the subsequent chapters provide detailed results obtained based on the techniques explained in this chapter, and corresponding discussions are also presented.

Chapter 4: Microstructure and Mechanical Properties

The previous chapter provides details on the manufacturing techniques and characterization schemes. In this chapter, some of the experimental results, such as density and mechanical tests, are presented. The AMSFs samples are prepared using the powder metallurgy route for three different volume fractions. The corresponding experimental studies are executed based on the particle size, volume fraction, and experimental conditions. Section 4.2 is further divided into three sub-sections which explain the results of the quasi-static room temperature studies, quasi-static high strain rate, and room temperature dynamic testing results.

4.1 MICROGRAPH ANALYSIS AND DENSITY MEASUREMENT OF AMSF

The microstructure of the syntactic foams consists of aluminum as a matrix, reinforced with alumina hollow particles of different sizes and volume fractions for each condition. A total of 9 samples are prepared for the current work, as shown in **Table 4.1**. The relative density of the samples is measured by normalizing using the matrix density (2.7 $g.cm^{-3}$). The experimental density is measured using density measuring kid as explained in Section 3.2.2. To study the distribution of the particles across the composite's cross-section freeze-fracture method is adopted to avoid the matrix fragments entering the void portion into the hollow particles. **Figure 4.1(a-c)** shows three representative micrographs of three different sizes of hollow particles (Size- 1, 2, & 3). The yellow pointer shows the alumina hollow particles, and the red markers represent the particle cracks and fractured particles during the freeze-fracture technique.

Table 4.1 : Experimental density and theoretical density of syntactic foam materials

Sample ID	Volume fraction	Particle average size (mm)	Experimental Density ($g.cm^{-3}$)	Theoretical Density ($g.cm^{-3}$)	Deviation from Theoretical Density (%)	Relative Density
#1	10	0.5	2.54	2.58	1.72	0.96
#2	20	0.5	2.37	2.433	2.53	0.90
#3	30	0.5	2.21	2.18	-1.24	0.81
#4	10	1	2.52	2.531	0.58	0.94
#5	20	1	2.33	2.391	2.44	0.89
#6	30	1	2.15	2.143	-0.28	0.79
#7	10	1.5	2.51	2.587	2.83	0.96
#8	20	1.5	2.33	2.348	0.88	0.87
#9	30	1.5	2.14	2.13	-0.52	0.79

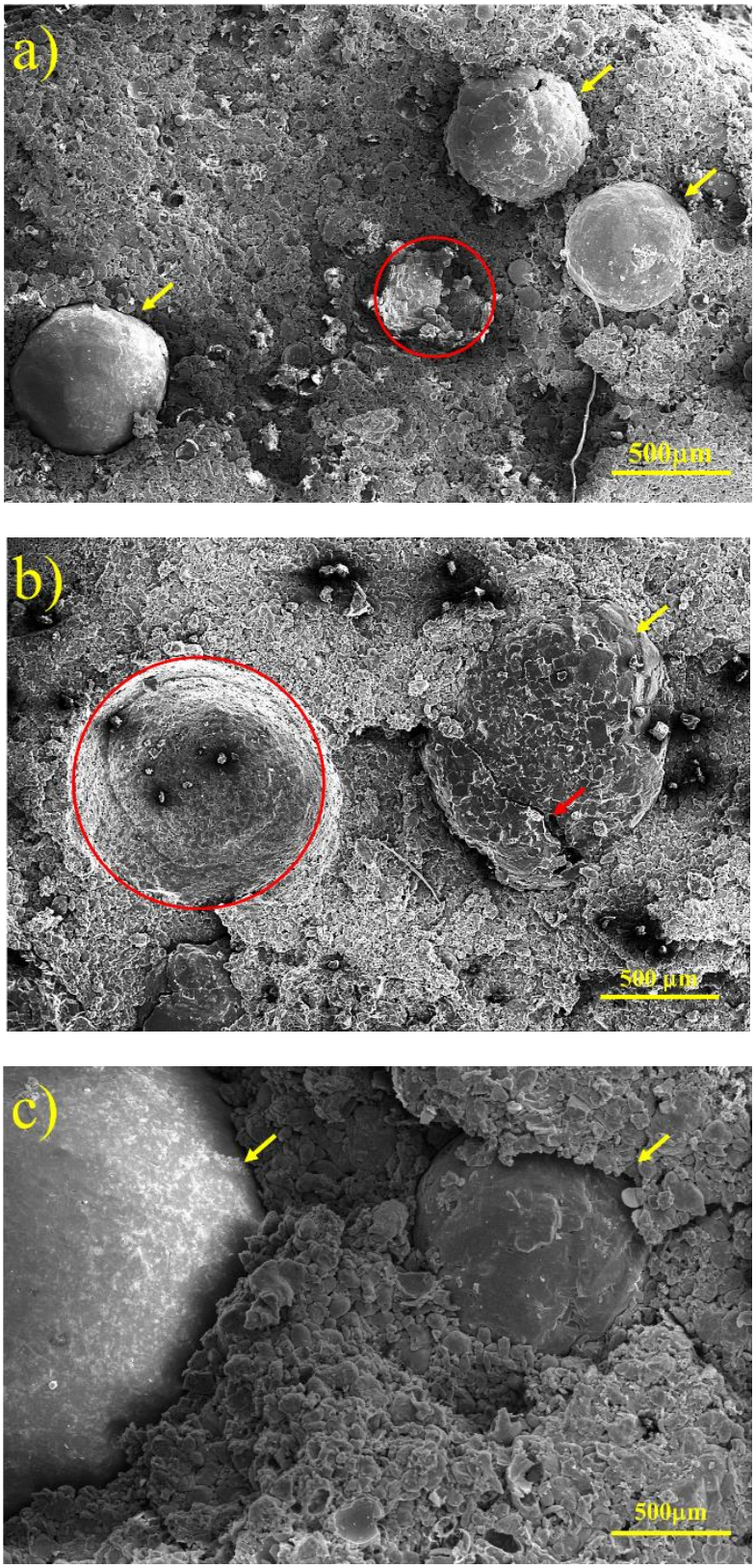

Figure 4.1 : Freeze fracture micrographs of 10% volume fraction samples of a) 500 μm, b)1000 μm, and c)1500 μm diameters.

4.2 COMPRESSION STUDIES

4.2.1 Quasi-Static Room Temperature

The performance of cellular materials is based on their ability to absorb large strains during external loading. It has been studied in several instincts that SFs show better energy absorption properties under compression. In this section, the mechanical response of the AMSFs is presented. Also, the respective sample's energy absorption properties and deformation behavior are discussed in Chapter 5. In this regards, the produced alumina reinforced aluminum syntactic foams are subjected to quasi-static compression at slow strain rate (0.001 s^{-1}) to understand the material's response. The sample are made out of different volume fractions of the hollow particles and different sizes.

The quasi-static compression (strain rate- 0.001 s^{-1}) studies of three different volume fractions and size ranges of Al_2O_3 hollow particles reinforced AMSFs are shown in **Figures 4.2(a-c)**. A quasi-static roome temperature studies on pure aluminum bulk material is also shown in **Figure 4.2(a)** for comparison purpose. The three distinct features typically observed in stress-strain data of SFs: a linear elastic region (up to ε: 0.03) followed by smooth transition with monotonous increment in stress at plateau (ε: 0.05-0.50) region and the densifications (ε: 0.5-end) area can be observed for all the conditions. This phenomenon can be attributed to the uniform deformation of the material without macroscopic brittle behavior in reinforcement, in contrast to earlier reports [31]. Also, visible cracks started appearing around 30 % strain (see **Annexure A1**).

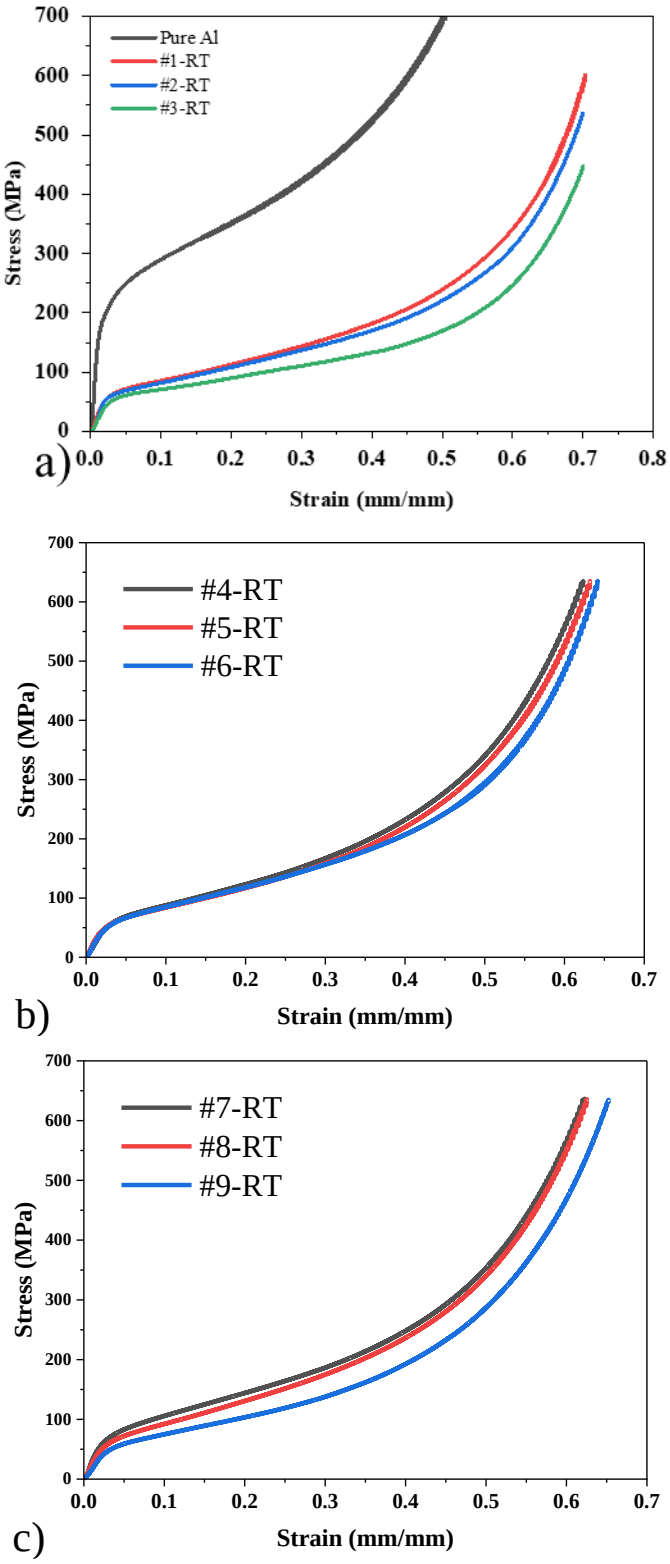

Figure 4.2 : Engineering stress-strain diagram of pure aluminum and aluminum matrix syntactic foams tested at room temperature (RT) (a) 500 μm, (b) 1000 μm, & (C) 1500 μm diameters

The compressive stress-strain behaviors of the specimens exhibit significant variations in relation to the dimensions of the Alumina particles. The observed behavior can be ascribed to the strain-hardening property exhibited by the foams, which has garnered considerable attention in the research community. Strain-hardening is observed within the plastic zone of the stress-strain curve. To quantify the strain hardening exponent n of the foam, a power-law relationship best suited to the stress-strain curves. In the present study, the value of n was determined by conducting a linear regression analysis on the actual stress-strain data, which were plotted on a logarithmic scale. This analysis was performed within the strain range of 5% to 40%. The effect of strain hardening is explained in detail in Chapter 7.

4.2.2 Elevated Temperatures

The quasi-static compression studies at elevated temperatures are conducted with 75 ºC intervals to understand the compression deformation behavior. The average stress-strain response of three samples tested for each condition is shown in **Figure 4.3(a-i)**. In the columns, variation in temperature data is represented, and the particle size is altered in the rows. Each graph contains data from three different volume fractions of hollow particles. The effect of temperature and particle size is evident in the graphs. Unlike reported elsewhere, the stress-strain data has shown a hardening behavior between elastic and plateau regions with increased temperature [43,82]. Also, the slope in the flow stress of the matrix is reduced as a function of temperature. This behavior can be attributed to the presence of alumina particles with a high melting point which contributes to a rise in the slope of the elastic region. The material response in the elastic region has shown dependence on the temperature.

Similar to room temperature conditions during the plateau region of the stress-strain data, no visible oscillations or distortions are observed up to 50 % strain, which implies uniform deformation throughout the plastic loading. The stress value of the corresponding strain in the plateau region has increased in the samples with a high t/D ratio (i.e., 0.5). On the contrary, the hardening effect is reduced with the decrease in the particle's wall thickness at the plateau and densification regions. The volume fraction effect is similar to the quasi-static condition. At higher temperatures, the cracks initiated before 30 % strain. The deformation is uniform in quasi-static conditions for all temperature conditions. In light of this, each test condition's results are calculated using an average of three samples measurement. The volume fraction of the hollow particles contributed to the relative density of the SFs. This variation in the relative density of a respective size has altered the slope of the plateau region in the stress-strain curve. This trend was consistent and matched the earlier studies [38,74].

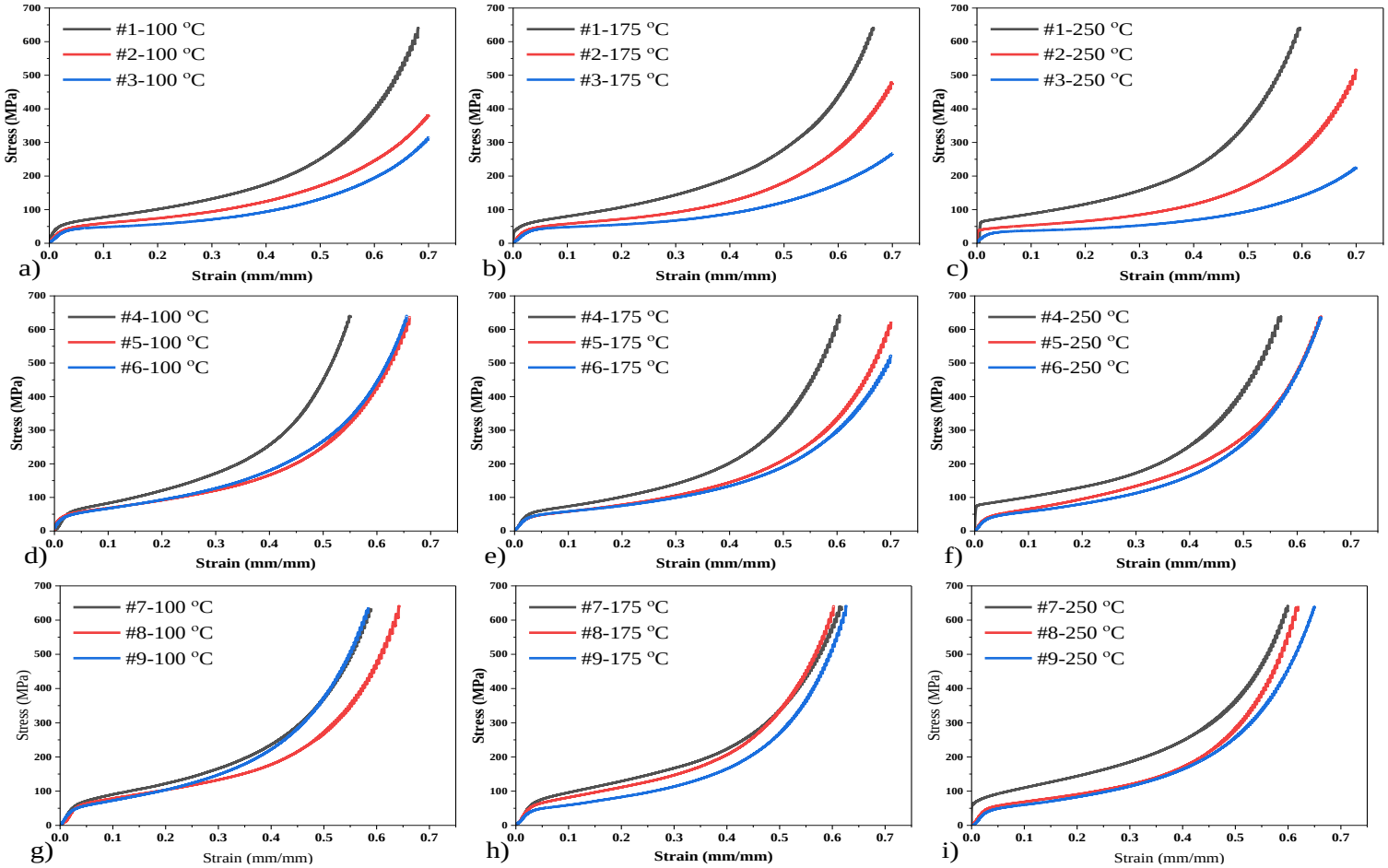

Figure 4.3 : Engineering stress-strain diagram of AMSFs tested at different temperatures (a, b, and c) 100 °C, 175 °C, 250 °C (d, e, and f) 100 °C, 175 °C, 250 °C, and (g, h, and i) 100 °C, 175 °C, 250 °C of particle sizes 500 μm, 1000 μm and 1500 μm, respectively

4.2.3 Dynamic Compression

In earlier studies, some SFs show better energy absorption properties under compression low-strain rates (0.001 s^{-1}) [87,92]. However, the performance under high strain rates is seldom discussed for aluminum alumina systems. The quasi-static and dynamic performance of AMSFs is compared here to understand the material response and corresponding energy absorption efficiencies under different strain rates.

Figure 4.4(a-i) displays the experimental stress-strain data of AMSFs at different strain rates. In **Figure 4.4**, the volume fraction of the hollow sphere size is changed along the columns, and along rows, the size of the alumina hollow spheres is increased. In the linear elastic region, the deformation of AMSFs followed the same trend irrespective of the strain rate without significant deviation. **Figure 4.4** also depicts the notable change in the yield point with respect to the change in the strain rate. The stress-strain data followed a smooth transition from linear elastic to plastic regions in all studies without stress drops. The hollow particles tend to fracture during the plateau region, and the pores inside the matrix may be filled. However, this behavior does not significantly affect the stress values during the deformation, resulting in the material's hardening behavior. The maximum stress values at low and high strains are 184 MPa and 288 MPa, respectively, at 0.45 strain. This hardening behavior is explored in detail later. Further, the slope of the curve follows a trend based on the hollow particles' size, volume fraction, and strain rate at which the samples are tested.

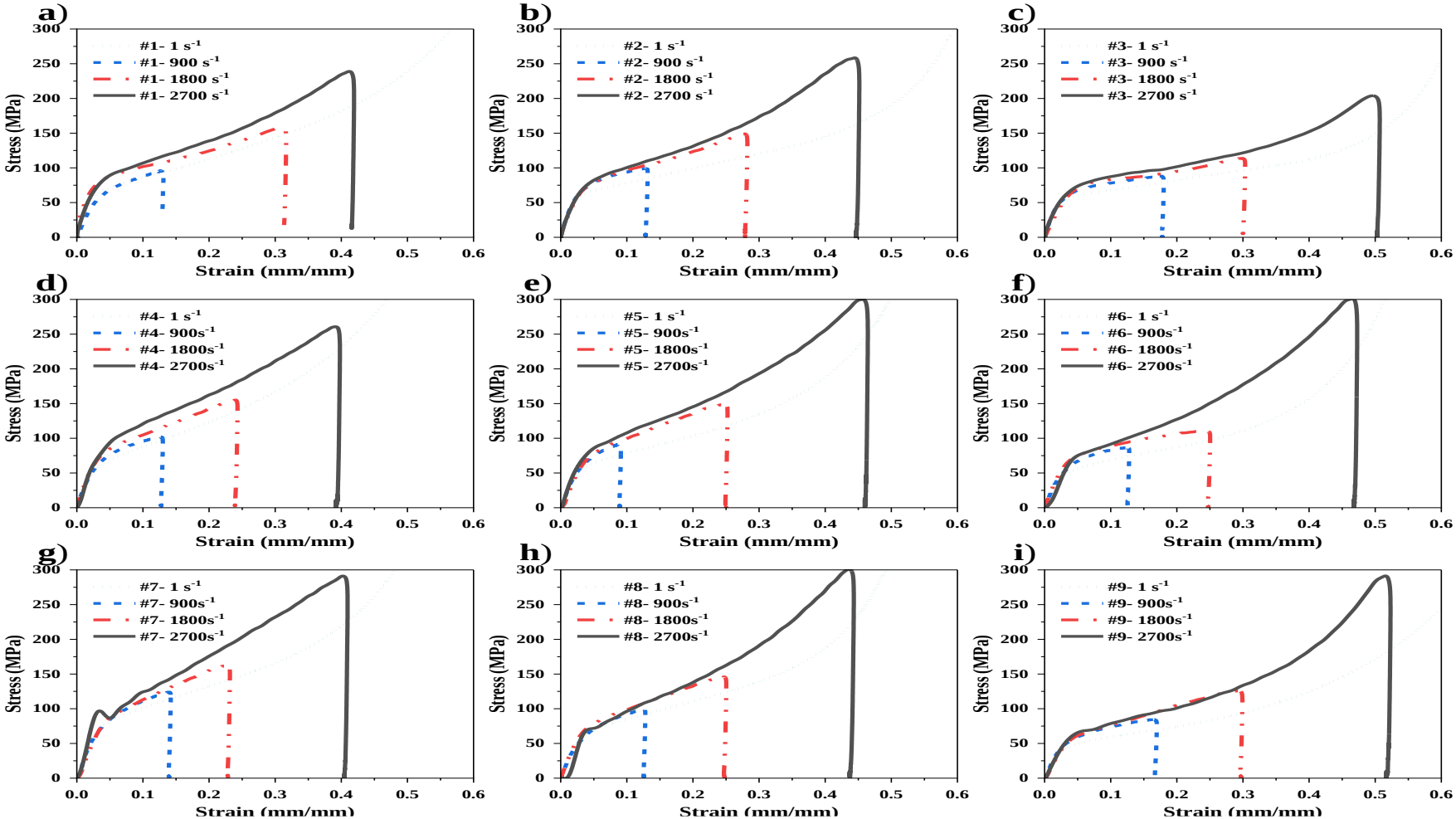

Figure 4.4 : Compressive stress-strain data of AMSFs at different strain rates of different Sample IDs (a) #1, (b) #2, (c) #3, (d) #4, (e) #5, (f) #6, (g) #7, (h) #8, and (i) #9

The deformation curves of the samples tested at higher strain rates showed a similar trend to the quasi-static tests up to the densification region. The typical strain observed in the samples corresponding to the deformation rate fall between 10-20% for 900 s^{-1} and 20-30% for 1800 s^{-1}. At a maximum strain rate of 2700 s^{-1}, the AMSFs deformed up to 40-50 % strain. This behavior indicates early densification of the AMSFs compared to quasi-static deformation, irrespective of size and volume fractions.

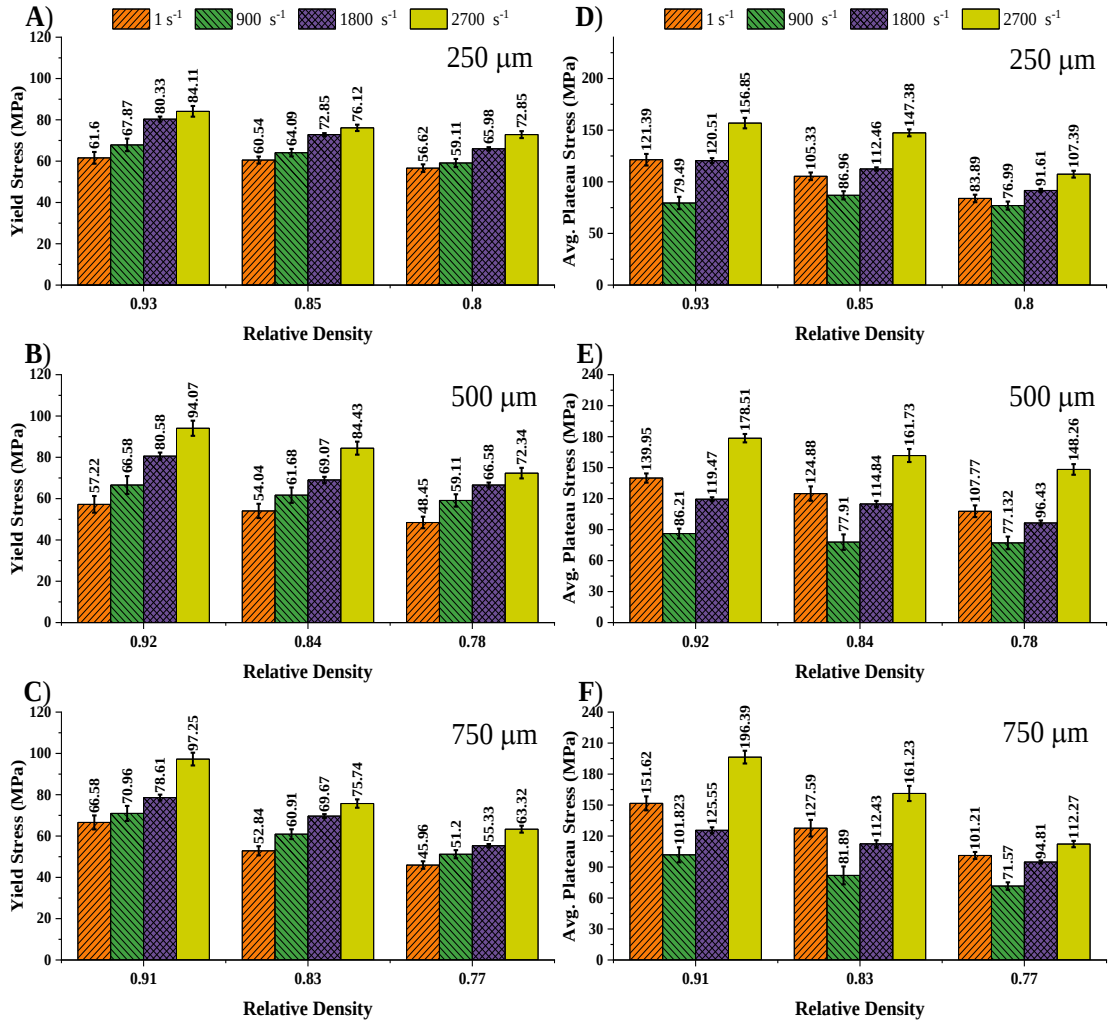

Figure 4.5 : Compressive properties of AMSFs, including yield stress and average plateau stress of three different sizes.

The yield strength data measured is considered at 0.2% offset to the linear region of the stress-strain curve, and the average plateau stress values for all the samples are shown in **Figure 4.5**. The yield stress values have followed an increasing trend with a rise in strain rate. This behavior is similar across different particle sizes. However, in samples tested at a particular strain rate (for example, at 2700 s^{-1} strain rate), there is a drop in the yield stress values with an increase in the volume fraction and particle size. The AMSFs exhibit the maximum yield strength of 151.62 and 196.39 MPa tested at 1 s^{-1} and 2700 s^{-1} strain rates, respectively. **Figure 4.5(A-C)** also suggests that the overall yield strength of AMSFs decreases with a decrease in relative density, typically between 0.77-0.93.

Similarly, the average plateau stress values of AMFSs, as shown in **Figure 4.5(D-F),** followed decreasing trend with an increase in the volume fraction and particle size. The AMSFs tested at medium strain rates (900 and 1800 s^{-1}) show minor deformation. This results in low plateau stress values. Statistically, the maximum deviation in the average plateau stress value among the low and high strain rates is observed at low volume fractions. However, as shown in **Figure 4.4**, the maximum strain obtained for lower volume fractions has shown early densification and low strains with larger particles. This behavior needs to be further studied to understand the overall effect of the particle size and volume fraction on the mechanical response at various strain rates.

After deformation, the cross-sectional image of the samples using SEM and their respective EDX spectrum is obtained as shown in **Figure 4.6**. The arrows indicate the compression direction of the sample tested. **Figure 4.6(a-c)** shows the particle deformation pattern of samples tested at three strain rates (900, 1800, and 2700 s^{-1}), respectively. A representative EDX spectrum of sample #3 tested at a high-strain rate

are shown in **Figure 4.6(d)**.The particles tested at 900 s^{-1} show fractured particles without complete failure of the shell structure of hollow particles. Similarly, the residual amount of hollow particles is observed in the sample tested at 1800 s^{-1}. However, at higher strain rates (2700 s^{-1}), the hollow particles are fractured entirely due to the brittle nature and the dynamic loading of the material. Also, the material is not entirely dense, and the gap is retained due to particle failure. This deformation behavior of AMSFs is attributed to the amount of plastic flow of the matrix materials, the brittle nature of Al_2O_3 hollow particles, and sample loading.

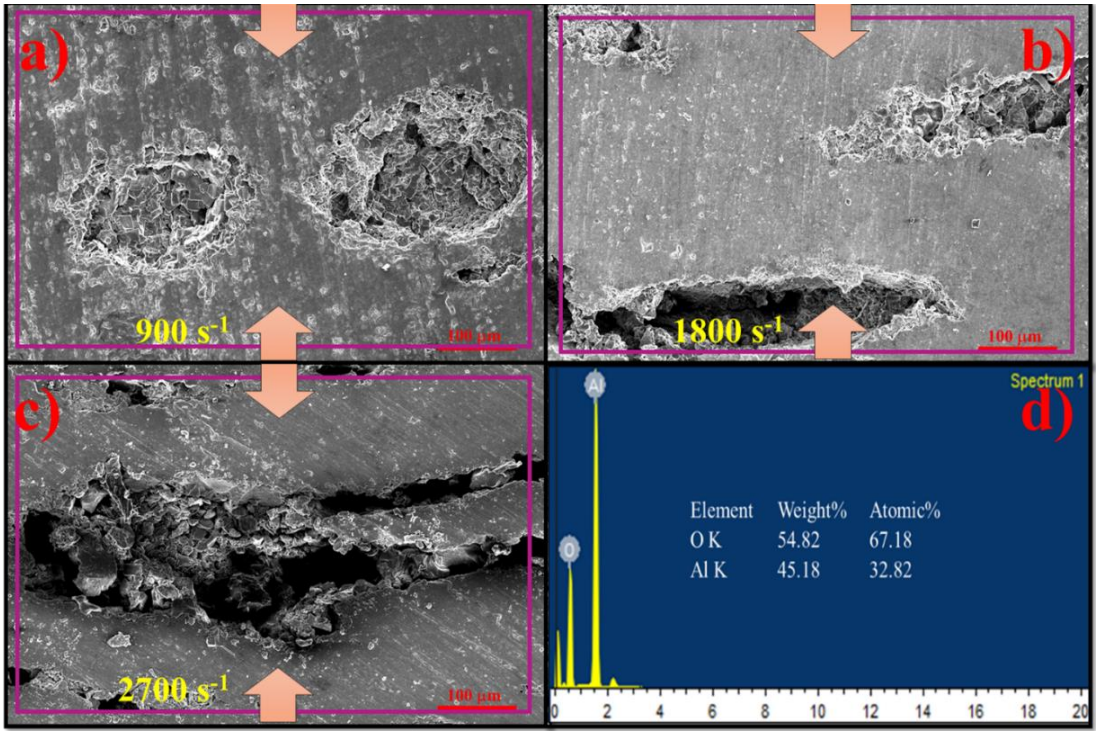

Figure 4.6 : Representative cross-sectional images of AMSFs sample #3 tested at (a) 900 s^{-1}, (b) 1800 s^{-1}, (c) 2700 s^{-1} strain rates, and (d) the EDX spectrum of (c).

4.3 SUMMARY

The experimental results obtained for alumina hollow sphere-reinforced syntactic foams are compiled in this chapter, which includes the microstructural studies using FE-SEM by adopting the freeze-fracture technique. The theoretical and experimental densities of AMSFs are compared for different volume fractions, showing a deviation of less than 3%. The mechanical compression test results suggest that the alumina hollow particles induced syntactic foams showed better performance than the cenospheres-based SFs. The particle's size and volume fraction effect has shown a clear differentiation concerning the plastic flow of each sample. However, further analysis is required to quantify the ability to absorb mechanical energy. Also, the essential aspects of the porous composite materials, including plateau stress and densification zones, need in-depth understanding. These aspects are discussed in Chapter 5.

4.4 ANNEXURE

Annexure A1:

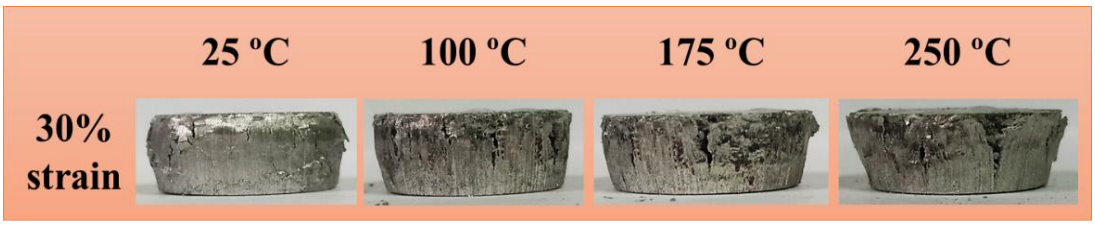

Figure 4.7: Shows the cracks that appeared during the compression test stopped at 30% strain (A1).

Chapter 5: Energy Absorption Studies

The Chapter 4 contains experimental results of alumina-based SFs tested under different loading rates and temperatures. The results have demonstrated a substantial impact on the dimensions of particles and the proportion of their volume. Further analysis of this behavior is required in order to have a more comprehensive understanding. The energy absorption qualities of the SFs are of utmost importance in comprehending the mechanical reaction and determining the material's suitability for an appropriate industrial application. In this context, a comprehensive examination of the energy absorption characteristics is carried out on aluminum-alumina SFs. This chapter elucidates three distinct properties pertaining to energy absorption, namely: energy absorption per unit volume, energy absorption efficiency, and ideal energy absorption efficiency. The energy absorption capacity (W) is typically quantified as the integral of the stress-strain curve. The foam's actual and ideal energy absorption ratio represents the desired energy absorption efficiency.

5.1 QUASI-STATIC COMPRESSION

Figure 5.1(a-c) shows the energy absorption efficiency (η), and ideal energy absorption efficiency (I) for the samples obtained in quasi-static testings. The energy absorption capacity (EAC), E and I, are estimated using the following relations:

$$\text{EAC} = \int_0^{\varepsilon} \sigma \, d\varepsilon \tag{5.1}$$

$$\eta = \frac{EAC}{\sigma_i} \tag{5.2}$$

$$I = \frac{EAC}{\sigma_i \varepsilon_i} \tag{5.3}$$

Where stress -σ, strain- ε , and subscript (*i)* represent the corresponding stress-strain data.

Table 5.1 : Material properties of Al-matrix syntactic foams tested under compression

Sample ID	Sample name	Relative Density	EAC (MJ/m^3)	Plateau stress ($\varepsilon_{0.05} - \varepsilon_{densification}$)	Densification Strain (mm/mm)	Quasi-static- η_{ideal} (%)
#1	SF11	0.95	140.50	152.57	0.53	67.89
#2	SF12	0.90	129.00	142.84	0.56	68.47
#3	SF13	0.86	103.77	114.06	0.57	70.61
#4	SF21	0.93	136.37	196.4	0.51	64.46
#5	SF22	0.88	132.77	185.69	0.53	64.63
#6	SF23	0.82	130.80	174.63	0.58	65.07
#7	SF31	0.95	143.61	210.10	0.52	63.98
#8	SF32	0.90	139.67	198.27	0.54	64.37
#9	SF33	0.86	131.30	167.16	0.57	65.14

The plateau stress data is measured between the plastic region of the stress-strain data up to the densification strain. A maximum of 210.10 MPa (SF31) plateau stress is achieved under room temperature studies. However, this information may not be sufficient to comment on energy absorption. Thus, the area under the stress-strain curve is equal to the EAC. **Table 5.1** shows the EAC, densification strain, and ideal energy absorption. The specific energy absorption is measured at densification strain.

The EAC ranges from 103.77 MJ/m^3 (#3) to 143.61 MJ/m^3 (#7). Similarly, with an increase in the V_f of the particles, the energy absorption decreases for different sizes of hollow particles. However, the energy absorption rises with the increase in particle t/D ratio. The effect of volume fractions is inversely proportional to the EAC in this scenario.

In a typical syntactic foam structure, the distribution of pores is random. Under the compression, these pour fill due to the particle breaking leading to the densification of the SFs. To identify the densification zone, the energy absorption efficiency is measured using Equation 5.1. The energy absorption is increasing linearly for all the samples concerning the strain. As suggested by Li et al., the corresponding strain at the maximum value of these curves is considered the densification strain of the material [111]. Among all the conditions, the densification strain varies between 0.51 to 0.58. The maximum strain value implies the resistance offered by the particles to withstand the deformation and more energy absorption efficiency.

Further, the ideal energy absorption efficiency data is calculated based on equation 5 as shown in **Figure 5.1(a-c)** (Refere to left axis). These curves represent the maximum amount of energy absorbed by the corresponding material. The ideal efficiency data in **Table 5.1** is obtained by taking the mean from 5 % strain up to the densification strain data. In general, the efficiency of a material is based on the plateau region's slope in a stress-strain curve [91]. The lower the slope of the curve, the higher the efficiency. So, the particles of smaller diameters have shown more efficiency under quasi-static conditions due to the curve showing less hardening during the plateau region. Also, across all the size ranges, the efficiency trend increases with respect to the volume fraction. At smaller sizes, this trend is prominently seen.

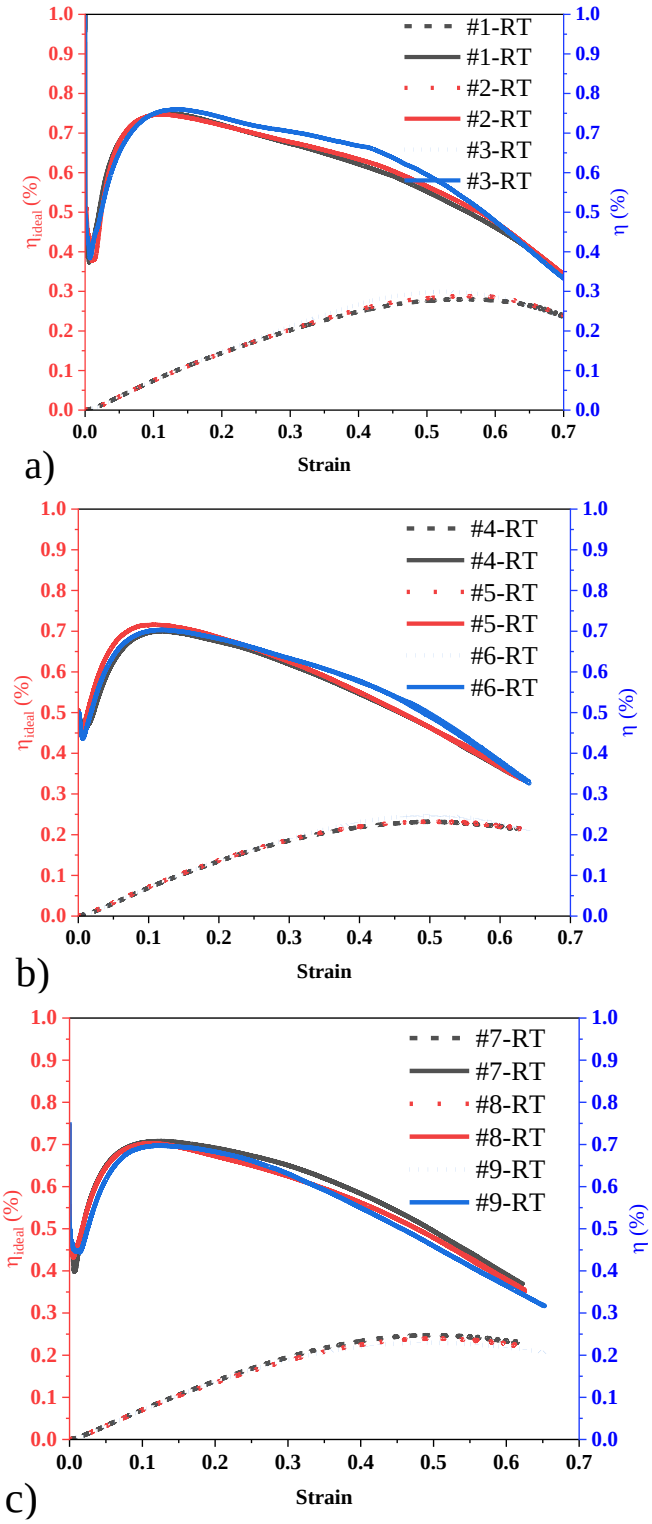

Figure 5.1 : Energy absorption efficiencies(η) vs. strain curves tested at ambient temperatures (a) 500 μm, (b) 1000 μm, & (C) 1500 μm diameters

5.2 EFFECT OF TEMPERATURE

The plateau stress is one of the significant factors that contribute proportionally to energy absorption. The energy absorption performance of the samples tested at elevated conditions is measured, and the energy absorption efficiency vs. strain data is shown in **Figure 5.2(a-i)**. **Table 5.2** presents properties such as EAC, densification strain and ideal energy absorption. Like the quasi-static room temperature studies, the EAC is recorded at 40% strain. The EAC data for all the combinations showed a decreasing trend with respect to porosity. However, EAC data is unaffected with increasing in volume fractions. This behavior may be attributed to the randomness in the particle distribution and internal defects in the structure.

In contrast to the RT studies, the densification strains are reduced, and a linear drop is observed with an increase in the temperature. The alumina hollow particles support the matrix during plastic deformation despite the low plastic flow stress of the matrix material. The densification strains are recovered at higher volume fractions of hollow particles. In general, a densification strain delays the material failure during the deformation. This study observed maximum densification strains of 0.56, 0.55, and 0.50 at 100 ºC, 175 ºC, and 250 ºC, respectively.

The ideal energy absorption at elevated temperatures is promising despite the thermal softening of the matrix, as shown in **Figure 5.2**. In contrast to the RT –studies, the ideal energy absorption efficiency data has not shown much improvement with an increase in temperature. However, at high temperatures (250 ºC), a linear rise in efficiency is observed. This trend is due to the fall in the slope of the stress-strain curve in the plateau region. The maximum efficiency of 75%, 72% & 73% is observed at 250 ºC with a mean average particle size of 500 μm, 1000 μm and 1500 μm, respectively. However, a fall in the slope of the stress-strain curve alone may not

contribute to the increment in efficiency. For example, the slope of the elastic region and the stress values increased despite the change in the slope of the stress-strain curves. As the matrix softening occurs, the particles offer resistance to the initial deformation due to the high melting points of the reinforcement, improving the modulus and enhancing the overall energy absorption efficiency.

Table 5.2 : Material properties of Al-matrix syntactic foams tested under compression at elevated temperature

Sample ID	Relative Density	W (MJ/m^3)			Plateau stress ($\varepsilon_{0.05} - \varepsilon_{densification}$)			Densification Strain (mm/mm)			Ideal energy absorption efficiency (%)		
		100 ºC	175 ºC	250 ºC	100 ºC	175 ºC	250 ºC	100 ºC	175 ºC	250 ºC	100 ºC	175 ºC	250 ºC
SF11	0.95	134.83	137.60	124.35	147.92	168.21	196.44	0.48	0.49	0.42	67.22	67.74	69.46
SF12	0.90	96.04	104.06	101.75	102.82	111.18	105.5	0.52	0.51	0.46	68.8	69.36	73.02
SF13	0.86	75.14	69.63	55.41	79.05	79.73	61.24	0.55	0.53	0.52	69.99	71.14	75.77
SF21	0.93	112.50	116.74	124.73	214.18	176.78	224.13	0.44	0.43	0.42	60.35	62.75	63.72
SF22	0.88	108.06	110.09	120.47	145.37	125.85	159.24	0.47	0.48	0.46	65.41	62.92	66.51
SF23	0.82	104.92	101.58	114.25	155.53	116.71	143.05	0.52	0.52	0.51	68.61	65.96	72.31
SF31	0.95	123.96	133.88	136.83	200.36	192.41	215.40	0.45	0.41	0.41	60.57	64.85	60.99
SF32	0.90	122.40	119.10	120.19	159.84	182.03	155.83	0.47	0.45	0.44	61.61	66.37	64.88
SF33	0.86	114.27	108.21	116.57	160.13	147.40	143.54	0.5	0.48	0.46	67.28	69.14	73.92

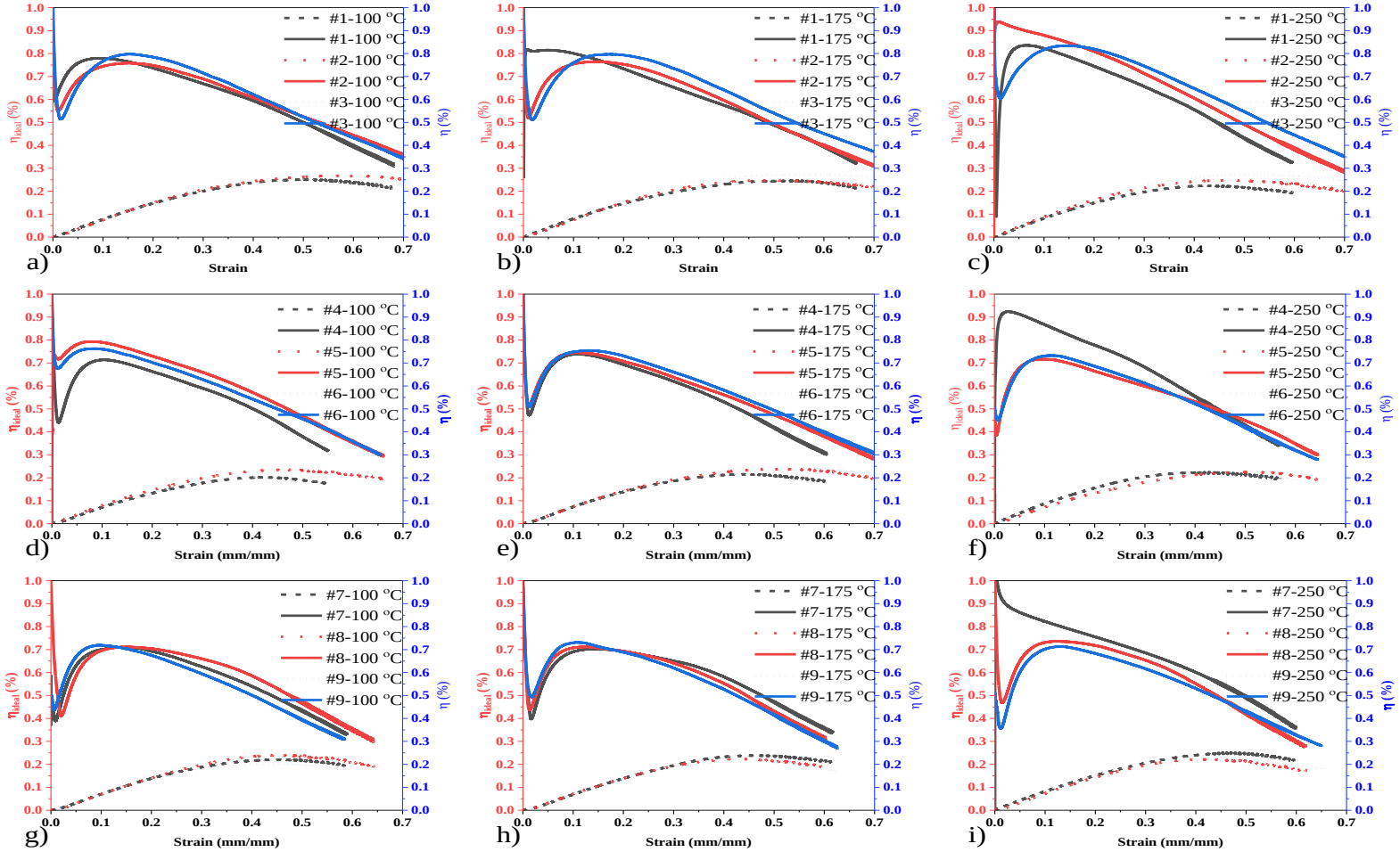

Figure 5.2 : Energy absorption efficiencies vs. strain curves at elevated temperatures (a), (b), (c)- 500 μm (d), (e), (f)- 1000 μm & (g), (h), (i)- 1500 μm diameters

5.3 EFFECT OF SIZE AND VOLUME FRACTION

5.3.1 Yield stress

Figure 5.3(a-c) shows the yield stress vs. relative density data from the stress-strain curve tested at different temperatures. The corresponding yield stress values are recorded at 0.1 % offset strain. Among the different t/D ratios this study chose for different volume fractions, the yield stress response showed a decreasing trend respective to the relative density. For room temperature studies, the deviation in the yield stress is minimal, whereas at high temperatures, a wide range of deviation is observed concerning the relative densities of the AMFSs. A deviation in the yield stress values is observed for the sample relative density with different t/D ratios. At higher temperatures, say 250 ºC, a sudden fall in the yield stress values is observed with a decrease in the relative density.

Similarly, a linear decrease in stress is observed at high-temperature conditions. This may be attributed to the matrix material's plastic flow due to the temperature increase. The matrix may tend to soften, increasing the matrix material's plastic flow, also referred to as the thermal softening of the matrix material. This trend is seen across all the tests at different temperatures. The effect of temperatures on the yield stress of the SFs is evident between 25 ºC – 100 ºC and 175 ºC – 250 ºC, particularly at high volume faction of hollow particles, and a similar trend was reported by Linul et al. [43]. The deviation in the yield stress concerning the relative density may also contribute to the energy absorption efficiency.

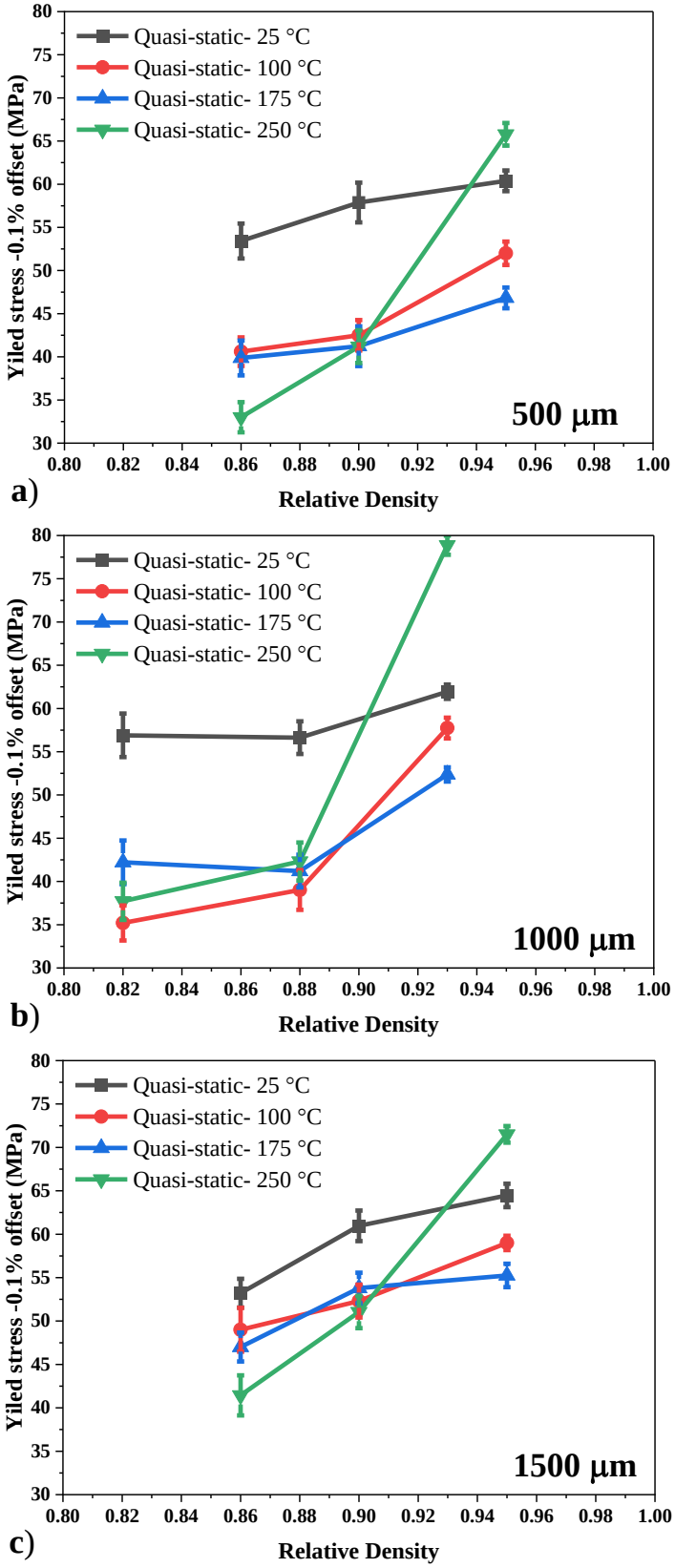

Figure 5.3 : Deviation in the yield stress (0.1% offset) concerning relative density for different t/D ratios.

5.3.2 Densification strain

The role of the particle size and volume fraction in various temperatures can be explained using **Figures 5.4(a-c)** and **5.5(a-c)**. The particle size strongly influences the volume fraction and relative density. The relative density of the syntactic foams can be controlled by the selection of volume fraction or by altering the cell wall thickness. It is observed from **Figure 5.4** that the densification strain of the AMSFs is higher for the particles with a high t/D ratio (i.e., 0.05). The densification strain results are consistent for samples tested at RT- conditions concerning the volume fraction and size. There is hardly any deviation in the densification strain for samples tested at 100 ºC and 175 ºC. But there is a drop in the strain with increased temperatures. At room temperature, randomly distributed fractured hollow particles remain in the matrix, which may contribute to the rise in the slope of the plateau region. In addition, with an increase in temperature, the matrix material failed to retain the particles inside the matrix. This behavior is displayed in the cross-sectional view of the deformed samples in **Annexure A1**. This trend continues when the temperature is raised to 250 ºC, which decreases the densification strain. This phenomenon can be attributed to the early failure of the particles due to the small t/D ratio for larger particle sizes. The load bearing offered by the alumina hollow particles is more in the case of a larger t/D ratio.

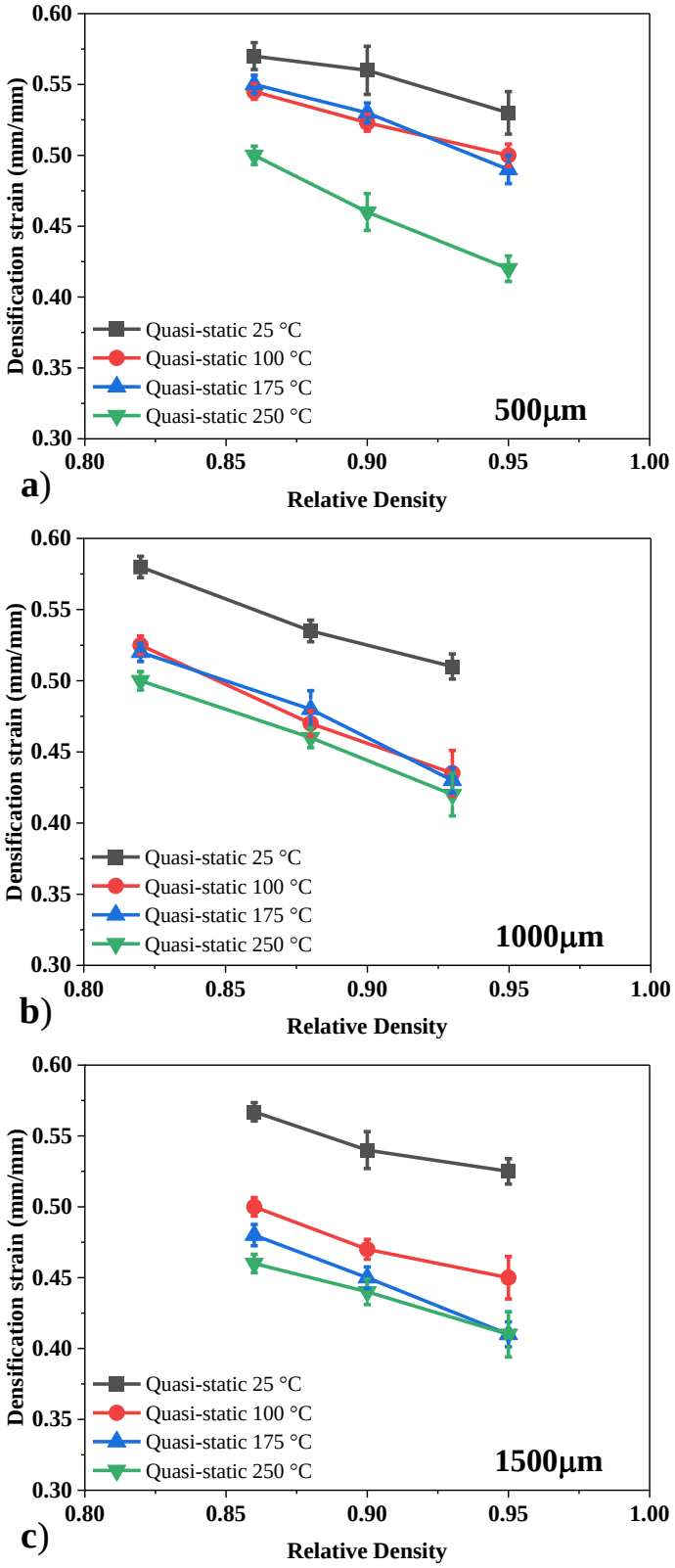

Figure 5.4 : Deviation of densification strain with relative density for different t/D ratios.

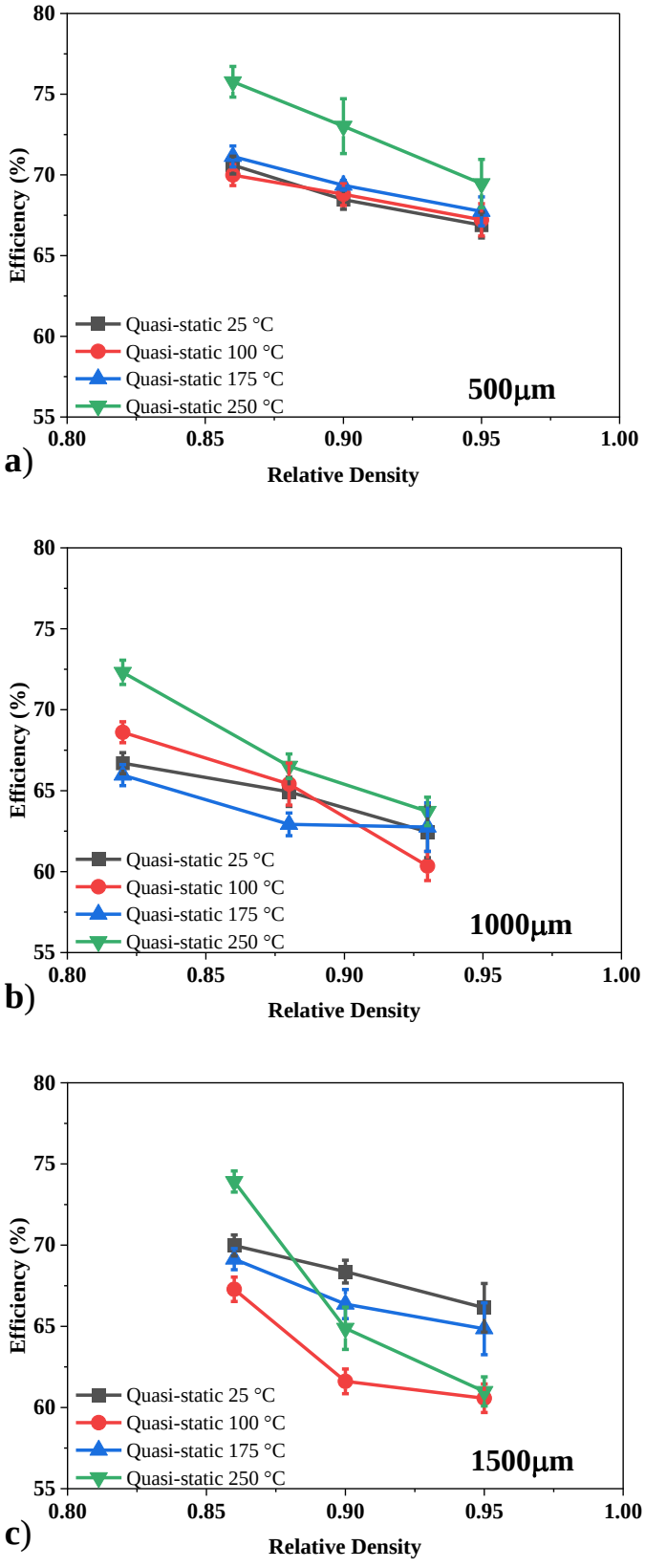

Figure 5.5 : Deviation of ideal energy absorption with relative density for different t/D ratios.

Further, the distribution of particles' typical geometry of the hollow spheres falls within a small range, as per **Figure 3.1** (Refer to Chapter 3). It is observed that the particle size distribution is of the log-normal type. The t/D ratio of the particles decreases with an increase in particle size, increasing the plateau region's slope. Also, the densification strain decreased with the increase in the size of the particles. The low particle diameter samples may withstand applied loads due to the effective stress distribution on the cell wall. During the deformation of the coarse particle samples in the stress-strain curve, the densification strain reached early.

5.3.3 Energy absorption efficiency

The slope of the plateau stress is sensitive to the relative density and temperature, as observed in **Figure 4.3** (Refere to Chapter 4). In energy absorption efficiency, the plateau region of the curve is considered, and the average value of the curve shown in **Figure 5.2** is taken for at least three curves for each condition and shown in **Figure 5.5**. It is evident that the efficiency has increased with a decrease in the plateau region's slope. The fluctuation in energy absorption efficiency shown by all conditions with relative density follows a consistent pattern. Also, at a selected relative density, the efficiency of the AMSFs decreases with respect to relative density. This drop in efficiency can be attributed to the change in the flow stress of the matrix materials. Since the melting point of the hollow particles is significantly high, there may be hardly any effect on the particle's behavior with the temperature range considered.

5.4 HIGH STRAIN RATE

5.4.1 Hardening Rate

To probe the hardening behavior of the AMSFs, the derivate of the stress-strain data is calculated and presented in **Figure 5.6.** These curves are plotted to the

maximum strain obtained from respective stress-strain data, as reported by Xia et al. and others [112–114]. The initial stage of the HR curves showed a sudden drop representing the linear elastic region of the stress-strain data. Later, a rise in the HR values represents the hardening of the material. The data for all the conditions are more significant than zero, and this behavior indicates a constant rise in HR without any stress drops. It is observed from **Figure 5.6** that the HR decreased with an increase in volume fraction and formed a local plateau region for quasi-static tests. The HR behavior is not evident in samples tested at medium strain rates (900and 1800 s^{-1}). After the initial stage, the curve followed quasi-static behavior. This indicates that the strain hardening in the samples is more significant beyond 1800 s^{-1} across all the samples of AMSFs.

In contrast to low and medium strain rates, the high strain rate curve continues to increase after the initial drop in HR data. This hardening behavior is significant with an increase in volume fraction. Also, the deviation between the low and high strain rates is evident at low densities. For example, the deviation in the low and high strain rate data for sample #9 (relative density-0.77) is higher than in sample #1 (relative density -0.93). Collectively, the produced AMSFs have shown the hardening behavior prominently at 2700 s^{-1} strain rates. However, the hardening behavior is not dominant at lower strain rates, which may be attributed to the material's response.

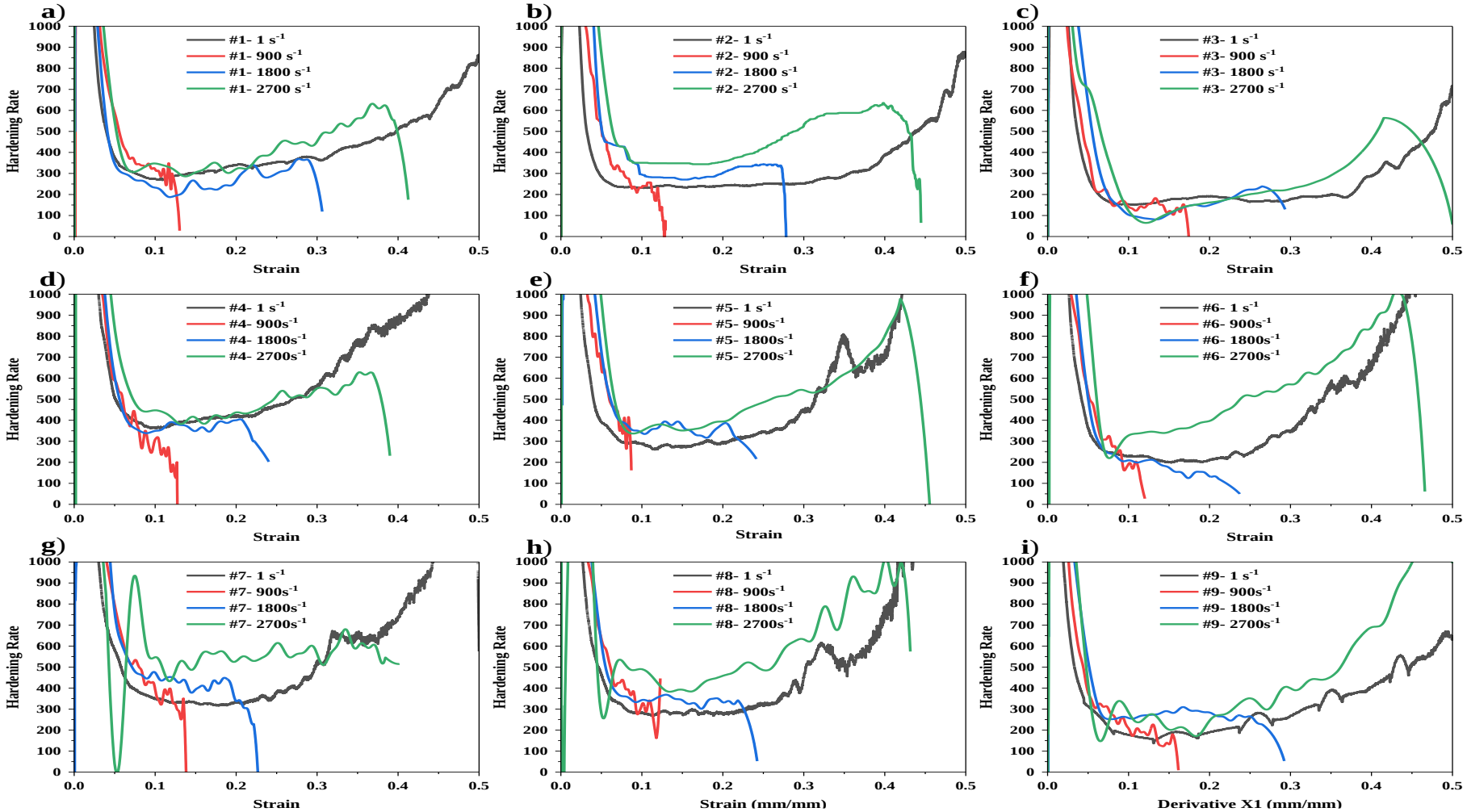

Figure 5.6 : Hardening rate vs. strain of different sample IDs (a) #1, (b) #2, (c) #3, (d) #4, (e) #5, (f) #6, (g) #7, (h) #8, and (i) #9

5.4.2 Energy absorption properties

The EA and SEA values for all the samples tested at low and high strain rates are shown in **Figure 5.7**. All the measurements are considered up to 40% strain for assessment purposes, as shown in **Table 5.3**. The EAC of quasi-static and dynamic tests followed a decrease in trend with relative density. The maximum EA and SEA data at low and high strain rates are 52.76 MJ/m^3 & 21.47 kJ/kg and 69.90 MJ/m^3 & 28.45 kJ/kg (Sample #7), respectively. Similarly, with an increase in the volume fraction of the particles, the energy absorption decreases for different sizes of hollow particles. This suggests that the volume fraction of the particles shows the minimum effect on energy absorption. But, the energy absorption rises with the increase in particle size. It is observed that, at 40% strain, the EA and SEA data of AMSFs showed better performance under dynamic loading. This behavior suggests that the AMSF performance is superior under dynamic loading (2700 s-1). However, further analysis is required to understand the overall performance of the samples.

The I-EAE data provides the maximum mechanical energy the sample absorbs under large deformation. The $\boldsymbol{\eta_{ideal}}$ values in **Table 5.3** are obtained by taking mean values between the 5% and 40% strain data (plateau region). In general, the efficiency of a material is based on the slope of the stress-strain curve in the plateau region. The lower the slope of the curve, the higher the efficiency. **Figure 4.4** (Refer to Chapter 4) qualitatively suggests that the particles of smaller diameters and high volume fractions may have more efficiency due to the less hardening in the plateau region. Also, the efficiency trend of all the size ranges increases concerning the volume fraction. At smaller sizes, this trend is prominently observed.

Table 5. 3 : Material properties of Al-matrix syntactic foams tested under compression

Sample ID	Relative Density	Quasi-static (1 s^{-1})				High Strain rate (2700 s^{-1})			
		EA (MJ/m^3) at 0.4 strain	SEA (kJ/kg) at 0.4 strain	Densification Strain	η_{ideal} (%)	W (MJ/m^3) at 0.4 strain	SEA (kJ/kg) at 0.4 strain	Maximum Strain	η_{ideal} (%)
#1	0.93	45.22	18.00	0.52	69.37	56.53	22.51	0.41	67.47
#2	0.85	38.99	16.98	0.54	70.61	54.32	23.67	0.45	68.78
#3	0.80	31.98	14.80	0.55	72.34	40.70	18.84	0.50	78.92
#4	0.92	50.72	20.41	0.50	63.56	62.09	25.00	0.44	62.27
#5	0.84	42.58	18.77	0.50	66.40	59.32	26.16	0.40	65.52
#6	0.78	35.64	16.92	0.51	66.56	53.06	25.19	0.46	65.66
#7	0.91	52.76	21.47	0.49	67.95	69.90	28.45	0.44	60.11
#8	0.83	44.33	19.78	0.50	67.63	56.93	25.40	0.39	65.01
#9	0.77	30.31	14.57	0.50	69.74	41.89	20.15	0.46	67.04

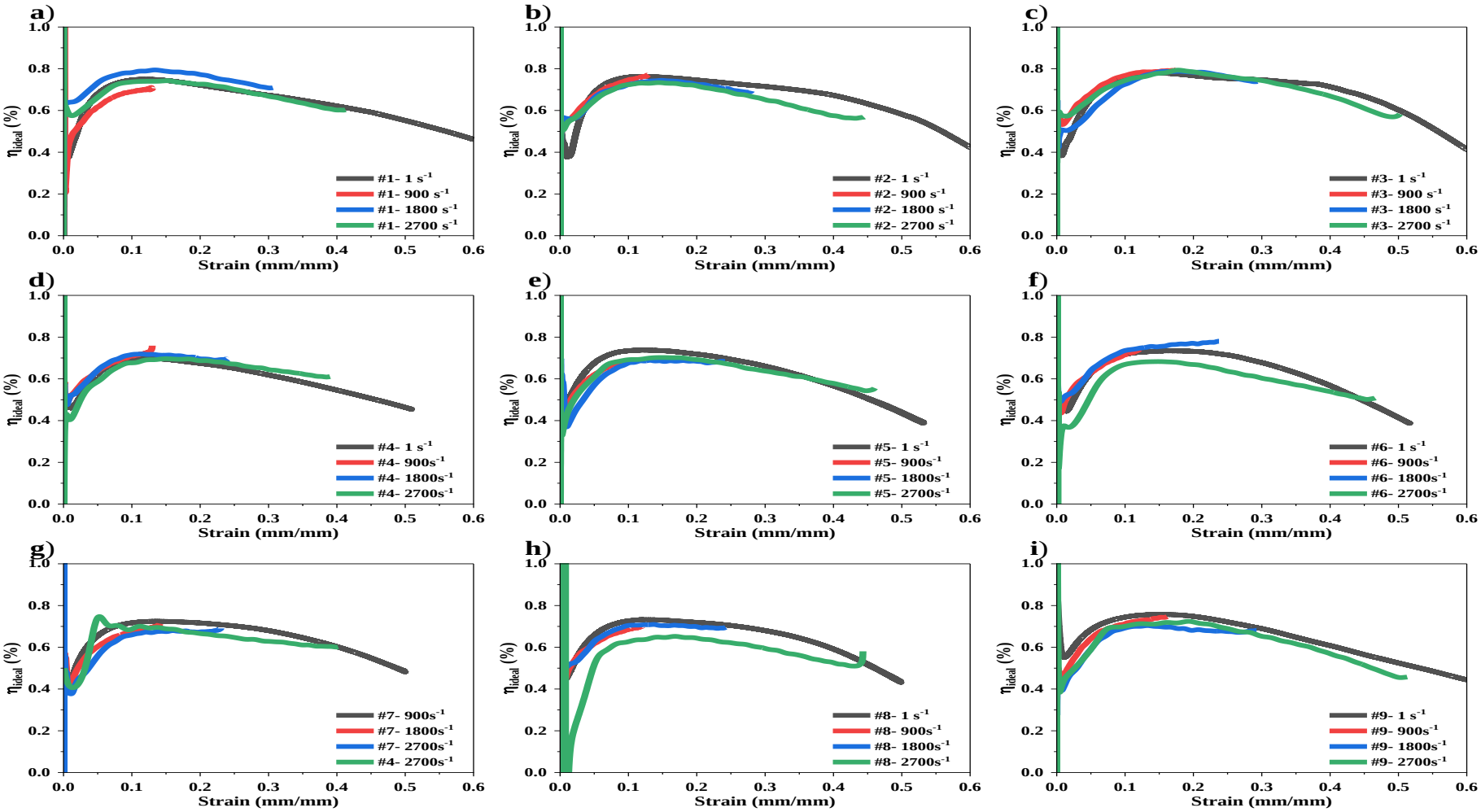

Figure 5.7 : Energy absorption efficiency of sample IDs (A) #1, (B) #2, (C) #3, (D) #4, (E) #5, (F) #6, (G) #7, (H) #8, and (I) #9

Under dynamic loading, the maximum strain attained is less than the sample's densification strain. As shown in Annexure, the EAC is considered at 40% strain, as explained in the previous section. The EAC data has increased under dynamic loading compared to static tests for low-volume fractions. However, the results are not encouraging for higher volume fractions. There is a drop in EAC values for all the size ranges. This behavior can be attributed to the catastrophic failure of the alumina ceramic hollow particles under dynamic loading. This behavior may also lead to the structural failure of these samples.

The ideal energy absorption data shown in **Table 5.3** of the AMSFs is encouraging up on its counterpart (quasi-static condition). There is no significant drop in the absorption efficiency, even at a high strain rate (2700 s^{-1}). The overall energy absorption has improved since there is an improvement in the yield stress data followed by a smooth transition to the plateau region without any stress drops during the deformation. Also, it is observed that with respect to the volume fraction of the particles, there is a rise in the $\boldsymbol{\eta_{ideal}}$ for both quasi-static and at a high strain rate. This accounts for the significant role of the volume fraction irrespective of the particle size. The maximum efficiency is attained at higher volume fractions attributed to the particles' volume fraction and their uniform deformation without significant stress drops. This may account for the reduction in the slope of the stress-strain curve and the increase in the overall EAE.

5.4.3 Compression behavior

The energy absorption capacity and energy absorption efficiency properties are discussed in the earlier sections. These properties are essential to design a material based on the maximum expected efficiency and absorption capacity. The correlation between the energy absorption properties and the stress needs to be further analyzed to

achieve a suitable porosity at a specific stress level. The results displayed in **Figure 5.8(A&B)** on a logarithmic normalized scale are energy absorption capacity vs. stress for quasi-static and high strain-rate data. The E_{Al} is the modulus of the matrix material (aluminum). Also, the normalized EAC vs. stress data can be divided into three regions similar to the stress-strain curve of cellular material, as shown in **Figure 5.8(A)** [115]. A linear elastic region (A) is where the mechanical energy is absorbed in bending and displacing the hollow particles inside the matrix. In plateau (B), the region dissipates energy to fracture the hollow particles and fill the newly evolved voids. In the later part, the material is a fully dense composite with no traces of pours inside the matrix. The densification point is termed the 'shoulder point' by Zhang et al., which is at the densification point [116]. At this point, the cellular materials tend to absorb maximum energy. Later, the W/E_{Al} vs. σ/E_{Al} curve becomes horizontal. Also, during the plateau region, the energy absorption is nearly constant. This study considers the shoulder point at 40% strain before the densification strain for evaluation purposes. Therefore, the summary of the normalized EAC vs. Stress data at 40% data.

In **Figure 5.8 (C)**, the shoulder points of quasi-static and high strain rate data are shown for different densities obtained from the various combinations of size and volume fractions. The data shows a linear rise in the W/E_{Al} value with an increase in the σ/E_{Al} in both testing conditions. However, a notable offset is observed in the high strain rate data. For example, for a known value of σ/E_{Al} (0.003) the normalized data of energy absorption value for quasi-static and dynamic testing is 6.78×10^{-4} and 7.31×10^{-4}.

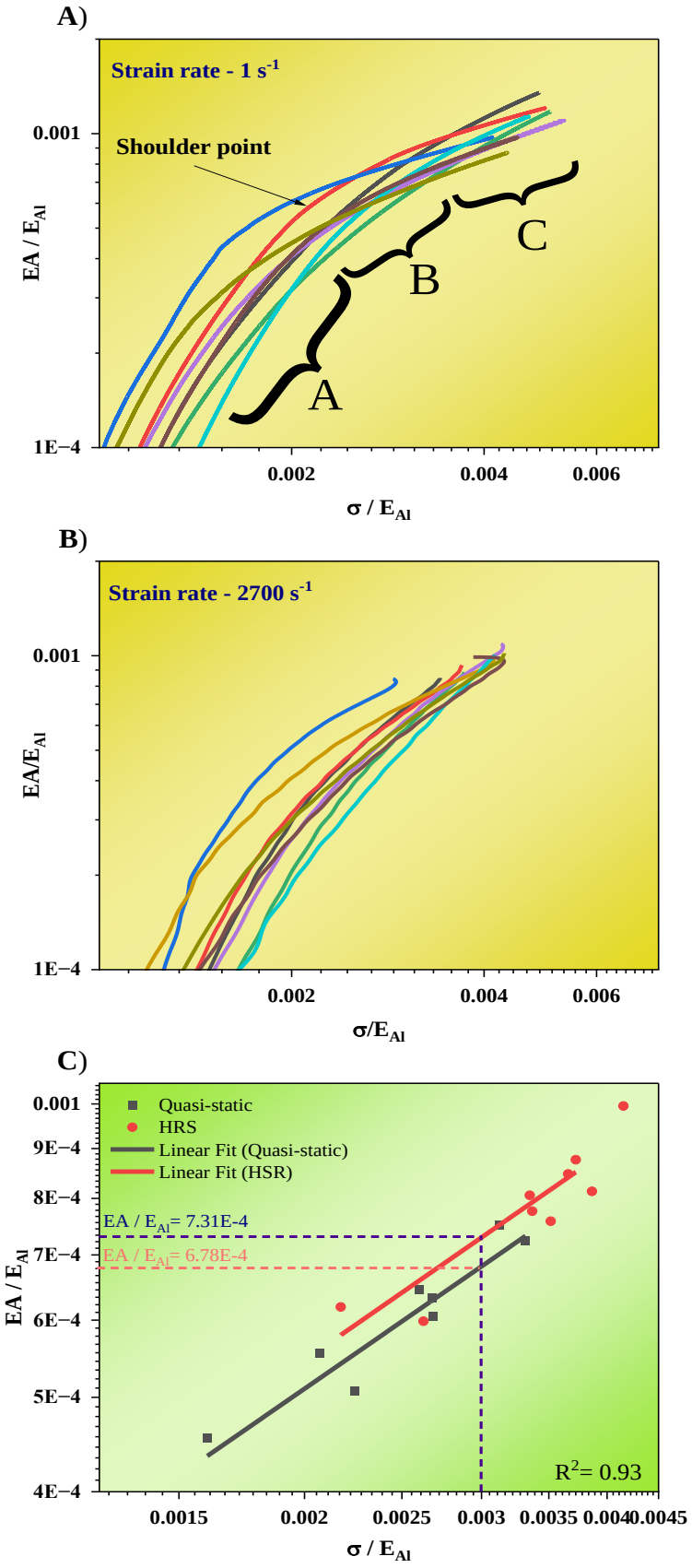

Figure 5.8 : Energy absorption diagram for (A) Quasi-static, (B) High strain rate studies, and (C) A Summary of the data at 40% strain for A & B

The slope of the linear fit curve for different shoulder points considered from **Figure 5.8(A & B)** and its intercept indicates the energy absorption capacity of AMSFs. This behavior suggests that the AMSFs showed better energy absorption properties at high strain rate conditions with maximum. W/E_{Al} value at a given σ/E_{Al}. Further, the mathematical expression for the shoulder point for different test conditions is shown in **Table 3**. These expressions come in handy to design a material with an optimum amount of energy absorption for a given test condition.

Table 5. 4 : Mathematical expression for different conditions

Condition	Mathematical expression of the shoulder point
Quasi-static	$log\frac{W}{E_{Al}} = 0.71log\frac{\sigma}{E_{Al}} - 1.37$
High strain rate	$log\frac{W}{E_{Al}} = 0.72log\frac{\sigma}{E_{Al}} - 1.33$

5.5 DEFORMATION BEHAVIOR

The deformation behavior can be better understood by examining the deformed samples, as shown in **Figure 5.9(a-d)**. **Figure 5.9(a)** shows the deformation behavior of the samples tested at room temperature. These images contain samples tested up to 60% of the strain under various temperature conditions. There are multiple cracks on the external surface of the cylindrical sample due to plastic deformation. These samples display mixed fracture modes, including a) rupture of the external surface of the samples, b) degradation of the external periphery of the samples with the center portion of the sample intact, and c) multiple hinge formation, particularly in samples with high volume fraction.

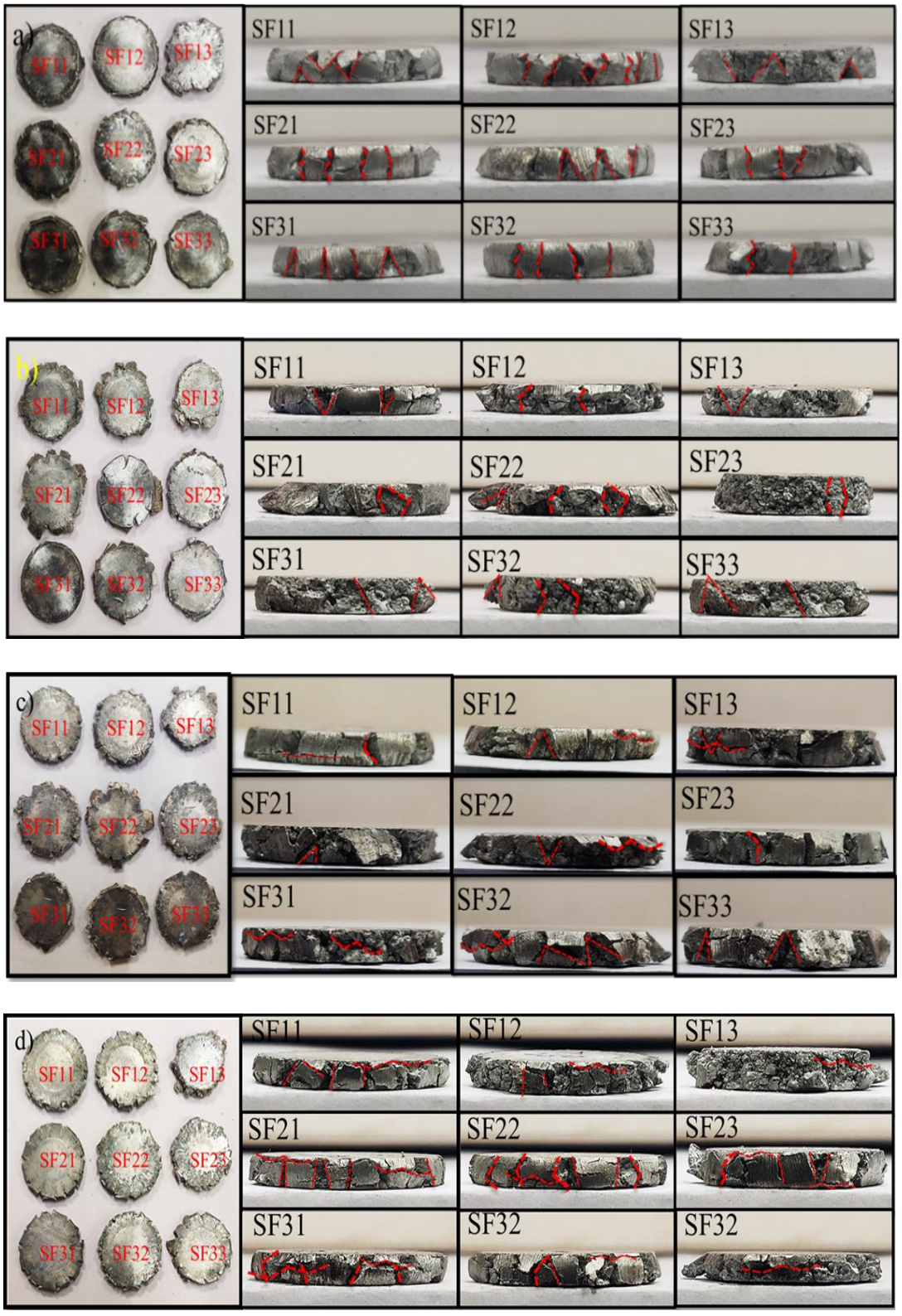

Figure 5.9 : Deformation behavior of SF (a) RT - Quasi-static (b) 100 ºC (c) 175ºC (d) 250 ºC

As observed from their corresponding stress-strain curve, no catastrophic failure can be seen in all the quasi-static conditions. In these conditions, the samples showed visible cracks at 30 % strain. Further, these cracks have grown into individual fragments due to the presence of multiple crack-initiating spots on the sample's surface. The hollow particles on the surface tend to fracture and leave a micro-pore that grows further. The failure of samples with V_f – 30 % of the hollow particles showed more cracks due to multiple locations for crack initiation. The crack initiation probability is higher for large higher volume fractions, which leads to mild structural failure at the out surface, as shown in the top view of the samples in **Figure 5.9(a-d)**.

It is essential to retain the structural integrity during the deformation, which is lacking at higher volume fractions and high temperatures. Due to the softening of the matrix materials, the deformation behavior is significantly affected at higher temperatures. This phenomenon is evident in **Figure 5.9(a & d)**. The deformation mechanism changed due to the matrix softening, considering the high melting point of the reinforcement particles. In contrast to the room temperature conditions, the overall efficiency and energy absorption at high temperatures are promising. Unlike reported elsewhere, the structural damage is minimal among all the conditions [48]. This behavior helps in applying such materials in various structural applications.

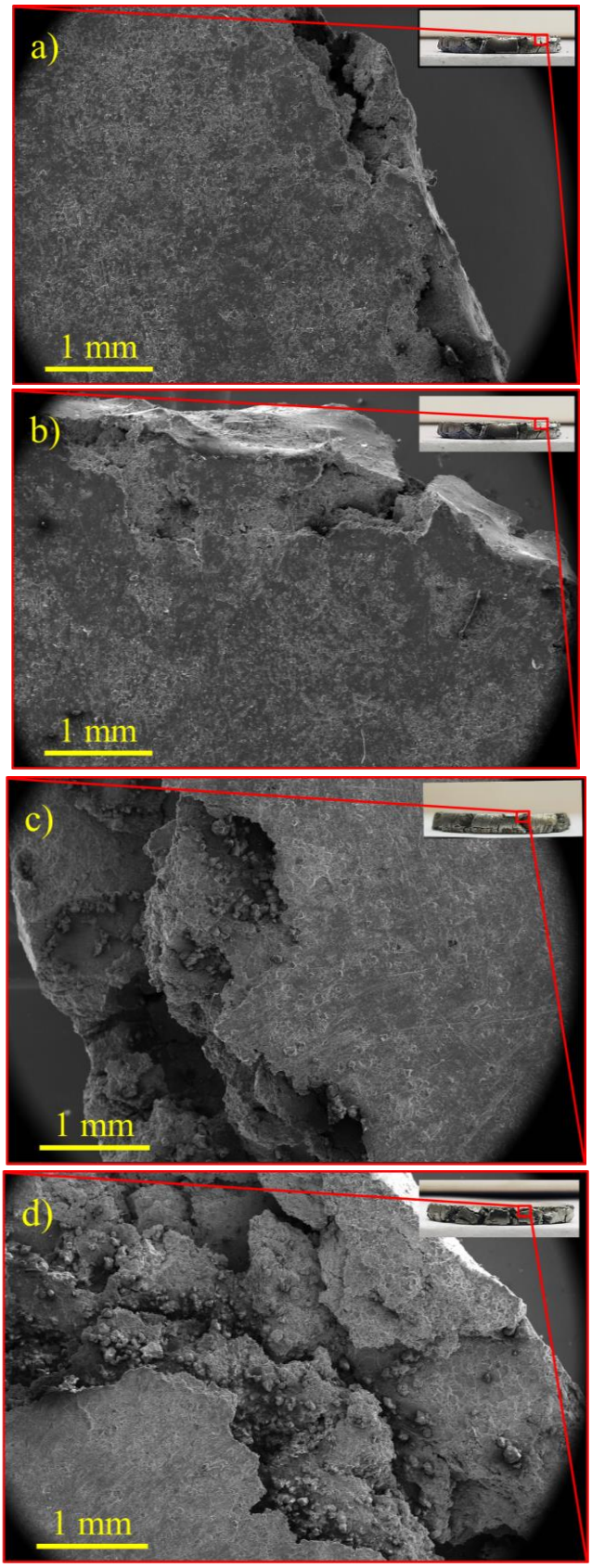

Figure 5.10 : The fracture surface of the 10% volume fraction AMSF observed using SEM (a) RT, (b) 100 ºC (c) 175 ºC (d) 250 ºC

So far, visible digital images have been studied to understand failure behavior. The SEM micrographs are shown below for a 10% volume fraction tested at different temperatures to examine the deformation behavior further. The SEM images in **Figure 5.10(a-d)** show a top view of the four conditions. The damage to the samples took place mainly on the circumference. In **Figure 5.10(a)**, the particles were restricted during the deformation, leaving no fractured particle segregation on the boundary. However, in **Figure 5.10(d)**, the particles have flowed toward the sample circumference. The cross-sectional micrographs in **Annexure A1** suggest that a limited number of porous sites were observed inside the matrix deformed at higher temperatures. This behavior may be attributed to the matrix flow behavior during high temperatures.

Therefore, there are multiple possible failure characteristics during the deformation of the AMSFs. The most important parameters influencing the primary failure mechanism of the AMSFs are the strength of the matrix alloy, the crush strength, and the particle t/D ratio of the filler materials. The manufacturing methods may also affect the failure behavior [19]. Based on the deformation behavior observed in **Figure 5.10 and Annexure A1**, the following are the two possible failure modes of AMSFs under quasi-static deformation, as shown in **Figure 5.11**. In mode-a, bulging and shear failure largely dominates, and cracks occur at the top face in the initial stage, and later, the cracks progress to the bottom face. This behavior is observed at low temperatures. In mode-b, the flow stress of the matrix and fracture particles contribute to crack growth. As the temperature increases due to matrix softening at high temperatures, the fractured hollow particles contribute more to crack growth. In **Figure 5.9(c & d),** the earlier ‘v’ and inverted ‘v’ shape cracks are replaced with

extended cracks. This behavior also supports the argument on the flow of particles to the circumference during high temperatures studies.

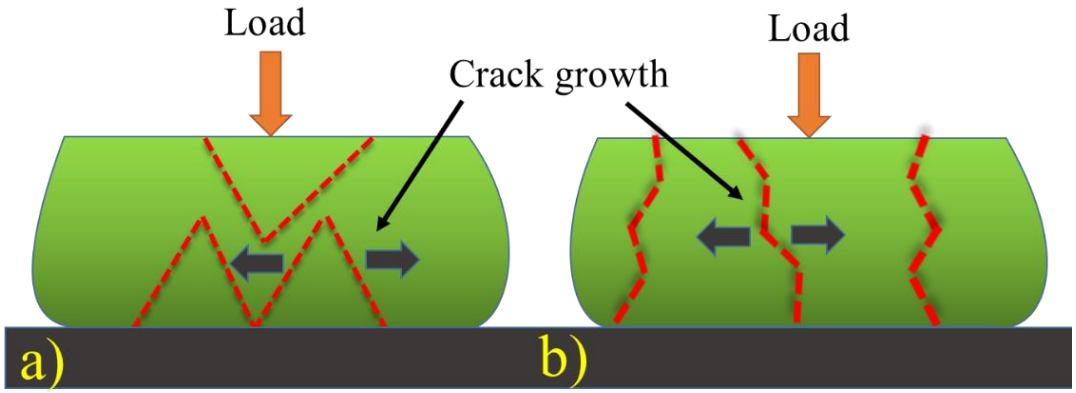

Figure 5.11 : A schematic representation of the AMSFs' probable failure modes observed from the fractured images

It is essential to retain the structural integrity during the deformation, which is lacking for higher volume fractions. Due to the softening of the matrix materials, the deformation behavior is significantly affected at higher temperatures. In this study, the alumina particles have contributed to the overall efficiency and energy absorption at high temperatures. A matrix behavior can be softened from the top view of the samples tested for different temperatures. The number of cracks has reduced with the temperature rise. Since the samples are tested below the recrystallization temperature of the matrix, thermal softening, and grain mobility contributed to the deformation. The DIC analysis was performed using Ncorr, a 2D image correlation software in Matlab, to analyze the discrete images to develop a correlation between the deformed and un-deformed samples. **Figure 5.12** displays the DIC analysis for three strain rates captured from the high-speed images. A uniform deformation is observed in the samples tested in all the strain rates up to the elastic limit. Also, during the shift from the elastic to the plastic stage, the deformation gradient shown in **Figure 5.12** is

uniform. This behavior agrees with the stress-strain response from **Figure 4.4** (Refer to Chapter 4).

Further, up to the 1800 s^{-1}, the material response is almost uniform. At a strain rate of 2700 s^{-1}, a significant distortion is observed after 0.2 strain. This behavior is attributed to the plastic flow of the matrix material as a result of cracking and fracture of the external surface of the samples. Also, it is observed that the DIC analysis failed to capture the significant distortion in the sample under compression after 0.2% strain. Further, **Figure 5.13(A & B)** shows the fractured samples of different particles size and volume fractions tested at low and high strain rates. In **Figure 5.13(A)**, the quasi-static test samples are deformed up to 60% strain. The fractured samples showed a minimum structural failure in all conditions. The failure initiates from the external surface due to the presence of a large number of unconfined hollow particles with matrix material. However, the confined particles inside the matrix tend to fracture and contribute to the densification of the material. These cracks extended further along the lateral direction to accommodate the external force, which resulted in random cracks along the surface of the samples. The appearance of such typical plastic deformation was due to the complete densification of the AMSFs.

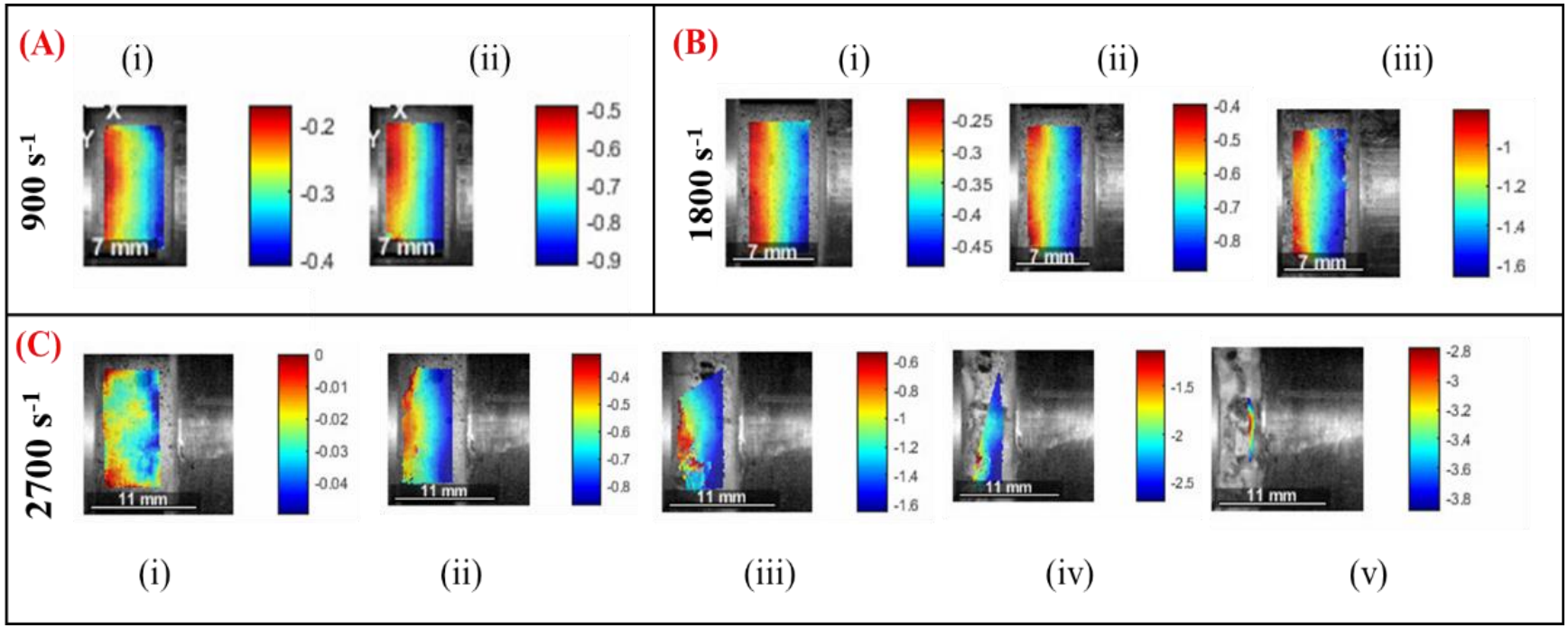

Figure 5. 12 : Deformation process of AMSFs at three strain rates (A) 900 s^{-1}, (B) 1800 s^{-1}, and (C) 2700 s^{-1} using DIC analysis with the axial displacement field captured at different strains (i) 0.005, (ii) 0.1, (iii) 0.2, (iv) 0.31, (v) 0.475.

Figure 5. 13 : Representative deformed samples tested at (A) low strain rate (1 s^{-1}) and (B) High strain rate (2700 s^{-1})

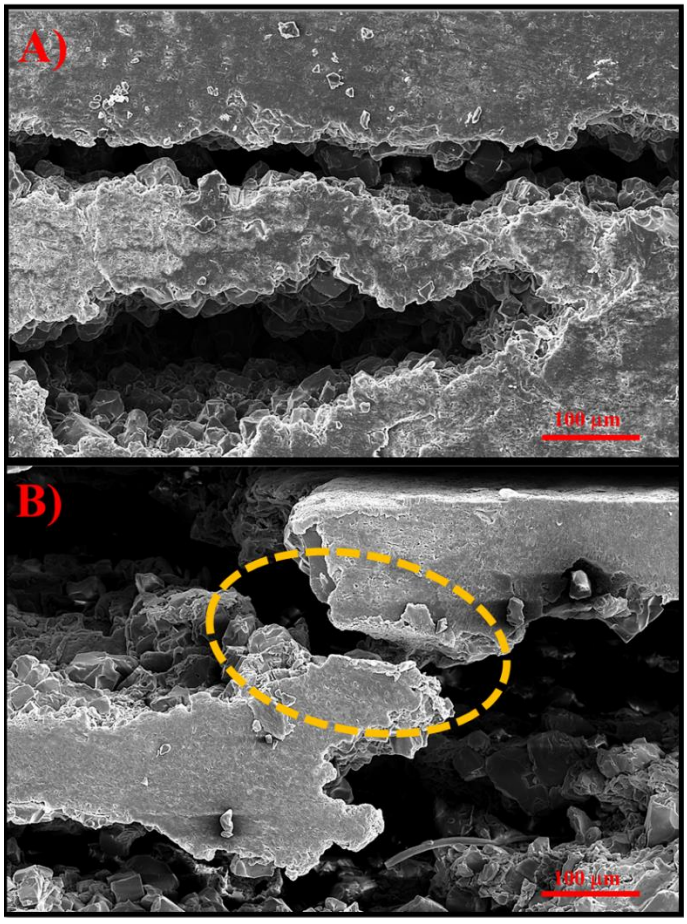

Figure 5.14 : Cross-sectional images of sample #9 with tested at (A) Quasi-static and (B) Dynamic conditions

In contrast to the low strain rate behavior, a large number of cracks are observed during high strain rate tests deformed up to 40-50% strain. Also, the samples' surface is significantly affected, and structural failures are observed in samples with hollow particles above 20 % volume fraction. This behavior is observed due to the reduced matrix percentage and rapid crack propagation due to the impact, which results in the hardening of AMSFs. Another factor affecting the hardening and delamination is matrix failure at the interface of two hollow particles. **Figure 5.14** shows the representative fracture images of samples tested at low and high strain rates. Based on observation of the cross-section of the samples, during quasi-static deformation, the hollow particles fractured during the deformation, and the matrix material buckled at the interface of the two particles. This behavior helps in more plateau slop during the hardening. However, the matrix interface fractured and failed during the dynamic loading before attaining the densification zone, as shown in **Figure 5.14(B)**.

Thus, during quasi-static deformation, the hollow particles and matrix material compensate for the energy absorption in the form of uniform particle failure and the plastic flow of the matrix. During high strain rates, they show hardening behavior due to the matrix failure at the interface after the failure of the hollow particles.

5.6 SUMMARY

The particles' size, volume fraction, and t/D ratio have significantly affected the energy absorption properties of the SFs. The yield stress increases with an increase in volume fraction, and the densification strain and plateau strain decrease. This behavior helps in the enhancement of energy absorption efficiency. The deformation behavior of all the test conditions is examined, and the two major fracture modes are observed and proposed. The sample examined at increased temperatures demonstrated a decrease in the 1 % offset yield stress values at a lower AMSFs relative density. At 250 ºC, the flow stress of 78.88 MPa is found at 0.92 relative density.

Similarly, a maximum energy absorption efficiency of 75.77 % and 78.92 % percent was achieved at 250 ºC and HSRs, respectively, with a relative density of 0.86. Despite high temperatures, the slope of the curve in the elastic area has led to the maximum amount of energy being retained. When relative density drops, densification strain, and energy absorption efficiency improve, this behavior applies to particles of all sizes. The deformation behavior of the samples roughly follows two failure scenarios. This effect is very dependent on the temperature at which samples were examined.

The study of SFs using computational techniques may help to design advanced materials for future needs. In this regard, different analytical and computational models are explored in Chapter 6. These models' data are compared and validated using the experimental results obtained in Chapter 5.

5.7 ANNEXURE

Annexure A1:

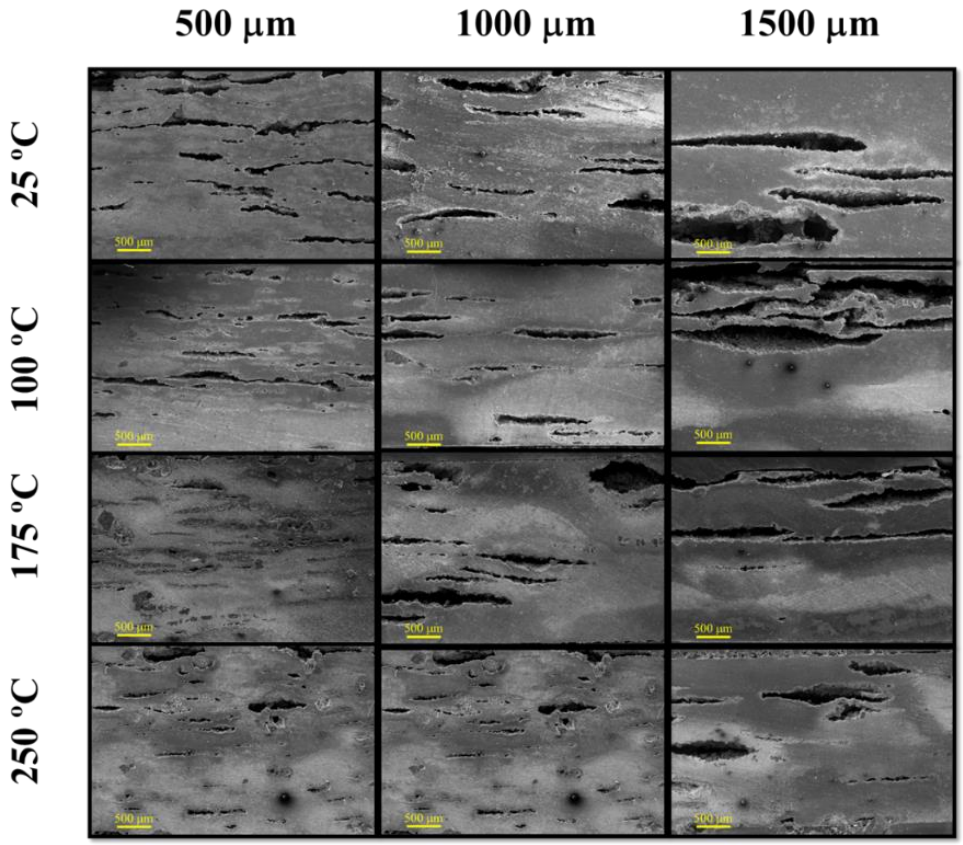

Figure 5.15 : Shows the cross-sectional view of the deformed samples tested at different temperature conditions (A1)

The image above shows the sectional view of the samples at different temperature conditions. These samples are representative images of the AMSFs with a 30% volume fraction of hollow particles.

Annexure A2:

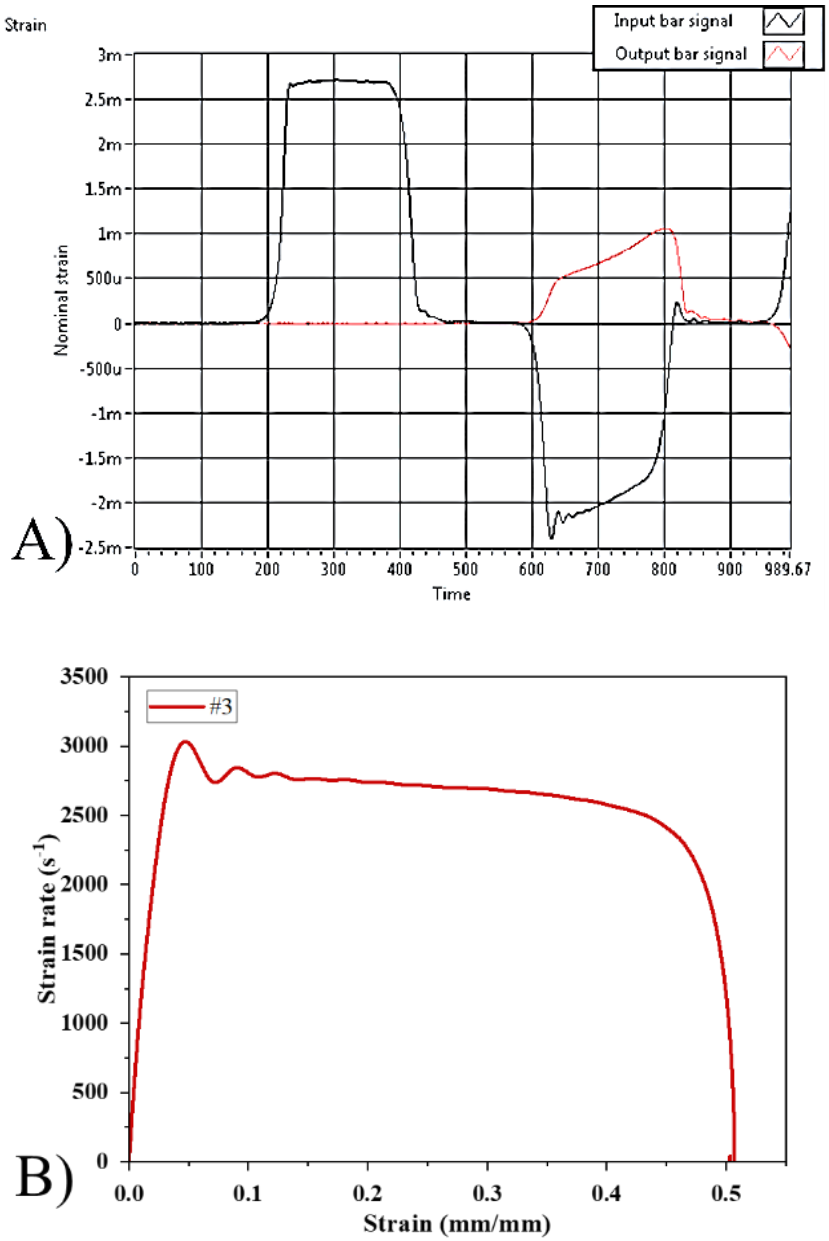

Figure 5.16 : The raw data and the strain vs. strain rate data from the SHPB studies for sample #3 (A2)

Annexure A3:

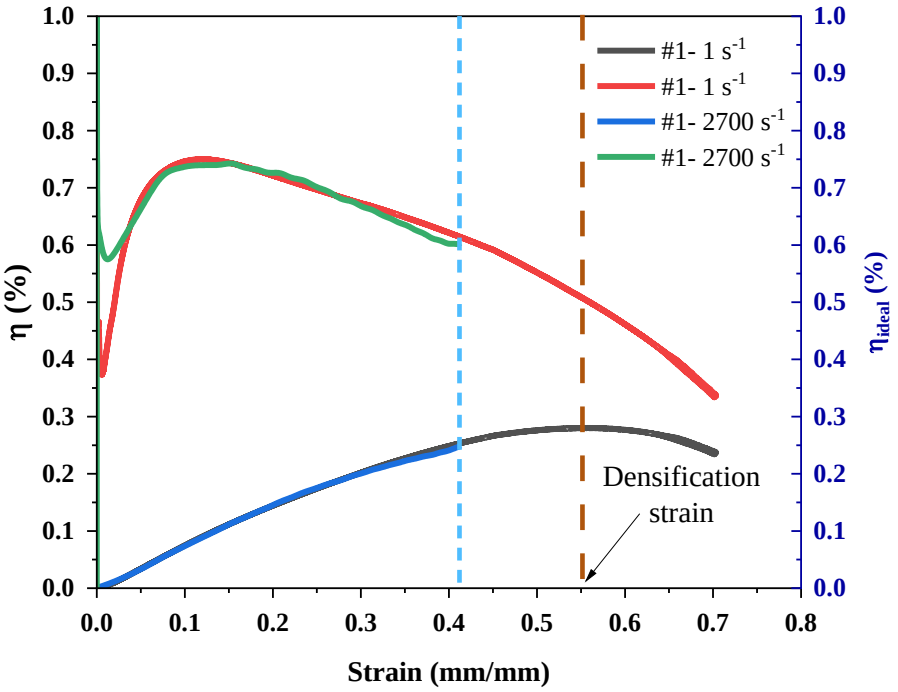

Figure 5. 17: A representative graph showing the densification strain for quasi-static deformation. (A3)

Chapter 6: Numerical and Analytical Methods

The experimental studies from the previous chapters provide the details of the mechanical response of AMSFs under quasi-static and dynamic loading. In this chapter, the syntactic foam materials are studied further using analytical models and numerical methods to predict the elastic and elasto-plastic properties of the syntactic foams. Also, the elastic properties obtained from the analytical models are compared against the numerical data. The key focus is the development of computational models of syntactic foams using representative volume elements (RVE) and predicting the elastic and elasto-plastic responses. Further, the macroscopic response of the syntactic foams is also presented with experimental validation.

In conclusion, numerical simulations have proven to be powerful tools in comprehending syntactic foams' mechanical, thermal, and acoustic behavior. The insights gained from these studies have immense practical implications for industries ranging from marine engineering and aerospace to automotive and packaging. As computational capabilities continue to advance, further investigations promise to unlock new possibilities for optimizing and innovating syntactic foam materials for various applications.

6.1 INTRODUCTION

Understanding the effective properties of composite materials using homogenization tools and methods has been reported since the 1900s. Recently, numerical method-based approaches have been developed to predict the actual and accurate data of the composite materials based on the microstructure. Conventionally,

to esses the material properties, experimental studies such as compression/tension are conducted. These measurements are the average values of the specimen, considering that the material is homogeneous. Similarly, despite utilizing empirical, analytical, semi-analytical, or numerical FE-based approaches, the assumption of homogenization is always made when employing any form of material property predictions.

Understanding the problem domain is necessary to use the computational method and to address problems. In computational models, the major challenge occurs in representing the actual physical model. Consequently, many FE users commonly adopt a representative volume element approach to solve complex problems and computationally expensive models. The RVE model captures the totality of the physical model so that the FEM results are obtained close to the predicted values. These RVE models are much smaller than the physical representation and original geometry to conserve computational time. Therefore it is essential to choose a representative volume that captures the effective properties of the original structure. The unrepresented portion of the model of the virtual domain can be considered by selecting the appropriate boundary conditions and eventually lead to accuracy in the effective numerical solution. **Figure 6.1** shows the schematic of the RVE model and homogenization approach.

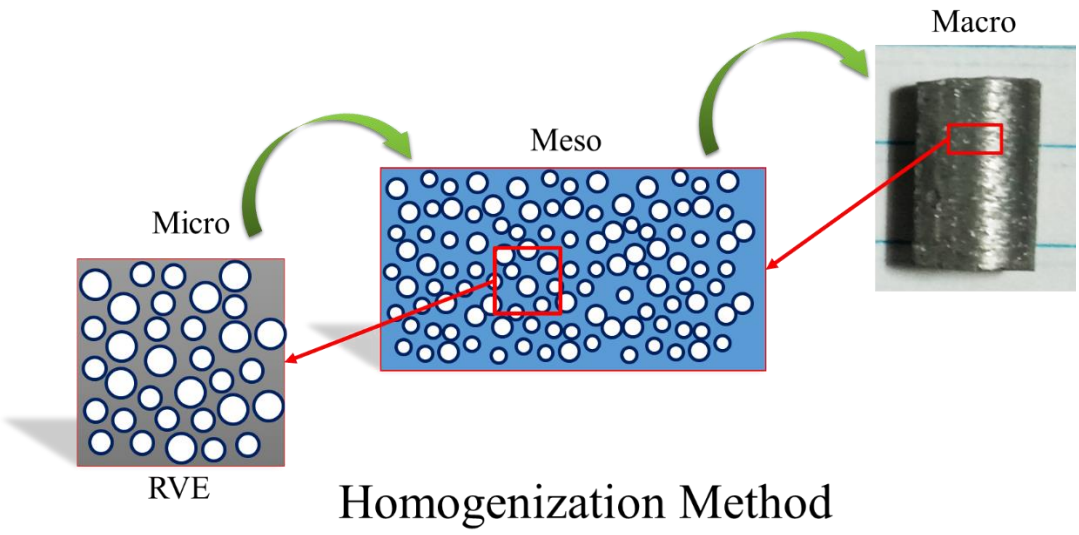

Figure 6.1: The schematic of the RVE model and homogenization approach

Apart from experimental studies, some literature works focused on estimating the SF's micro and macroscopic properties using analytical and finite element (FE) models [93–96]. The micromechanics-based models provide few insights into the compressive behavior of the foams [95,117]. Estimation of the effective elastic properties of the metal matrix syntactic foams (MMSF) is challenging using both the analytical and FEM models due to their structural heterogeneity [40]. Unlike particulate composite materials, the micromechanical models for SFs require sophisticated methods to estimate the effective elastic modulus. In earlier studies, Lee and Westmann developed a model to identify the upper and lower bounds for shear and bulk modulus values [93]. Later, in subsequent investigations, a significant amount of work is performed on polymer-based foams [29,30]. The shear and bulk modulus of polyester resin-based foams with a 35% volume fraction of hollow particles is reported by Huang and Gibson [94]. In this model, the particles are considered suspended in a dilute medium. Their results overestimated the effective modulus at high-volume fractions since the displacement due to the particle interactions is not

considered. Porfiri and Gupta proposed a single inclusion problem-based model to find effective properties even at higher volume fractions [38].

The micromechanics-based analytical models consider the interface between the matrix and the particles as perfectly bonded and provide upper and lower bounds of the predicted data. Also, these models may not consider the distribution of the particles and bond interface properties [95]. In this regard, computational micromechanics-based finite element (FE) models based on the representative volume elements (RVE) are developed, which may predict the material properties more accurately. These FE models of SFs may consider the random distribution of particles inside the matrix. Bardella *et al*. developed an RVE-based FE model to study the elastic properties of the polymer SFs and compared it using theoretical models such as Mori-Tanaka, and Self-Consistent [97]. Szlancsik *et al*. studied the micromechanical properties of aluminum foams and compared them against the numerical and FE element modeling using a macroscopic finite element model [40]. They further developed RVE-based macroscopic models to study the elasto-plastic behavior under free compression [50]. Additionally, few works focused on generating the RVE domain using advanced algorithms and micro-computer tomography scans [98,99]. Initially, RVE-based modeling techniques to predict elastic properties were studied. Later, they were extended to a macroscopic model to reproduce the stress-strain response during plastic deformation [6]. A mathematical approach to stress-strain behavior is reported by Lorgeril *et al*. [100]. This study is extended to a continuous approach by Orbulov & Májling to produce the macroscopic behavior of the SFs and the peak function [101].

Historically, experimental testing has been the primary means of characterizing the behavior of syntactic foams. While experiments provide valuable data, they can be time-consuming, costly, and limited in scope, especially when studying complex

phenomena or exploring a wide range of material configurations. This limitation has spurred the adoption of numerical simulations as an effective alternative or complement to experimental studies.

Numerical studies influence the power of computational methods, such as finite element analysis (FEA), computational fluid dynamics (CFD), and discrete element modeling (DEM), to analyze the response of syntactic foams under different loading conditions and environmental factors. Through sophisticated numerical simulations, researchers can gain deeper insights into these foams' mechanical properties, failure mechanisms, and deformation behavior. Additionally, numerical models provide a platform to investigate the influence of microstructural features, such as particle distribution and interfacial bonding, on the overall performance of the foam.

Moreover, numerical simulations extend beyond mechanical properties and encompass investigations into syntactic foams' thermal and acoustic behavior. These studies play a pivotal role in optimizing the thermal insulation capacity of foams for applications in extreme temperature environments and in designing acoustic absorption materials for noise control.

In literature, most studies have analyzed polymer matrix SFs' behavior using analytical or numerical techniques [93,118]. Limited works are presented that focus on the behavior of AMSF. As the use of AMSF is increasing in structural applications, we aimed to study in detail the behavior of AMSFs by the elastic and elasto-plastic responses of AMSFs under compression using experimental, analytical, and FE-based techniques. The AMSFs were processed using the powder metallurgy method, and their quasi-static compression studies were performed. The elastic constants are estimated using different analytical models and are compared with the experimental

data. The sensitivity of different model parameters is examined. Also, RVE-based FE methods are used to estimate the effective properties of AMSFs. The computational RVE domain has been generated in the ABAQUS using user-defined algorithms at different volume fractions by considering the microstructural inhomogeneities. Further, the RVE-based models are extended to study the elasto-plastic behavior of AMSF.

6.2 SHELL GEOMETRY AND PARTICLE DISTRIBUTION

Many previous studies estimated the elastic properties of the polymer syntactic foams and MMSFs using linear homogenization (LH) techniques such as the Rule of mixtures (RM), Hashin-Shtrikman (HS), Mori-Tanaka (MT), Classic self-consistent (CSC) and Differential self-consistent (DSC) [40,95,119]. Apart from these models, empirical relations such as Halpin-Tsai (HT) equations are also used. These LH models have proven to predict accurate results for continuous fiber-reinforced and particulate composites. When applied to SFs, these models failed to predict a close match with the experimentally obtained values for polymer syntactic foams [120] and for aluminum matrix syntactic foams [40]. On the other hand, it is reported in the literature that the finite element-based RVE homogenization models can predict better estimates than LH models [121]. This is because, in FE-based models, geometric aspects such as particle size and randomness can be implemented. In this work, we aim to compare the estimates of LH and RVE-based models specifically applied to AMSFs. The mathematical expressions of LH models are presented in many previous articles. However, for the sake of completeness, the expressions are given in the Appendix.

For RVE models, the geometry of the hollow particle and RVE domain size is the crucial input parameters. The typical geometry of a circular hollow particle (diameter and shell thickness) can be represented through the particle radius ratio (η). In the earlier studies reported for polymer-based syntactic foam reinforced with glass/ceramic hollow particles [95,118], the particle radius ratio (η) considered is above 0.95. The value η suggests the amount of shell thickness for the corresponding particle diameter. The hollow particle's relative density and particle radius ratio can be evaluated using [56].

$$\eta = 1 - 2\left(\frac{t}{D}\right) \tag{6.1}$$

$$\frac{\rho_{hollow\ sphere}}{\rho_{Al_2O_3}} = \left(1 - \frac{d^3}{D^3}\right) \tag{6.2}$$

$$\frac{t}{D} = 0.5\left[1 - \left(1 - \frac{\rho_{hollow\ sphere}}{\rho_{Al_2O_3}}\right)^{1/3}\right] \tag{6.3}$$

where *t* is the thickness of the shell, *d* is the inner diameter, and *D* is the outer diameter of the particles. The $\rho_{Al_2O_3}$ represents the bulk density and $\rho_{hollow\ sphere}$ represents the hollow particle density of Al_2O_3.

The wall thickness *t* is estimated based on the FE-SEM images of unbroken and broken hollow particles, as shown in **Figures 6.2(a) and (b). Figures 6.2(c) and (d)** depict the particle distribution and the wall thickness details.

After measuring the wall thickness, the particle radius ratio (η) is calculated as 0.88 for AMSF using Equation 6.1. This is less than the reported values from the earlier studies on polymer foams. This may be attributed to the significant effect of density and processing techniques of the alumina. Since the alumina particles are hollow, the

actual density of these particles may alter from the bulk properties. For the present case, thickness is estimated as 15 μm, outer diameter as 250 μm, and $\eta = 0.88$.

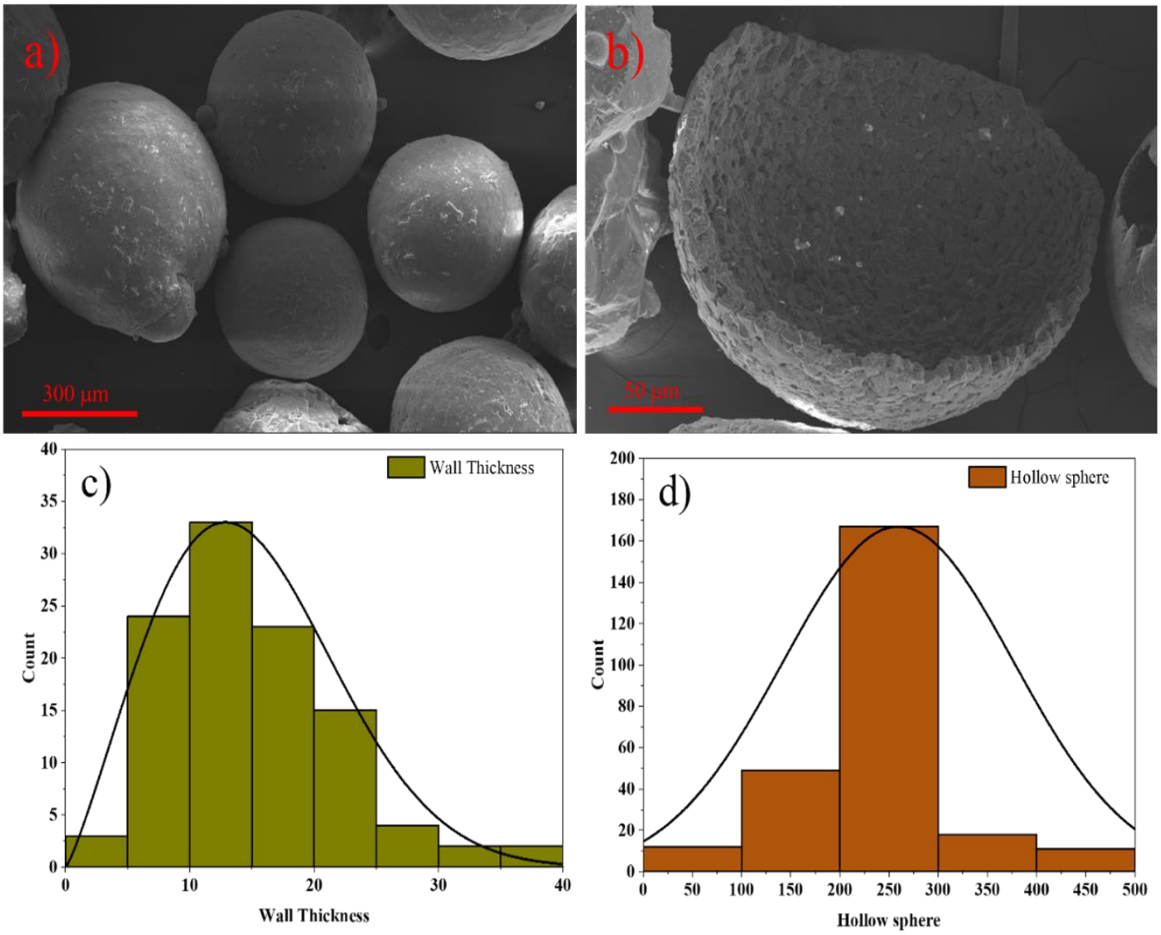

Figure 6.2: (a) & (b) Scanning electron micrographs of Al_2O_3 hollow particles and (c) & (d): Distribution histogram for particle shell thickness and diameter

6.3 NUMERICAL MODELING OF SYNTACTIC FOAMS

The mathematical models are presented for estimating the elastic properties such as shear, bulk, and elastic modulus. Many previous studies estimated the elastic properties of polymer syntactic foams [93,95,118] and metal syntactic foams [40] using linear homogenization (LH) techniques such as Rule of the mixtures (RM), Hashin-Shtrikman (HS), Halpin-Tsai (HT), Mori-Tanaka (MT), Classic self-consistent

(CSC) and Differential self-consistent (DSC). These LH models have proven to predict accurate results for continuous fiber-reinforced and particulate composites. When applied to syntactic foams, these models failed to predict a close match with the experimentally obtained values as reported in [95] for polymer syntactic foams and in [40] for aluminum metallic syntactic foams. On the other hand, it is reported in the literature that the finite element-based RVE homogenization models can predict better estimates than LH models. This is because, in FE-based models, geometric aspects such as particle size and randomness can be implemented. In this work, we would like to compare the estimates of LH and RVE-based models specifically to Al-Al_2O_3 syntactic foams. The mathematical expressions of LH models are presented in many previous articles. However, for completeness, we are providing the expression below.

The analytical estimates such as the Rule of the mixtures (RM), Hashin-Shtrikman (HS), Halpin-Tsai (HT), Mori-Tanaka (MT), Classic self-consistent (CSC), and Differential self-consistent (DSC) were applied to the AMSF. These models estimate the effective shear and bulk modulus for different volume fractions.

6.3.1 Analytical models

The RM is the most commonly used technique to attain the initial estimate of modulus values in composite systems. The shear (G_{RM}) and bulk (K_{RM}) modulus are calculated using the RM for AMSF [95],

$$G_{RM} = f(1-\eta^3)G_m + f(1-\eta^3)G_r \quad (6.5)$$

$$K_{RM} = f(1-\eta^3)K_m + f(1-\eta^3)K_r \quad (6.6)$$

Where η is the radius ratio of particles and f is the volume fraction.

The HT relation considers the shape of the matrix and reinforcement, which may provide a better estimate for particulate-reinforced composites [122]. To incorporate the thickness of the hollow particles, the aspect ratio term is altered using the thickness-to-diameter ratio, i.e., $s = t/D$. The reinforcement parameter $\xi = 2s$ is derived from reinforcement geometry, distribution, and loading conditions. Since the particles are spherical, the angle factor (a) is considered 1. The following equations are proposed for estimated properties using HT relations with thickness-to-diameter ratio,

$$E_{HT} = \frac{E_m(1 + 2sq)V_p}{1 - qV_p} \tag{6.7}$$

$$q = \frac{\left({M_r}/{M_m}\right) - 1}{\left({M_r}/{M_m}\right) - 2s} \tag{6.8}$$

$$E = \frac{9KG}{(3K + G)} \tag{6.9}$$

$$K = \frac{EG}{3(3G - E)} \tag{6.10}$$

The bulk and shear modulus data are calculated by substituting the proposed modification in equations (8) and (9).

The shear and bulk modulus are computed using the Classical Hashin-Shtrikman method [97],

$$G_{HS} = \left\{ \frac{f(1-\eta^3)G_r + (1-f)\dfrac{G_r}{\left(1 + \dfrac{G_w(9K_r + 8G_r)}{6G_m(K_r + 2G_r)}\right)\beta_m}}{f\eta^3\,\dfrac{6(K_r + 2G_r)}{9K_r + 8G_r} + (1-f)\,\dfrac{(G_r - G_m)}{G_m + \dfrac{G_r(9K_r + 8G_r)}{6(K_r + 2G_r)}} + 1} \right\} \tag{6.11}$$

$$K_{HS} = \left\{ \frac{f(1-\eta^3)K_r + (1-f)\dfrac{3K_rK_m}{(3K_m+4G_r)\alpha_r}}{f\eta^3\ \dfrac{3K_r}{4G_r} + (1-f)\ \dfrac{3(K_r-K_m)}{3K_m+4G_r} + 1} \right\} \tag{6.12}$$

The subscripts r and m refer to properties associated with reinforcements and matrix. Similarly, α and β are constants that can be calculated using the following equations:

$$\alpha(G,K) = \frac{3K}{3K+4G} \tag{6.13}$$

$$\beta(G,K) = \frac{6(K+2G)}{5(3K+4G)} \tag{6.14}$$

The following equations calculate the shear (G_{MT}) and bulk (K_{MT}) moduli of SFs using MT estimation,

$$G_{MT} = \left\{ \frac{(1-f)G_m + f(1-\eta^3)\left(\dfrac{G_m}{\left(1+\dfrac{G_m(9K_m+8G_m)}{6G_r(K_m+2G_m)}\right)\beta_m}\right)}{f\eta^3\ \dfrac{6(K_m+2G_m)}{9K_m+8G_m} - f(1-\eta^3)\left(\dfrac{(G_r-G_m)}{G_r+\dfrac{G_m(9K_m+8G_m)}{6(K_m+2G_m)}}+1\right)} \right\} \tag{6.15}$$

$$K_{MT} = \left\{ \frac{(1-f)K_m + f(1-\eta^3)\left(\dfrac{3K_rK_m}{(3K_r+4G_m)\alpha_m}\right)}{f\eta^3\ \dfrac{3K_m}{4G_m} - f(1-\eta^3)\ \left(\dfrac{3(K_r-K_m)}{3K_r+4G_m}+1\right)} \right\} \tag{6.16}$$

The Classic Self-Consistent (CSC) estimation applied to the aluminum matrix syntactic foam material is

$$\left\{\frac{f\eta^3}{(1-\alpha_{csc})}+\frac{f(1-\eta^3)}{1+\alpha_{csc}\left(\frac{K_r}{K_{csc}}-1\right)}+\frac{(1-f)}{1+\alpha_{csc}\left(\frac{K_m}{K_{csc}}-1\right)}\right\}=1 \tag{6.17}$$

$$\left\{\frac{f\eta^3}{(1-\beta_{csc})}+\frac{f(1-\eta^3)}{1+\beta_{csc}\left(\frac{G_r}{G_{csc}}-1\right)}+\frac{(1-f)}{1+\beta_{csc}\left(\frac{G_m}{G_{csc}}-1\right)}\right\}=1 \tag{6.18}$$

In the equation (16) and (17), $\alpha_{csc}\,(K_{csc}, G_{csc}) = \alpha_{csc}$ and $\beta_{csc}\,(K_{csc}, G_{csc}) = \beta_{csc}$ are calculated based on equations (8) & (9).

The self-consistent differential estimations (DSC) for different volume fractions can be calculated using the following equations.

$$\left\{\frac{1}{1-s}\left(\frac{(1-\eta^3)K_{Dsc}(s)[K_r-K_{Dsc}(s)}{K_{Dsc}(s)+\alpha_{Dsc}(s)[K_r-K_{Dsc}(s)]}+\frac{K_{Dsc}(s)\eta^3}{(\alpha_{Dsc}-1)}\right)\right\} = \frac{dK_{Dsc}(s)}{ds} \tag{6.19}$$

$$\left\{\frac{1}{1-s}\left(\frac{(1-\eta^3)G_{Dsc}(s)[G_r-G_{Dsc}(s)}{G_{Dsc}(s)+\beta_{Dsc}(s)[G_r-G_{Dsc}(s)]}+\frac{G_{Dsc}(s)\eta^3}{(\beta_{Dsc}-1)}\right)\right\} = \frac{dG_{Dsc}(s)}{ds} \tag{6.20}$$

In which $\alpha_{Dsc}\,(K_{Dsc}, G_{Dsc}) = \alpha_{Dsc}$ and $\beta_{csc}\,(K_{csc}, G_{csc}) = \beta_{csc}$ calculated according to equations (8) & (9). The DSC estimates of bulk and shear modulus are obtained using the explicit Euler method, as reported by Szlancsik et al. [40]. The young's modulus values for the above equations are determined using equation (8).

6.3.2 Elastic constants using the RVE model

A composite foam reduces the weight of the high-performance component without sacrificing mechanical properties. These qualities make these materials well-suited for aeronautical, marine, defense, and transportation applications. Lightweight

and load-bearing properties are essential in these applications. A syntactic foam induces porosity using impermeable micro hollow particles. Due to these hollow particles, these materials are stiffer than the typical foams.

The syntactic foams contain two significant phases, matrix and hollow particles, with a shell thickness. Another phase may occur due to the processing technique, and particle geometry is external/undesired porosity. In this study, the external/undesired porosity is not considered. The tailored properties of the SFs can be achieved by varying the type of matrix and hollow particle material, the volume fraction, and the size of the particles. The experimental studies and the FE models are extensively studied in the literature for polymer and some studies on the metal matrix-based syntactic foams.

In the literature, the FE-based macroscopic models are created to simulate the elasto-plastic behavior of the SF structures. The objective of the RVE models in the literature is to explore elastic behavior. The elastic and elasto-plastic responses of AMSFs under compression are investigated in this work. Different volume percentages of RVE models are built and investigated using a user-defined method. The analytical and FE-RVE models are used to determine the elastic constants. The properties found using numerical approaches are explored and compared to other analytical models.

Al_2O_3-reinforced AMSF comparisons to experimental data and the elasto-plastic behavior of this material are also reviewed. The experimental data and the FE-based stress-strain responses are compared. It is investigated how well various models' sensitivity settings work against the RVE.

RVE Modeling of AMSFs:

The representative volume element approach is part of the computational modeling of materials. This technique considers the constitutive feature of materials such as size, shape, volume fraction, and particle distributions for modeling. The RVE models are typically modeled in the size range to capture the microstructural features of materials. These are replicas of the constituent material in smaller ranges to enhance computational efficiency. Some studies have proven this estimates the properties using numerical modeling [95,123].

The microstructure of SF is considered to be randomly distributed hollow particles across the matrix phase. The modeling of SF RVE involved three significant steps: 1) selection of the matrix cube/cylinder size, 2) selection of the particle size, wall thickness, and volume fraction of the particles, and 3) Arrangement of the non-overlapping particles across the matrix. Cubic RVE models of dimension 1.5 × 1.5 × 1.5 mm are considered to imitate the syntactic foam microstructure. A series of non-overlapping random points are generated using a user-defined python code and the sample data for XYZ coordinates of particle position (See **Annexure 1 and Table 6.4**).

The volume fraction component is introduced into the matrix by varying the number of particles instead of the size and wall thickness of the hollow particles. This approach was adopted to make the RVE microstructure resemble the manufactured samples. At least three RVE models are produced for each volume fraction with different distributions in a matrix volume to measure the properties. The periodicity in the geometry was introduced by matching the total number of particles and size on one plane matches with the opposite plane. A total of eight models are produced with

particle volume fractions with 10% intervals to evaluate the elastic constants (including particles and voids together). The micromechanics plugin version 1.16 in ABAQUS estimates the elastic and shear modulus data for different volume fractions of RVE models. After creating the models and assigning the material models, the RVE plugin applies the boundary conditions and provides the model's material properties. The scheme of the RVE modeling and simulations is shown in **Figure 6.3**.

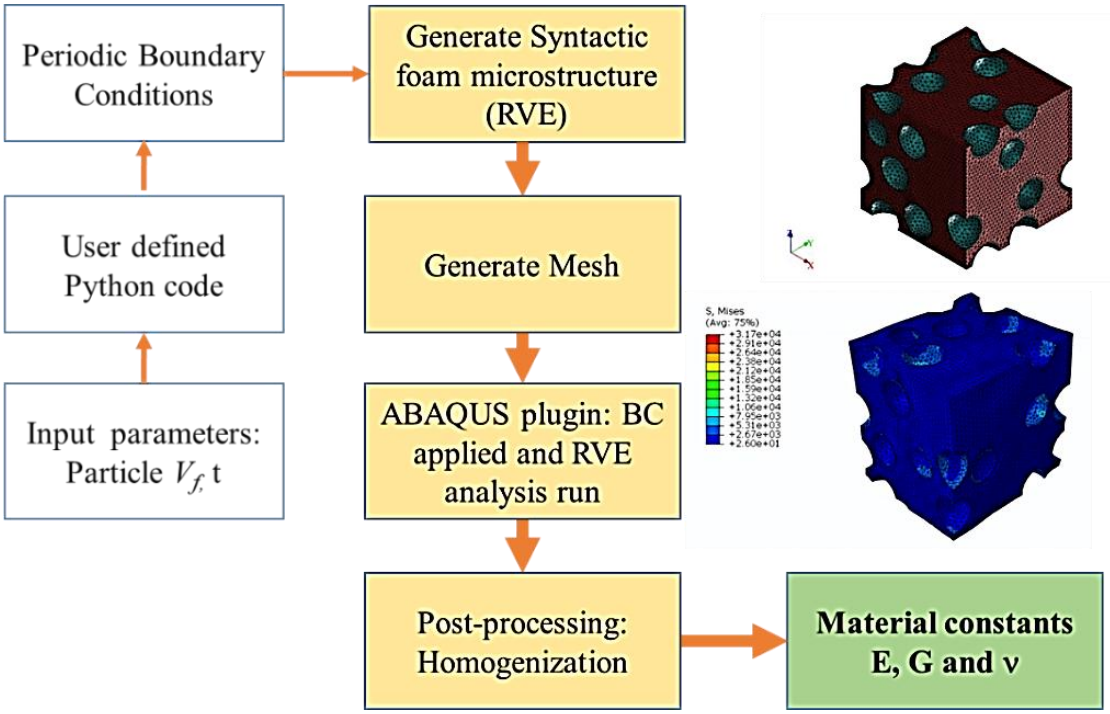

Figure 6.3: Schematic of RVE microstructure generation steps followed and the FEM analysis to obtaine the material properties. Inset image showing the distribution of the particles (Left) and Boundary condition of RVE (Right).

Mesh Density and Convergence studies:

The convergence of the FE solution is essential to support the solutions obtained. There is much emphasis on mesh convergence studies, and significant computational power is invested to achieve convergence in the results based on the number of elements in the FE solution. Syntactic foams are considered geometrically complex

structures[6]. The quadrilateral elements are generally used to obtain accurate results in a FE solution. However, complex geometry like SFs is challenging to mesh using quadrilateral and brick types of meshing. So to address this issue, the triangular or tetrahedral element type can be used.

The model assembly with hollow particles and matrix is meshed automatically using tetrahedral elements. After performing a mesh convergence study, the computational domain has meshed with a mesh length of 0.0125 mm using C3D10-type elements. To address meshing error issues during the simulation, the mesh size of hollow particles and matrix are maintained the same. The mesh is refined automatically at the interface of the matrix and particles. The matrix and particle surface interface is fixed without any frictional penalty. The sample mesh for the 10% and 60% RVE model is shown in **Figure 6.4**. Also, **Figure 6.4** shows the model and mesh view of the generated RVE microstructure for 10% and 60% volume fractions. The discretization density is optimized, as shown in **Figure 6.5**. The elastic modulus value converges with a decrease in mesh element thickness. The elastic modulus of a computational domain is measured for different mesh sizes. The model started giving uniform modulus values at 0.0125 mm.

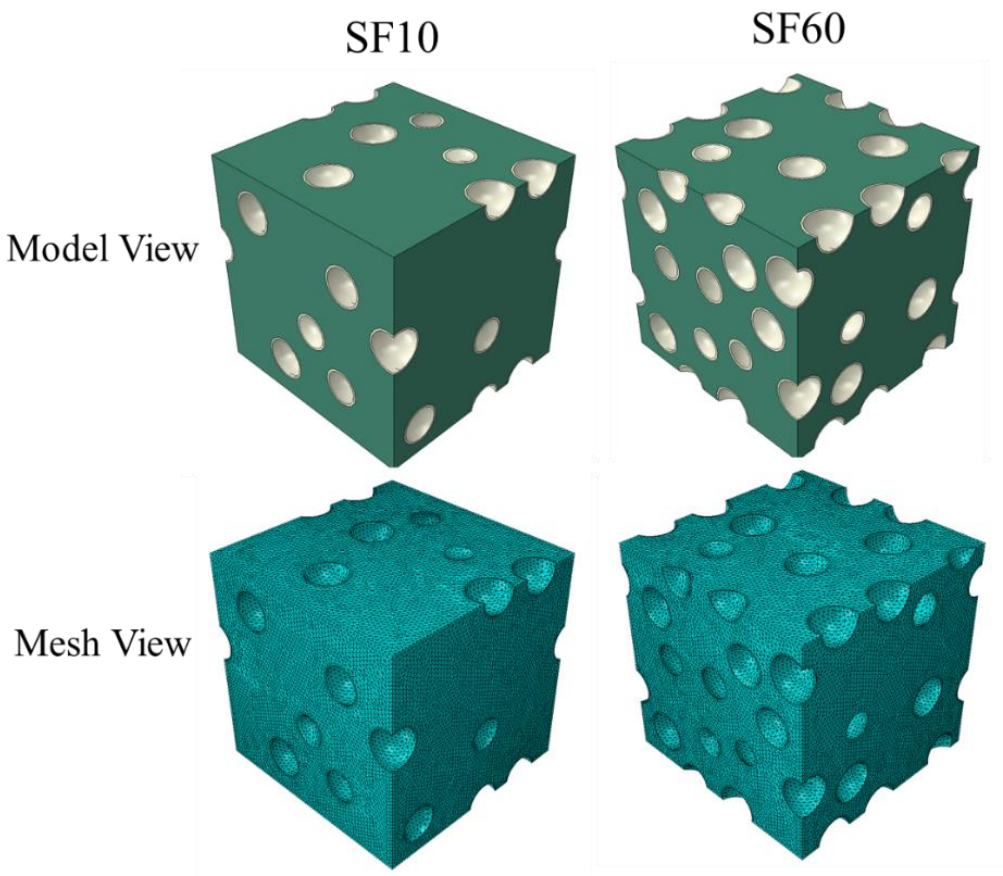

Figure 6.4: Representative RVE model and mesh view of syntactic foams of volume fraction-10 % and 60 %.

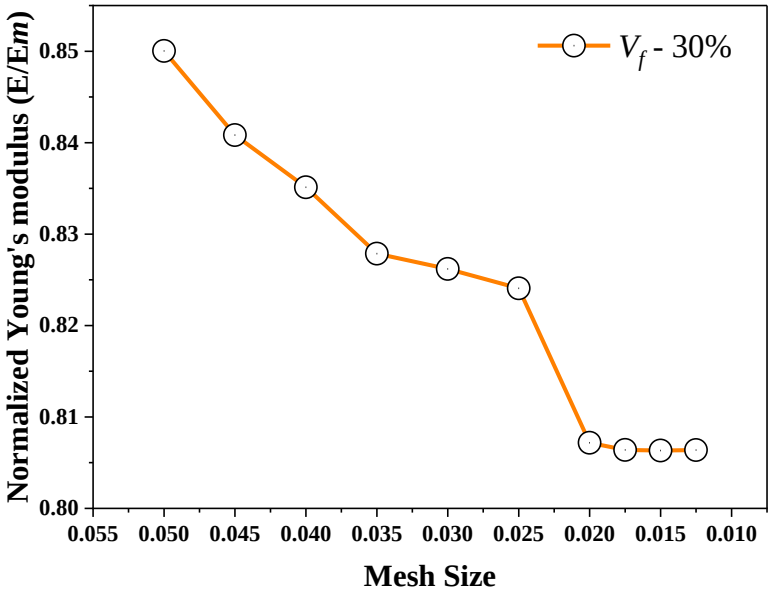

Figure 6.5: A mesh sensitivity study on the RVE model for 30% volume fraction.

The sample ID is represented as 'SF ##,' where SF- stands for SFs and '##' stands for the corresponding volume fraction. In the RVE models, the hollow alumina particles were considered perfectly bonded to the matrix without cracks. The particle dimensions and the geometry of the RVE details are shown in **Table 6.1**.

Table 6.1: Geometry of RVE models

Foam ID	Mean diameter (μm)	Particle shell thickness (μm)	Number of Particles in RVE	Effective volume fraction (%)
SF10	250	15	12	9.08
SF20	250	15	22	20.45
SF30	250	15	30	29.32
SF40	250	15	44	39.87
SF50	250	15	58	40.03
SF60	250	15	72	59.81

6.3.3 Elasto-Plastic FE models

The elastic behavior of MMSF was evaluated using a commercially available ABAQUS/Standard (2020) solver. The computational domain is the same as proposed in Section 6.3.2. Three-volume fractions of Al_2O_3 particles (10 %, 20 %, and 30 %) are considered to study the elasto-plastic properties. The earlier studies on the modeling of composite materials suggested that the periodic boundary conditions (PBC) better estimate the experimental works' results [124]. The periodicity is maintained along with the faces of the cube in all three XYZ directions. For instance, Bardella et al. and Xia et al. incorporated PBC constraints to attain material response [95].

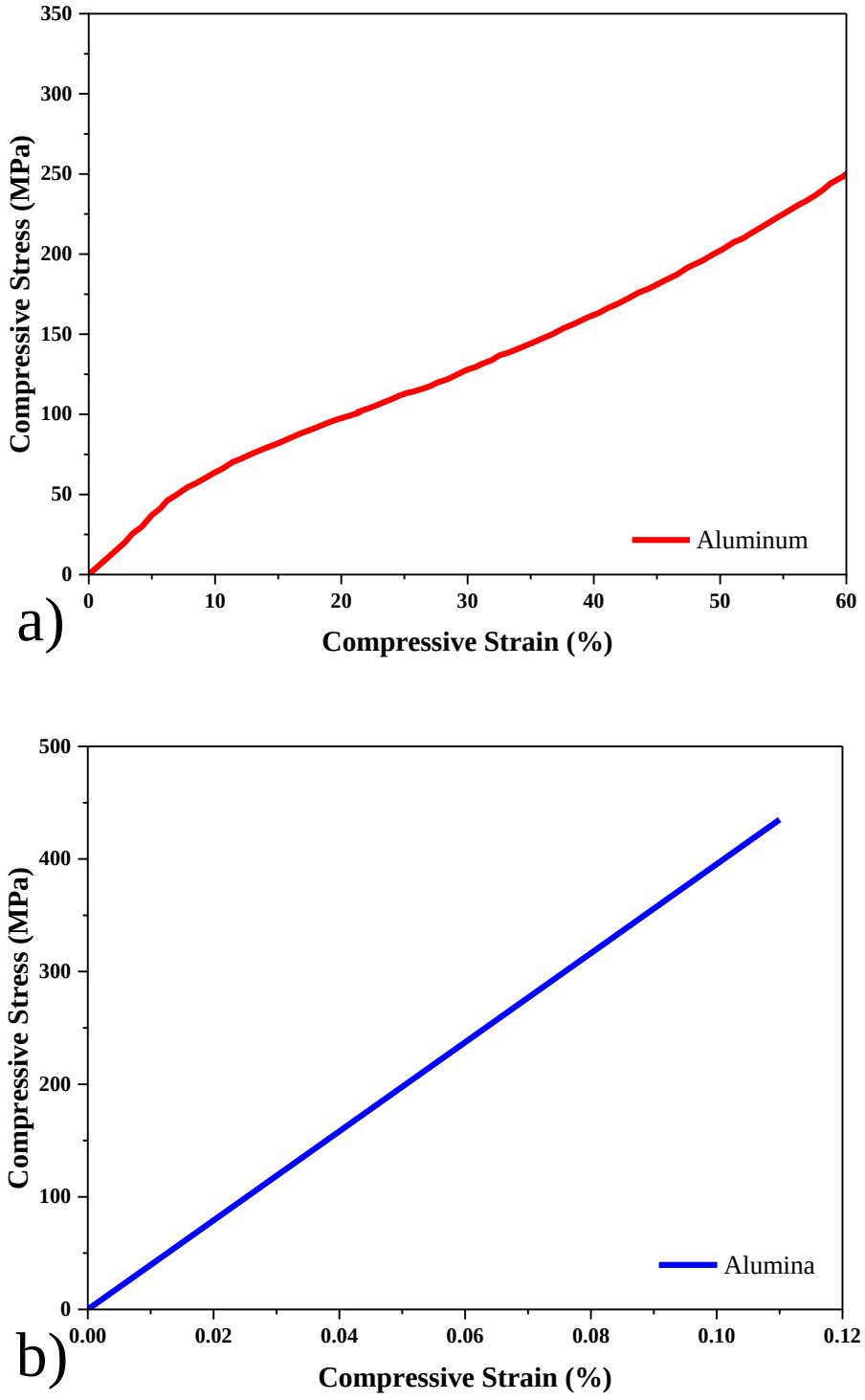

Figure 6.6: Stress-strain relations of the (a) Aluminum [10] and (b) Alumina [109] are used in simulations

The surface of the hollow spheres is considered smooth and traction-free. The material properties and stress vs. strain curve of Al [10] and Al_2O_3 [125] used in this analysis are shown in **Figures 6.6(a)** and **(b),** and **Table 6.2**. The plastic data is considered in **Figure 6.6(a)** while performing the elasto-plastic simulations. The displacement load is applied, and stresses are equal throughout the volume during the simulation. The RVE size and microstructure shown in Figure 6.4 are used to study the elasto-plastic behavior of the SFs.

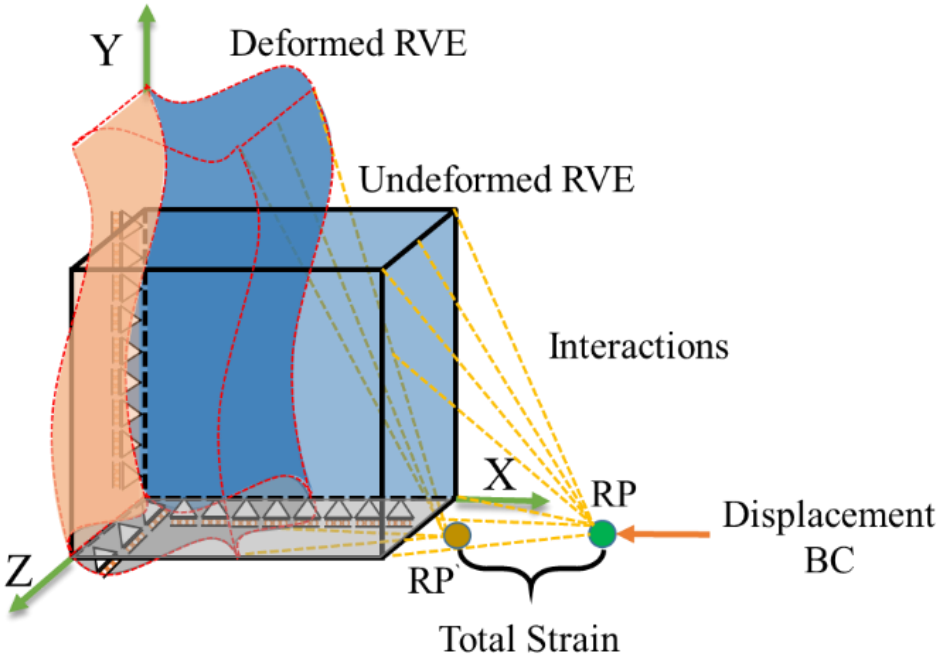

Figure 6.7: Boundary conditions, interactions, and deformation representation of micro-scale transitions for an SF.

Table 6.2: Material properties used for numerical simulations

Material	**Density (g/cm^3)**	**Young's modulus (GPa)**	**Poisson's ratio**
Aluminum	2.7	70	0.33
Alumina	3.9	350	0.22

Figure 6.7 shows the boundary conditions of the RVE before deformation. The RVE models are allowed to deform homogeneously during the loading in the X-direction periodic boundary conditions applied on all three backside faces of the models in XYZ directions. These planes can roll in their respective directions, allowing the models to replicate the desired loading scenario. Also, a compressive uniaxial load is applied to the reference point (RP). This reference point has assigned an interactive property respective to the front face of the RVE in the X-direction. The RP is kinematically tied to the front face of the RVE in the X-direction to apply uniform deformation during the loading[121].

$$U_x^{XFront} - U_x^{RP} = 0 \qquad (6.21)$$

Where U_x^{XFront} and U_x^{RP} are the displacement vectors of the front face of the RVE and reference points, respectively.

6.4 ELASTIC PROPERTIES OF SYNTACTIC FOAMS

The elastic properties of the AMSF are estimated using various analytical models and FE-based RVE models. The properties obtained from these models generally depend on the constituent material properties and particle volume fraction. Also, the effective moduli difference between the matrix, hollow particles, and geometric features of the particle are crucial parameters. **Figure 6.8(a-c)** shows the shear, bulk, and elastic modulus values of AMSF predicted by different analytical and RVE models. The shear and bulk modulus values are estimated based on the models given above (See Section 6.3.2). Later, the elastic modulus values are calculated from the bulk and shear modulus values. The obtained elastic modulus values are compared with experimentally measured values. It is to be noted that from FE-based RVE

models, the elastic modulus is also estimated. Since the FE-based model results are susceptible to the chosen mesh size, a mesh convergence study has been conducted. **Figure 6.8(c)** shows the elastic modulus values of AMSF obtained from experiments and different models.

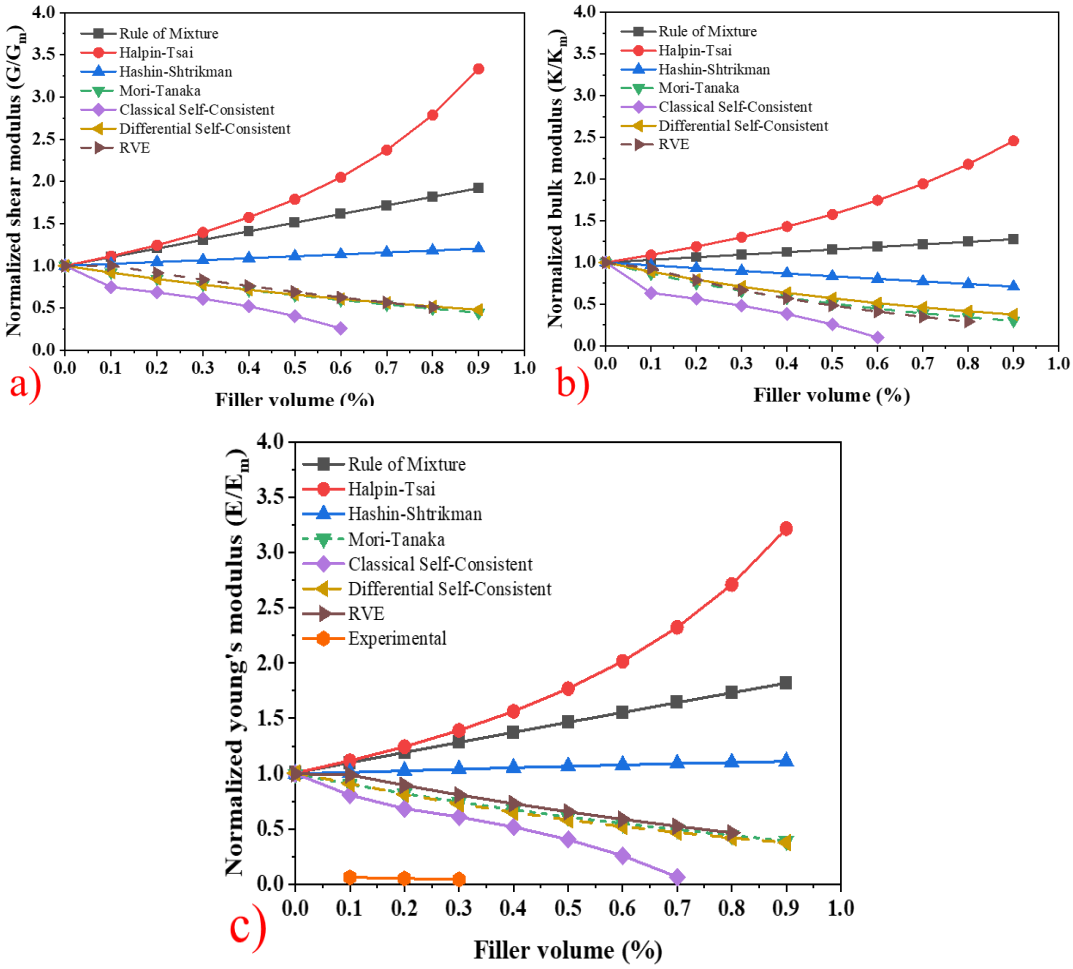

Figure 6.8: (a) and (b) The effective shear and bulk modulus of different homogenization and FE-RVE models. (c) Comparison of the effective elastic modulus of different homogenization models, FE-RVE, and experimental results;

It can be observed that the RM data increases linearly with an increase in volume fraction. However, the experimental elastic modulus values decrease with volume fraction. The RM failed to capture the foam behavior because this model is based on an iso-strain assumption. This assumption implies an equal amount of strain among

matrix, reinforcement, and composite. However, this assumption is not valid in reality. The HS model, which works on the concept of minimum potential energy, also predicted a linear increase in elastic modulus with volume fraction. The model failed to capture the aspects of geometry and particle distribution. It is noted that predicted values refer to the upper bound of the HS model. The lower bound is assumed to be null for this case, similar to others for syntactic foams [95].

The HT model is an empirical-based model developed to predict the elastic properties of composite materials. In this model, the shape factor (ξ) is used to consider the geometric aspects of the reinforcement [122]. However, the HT model's major difficulty is estimating this shape factor (ξ). When $\xi \to \infty$, the HT model reduces to RM. The literature uses curve fitting with the experimental data to find the shape factor. It is observed that this model shows a non-linear increasing trend for AMSFs. This may be because the thickness-to-diameter ratio alone does not contribute to predicting the effective modulus of AMSFs. Therefore, the HT model also failed to capture the effective properties. Generally, the modulus data of AMSF follow a decreasing trend concerning the volume fraction [40]. Hence, the modulus data obtained by the models (RM, HT, and HS) may not give the best prediction regarding MMSF.

The CSC model considers a particle in an infinite medium. The major limitation of this model is that it cannot be used at higher volume fractions [117]. For evaluating the modulus properties of AMSFs, the CSC model predicts a decreasing trend with respect to the volume fraction. After a 60% volume fraction, the model yields negative values. Further, in finding the effective modulus of a composite, the DSC follows a different approach than the CSC models [95,117]. In this approach, the particles are

iteratively added into the medium to calculate the properties. The final properties are obtained when the required volume is achieved. This technique is also called the variable volume approach [117]. In these analytical models, the matrix is considered a continuous phase without considering the adjacent void phases in the physical samples. For AMSF, the DSC method predicted higher modulus values than the CSC models. The general MT model considers a single ellipsoid particle immersed in a large medium (matrix) without interaction of the particles and their influence. This consideration may be suitable only during low-volume fractions in a practical scenario [40,96]. Despite its broad application to predict the average stress in a matrix, the major challenge is that this model fails to apply to the non-dilute cases when the interaction of the nearby particles is considered. For AMSF, the MT model predicts a linear decrease of elastic modulus with volume fraction.

The CSC, MT, and DSC estimates closely match the RVE model results. Though the MT and RVE models follow a decreasing trend similar to the experimental values, a significant deviation is observed due to the microstructure-based anisotropy in the samples. The interaction between the particles is not considered in the analytical models, which is influenced by factors such as particle geometry and manufacturing process.

6.4.1 Sensitivity coefficients

The numerical model data for the Al-Al_2O_3 system are discussed in the previous section, showing variability in the elastic properties. This behavior needs further study to understand the variation in property sensitivity concerning the models. The sensitivity coefficients govern the response of the composite structure responses. The coefficients are computed using the state function's partial derivatives concerning the

input parameters[126,127]. In general, the sensitivity coefficients identify the model's accuracy or parameter to predict the properties of the composite materials. Similar studies are reported in detail by Noor et al., discussing the effect of micro-mechanical models and their sensitivity study on various parameters.

Figure 6.9 shows the normalized sensitivity coefficients $(\lambda\ \partial Z/\partial\lambda)/Z$ vs. volume fraction data for different normalized Young's modulus data for different RVE and numerical models. Here Z refers to the elastic properties (E/E_m), and λ refers to the properties related to the constituent materials (Vf). **Figure 6.9** shows that all the elastic modulus predictions using micro-mechanical models are not in close agreement with the RVE data. Most of the derivatives of the elastic properties concerning the constituent properties are more than RVE predictions, except for the CSC model.

These models, such as the Rule of the mixture, HT, and HS, have shown significant deviation in the derivatives of the elastic modulus from the FE models. The derivatives of the elastic modulus concerning the volume fractions increase in these three models. On the contrary, the MT and DSC models are reasonably close to the FE model data. These derivatives are decreasing concerning the volume fraction. In the CSC model, the sensitivity coefficient data matches the RVE data at low-volume fractions. At higher volume fractions, a significant deviation is observed. It is worth noting that DSC, the elastic modulus data in **Figure 6.8**, shows a close agreement with the RVE model. However, the sensitivity data follows the trend of the RVE model at initial volume fractions at about Vf - 40% a deviation is observed. This behavior suggests the model is relatively less sensitive at higher volume fractions.

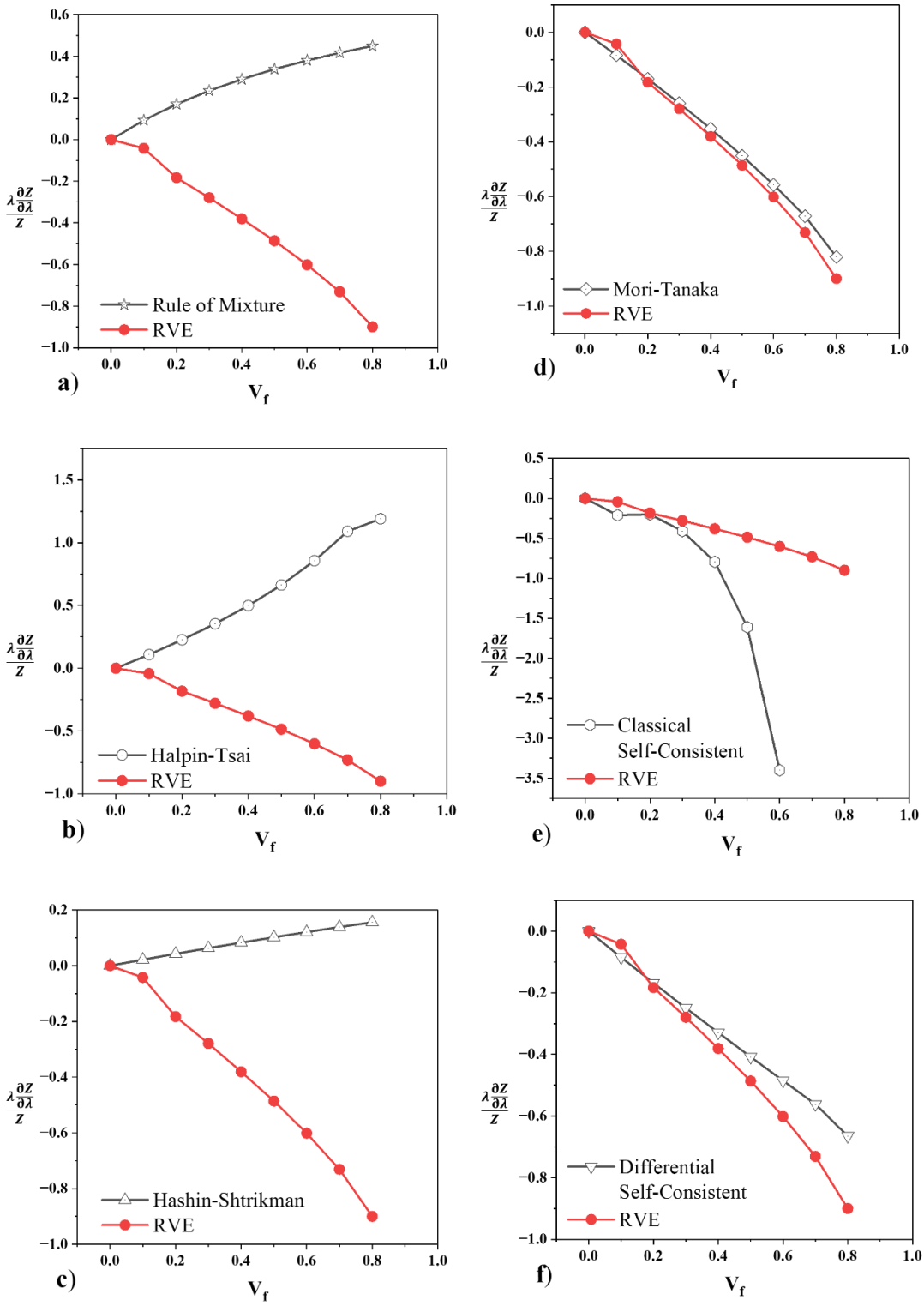

Figure 6.9: Comparing the sensitivity coefficients predicted by the RVE and micro-mechanical models.

6.4.2 Elastio-Plastic Properties

This section discusses the predicted elasto-plastic behavior of AMSFs under uniaxial compression by RVE-based FE models. The complexity in generating RVEs with high-volume fractions is that many particles must be introduced in the computational domain. Such models may lead to a complex geometry that requires fine mesh and high computational capacity for macroscopic studies. In this regard, we limited to three volume fractions to study the elasto-plastic response, i.e., 10%, 20%, and 30%. The FE model is solved for the stress and strain by applying displacement boundary conditions. Following the mesh convergence in **Figure 6.8(d)**, the same mesh size is used to estimate the elasto-plastic behavior of AMSFs. The volume-average technique given in Equation 6.5 is used for computational homogenization to obtain the mechanical response of the AMSFs. The obtained homogenized macroscopic response (stress-strain data) by RVE models are compared against the experimental data.

Figure 6.10(a-c) shows the representative graphs of measured compressive stress-strain data for three different volume fractions of AMSFs using both FE and experimental results. The displacement-based contour images of FE models after deformation are shown in **Figure 6.10 (d-f)**. The experimental and FE data show three typical phases commonly observed in foam-based materials, such as **1**. Elastic region, **2**. Plateau region, and **3**. Densification zone. In the plateau region, stress values constantly increase with respect to the nominal strain range (0.05 - 0.5). Further, the densification arises from the failure of the hollow particles, plastic flow in the matrix, and filling up pores with fragmented particles and matrix.

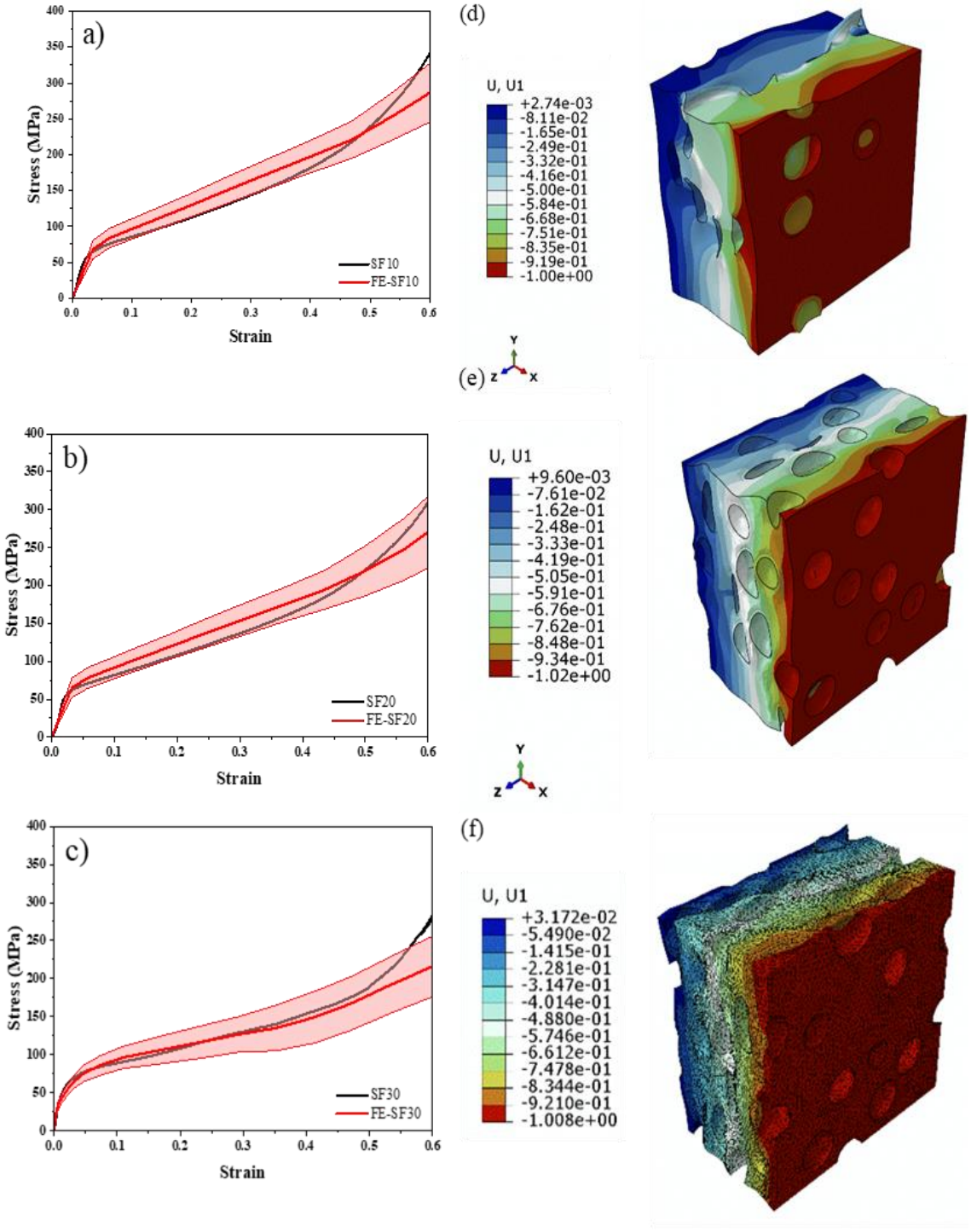

Figure 6.10: (a) (b) & (c) Comparison of simulation results and experimental data obtained for different volume fractions of S.F.s. (d), (e) & (f) FE contour plots of uniform distribution of displacement up to 60% on respective RVE models.

The FE-based RVE model was able to capture the uniaxial compression behaviour. The stress-strain response obtained from the FE model followed a linear response in the elastic region. The stress value of the FE model at the yield point (0.2% strain) is more than the measured value for SF10 and SF20. This stress values continues to increase in the plateau region with a constant plastic stiffness. But the model overestimated the stress values in this region. This is due to the deformation of hollow particles and matrix densification translated into the stress-strain response in the plastic regime.

However, the deviation from the experimental results accounts for different physiological factors such as friction between the particles and matrix, deviation in the particle geometry, and testing conditions that may influence the data. After the densification zone, the FE models largely deviate from the measured values for SF10 and SF20. Further, for slightly larger volume fractions SF30, the FE domain closely matches the experimental results from the elastic region to the densification zone. This suggests that the model was able to follow the physical behavior of the AMSFs under uniaxial deformation.

The deformation behavior based on the measured and predicted stress-strain response can be further studied using deformation energy and energy absorption efficiency (EAE). The deformation energy is obtained by measuring the area under the stress-strain curve. The efficiency is calculated by dividing the deformation energy with the stress at each instance, i.e., EAE. The deformation energy obtained from the simulation data and experimental results are compared in **Figure 6.11**. It can be observed that the FE model predicted the deformation energy values close to the experiments.

The deformation energy is obtained by measuring the area under the stress-strain curve and $EAE = \int_0^{\varepsilon} \sigma d\varepsilon / \sigma^{\circ}$. Where σ°, the stress corresponding to the stress-strain data. The deformation energy of experimental data showed a maximum value of up to V_f - 20%. Apparently, for the V_f - 30%, the trend altered (FE- 82.41 MJ/m^3 and Experiment- 78.56 MJ/m^3, and the simulation data showed high values. The deviation between the experimental and FE results seems to be reduced with increased volume fraction. All the FE curves showed similar deformation behavior under the given boundary conditions concerning the experimental.

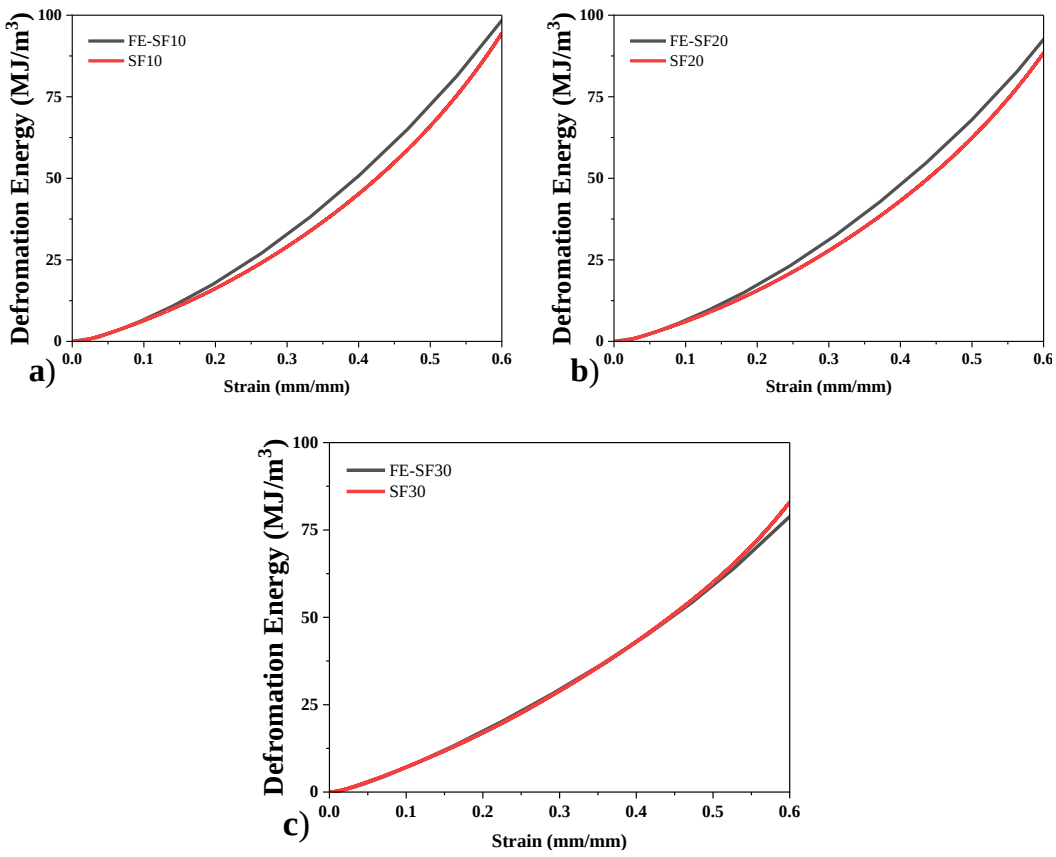

Figure 6.11: Deformation Energy vs. Strain curve for experimental and simulation data

The EAE curves obtained from the experimental and FE model are shown in **Figure 6.12**. The earlier studies stated that the peak value of the EAE curve represents the densification starting point in porous materials [48,101]. The densification starting point and the respective energy absorption efficiency values are shown in **Table 6.3**. It is observed that the FE model and experimental densification starting points matched for SF30 FE model. This is due to the fact that the current model predicts the exact experimental stress-strain behavior for the 30% volume fraction, as shown in **Figure 6.10**. The densification starting point decreases with an increase in volume fraction.

Table 6.3: Densification strain and energy absorption efficiency data for experimental and FE models.

Sample ID	Densification Strain		Energy absorption efficiency at Densification Strain	
	Experimental	FE model	Experimental	FE model
SF10	0.54	0.62	0.276	0.348
SF20	0.56	0.573	0.284	0.33
SF30	0.492	0.52	0.32	0.34

The RVE macroscopic stress-strain behavior predicted for AMSF agrees with the experimental data. The model trend in the elastic region followed the linear behavior similar to the experimental data. Later during the plateau region, the simulation results overestimated the stress values. This trend is observed for the initial two volume fractions where the matrix fraction is dominant. In the FE-SF30, the model trend followed the observed hardening behavior. Also, in this model, the stress value at the yield point is more than the measured values. Later, the model follows the measured path up to the densification strain as shown in **Figure 6.12**.

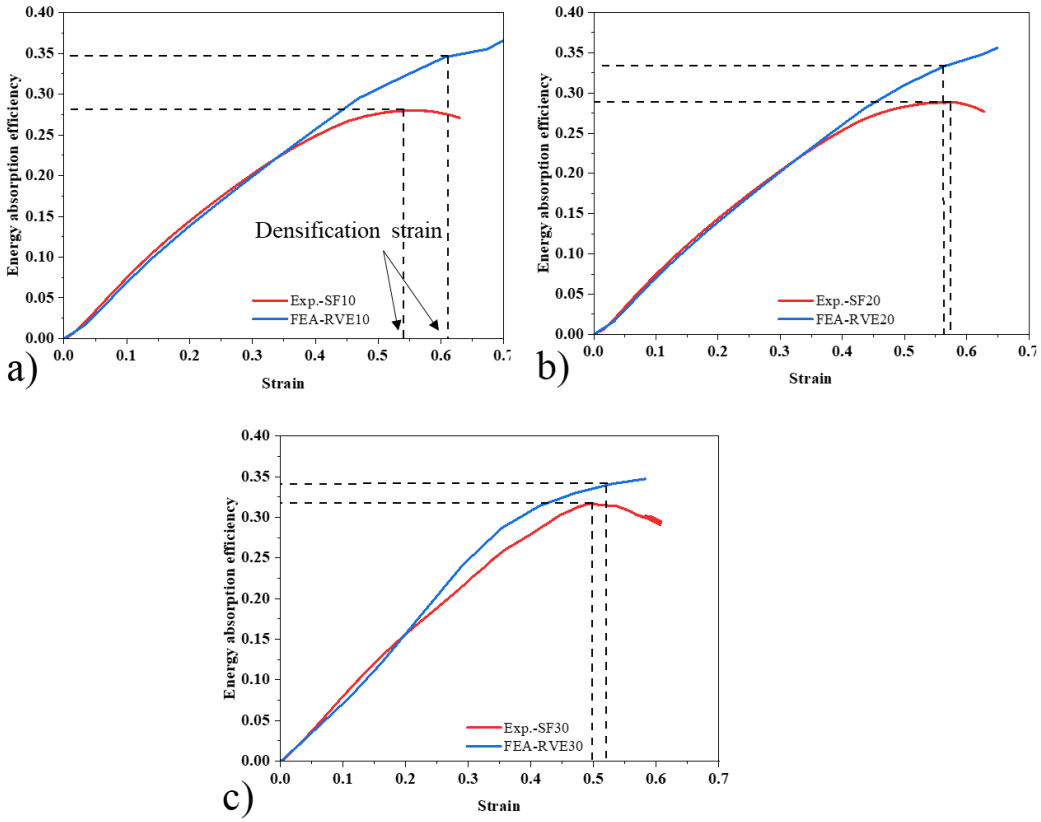

Figure 6.12: Energy absorption data for experimental and FE models

The EAE follows an increase in trend concerning the volume fraction with a maximum of 0.29 and 0.34 for SF30. The earlier studies state that the peak value of the EAE curve represents the densification point in the porous materials [49]. The FE models for *f*-10 % and 20 % have shown a significant deviation in the densification point. These models overestimate the densification density concerning their experimental data. However, the FE- SF30 model with a maximum number of particles inside the matrix has shown better agreement with the experimental data.

Hence, this suggests that the material model (elasto-plastic) combined with the representative geometry selected for the respective volume fraction led to the closest representation of the experimental data. However, the trend is similar to experimental data in all the stress-strain curves during the elastic region. The simulation data

differing from the experimental data in the plateau zone may be attributed to the RVE geometry. This deviation has been reduced for models with an increase in particles. The other sources of variations can be due to the assumptions taken while modeling the RVE.

6.4.3 Effect of particle wall thickness on the macroscopic behavior

It is to be noted that the wall thickness has a significant influence on the macroscopic stress-strain behavior. Therefore, a parametric study has been conducted to investigate the effect of particle wall thickness. The wall thickness is altered for 30 % volume fractions by keeping the volume fractions constant. **Figure 6.13** illustrates the compressive stress-strain responses of SF30 AMSFs FE models. However, the number of particles may change to maintain the volume fraction. Also, the boundary conditions and analysis steps are similar to the details given in Section 6.3.2. In these models, three different wall-thickness ±5 μm to the earlier simulation domain. The three computational models corresponding to the hollow particle's wall thickness are compared. There is an increase in yield stress and densification strain with respect to wall thickness. The densification stress has shifted to the left side with an increase in wall thickness. This shows that the model is able to capture the geometric features. These parameters can significantly affect the mechanical properties and energy absorption behavior of SFs.

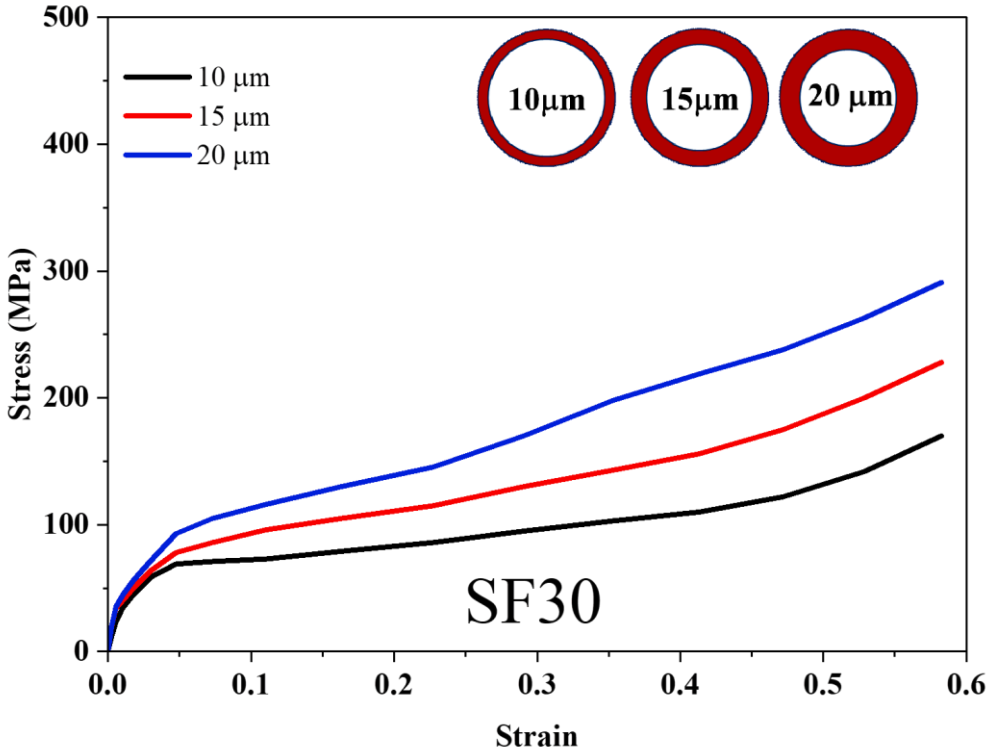

Figure 6.13: FE compressive stress-strain data of AMSFs of 30% volume fraction

6.5 SUMMARY

The simulation results obtained for alumina hollow sphere-reinforced syntactic foams are compiled in this chapter, which includes the estimation of the elastic properties of the SFs using different analytical models. The FE results obtained using a representative volume element model showed a close agreement at higher volume fractions. The macroscopic stress-strain response of the SFs for three-volume fractions has shown good agreement with the experimental results. The deviation in the slope of the stress-strain curve produced based on the wall thickness of the hollow particles is shown strong dependency. The FE model was able to capture this effect. These results suggest that the homogenized models can predict the macroscopic properties. Also, there is scope to explore further by introducing the cohesive effect between matrix and hollow particles.

Further, to understand the AMSF's response under the influence of different chemical solutions such as acidic, neutral, and base with varying molar and pH concentrations the electrochemical studies are studies in Chapter 7.

6.6 ANNEXURE

The following is the python code used to arrange the random hollow particles inside the matrix material.

```
# ------------------------------------------------
from abaqus import *
from abaqusConstants import *
from caeModules import *
from driverUtils import executeOnCaeStartup
executeOnCaeStartup()
import numpy
# -------------------------------
# Inputs
#cube dimensions
height,width,depth=1.0,1.0,1.0
# Void dimensions
dia = 0.25
th = 0.02
# Part names
voidmat,void,cube = 'void_mat','voids','cube'
# Part Instances name
voidMatisn,voidisn,misn = 'void_mat-1', 'voids-1','cube-1'
# Coordinates file name
inpFile = 'RVE30.txt'
# -------------------------------
vp = session.currentViewportName
viewport = session.viewports[vp]
mdl = mdb.models['Model-1']
```

```
s = mdl.ConstrainedSketch(name='__profile__', sheetSize=200.0)

s.setPrimaryObject(option=STANDALONE)

s.rectangle(point1=(0.0, 0.0), point2=(width,height))

pcube = mdl.Part(name='cube', dimensionality=THREE_D,
type=DEFORMABLE_BODY)

pcube.BaseSolidExtrude(sketch=s, depth=depth)

s.unsetPrimaryObject()

viewport.setValues(displayedObject=pcube)

del mdl.sketches['__profile__']

s = mdl.ConstrainedSketch(name='__profile__', sheetSize=200.0)

s.setPrimaryObject(option=STANDALONE)

s.ConstructionLine(point1=(0.0, -100.0), point2=(0.0, 100.0))

s.resetView()

mdl.sketches['__profile__'].sketchOptions.setValues(gridSpacing=0.1,
gridAuto=OFF)

s.ArcByCenterEnds(center=(0.0, 0.0), point1=(0.0, dia/2.0), point2=(0.0, -
dia/2.0),

   direction=CLOCKWISE)

s.Line(point1=(0.0, dia/2.0), point2=(0.0, -dia/2.0))

pvd = mdl.Part(name=void, dimensionality=THREE_D,
type=DEFORMABLE_BODY)

pvd.BaseSolidRevolve(sketch=s, angle=360.0, flipRevolveDirection=OFF)

s.unsetPrimaryObject()

viewport.setValues(displayedObject=pvd)

del mdl.sketches['__profile__']

s1 = mdl.ConstrainedSketch(name='__profile__',  sheetSize=200.0)

s1.setPrimaryObject(option=STANDALONE)

s1.ConstructionLine(point1=(0.0, -100.0), point2=(0.0, 100.0))
```

```
s1.ArcByCenterEnds(center=(0.0, 0.0), point1=(0.0, dia/2.0), point2=(0.0, -dia/2.0),
                    direction=CLOCKWISE)
mdl.sketches['__profile__'].sketchOptions.setValues(gridSpacing=0.05, gridAuto=OFF)
s1.ArcByCenterEnds(center=(0.0, 0.0), point1=(0.0, dia/2-th), point2=(0.0,
   -dia/2+th), direction=CLOCKWISE)
s1.Line(point1=(0.0, dia/2), point2=(0.0, dia/2-th))
s1.Line(point1=(0.0, -dia/2), point2=(0.0, -dia/2+th))
pvmat = mdl.Part(name=voidmat, dimensionality=THREE_D, type=DEFORMABLE_BODY)
pvmat.BaseSolidRevolve(sketch=s1, angle=360.0, flipRevolveDirection=OFF)
s1.unsetPrimaryObject()
viewport.setValues(displayedObject=pvmat)
del mdl.sketches['__profile__']
# Assembly
asm = mdb.models['Model-1'].rootAssembly
asm.DatumCsysByDefault(CARTESIAN)
asm.Instance(name=misn, part=pcube, dependent=ON)
asm.Instance(name=voidMatisn, part=pvmat, dependent=ON)
asm.Instance(name=voidisn, part=pvd, dependent=ON)
# -------------------------------------------------------
fin = open(inpFile)
coords = []
for line in fin:
   if not line: break
   if not line.strip(): break
   data = [float(i) for i in line.split()]
   coords.append(data)
```

```
fin.close()
# ----------------------------------------------------
vmisns,visns = [voidMatisn,], [voidisn,]
n1 = 2
spc1,spc2=0.25,0.25
n = len(coords)
origin = 0,0,0   # center coordinates of void and void material
if n%2.0 != 0.0:
   n2 = n//2 + 1
else:
   n2 = n//2
# Creating the linear pattern of void and void material part instances
mdl.rootAssembly.LinearInstancePattern(instanceList=(voidisn,voidMatisn ),
   direction1=(1.0, 0.0, 0.0), direction2=(0.0, 1.0, 0.0),
   number1=n1, number2=n2, spacing1=spc1, spacing2=spc2)
for i in range(n1):
   if i == 0:
      nstart = 1
   else:
      nstart = 0
   for j in range(nstart,n2):
      visns.append(voidisn+'-lin-%d-%d'%(i+1,j+1))
      vmisns.append(voidMatisn+'-lin-%d-%d'%(i+1,j+1))

# Translating the void and void material instances
ic = len(visns)//2
idir = numpy.array([0.0, 0.0, 0.0])
```

```
offset = spc1
kk = 0
for k,coord in enumerate(coords):
    if k == ic:
        print('In the if condition')
        idir = numpy.array([spc2, 0.0, 0.0])
        offset = spc2
        kk = 0
    # origin of each instance w.r.t original instance
    # idir2 = idir * offset*kk
    idir2 = idir[0] ,spc1*kk, idir[2]
    # origin of each instance w.r.t. global coordinate system
    origin2 = numpy.array(origin) + numpy.array(idir2)
    vec =  numpy.array(coord)- numpy.array(origin2)
    # print(k+1,origin2)
    kk += 1
    # break
    # moving the void material instance
    mdl.rootAssembly.translate(instanceList=(vmisns[k], ),
                               vector=tuple(vec),)
    # moving the void instance
    mdl.rootAssembly.translate(instanceList=(visns[k], ),
                               vector=tuple(vec),)

if len(visns) > len(coords):
    visns = visns[:len(coords)]
    vmisns = vmisns[:len(coords)]
```

```
# ----------------------------------------------------
# Cutting the cube instance using void part instances
mainisn = mdl.rootAssembly.instances[misn]
visnObj = []
for visn in visns:
    visnObj.append(mdl.rootAssembly.instances[visn])
newISN = mdl.rootAssembly.InstanceFromBooleanCut(name='cube_merged',
    instanceToBeCut=mainisn,cuttingInstances=tuple(visnObj),
    originalInstances=SUPPRESS)
# originalInstances=DELETE - for deleting the original part instances.
```

Table 6.4: Random distribution of the hollow particle position in size the computational domain used in the python code (RVE30).

X	Y	Z
0.845145	1.86733	2.4485
0.845145	1.86733	-0.0515
0.640718	1.59318	0.841591
0.552693	0.461975	2.0218
0.331097	2.21934	0.721202
2.10905	1.29193	2.46865
2.10905	1.29193	-0.03135
0.429503	1.21779	2.02118
1.10155	1.18514	1.87482
0.555354	0.76264	0.299671
2.4299	0.097298	2.15556
-0.0701	0.097298	2.15556
2.4299	2.5973	2.15556
-0.0701	2.5973	2.15556
0.536279	2.42193	1.46966
0.536279	-0.07807	1.46966
-0.09102	0.451033	1.04992
2.40898	0.451033	1.04992
2.51295	1.39036	1.52273
0.012952	1.39036	1.52273
0.040862	1.58342	0.735412
2.54086	1.58342	0.735412
1.10841	2.61752	2.20444
1.10841	0.117518	2.20444
1.07154	0.697614	1.23897
1.52864	1.37108	0.855993
1.48904	1.75633	2.07908
1.42076	0.501911	1.86438
2.53118	0.809049	2.06452
0.031182	0.809049	2.06452
1.66951	0.77742	0.901238
2.04129	2.51589	0.389099
2.04129	0.015886	0.389099
0.854594	0.270385	0.352833
1.54293	1.17824	2.54119
1.54293	1.17824	0.041195
1.00214	0.008146	1.02664
1.00214	2.50815	1.02664

Chapter 7: Corrosion Studies on AMSFs

The previous chapters extensively present the microstructural and mechanical response of the AMSFs. This chapter studies the electrochemical response of the produced AMSFs in detail. The AMSFs have a broad range of applications not limited to automotive, marine, and aerospace, and it is essential to understand the environmental aspects, such as the corrosion response under various environmental conditions. In this regard, the corrosive response and the mechanism of the AMSFs for different volume fractions of the hollow particles are explored. In this chapter, the electrochemical response of the AMSFs is explored using techniques such as potentiodynamic polarization and the electron impedance spectroscopic response. The obtained results are further analyzed by exploring the affected surface under SEM.

7.1 INTRODUCTION

Aluminum matrix syntactic foams (AMSF) are cellular materials that offer extended plateau stress and multifunctional properties in contrast to metal foams. Due to their low-density high performance, applications of syntactic foams have increased during the past few decades. The syntactic foams (SF) contain ceramic/metal-based hollow particles in a matrix. This may account for high specific stiffness and up to 80% of energy absorption efficiency, and metal foams are the materials that exhibit a unique mix of physical and mechanical qualities. Most commercially available cellular metals do not possess the mechanical characteristics expected by scaling relations. This is partly attributable to morphological flaws in the structure, such as missing cell walls and wall wiggles. However, syntactic foams exhibit mechanical and structural

properties under different loading conditions[92,128]. Most SFs find their applications in marine, automotive, aerospace, and defense industries to reduce weight and retain structural stability. The electrochemical characteristics are still unexplored despite its high reputation for structural properties. In the literature, polymer and metal-based syntactic foams are studied.

Many technical applications, such as aircraft, automotive, and railway, require energy absorption materials with low weight and high strength. Aluminum foams are widely suited for lightweight energy absorption applications due to their low relative density, high specific energy, and significant compressive deformations. AMSFs that contain hollow ceramic particles, such as alumina hollow spheres, contribute to the foam's structure. As a result of the support provided by the shells of the alumina hollow particles, SFs have greater moduli and strengths than conventional foams synthesized using gas-releasing chemicals.

There are few studies on the corrosion behavior of AMSFs. In research on Al-Alloy syntactic foams, including hollow glass particles, the authors indicate that the syntactic foam samples exhibit more excellent corrosion resistance in a 3.5% sodium chloride (NaCl) solution than the base alloy[106]. This is due to alumina hollow particles, which lower the matrix's surface area. Similarly, it has been observed that silica nanospheres increase the corrosion resistance of Mg in both Hank's buffered saline and PBS solutions. There is potential for using syntactic foams in structural applications where they may be subjected to a corrosive environment. Several investigations are insufficient to verify their corrosion behavior sufficiently. Thus, more research is necessary to give additional information and understanding of their corrosion behavior, particularly for those manufactured using a powder metallurgy (PM) technique. So, the present work aims to contribute to the body of knowledge in

this area by elucidating the influence of microspheres on the microstructure and corrosion behavior of AMSF.

7.2 Potentiodynamic Polarization Measurements and Surface Morphologies

7.2.1 HCL

The potentiodynamic polarization behavior of the three different ASF (#1, #2, and #3) of 30% volume fraction of alumina hollow particles(HP) each were evaluated using potentiodynamic polarization (PDP) measurement. The sample ID is assigned based on the size of the alumina HP, as shown in **Table 7.1**. The PDP measurements were in various molar concentrations (0.01, 0.1, and 1 M) in an acidic (HCl), neutral (NaCl) , and alkaline media (8, 10, and 12). The corrosion parameters, corrosion current density (Icorr) and corrosion potential (Ecorr), were obtained from the Tafel extrapolation measurement, and data presented in **Table 7.1**.

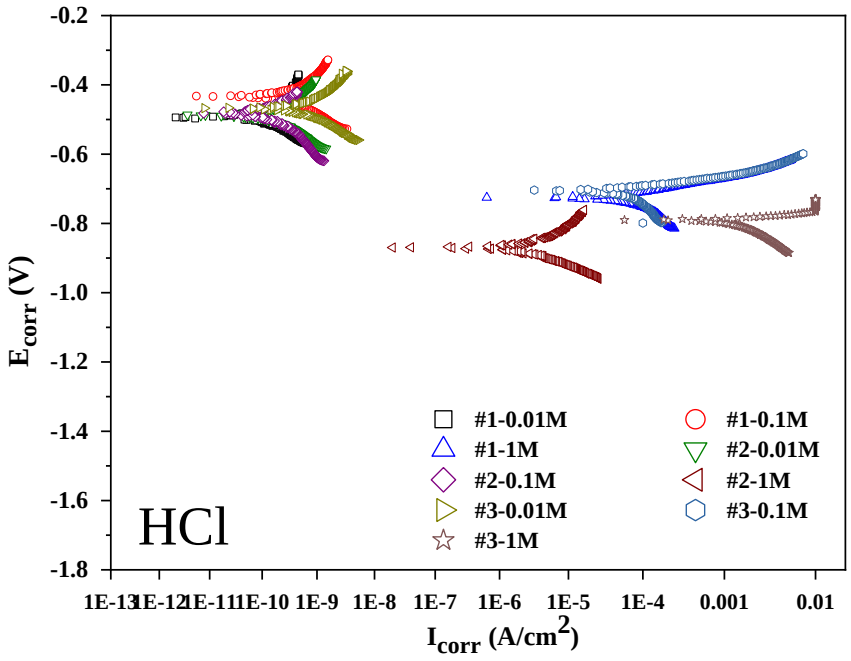

Figure 7.1: The polarization curve of AMSF #1, #2, and #3 samples were tested in an acidic HCl solution.

Table 7.1: Corrosion current (I_{corr}) and corrosion potential (E_{corr}) at different HCl molar concentrations

Type of solution	Sample ID	Particle size (µm)	Molarity (M)	I_{corr} (A/cm^2)	E_{corr} (V vs. sec)
HCl (Acidic)	#1	500	0.01	5.68E-11	-0.49
			0.1	1.26E-10	-0.5
			1	2.96E-05	-0.72
	#2	1000	0.01	1.18E-10	-0.48
			0.1	1.20E-10	-0.56
			1	2.05E-06	-0.86
	#3	1500	0.01	3.94E-10	-0.46
			0.1	5.50E-05	-0.7
			1	1.25E-03	-0.79

In **Figure 7.1**, the Polarization curves (PDP) for three distinct samples (#1, #2, and #3) were immersed in an acidic (HCl) solution with different molar concentrations, and corresponding Icorr and Ecorr values are represented in **Table 7.1**. From polarization curves **Figure 7.1** and **Table 7.1**, noticed that Al-500 µm-1.3 in 0.01 exhibited notably low Icorr value (5.68E-11 A/cm^2) in 1M HCl solution, in comparison with 0.1 and 1M concentrations. there is a minor increment in Icorr values is observed, i.e 5.68E-11 A/cm^2 to 1.26E-10 A/cm^2 **(Table 7.1)**. Also, the Ecorr was found to shift towards the negative side (-0.49 to -0.5). Generally low Icorr values represent lower corrosion rates and better corrosion resistance. The ASFs with low particle size (500 µm) showed excellent corrosion resistance in 0.01 and 0.1 M HCl solution. However, as the Cl- ion concentration in the HCL solution reaches to 1M, high Icorr values (2.96E-05 A/cm^2) and a decrease in the Ecorr value of -0.72 can be observed in #1 sample, indicates high corrosion rates. The observed high corrosion rates imply high

rate of metal dissolution at Ecorr, due to the breakdown of the passive layer on the alloy surface.

In another case, the 1000µm sample (#2) tested at 0.01 M HCl solution displays higher Icorr values, i.e., 1.18E-10 A/cm^2, than sample #1. Also, the corresponding corrosion rate of Ecorr is -0.48. When the Cl- ion concentration increased from 0.01M to 0.1M, displayed negligible variance Icorr values, holding steady at the rage of 1.18E-10 to 1.20E-10 A/cm^2 **(Table 7.1)**, and the Ecorr moved to a more negative side. Upon further increase in the Cl- a concentration in a 1M HCl solution, no marginal change in the Icorr values (2.05E-6 A/cm^2) are noted, and the sample demonstrated enhanced resistance to corrosion across all three different molar concentrations of the acidic HCl solutions.

Sample #3 showed good corrosion resistance when tested in 0.01M HCl solution (3.94E-10 A/cm2) among three molar concentrations, but compared to #1 and #2 the Icorr value of the #3 is found to be slightly higher. As the Cl- ion concentration increased from 0.01M to 1M, a drastic increase in the Icorr value is observed (**Table 7.1**). The Icorr values were significantly increased in the other two solutions (0.1 and 1M), indicating a high metal dissolution rate at Ecorr. This suggests that the ASF becomes anodically activated as the Cl- ion concentration increases, leading to the deterioration of the passive layer, and consequently, an increase in metal dissolution rate. Further, it was observed that the rate of corrosion tends to increase with the particle size.

Thus, the Al-500µm sample (#1) shows excellent corrosion resistance in the acidic environment at various molar concentrations than the other two ASFs **(Figure 7.1 and Table 7.1**). However, a significant difference was not observed in the Icorr

values at lower concentrations of Cl ions (0.01 M to 1 M) in different sizes of hollow particles (#1 and #2). High Icorr values lead to elevated corrosion rates, as observed in sample #3. Generally, it has been found that metal matrix composite (MMCs) exhibits better corrosion resistance than pure Al alloys due to the presence of oxide particle inclusions possessing higher corrosion resistance [6,13]. Interestingly, even though the corrosion rate tends to increase with particle size (from samples #1 to #3), the ASFs exhibit superior corrosion resistance than the reported MMCs (Al+SiC) due to the high agglomeration percentage of the alumina hollow particle as compared to the conventional MMCs [13]. These hollow particles are distributed uniformly throughout the sample, forming a protective layer acts as a corrosion barrier, effectively preventing corrosion. Based on the present corrosion test parameters from **Table 7.1**, the outcomes establish a corrosion rate hierarchy for the ASFs in an acidic medium is #3 > #2 > #1. This ranking suggests that an increase in alumina HP size along with the Cl- ion concentration leads to accelerated metal dissolution rate.

After performing the PDP analysis, the affected surface of the samples exposed to different corrosive environments is examined using SEM. **Figure 7.2(a-f)** shows representative surface morphologies of the corroded surface of the samples (#1, #2, and #3) tested in HCl solution at 0.01M and 1M. For 0.01M HCl solution, The surface shows a deep pit without significant cracks**.** But in the case of sample #2 (**Figure 7.2(c)**), the corroded surface is covered with multiple pits and finer cracks. This correlates well with PDP results, in which #1 showed better corrosion resistance. Further, for particles of 1500 μm (**Figure 7.2(e)**) tested in 0.01M HCl solution, the whole surface was affected with deep pits and cracks. This may be attributed to the breakdown of the aluminum hydroxide ($Al(OH)_3$) passive layer, which causes a high corrosion rate on the alloy surface.

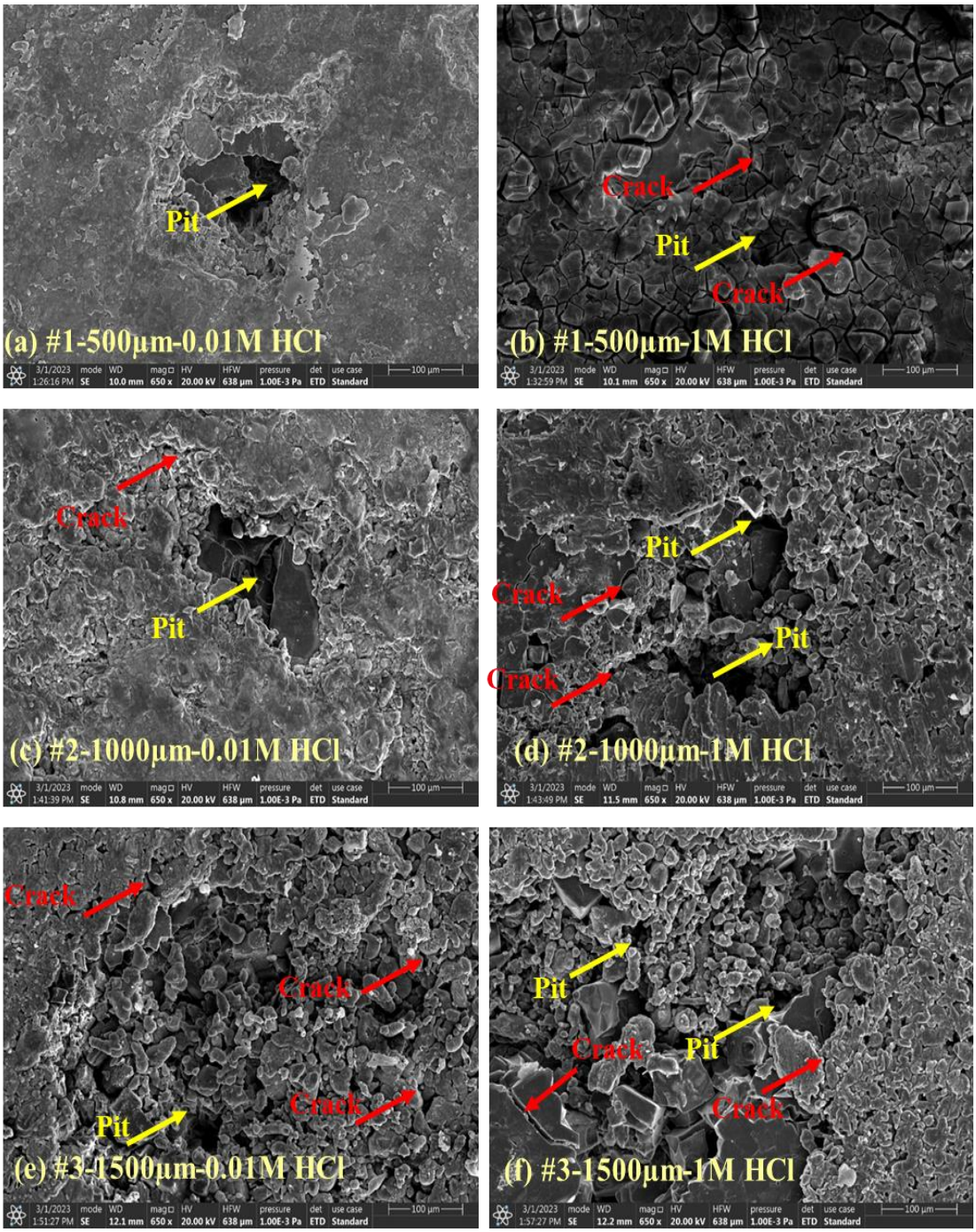

Figure 7.2: SEM morphologies of the corroded surface of #1, #2, and #3 samples tested in HCl solution at 0.01 M and 1 M.

Subsequently, at higher Cl- ion concentrations of 1M, the entire surface of all three ASFs was corroded with multiple deep pits and large cracks, as observed in **Figure 7.2(b, d & f)**. This behavior indicates the surface of the ASFs shows high corrosion rates. Based on the Pourbaix diagram [14], Al and its alloys are found to be resistant to corrosion within moderatly aggressive environments, attributed to the development of a protective aluminum hydroxide ($Al(OH)_3$)/ Al_2O_3 passive layer. This protective layer acts as a barrier and can repair damaged parts by itself in an oxide environment [14]. However, in acidic condition at low pH levels (pH<7) and Cl^- ion concentration, ASFs displays less stable. This is mainly due to the increase in anodic current density, causes excessive release of hydrogen gas from the alloy surface. This leads to local breakdown of the $Al(OH)_3$ surface passive layer [12]. Consequently, more pronounced and extensive cracks and pits become evident on the sample surface, resulting in high corrosion rate. The SEM morphologies shown in **Figure 7.2** are in complete agreement with the polarization results from **Figure 7.1** and the data in **Table 7.1**. Pitting with minor cracks was observed in the 0.01 M HCl solution, mainly due to the low chloride ion concentrations. In contrast, the whole surface damage is observed under the conditions of a 1 M HCl.

7.2.2 NACL

Figure 7.3 presents the anodic and cathodic polarization curves of AMSFs tested in different molar concentrations of the NaCl solution. The corresponding data is displayed in **Table 7.2**. **Figure 7.3** shows sample #1 in 0.01M NaCl solution exhibits a low I_{corr} (2.36E-11 A/cm^2) value and the corresponding $E_{corr,}$ which is -0.96 V. Also, with an increase in the Al_2O_3 particle size to 1000 µm**,** a slight increment in the I_{corr} value (3.86E-10 A/cm^2) was observed at 0.01M NaCl solution. Further, with an increase in the Cl^- ion concentration drastic increase in the current density values is

observed for 1 M NaCl solution, i.e., 1.51E-05 A/cm^2. For a 1 M NaCl solution, compared to an HCl solution, there is no drastic change in the I_{corr} value observed, and it exhibits similar behavior. Interestingly, the corrosion behavior of AMSF samples (#1 and #2) revealed similar corrosive behavior.

Table 7.2: Corrosion current (I_{corr}) and corrosion potential (E_{corr}) at different NaCl molar concentrations

Type of solution	Sample ID	Particle size (µm)	Molarity (M)	I_{corr} (A/cm^2)	E_{corr} (V vs. sec)
NaCl (Neutral)	#1	500	0.01	2.36E-11	-0.96
			0.1	1.68E-10	-0.95
			1	1.51E-05	-1.22
	#2	1000	0.01	3.86E-10	-0.91
			0.1	3.08E-10	-0.9
			1	4.43E-05	-1.16
	#3	1500	0.01	2.03E-10	-0.9
			0.1	9.74E-06	-0.82
			1	3.86E-05	-1.09

In the case of sample #3, there is a noticeable difference when compared to the other two ASF samples. As the Cl^- ion concentration increases from 0.01 M to 1 M in the NaCl solution, higher Icorr values are observed. concurrently, Ecorr values shift towards the more negative side -0.9 to -1.02 V. this shift in Ecorr values indicates reduced stability of the alloy in the presence of increasing chloride ion concentrations. A significant change in Icorr values is observed with shift in Cl^- ion from 0.1 to 1M in NaCl solution, suggesting a high corrosion rates under these conditions. Compared to the HCl data (**Figure 7.1**), the samples tested using NaCl solution (**Figure 7.3**) showed better passivity in all molar concentrations. This implies that the ASFs exhibited

elevated corrosion resistance in NaCl solution compared to corrosive effect of the acidic HCl media.

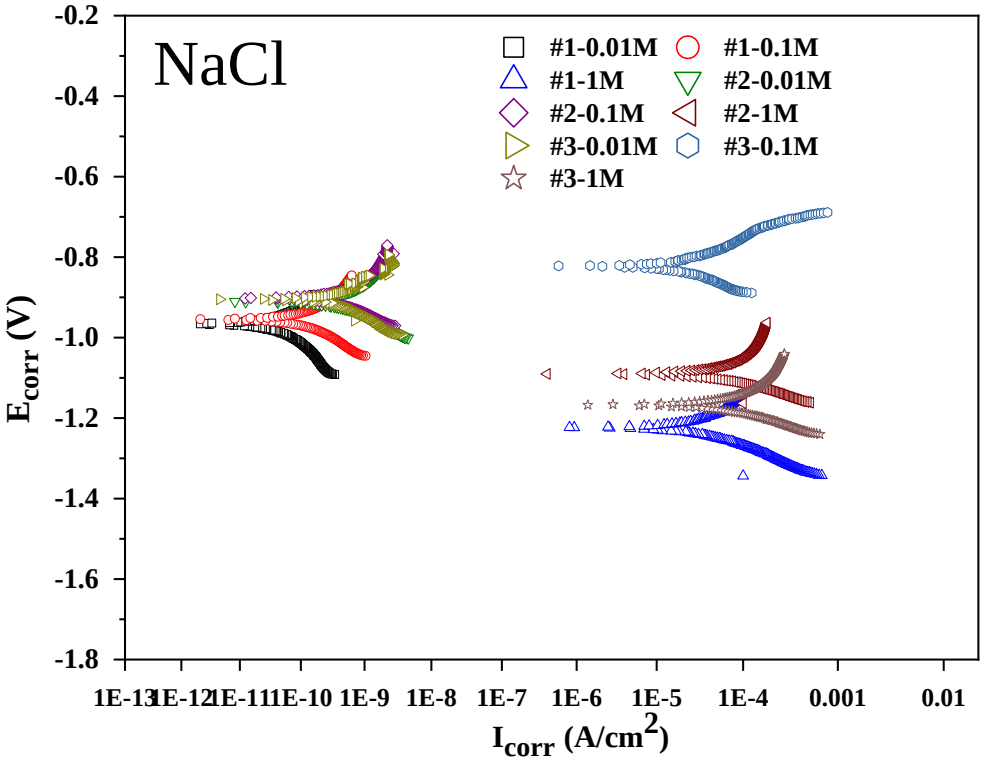

Figure 7.3: The polarization curve of AMSF #1, #2, and #3 samples were tested in a neutral salt NaCl solution.

Figure 7.4(a-f) provides visual insights into the surface morphologies of the corroded samples (#1, #2, & 3) when exposed to NaCl solutions at concentrations of 0.01 M and 1 M. In **Figure 7.4(a**) shows sample #1 tested in 0.01M NaCl solution, it was observed that a small pit was detected, and no significant surface damage was observed on the surface. Pit along with more surface damage was identified with an increase in the hallow particle size to 1000 µm (**Figure 7.4(c)**). In the case of sample #3 (**Figure 7.4(e)**), for 0.01M NaCl solution, the surface damage has increased with broader pits was noticed, as compared to #1 and #2. This suggests that compared to

both the large particle size foams, samples with 500 μm exhibited excellent corrosion resistance, this conclusion aligns well with the Icorr values provided in **Table 7.2**.

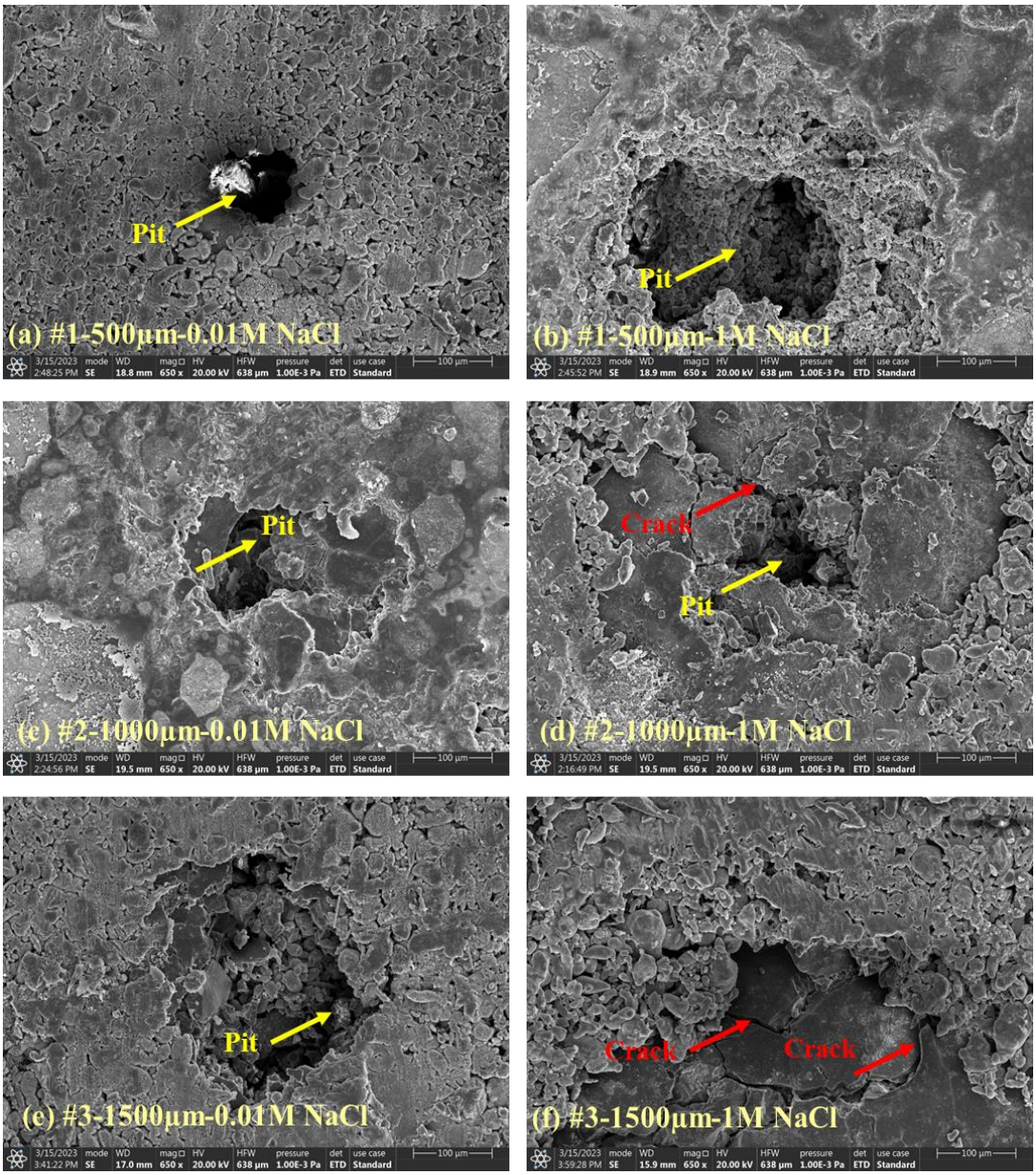

Figure 7.4: Morphologies of the corroded surface of #1, #2, and #3 samples tested in NaCl solution at 0.01 M and 1 M.

Additionally, as the chloride ion concentration increased to 1 M for 500 μm samples (**Figure 7.4(b)**), the size of the pit grew along with minor surface damage, and no cracks were found. The SEM micrographs of samples with 1000 μm and 1500

μm HPs revealed surface cracks with broader pits and deeper cracks. Among all, sample #1 exhibited low corrosion rates, and sample #3 displayed high corrosion rates.

Nevertheless, compared to HCl data, the surface damage in all the samples is less aggressive compared to the NaCl solution. Based on the Pourbaix diagram for aluminium, in a neutral solution (pH=7), aluminium tends to move towards a more passive side, forming an oxide layer owing to the less aggression of Cl^- ion. The formed Al2(OH)3 passive layer is partially stable, thereby acting as a barrier against the corrosion. Thus, lower corrosion rates were detected in the NaCl solution compared to the HCl solution.

7.2.3 NAOH

Figure 7.5 and **Table 7.3** represent the polarization curves of three different sizes of alumina HP-reinforced ASFs tested in alkaline NaOH solution under varying pH levels, i.e., 8, 10, and 12. From **Figure 7.5**, sample 1# tested in all pH levels showed low Icorr values indicating good corrosion resistance, suggesting excellent corrosion resistance. Similar behavior was observed for sample #2. Compared to #1 and #2, slightly higher Icorr values were observed in sample #3, indicating high corrosion rates in alkaline. Among all, Al-500μm composite at pH8 shows very less Icorr values i.e 1.51E-10 A/cm^2, suggesting excellent corrosion resistance.

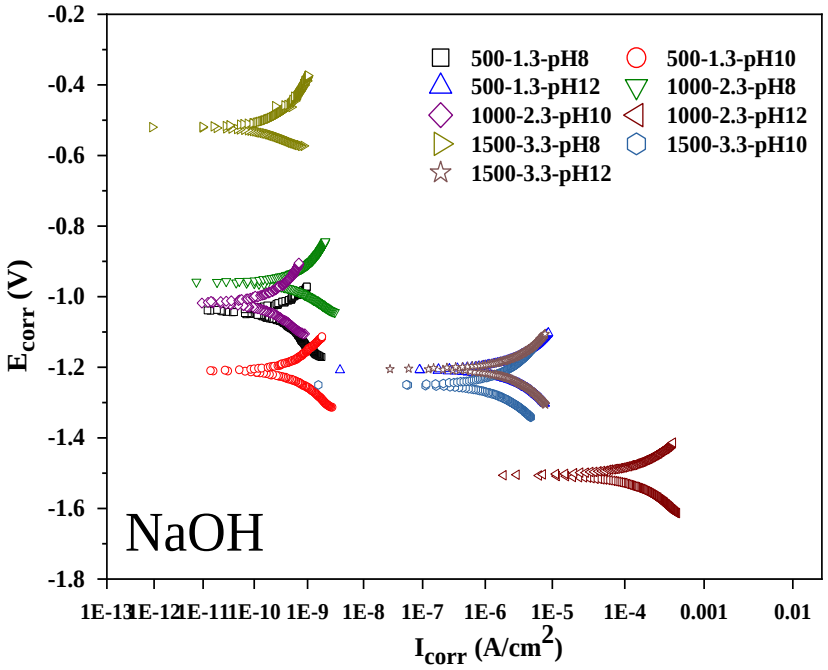

Figure 7.5: The polarization curve of AMSF #1, #2, and #3 samples were tested in a NaOH solution.

Table 7.3: Corrosion current (I_{corr}) and corrosion potential (E_{corr}) at different NaOH molar concentrations

Type of solution	Alloy	Molarity (m)	I_{corr} (A/cm^2)	E_{corr} (V vs. sc)
NaOH (alkaline)	500-1.3	pH8	1.45E-10	-1.03
		pH10	4.56E-10	-1.21
		pH12	6.96E-07	-1.2
	1000-2.3	pH8	2.98E-10	-0.96
		pH10	1.51E-10	-1.01
		pH12	8.59E-05	-1.5
	1500-3.3	pH8	1.68E-10	-0.52
		pH10	6.65E-07	-1.24
		pH12	1.30E-06	-1.2

The SEM morphologies of the three ASF samples tested NaOH alkaline media at different pH environments are shown in **Figure 7.6**. From **Figure 7.6(e & f)**, a

deeper pits and cracks with surface damage were observed in sample #3 when tested in pH8 and pH12. This could be attributedto the deterioration of the passive layer, an indication of high corrosion rates. The number of pits and size of the pit increase in pH12 compared to pH8. With a decrease in the HP to 1000 µm (**Figure 7.6(c & d)**), only a few micro-pits and no significant surface damage were identified. Further, reducing the particle size in 500µm (**Figure 7.6(a & b)**) only single pit with no surface damage was observed. This suggests the presence of an $Al(OH)^3$ protective layer covering the entire surface and helping to protect from corrosion, which is insoluble in NaOH solution [15]. Therefore, less degradation in NaOH alkaline media can be noticed. As the pH level from pH8 to pH12, aluminium degradation intensifies by the strong adsorption of the OH- ions. This resistance to the formation of an active anodic region results in an increase in corrosion rates in alkaline media. Interestingly, the corrosion rate at pH 12 in alkaline NaOH solution was found to be lower than that observed in neutral NaCl and HCl solutions. This highlights the complex nature of corrosion behaviour in different environments. The SEM images of ASFs in the alkaline medium, in **Figures 7.6(a-f)**, indeed correlate well with the polarization results presented in **Figure 7.5** and the data in **Table 7.3**.

While comparing the overall corrosion behavior of the samples (#1, #2, and #3) tested in acidic, neutral, and alkaline media in both acidic and neutral solutions with increasing the concentration from 0.01M to 1M, noticed that an increase in the I_{corr} values and the corrosion current density decreases with increasing the concentration of Cl^- ion. The increase in pH value leads to the dissolution of the AMSFs. The value of the I_{corr} reducing is in the following order based on the pH level in electrolyte solutions: $I_{corr\text{-}NaOH} > I_{corr\text{-}NaCl} > I_{corr\text{-}HCl}$.

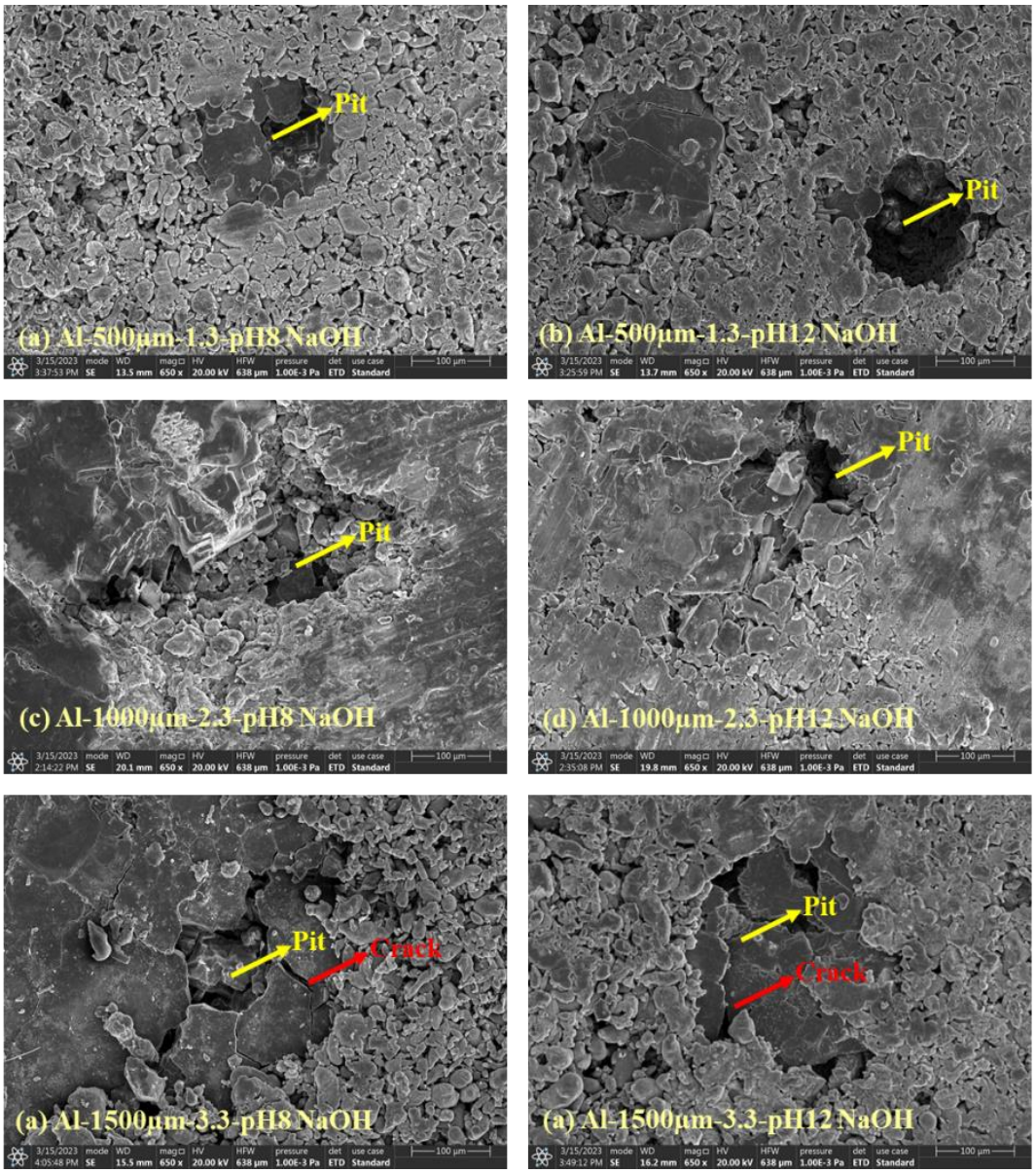

Figure 7.6: Morphologies of the corroded surface of #1, #2, and #3 samples tested in NaOH solution at pH 8 and pH12.

On the other hand, in all three media, acidic (HCl), neutral (NaCl), and alkaline (NaOH), AMSF with 500 μm shows less I_{corr} values, indicating excellent corrosion resistance and samples with 1500μm HP displays high I_{corr} values, suggesting high corrosion rates. Sample #2 showed high corrosion resistance in 1M acidic HCl media. This could be due to the optimal distribution of the hallow particles (Al_2O_3) into the Al matrix, thus forming the strong $Al(OH)_3$ passive layer, which resists high Cl^- ion concentration. Overall, the order of the corrosion is as follows #1>#2>#3 of AMSFs.

The produced AMSFs samples were compared with the other syntactic foam samples such as $Al_2O_3$3D/5083Al foam [129], AA2014 - 45% cenosphere syntactic foams [130], Al+5%Al_2O_3 [131], and Magnesium alloy AZ61/fly ash microspheres (FAMs) syntactic composite foams [105]. All these syntactic foams were tested in 3.5% NaCl neutral solutions, as shown in **Table 7.4**. and the corresponding I_{corr} values are 6.41E-6 A/cm^2, 9.32E-6 A/cm^2, 1.33E-4 A/cm^{2,} and 2.79E-6 A/cm^2.

Compared with the literature data, the I_{corr} values of all AMSFs (Al-Al_2O_3 SFs) at NaCl solution were found to be lesser. In the present investigation, for the HCl and NaOH solution, it is interesting to note that the I_{corr} values were found to be significantly less in all three different Cl^-ion concentrations (**Table 7.1**) and pH environments (**Table 7.3**). This may be attributed to forming of a stable Al_2O_3 protective oxide layer. This layer helps to protect from aggressive corrosion. To the best of the author's knowledge, most of the syntactic foams are only tested with NaCl solutions; the present AMSFs are tested in all three aqueous environments and showed lower I_{corr}, indicating superior corrosion resistance.

Table 7.4: I_{corr} values of AMSF at different molar concentrations from literature

Material	Electrolyte	Molarity (M)	I_{corr} (A/cm^2)
$Al_2O_3$3D/5083Al foam [129]	NaCl	3.5	6.41E-06
AA2014 - 45% cenosphere syntactic foams [130]	NaCl	3.5	9.32E-06
Al+5%Al_2O_3 [131]	NaCl	3.5	1.33E-04
AZ61/ FAMs syntactic composite foams [105]	NaCl	3.5	2.79E-06

7.3 Electrochemical Impedance Spectroscopy (EIS) Measurements

Electrochemical impedance spectroscopy (EIS) is a powerful tool for studying corrosion behavior. It provides insights into physical, electrochemical, and electrical processes. **Figure 7.7** displays Bode and Nyquist plots for samples tested in acidic, alkaline, and neutral environments. Here **Figure 7.7 (a-c)** and **Figure 7.7 (d-f)** displays Bode plots of impedance (Z) and phase angle (Ɵ) plots vs. frequency (f). **Figure 7.7 (g-i)** presents Nyquist plots. The position of absolute impedance (|Z|) and phase angle (Ɵ) curves in these plots reveals the corrosion mechanism of the syntactic foam samples. This mechanism is influenced by factors like pH, chloride ion (Cl-) concentration, and alloy composition. The impedance analysis was analyzed byusing an equivalent circuit to better understand these corrosion mechanisms.

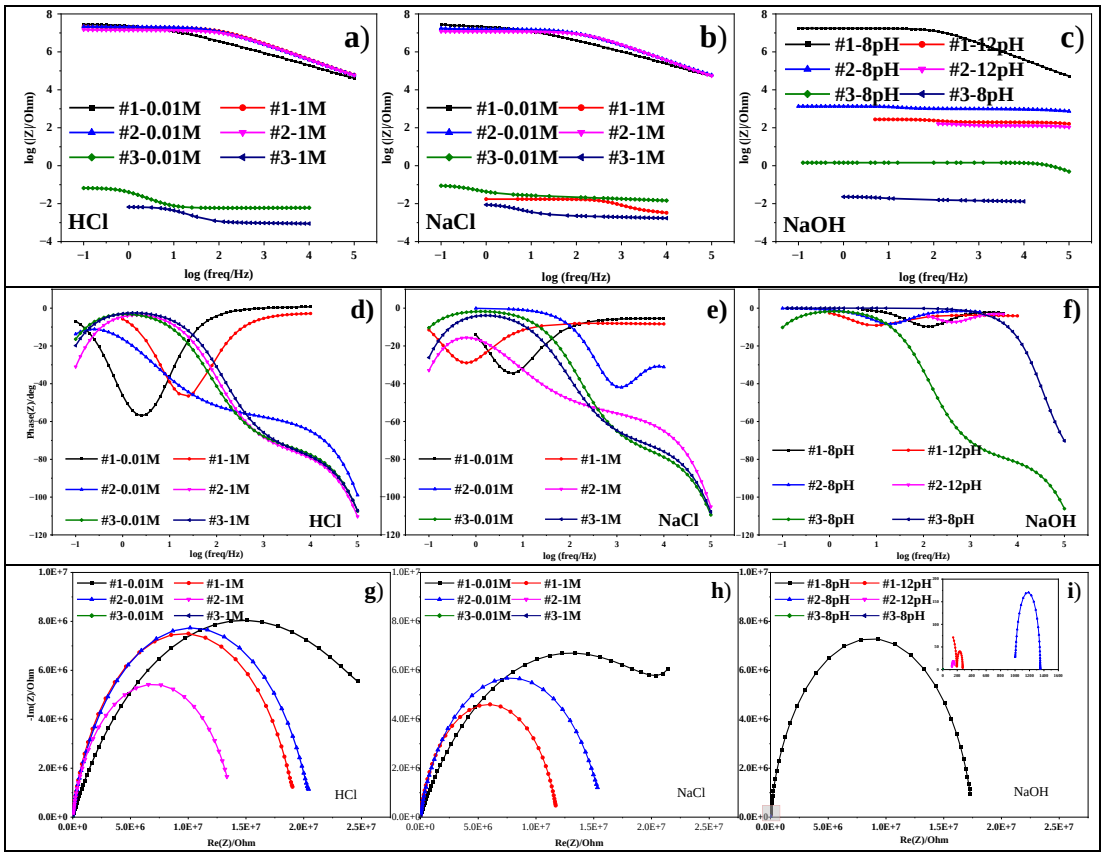

Figure 7.7: Bode plots [a–c represents log f vs. log Z; and d-f represent log f vs. Θ] and Nyquist plots [g-i represent the Z_{real} vs. Z_{im}] of Al-500 µm-1.3, Al-1000 µm-2.3, and Al-1500 µm-3.3 syntactic foam samples. (a-b) Acidic HCl and Neutral NaCl solutions in 0.01 M, 0.1 M, and 1 M and (c) basic/ alkaline NaOH solution at different pH levels.

Figure 7.7(a & d) displayed the bode impedance and phase angle plots of the ASFs samples (#1, #2, & #3) tested in acidic HCl solution at various molar concentrations. The results showed that ASF of 500µm tested in 0.01M solution displayed a high absolute impedance value |Z| is evident within the low-frequency regions in compared to samples #2 & #3, indicating good passivation behavior. With an increase in the hallow particle size from 500 to 1000 µm, little difference towards the negative side is witnessed in sample #2 (1000 µm). With further increase in the particle size to 1500 µm, absolute impedance value |Z| shifting even further to the

negative side at low-frequency regions, thus suggesting high corrosion rates. When investigating the impact of increasing Cl-ion concentration from 0.01 M to 1 M (**Figure 7.7(a)**), it is observed that both samples #1 and #2 exhibited high impedance values at low-frequency regions. Whereas in the case of sample #3 at 1M HCl solution, there were less impedance values than the other two samples, indicating high corrosion rates. **Figure 7.7(d)** represents the phase angle plots for all samples (#1, #2, & #3). For sample #1 tested in 0.01 M HCl, a high phase angle at a high-frequency region with a large curvature radius signifies high corrosion resistance. As the Cl- concentration increases from 0.1 M to 1 M, a suppressed phase maximum is observed, aligning with the polarization results in **Figure 7.1** and **Table 7.1**.

The Bode impedance and phase angle plots of the ASF samples tested in neutral NaCl solution at different Cl^- ion concentrations, as presented in **Figure 7.7(b & e)**. The bode impedance results revealed that the behavior of the samples at NaCl is similar to the HCl solutions. In **Figure 7.7(b)**, we observe high absolute impedance |Z| values at low-frequency regions across all concentrations in NaCl, which is different from the HCl solution (**Figure 7.7(a)**). Likewise, in **Figure 7.7(e)**, in sample #1 observed high-phase maxima in the high-frequency region, indicate better corrosion resistance and strong passivation behavior. This is because of the formation of a stable alumina passive layer. It indicates the sample shows good passivation behavior with increased pH levels from acidic to neutral. Within this, #1 sample displayed high impedance values indicating good corrosion resistance, and low impedance values recorded in #3 samples suggesting high corrosion rates, due to the sample was less aggressive in a neutral solution.

Figure 7.7(b & e) represents the bode impedance and phase angle plots of the samples tested in neutral NaCl solution at different molar concentrations. The bode

impedance results revealed that the behavior of the samples at NaCl is similar to the HCl solutions. Nevertheless, the high absolute impedance |Z| values were recorded at low-frequency regions in all concentrations in **Figure 7.7(b),** compared to the HCl solution (**Figure 7.7(a)**). The sample shows good passivation behavior with increased pH levels from acidic to neutral. Within this Al-500 µm-1.3 sample displayed high impedance values indicating good corrosion resistance, and low impedance values recorded in Al-1500 µm-3.3 samples displayed high corrosion rates.

Similarly, from **Figure 7.7(e),** high-phase maxima were observed in the high-frequency region. The high phase maxima observed in Al-500µm-1.3 displayed better corrosion resistance and good passivation behavior. NaCl showed improved results compared to HCl due to the formation of the stable Al_2O_3 passive layer, and the sample was less aggressive in a neutral solution.

The Bode impedance and phase angle plots of all samples tested in NaOH alkaline media at different pH environments (**Figure 7.7(c & f)**). Compared to the HCl (**Figure 7.7(a & d)**) and NaCl (**Figure 7.7(b & e)**), high impedance value at low-frequency region and dominated phase maxima at high-frequency region observed in Al-500µm-1.3 sample, followed by samples #2 & #3. However, #1 at pH8 displayed excellent passivation behavior and corrosion resistance. By combining all the bode results of HCl (**Figures 7.7(a & d))**, NaCl (**Figures 7.7(b & e)),** and NaOH (**Figures 7.7(c & f)**), Al-500 µm-1.3 displayed high impedance and phase maxima at a high-frequency region in all media, very high in alkaline medium. Low impedance values and suppressed phase maxima were observed in the Al-1500 µm-3.3 sample. This means sample #1 is more stable than the other two samples in all the pH environments, which agrees with the polarization results (**Figures 7.1, 7.3 & 7.5**).

Figures 7.7 (g, h, i) represents the Nyquist plots all AMSFs tested in acidic, neutral, and alkaline media at different Cl^- concentrations and pH environments. **Figure 7.7(g)** shows the Nyquist plot of the syntactic foam samples tested in HCl solution at 0.01M and 1 M concentrations. It was observed that sample #1 displayed a large radius of curvature and high imaginary values. The large radius of curvature and high imaginary values indicate high corrosion resistance. With an increase in the hallow particle size (1000 µm), a radius of curvature and imaginary values is reduced, followed by very low in sample #3. With an increase in the Cl^- ion concentration from 0.01 M to 1 M (**Figure 7.7(g)**), a small radius of curvature and low imaginary values were observed in all three samples. It means that the composite absorbs the anions on the surface. With an increase in hollow particle size, the adsorption rate increases due to the less compact nature because of the increase of oxidation by consuming the metal electrons from the alloy. This leads to pit initiation on the sample surface, as seen in **Figure 7.2**. The curves are too small at 1M HCl solution, indicating high corrosion rates. The Nyquist plots of the HCl correlate well with the polarization results (**Figure 7.1**) and SEM morphologies (**Figure 7.2**). Similar results were observed from Nyquist plots in **Figures 7(h) and 7(i)**, which correlate well with PDP results.

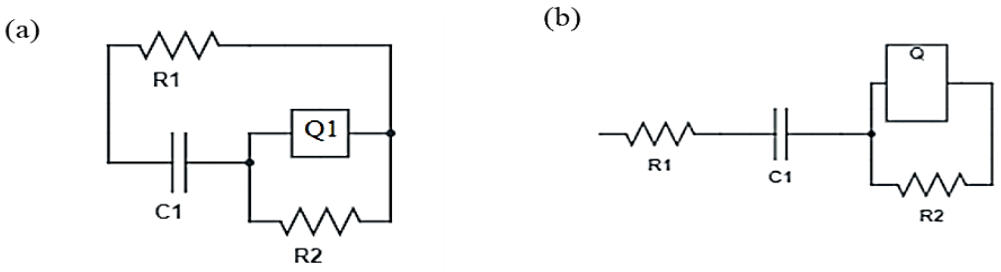

Figure 7.8: Randle's equivalent circuit for (a) Al-500 µm-1.3 (b) Al-1000 µm-2.3 and Al-1500 µm-3.3 syntactic foam samples tested in the present alloy in HCl, NaCl, and NaOH.

Quantitative results of the EIS plots were obtained from the impedance analysis by EC lab software, as displayed in **Tables 7.4, 7.5, and 7.6**.The **Figures 7.8 (a & b)** shows the equivalent circuits that explain the corrosion behavior of the three syntactic foams tested in various aqueous solutions. To simulate the impedance spectra, two different equivalent circuit models were developed. The two equivalent circuit models were fitted by adjusting the individual parameters through iterations to reduce the residual error in both real and imaginary impedance components. This indicates the difference in forming the passive surface film characteristic and electrochemical response in the presence of ions [132]. These equivalent circuit models signify the metal/oxide layer/electrolyte reaction. **Figure 7.8(a)** is the simple Randle's equivalent circuit of sample #1 tested in HCl, NaCl, and NaOH solutions, with a description code (CDC) as R+(C+Q/R) for the Nyquist plots. Similarly, **Figure 7.8(b)** shows the equivalent circuit description code (CDC) as R/(C+Q/R) for samples #2 and #3 tested in HCl, NaCl, and NaOH solutions.

Table 7.5: Electrochemical parameters of the #1 AMSFs from impedance fitting diagram.

Material	CONCENTRATION	R1(Ω)	R2(Ω)	C1 (µF)	Q1($F.S^N$)	n
#1	0.01M HCl	0.01	0.04	232.9	3.42	0.8
	1M HCl	7.60E-04	0.01	5.74E+15	3.94	0.8
	0.01M NaCl	7.80E-03	0.09	1.59E+09	74	0.8
	1M NaCl	9.80E-04	0.07	2.48E+12	9.03	0.8
	pH8 NaOH	0.01	9.56 E-3	74.39	0.11	1
	pH12 NaOH	0.14	0.43	4.60E+14	0.96	0.5

Table 7.6: Electrochemical parameters of the #2 AMSFs from impedance fitting diagram.

Material	CONCENTRATION	R1(Ω)	R2(Ω)	C1(µF)	Q1(F.S^N)	n
#2	0.01M HCl	0.036	9.50E+11	0.81	40.77	0.1
	1M HCl	4.45E-03	9.30E-04	2	7.65E-03	1
	0.01M NaCl	0.059	4.50E+11	0.67	14.23	0
	1M NaCl	5.62E-03	1.56E-05	1.43	1.92E-03	1
	pH8 NaOH	0.24	2.81E+12	0.74	2.47	0.1
	pH12 NaOH	0.044	7.99E+12	3.55	7.99	0.1

The circuit in **Figure 7.8 (a & b)** consists of two resistors (R), one capacitor (C), and one constant phase element (Q). Electrochemical parameters such as solution resistance (R1 Ohms), charge transfer resistance (R2 Ohms), double-layer capacitance (C1 µFarads), constant phase element (Q), and Constant phase element exponential (n) of the circuit were obtained from the EC lab software, displayed in **Table 7.4, 7.5 and 7.6**. Here, the 'n' value varies between 0 to 1. The "n" value gives information about the Warburg impedance (Z_w) and coating capacitance. The equation for the infinite Warburg impedance (Z_w) is:

$$\text{Warburg impedance } (Z_w) = (\sigma\omega)^{-1/2}(1-j) \quad (7.1)$$

where σ is the Warburg coefficient ($\Omega\ cm^2\ s^{-1/2}$) and $\omega = 2\pi f$ (rad s^{-1}). Here $(\sigma\omega)^{1/2}$ is the frequency impedance real part, and $(\sigma\omega)^{-1/2}(-j)$ is the imaginary part [133]. These parameters are used to study the corrosion process kinetics.

Table 7.7: Electrochemical parameters of the #3 from impedance fitting diagram.

Material	CONCENTRATION	R1(Ω)	R2(Ω)	C1(μF)	Q1(F.S^N)	n
#3	0.01M HCl	0.067	0.017	2.88	93.92	0
	1M HCl	6.69E-03	2.19E+09	2.39	682.5	0
	0.01M NaCl	0.092	2.74E+12	3.75	17.26	0.1
	1M NaCl	9.32E-03	1.89E+09	4.25	2.14.1	0
	pH8 NaOH	1.44	0.44	0.32	1692	1
	pH12 NaOH	0.023	95.22	3.05	10.7	0.1

The electrochemical parameters such as R1, R2, C1, Q, and n are obtained from the EIS measurement for HCl, NaCl, and NaOH solution (listed in **Tables 7.4, 7.5,** and **7.6**). From the above tables, it can be observed that AMSFs in both acidic and neutral solutions, with an increase in the Cl^- concentration from 0.01M to 1M, decrease the R2 value. This indicates that the corrosion resistance of the alloy decreases with an increase in the Cl^- ion concentration and does not form a protective layer on the surface. Correspondingly, with an increase in the Cl^- ion concentration, the C1 value of the SF increased from 0.01 M to 1 M in both HCl and NaCl solutions (**Tables 7.4, 7.5, and 7.6**), suggesting an increase in defects on the oxide film and restrict the AMSF to form a protective layer in aqueous solution. This can be correlated with increased pores/defects on the alloy surface (from SEM images **Figure 7.2 & 8.4**). In the NaOH alkaline medium, the R2 value decreases, and the C1 value increases with an increase in pH concentration from 8 to 12 (**Tables 7.4, 7.5, and 7.6**). This further suggested that the protective layer is less stable with an increase in the pH level.

On the other hand, at pH 8, fewer C1 values were observed. This happened mainly due to the Al^{3+} metal ion reaction and oxidization and formed Al^{3+} and OH^- ions at the oxide/solution interface, forming the Al_2O_3 protective oxide layer, causing high corrosion resistance with minor defects on the sample surface at pH 8. It is also observed from **Table 7.4** that the CPE exponential value of sample #1 is nearer to 1, signifying the ideal capacitor behavior indicating the formation of a passive oxide layer on the alloy surface. It also reveals that with an increase in the pH value, the concentration of the Cl^- ions reduces, and an excellent passive layer forms on the surface. The R2 and C1 values agree with the corrosion rate measured by polarization curves (**Figures 7.1, 7.3 & 7.5**) and SEM morphologies (**Figures 7.2, 7.4 & 7.6).**

7.4 EDX ANALYSIS

The chemical composition of the ASF samples was performed by using Energy Dispersion X-ray Spectroscopy (EDS) to support the polarization results (**Figures 7.1, 7.3 & 7.5**), SEM (**Figures 7.2, 7.4 & 7.6**) and EIS results (**Figure 7.7**). The chemical composition with an atomic percentage of the syntactic foam samples is displayed in **Table.7.8**. The composition of all three syntactic foam samples tested in 1M HCl solution identified that the sample contains Al, O, and Cl content. The composition reveals a reduction in Al content with an increase of O and Cl content near the pit and cracks region in all three samples. From **Table 7.8**, sample #1 in 1M HCl solution shows that Al content is 54.82, O is 44.53, and the Cl content is 0.2. With further increase in the particle size from 500µm to 1000µm and 1500µm, both samples observed that the reduction in the Al content increases in the O and Cl content.

Table 7.8: Composition of a passive film obtained by EDS on the ASFs in different aqueous solutions.

Material	Solution	Al (at%)	O (at%)	Cl (at%)	Na (at%)
#1	HCl(1M)	54.82	44.53	0.2	-
	NaCl(1M)	73.6	27.1	0.07	0.44
	NaOH(pH8)	75.37	24.55	-	0.17
#2	HCl(1M)	48.03	51.48	0.49	-
	NaCl(1M)	70.87	28.91	0.19	0.46
	NaOH(pH8)	72.87	26.64	-	0.3
#3	HCl(1M)	47.61	51.67	0.72	-
	NaCl(1M)	58.62	41.22	0.28	2.23
	NaOH(pH8)	64.58	35.22	-	0.4

No chemical composition difference was detected in samples #2 and #3 for 1M HCl solution. Based on the chemical composition from **Table 7.8,** it was observed that sample #1 displayed good passivation behavior in the HCl solution. The corrosion behavior of any material mainly depends on the chloride ion concentration, pH value, and environmental conditions. Mainly corrosion happens due to the adsorption of corrosive ions present in the environment, such as Cl^- and OH^- ions [134]. Generally, in aqueous solutions, Al or Al_2O_3 reacts with the water molecules (H_2O), forming a thick Aluminum hydroxide passive layer ($Al(OH)_3$). The probable chemical reaction is given in equations**.7.2 & 7.3** [135]. Based on **Table 7.8**, in an acidic medium (HCl) at high Cl^- ion concentration, Cl^- ions contact with the $Al(OH)_3$, Cl^- ions adsorbed on the interface between the passive layer and alloy surface. Due to contact with Cl^- ions causing Al dissolution with the evolution of the hydrogen. Thus Cl^- replaces the OH^- ions to produce aluminum chloride ($AlCl_3$), as shown in **Eq. 7.4 & 7.5**. From equation **7.5,** it was observed that the presence of O^{2-} ions makes Al_2O_3 basic in nature, implying that it can react with acid. This leads to the breakdown of the $Al_2O_3.3H_2O$/

$Al(OH)_3$ passive layer. As a result, larger pits and deeper cracks were observed at a higher molar concentration resulting in a higher corrosion rate in the acidic medium (from **Figure 7.1 and 7.2**).

$$2H_2O + 2e^- \rightarrow 2OH^- + H_2xx \quad (7.2)$$

$$Al_2O_3 + 3H_2O \rightarrow 2Al(OH)_3 \quad (7.3)$$

$$Al(OH)_3 + 3HCl \rightarrow AlCl_3 + 3H_2O \quad (7.4)$$

$$Al_2O_3 + 6HCl \rightarrow 2AlCl_3 + 3H_2O \quad (7.5)$$

The EDS data of ASFs were tested in 1M NaCl solution. The results are displayed in **Table.7.8**. The results indicate that, compared to 1M HCl solution with increasing the pH level from acidic to neutral media, in ASF with 500 μm particles, there is a great reduction in O content from 44.53% to 27.1% and Cl content from 0.2% to 0.07% along with an increase in the Al content from 54.82% to 73.6% and addition of Na element. Whereas in the case of samples #2 and #3, the O content is slightly higher (**Table 7.8**). Al^{3+} ion reacts with Cl^- ions present in the NaCl solution form $AlCl_3$ (equation **7.6**). However, compared to HCl, Cl^- ions are less aggressive in NaCl solution, and corrosion potential moved to the more positive side leading to the formation of the partial passive layer. It means the Al ions are less soluble in the NaCl solution. Thus the protective oxide layer does not break down completely, leading to lesser corrosion rates observed in the NaCl solution (**Table 7.2**). Overall, all three syntactic foam samples show less soluble in NaCl solution than the HCl, observed improved corrosion resistance. However, some pits and cracks were observed with increased Cl^- ion concentration.

$$Al^{3+} + 3NaCl \rightarrow 3Na^{+} + AlCl_3 \quad (7.6)$$

The EDS mapping of ASFs samples tested in pH8 NaOH alkaline solution displayed the results in **Table 7.8**. compared to the HCl and NaCl solutions, Al content is the highest, with a significant reduction in O and Na content (**Table 7.8**) in the NaOH solution. Generally, in aqueous solutions, the alloy forms $Al(OH)_4$ passive layer, which is naturally formed, highly stable, and gives significant protection from corrosion to the alloy. In NaOH alkaline solution, Al^{3+} ions have a very high positive charge density which makes it possible to attract and react with OH- ions present in alkalis to form $Al(OH)_4$ (Equation **7.7**), leading to less degradation of the passive film in NaOH at pH 8 (**Figure 7.5 & 7.6**). Moreover, with an increase in the pH level from 8 to 12, Al degrades due to the strong adsorption of the OH^- ions than the Na^+ ions. This behavior resists the formation of an anodic region, leading to an increase in the corrosion rate.

$$Al(OH)_3 + OH^- \rightarrow Al(OH)_4 + 2e^- \quad (7.7)$$

$$\text{(or)} \quad Al_2O_3 + 2NaOH + 3H_2O \rightarrow 2NaAl(OH)_4 \quad (7.8)$$

Interestingly, it was observed that in alkaline media at pH12, fewer corrosion rate values were observed than the NaCl solution due to the absence of Cl^- ion. This contributes to excellent passive behavior with increased pH, thus resulting in excellent corrosion resistance in alkaline NaOH solution. EDS results in **Table 7.8** correlates well with polarization and EIS analysis. The high degradation with poor corrosion resistance was observed in acidic HCl solution compared to NaCl and NaOH solution. High passivation behavior with lower corrosion rates was observed in NaOH alkaline media.

In a related investigation, Zhichao Zhang et al. [136]conducted electrochemical tests on a pure Al 2024 coating and an Al 2024-Al_2O_3 composite tested in a 3.5% neutral NaCl solution to evaluate the effects of Al_2O_3 on corrosion behavior. The results of the corrosion test reveal that significant anodic protection with the best corrosion resistance and no pores were observed in Al 2024-20 wt% Al_2O_3 composite, compared to Al 2024-40 wt% Al_2O_3 and Al 2024-60 wt% Al_2O_3 composite. This is mainly due to the denser arrangement of Al_2O_3 particles. In the case of the Al 2024-60 wt% Al_2O_3 composite, it was observed that, even though the composite contains more Al_2O_3 particles, there are large cracks and pores on the sample surface, implying severe dissolution of the Al 2024 matrix. Similarly, in the present investigation, an increase in the composition of the Al_2O_3 particle size from ASFs of 500µm and 1500µm size particles along with the Cl^- ion concentration, leads to a high rate of metal dissolution. It is also interesting to note that, based on current investigations such as polarization results (**Figures 7.1, 7.3 & 7.5**), SEM images (**Figures 7.2, 7.4 & 7.6**), EIS measurement (**Figure7.7**), and EDS results (**Table 7.8**) of ASF samples reveal significant passive behavior in all the three different solutions (acidic, neutral and alkaline) compared to the previously developed syntactic foams. Among all, high corrosion resistance was observed in sample #1 and low in sample #3 syntactic foam sample in all three solutions. The low corrosion rates in the sample are mainly due to the better hallow particle distribution in sample #1.

7.5 SUMMARY

Based on the current investigation, such as polarization results (**Figures 7.1, 7.3 & 7.5**), SEM images (**Figure 7.2, 7.4 & 7.6**), and EIS measurement (**Figure 7.7**) of three different solutions. Samples #2 and #3 revealed significant passive behavior in all three solutions (acidic, neutral, and alkaline) compared to the previously developed

syntactic foams. High corrosion resistance was observed in AMSF sample #1 and low in samples with 1500 μm syntactic foam sample in all three different solutions. The low corrosion rates in the sample are mainly due to the better hallow particle distribution in AMSF #1 was tested in various Cl^- ion concentrations and at different pH levels to identify their biodegradable behavior. The SFs are found to be exhibited good corrosion resistance in all solutions. So far, the studies are focused on alumina-reinforced syntactic foams. Further, in the next chapter attempt is made to reduce the relative density of the SFs by combining multiple particles in the matrix. The effect of multiple hollow particles in the aluminum matrix in the microstructure and mechanical properties are explored.

Chapter 8: Novel Hybrid Syntactic Foams

In the earlier chapters, the effect of alumina hollow particles is extensively discussed in the context of quasi-static room temperature, high temperature, and dynamic compression. The mechanical properties and energy absorption behavior are explored in detail. The alumina hollow particles have shown some effect on the overall density of the syntactic foams. However, due to the high density of the alumina (4 g/cm^3), the relative density achieved at a low volume fraction is limited. In this regard, a novel combination of multi-particle combination is attempted in this chapter. Adding another hollow particle (cenosphere, density-0.8 g/cm^3) to the alumina-based SFs is studied in detail. This study aims to reduce the relative density with minimum deviation from the structural strength.

8.1 INTRODUCTION

In the quest for materials that push the boundaries of strength, lightweight, and versatility, researchers' search for advanced materials has led to hybrid syntactic foams. These extraordinary materials represent an intriguing blend of disparate components, ingeniously combined to harness the best of both worlds. Hybrid syntactic foams seamlessly integrate different types of hollow particles or microspheres, each possessing unique properties within a matrix material, resulting in an interaction surpassing traditional foams' capabilities. This innovative approach opens possibilities where the tailored combination of constituents empowers these foams with enhanced mechanical, thermal, and acoustic characteristics. From aerospace applications demanding impeccable strength-to-weight ratios to underwater systems requiring exceptional corrosion resistance, hybrid syntactic foams offer a

tantalizing array of solutions for the most challenging engineering conundrums. Embark on a journey with us as we unravel the secrets of hybrid syntactic foams, exploring their ingenious composition and delving into the astounding array of applications that harness their remarkable potential. Together, let us embark on a path towards materials engineering excellence, where the fusion of diverse elements ushers in a new era of limitless possibilities. The metal matrix syntactic foams are low-density, high-strength porous composite materials [31,55]. In recent years, the demand for advanced and alternative materials increased. These materials also need to possess properties that operate under different loading conditions.

Owing to the lightweight and high performance of SFs, conventional SFs are engineered using different combinations of materials, such as multi-particle SFs (MPSFs, also known as hybrid SFs) and alternative materials. The reported hybrid foams showed limited plateau strength under dynamic loading [137]. The cenospheres and glass-based particles significantly reduce the SFs' density. However, they exhibit little mechanical strength even at high-volume fractions of the particles [48]. The alumina-based SFs have proven to show maximum yield stress up to 80 MPa under quasi-static loading. However, despite high-strength ceramic particles, the samples failed to retain their structural integrity during large deformations due to their large size and repaid crack growth during the deformation.

The major applications of the SFs are sandwich panels and engineering structures. Combining the two brittle materials has enhanced properties under quasi-static compression [48]. However, sparse literature is available on the mechanical behavior of MPSFs at quasi-static and HSR. The MPSFs are produced using a low-cost hot compaction technique, and the energy absorption behavior under dynamic loading up to 2700 s^{-1} is investigated to fill this gap.

8.2 MICROSTRUCTURE AND PHYSICAL PROPERTIES

Figure 8.1(a-e) represents the freeze-fracture micrographs of the syntactic foam materials produced using different volume fractions of cenospheres, alumina, and both. There is a uniform distribution of the hollow spheres concerning their volume fraction. In **Figure 8.1(c) - (d),** the hollow spheres are submerged in the matrix, which appears small concerning the size mentioned by the authors. Random cavities are formed due to the spurt of spheres during the sample preparations.

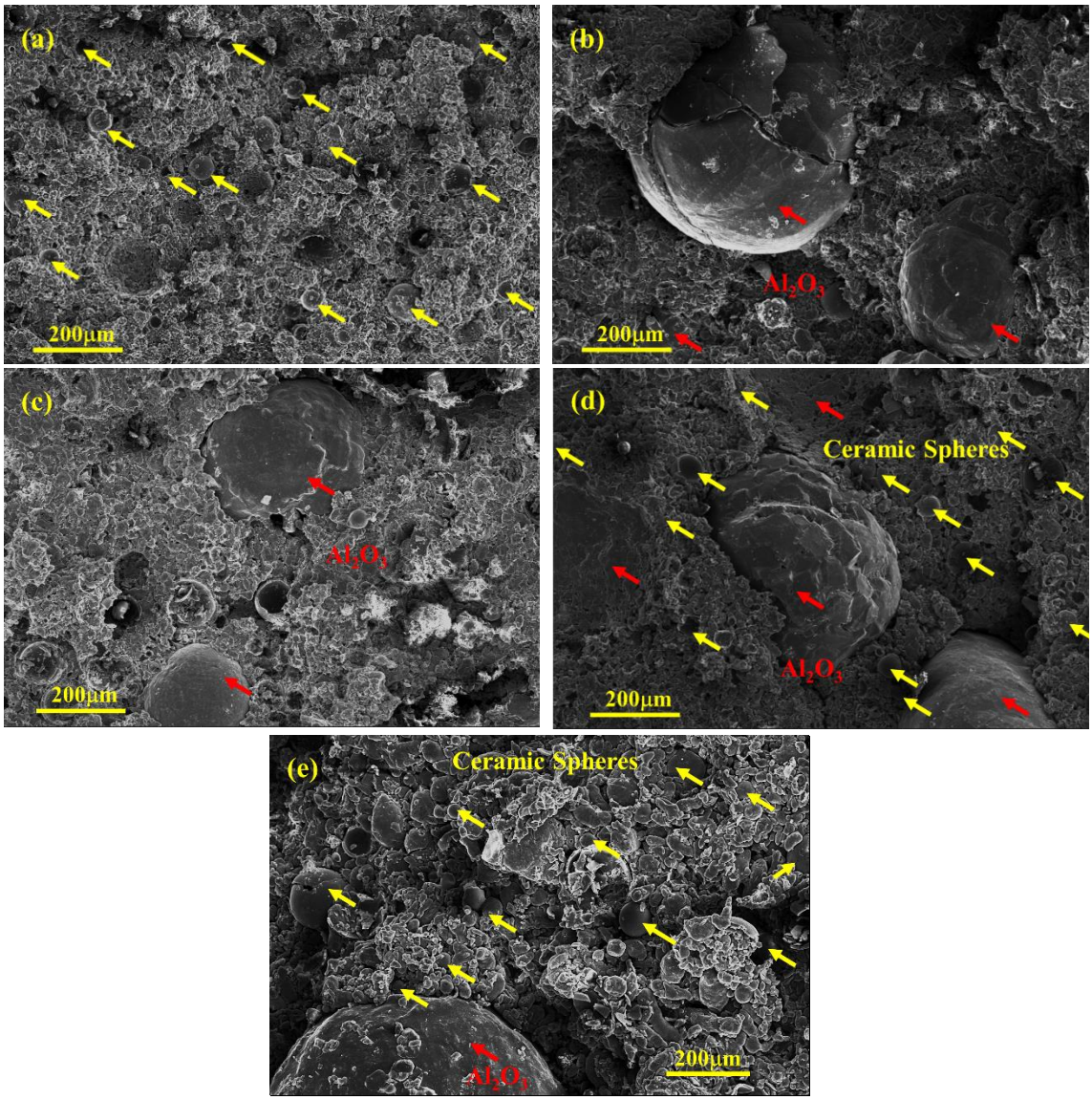

Figure 8.1: Micrographs of syntactic foam materials (a) #1 (b) #4 (c) #7 (d) #11 (e) #14.

The physical properties of aluminum-based syntactic foam samples are listed in **Table 8.1**. The densities of the hybrid syntactic foam materials produced are in the range of 2.17 g. cm^{-3} to 2.57 g. cm^{-3}. The experimental density reported for alumina samples shows different values for the same volume fraction, which may be attributed to the size difference in the sphere diameter [88]. Due to the combination of both spheres, the properties of the hybrid syntactic foams (H-SF) samples are enhanced. The overall density is reduced in contrast to #3 and #9.

8.3 MECHANICAL PROPERTIES

8.3.1 Single-sphere syntactic foam materials

Figure 8.2(a) shows the compressive stress-strain curve of cenospheres reinforced aluminum matrix syntactic foam (#1, #2, #3). In these samples, initially, there is a linear rise in the flow stress to the maximum in the plastic region (yield strength – 55MPa) and then drops gradually to complete failure of the structure after 40% of strain. The crushing strength of the composite decreased with respect to the volume fraction of the reinforcement. These curves show many fluctuations beyond the yield point during the plastic flow region. Though a plateau region was observed, the material failed before it attained the densification region, as reported earlier [66,128,138]. This deviation may be attributed due to the processing technique adopted. The inset image shows the sudden drop in the stress values for 20% and 30% volume fractions of the hollow spheres inside the aluminum matrix.

Table 8.1: Experimental density and relative density of syntactic foam materials

Sample ID	Materials Composition	Vf (%)	Mass (grams)	Diameter (cm)	Height (cm)	Volume (cm^3)	Experimental Density ($g.\ cm^{-3}$)	Relative density
#1	**Matrix** – Aluminum **Filler** – Cenospheres	10	58.61	3.56	2.40	23.90	2.45	0.91
#2		20	59.07	3.56	2.54	25.33	2.33	0.86
#3		30	58.28	3.56	2.66	26.51	2.20	0.81
#4	**Matrix** – Aluminum **Filler** – Alumina	10	56.57	3.56	2.28	22.73	2.49	0.92
#5		20	56.30	3.56	2.31	23.03	2.44	0.90
#6		30	56.61	3.56	2.44	24.30	2.33	0.86
#7		10	55.32	3.57	2.30	22.98	2.41	0.89
#8		20	58.08	3.57	2.59	25.88	2.39	0.89
#9		30	56.68	3.56	2.48	24.73	2.29	0.85
#10	**Matrix** – Aluminum **Filler** – Alumina + Cenospheres	10+20	57.71	3.56	2.65	26.38	2.19	0.81
#11		15+15	48.64	3.57	2.18	21.81	2.23	0.83
#12		20+10	55.00	3.60	2.39	24.33	2.26	0.84
#13		10+20	56.55	3.56	2.62	26.08	2.17	0.81
#14		15+15	49.23	3.57	2.24	22.41	2.20	0.82
#15		20+10	53.48	3.60	2.36	24.02	2.23	0.83

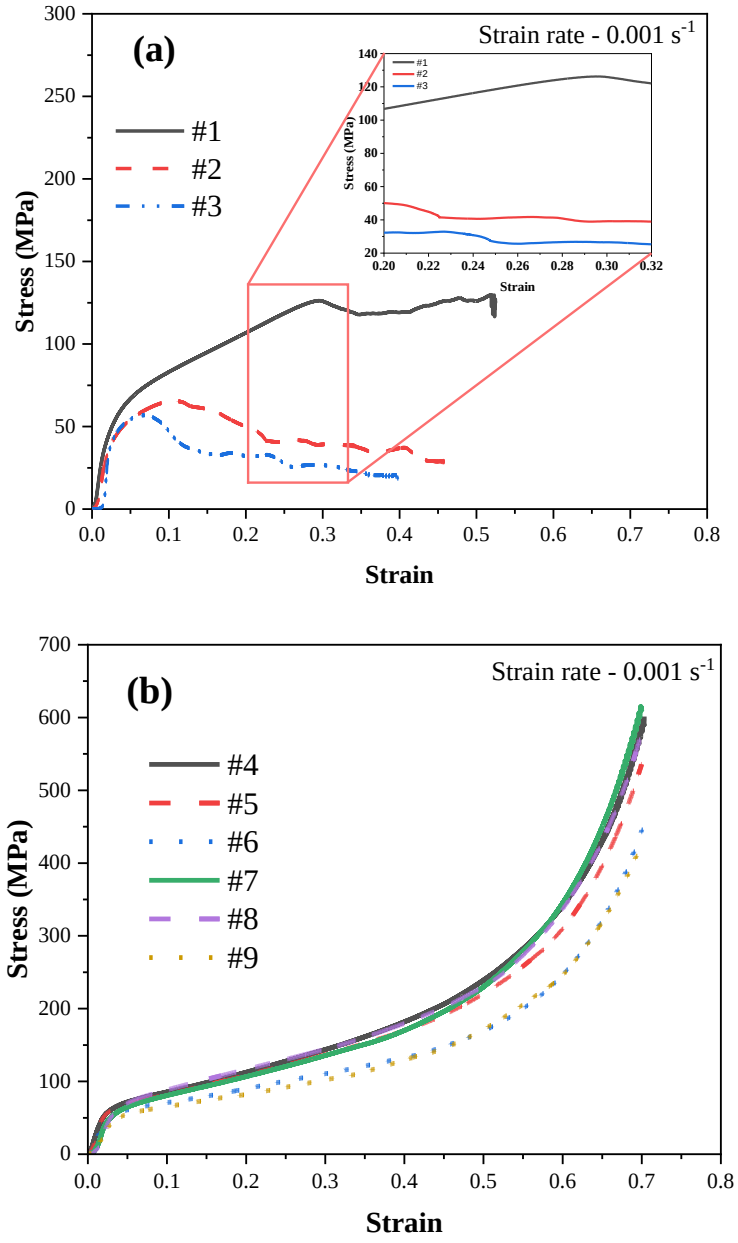

Figure 8.2: Stress-strain curve of (a). cenosphere-reinforced syntactic foam material. (b). alumina spheres reinforced syntactic foam materials.

Figure 8.2(b) shows the compressive stress-strain curve for the alumina-reinforced syntactic foams for two average sphere diameters, i.e., 0.6 mm and 1.7 mm. In contrast to cenosphere samples, all curves follow the typical stress-strain curve pattern of metal matrix syntactic foam materials, which contain an elastic region (5% strain), plateau region (5% - 54% strain), and densification region (54% - end of test

strain). No significant fracture was observed during loading up to 40% of the strain. A linear stress increment is noted during the plastic region (>5% strain), where the sphere deforms plastically. The effect of volume fraction is not significantly observed among 10% and 20% except in the 30% volume fraction. Regardless of the type of reinforcement and size, the lower volume fraction of samples has shown higher compressive strength due to the composites' porosity. Unlike cenosphere-based samples, they continuously harden in the plateau region between stains 0.1- 0.6, often observed in aluminum systems due to their crystal structure. It is also noteworthy that the continuous hardening reduces as the volume fraction increases.

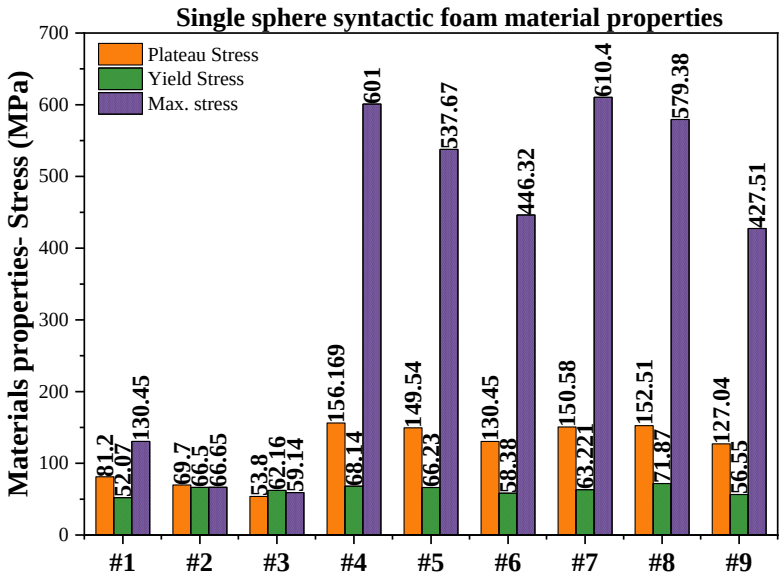

Figure 8.3: Compressive properties of syntactic foam reinforced with cenosphere and alumina hollow spheres

Figure 8.3 compares the material properties of cenosphere and alumina-based syntactic foam materials. It can be observed that there is no significant difference in the yield point concerning the type of reinforcement and volume fraction. This trend suggests that matrix materials initially took the applied load on the syntactic foams. In other words, a hollow sphere may contribute minor plastic deformation up to the yield

point. Beyond the elastic region, the matrix transfers the load to reinforcements, as observed from the plateau stress value of alumina hollow spheres reinforced composites in **Figure 8.2**. However, this phenomenon is not observed in cenosphere-reinforced materials due to the reinforced particles' low crushing strength (20MPa). Large stress values are observed in the alumina-based samples, attributed to particle distribution and interfacial bond strength between matrix and reinforcement.

Further, the plateau and maximum compressive stress follow a similar trend as Su et al. concerning ceramic sphere volume fraction. The stress values are reducing, except for 1.7 mm alumina spheres in the plateau stress [61].

8.3.2 Hybrid syntactic foam materials

Figure 8.4 shows the stress-strain curves of hybrid syntactic foam materials tested under quasi-static compression. The volume fraction of both spheres is adjusted for the $SF_{30\%,}$ as explained in section 2. In contrast to the conventional SFs**,** these curves differ from the AM-reinforced composites. However, there is a significant improvement in the material properties in samples #11 and #14 compared to counterparts #6 and #9. Samples #10 and #13, produced with a maximum volume fraction of cenosphere-based foam, have recovered from catastrophic failure due to the presence of alumina hollow spheres. During the deformation, the load is distributed among the spheres and matrix, thus delaying the rapid failure of SFs and reducing the sudden stress drop at the yield point. The summary of material properties for hybrid materials is represented in **Figure 8.5.**

The plateau and yield stress of samples #10 and #13 have significantly improved compared to #6. However, these properties are not enhanced in the samples with 1.7 mm diameter spheres (#14 & #15) due to the rapid failure during compression. The

compressive stress of SFs is dropped during the densification region; this accounts for the early failure of the structure. Also, softening occurred due to the cenospheres' presence under the densification region. The overall trend in the plastic zone has been affected due to the hybridization of the spheres.

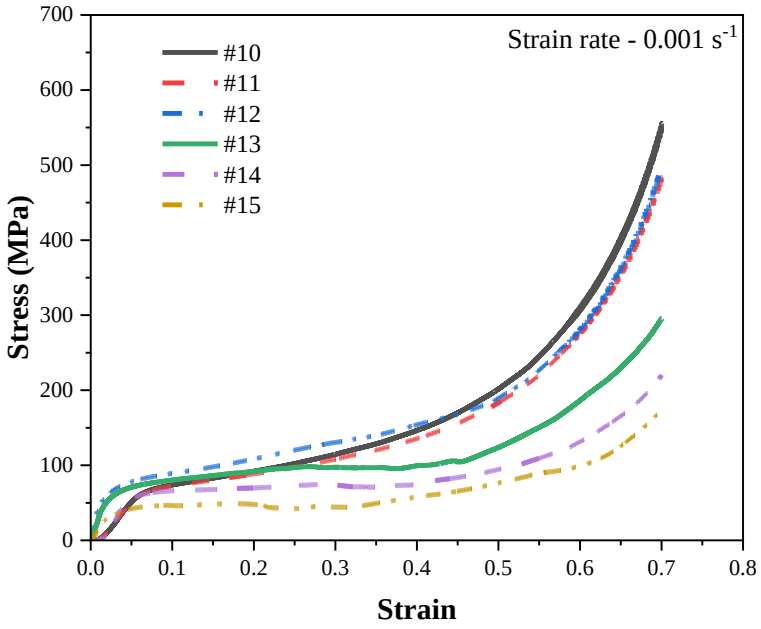

Figure 8.4: Compressive stress-strain curves of hybrid composites

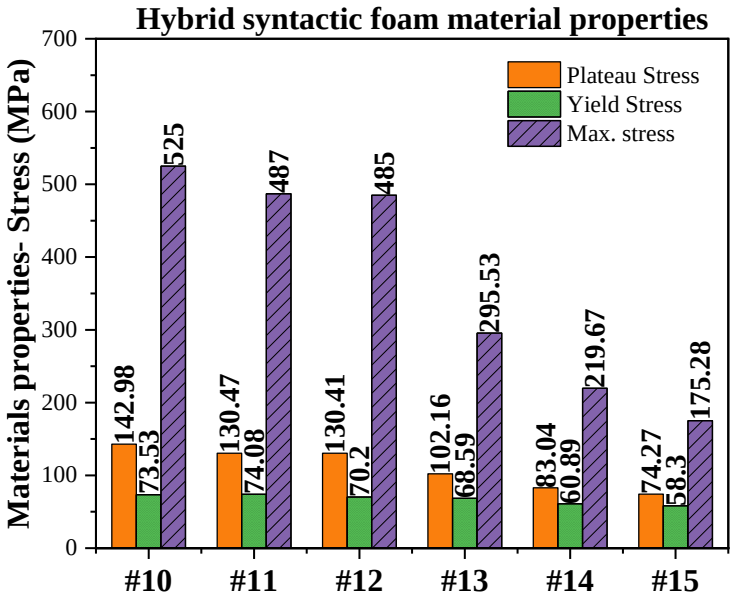

Figure 8.5: Material properties of hybrid composites

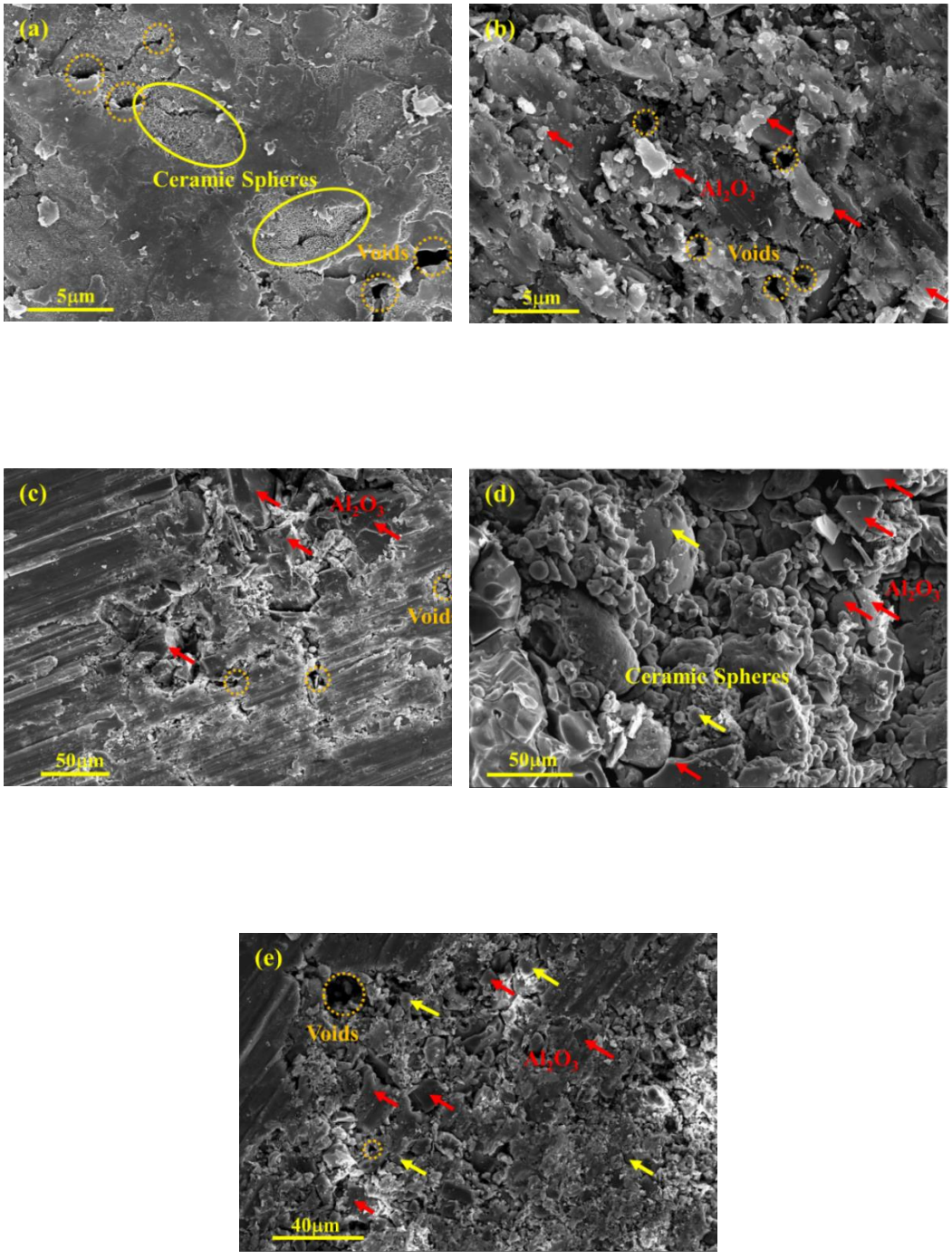

Figure 8.6: Fracture image of syntactic foam materials (a) #3 (b) #6 (c) #9 (d) #11 (e) #14

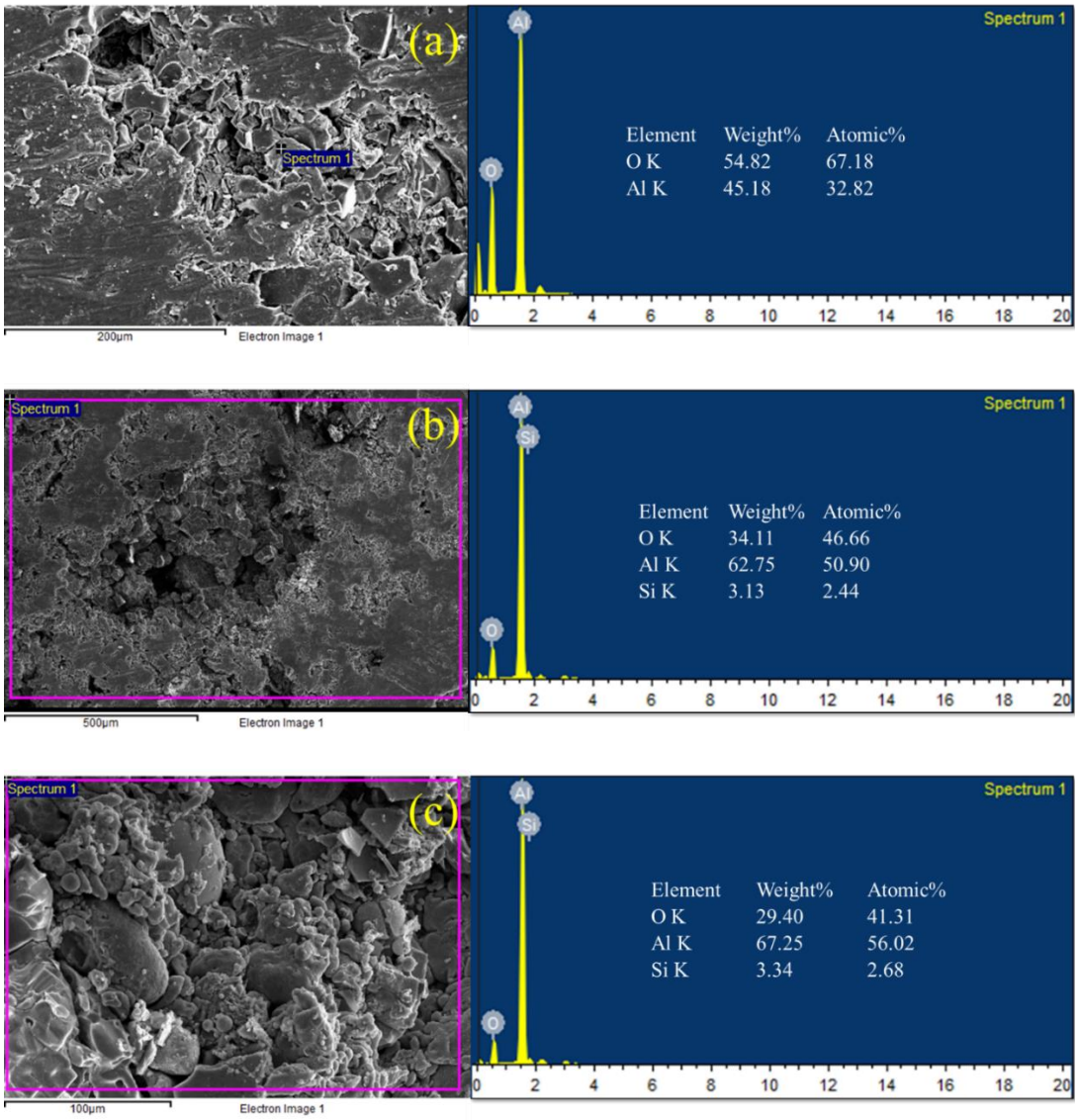

Figure 8.7: EDX spectrum of fracture samples (a) #9 (c) #11 (d) #14

In **Figure 8.6(a-e)**, the fracture images for different sphered hollow spheres show the fracture morphology of syntactic foams for different samples. (#3, #6, #9, #11 and #14). **Figure 8.6 (a)** shows the distribution of fractured spheres and voids generated during the deformation. Among all the samples, plastic flow can be observed in the matrix material, and the spheres are fractured into micro and macro fragments. The voids in the matrix shown here can be formed owing to the absence of spheres due to fracture. Also, clusters of fractured sphere particles are distributed across the cross-section during the plastic flow of matrix material. The micro-voids formed due to the

fracture of hollow spheres have provoked crack initiation and fracture in another case, as shown in **Figures 8.6 (a) & (c)**. Most of the samples have several random Iceland of fragmented spheres surrounded by matrix material, and it is observed both on the top and bottom portion of the samples, as shown in **Figure 8.6(a)**. The respective EDAX spectrum of fracture images (**Figure 8.7**) confirms the presence of alumina and ceramic spheres after the deformation.

8.4 DISCUSSIONS

The potential application of syntactic foam materials is evaluated based on the energy absorption during the deformation. The results from single-sphere samples show continuous hardening. To attain the maximum amount of energy absorption, we need to look into aspects such as energy absorption and deformation behavior, which shall be further examined.

8.4.1 Energy Absorption

Cellular and porous materials are often quantified based on energy absorption and efficiency. The energy absorbed ($W = \int_0^{\varepsilon_d} \sigma d\varepsilon$) and specific energy absorbed ($E = W/\rho_o$) by alumina-based and hybrid syntactic foam, materials are shown in **Figure 8.8**. The energy absorption of the samples up to densification strain (ε_d) is measured using the tangent line technique shown by Basit and Cheon. [139]. The material deformation, the resistance offered during the plateau region, and the overall compressive strength attained could influence the overall energy absorption of the material. Under single spheres, the cenosphere-reinforced composites have failed to achieve densification, but alumina hollow spheres reinforced samples have shown the highest compressive strength corresponding to the energy absorption (#10 - 69.75

MJ/m^3). From both the compressive properties and the energy absorption calculations, it is apparent that the overall material properties are decreasing with the increase in size and volume fraction of the spheres. This trend could be due to the increase in the void percentage in the matrix, shell geometry, and limited plastic deformation during the plateau region.

Further, to understand the effect of hollow spheres on energy absorption, the energy absorption values at densification strain are normalized with sample density. The trends' Specific Energy Absorption (SEA) values are not the same as energy absorption values. In the alumina hollow sphere reinforced foams, a 20% volume fraction shows high SEA values in 0.6 and 1.7 mm diameters. Similarly, the 30% volume fraction samples show low performance.

The SEA values with a high volume fraction of alumina spheres in hybrid systems are 26.61 kJ. kg^{-1} and 23.07 kJ. kg^{-1}. Due to the presence of alumina hollow spheres, there is considerable improvement in the energy absorption, despite being the lowest observed values among the tested specimens. However, there is a significant drop in the energy absorption in single-sphere samples by 30% volume fraction with respect to H-SF samples. The deviation in SEA values for the same is minimum. This phenomenon suggests that the amount of energy absorption with respect to their density may not be significantly affected by the addition of hollow spheres of low strength.

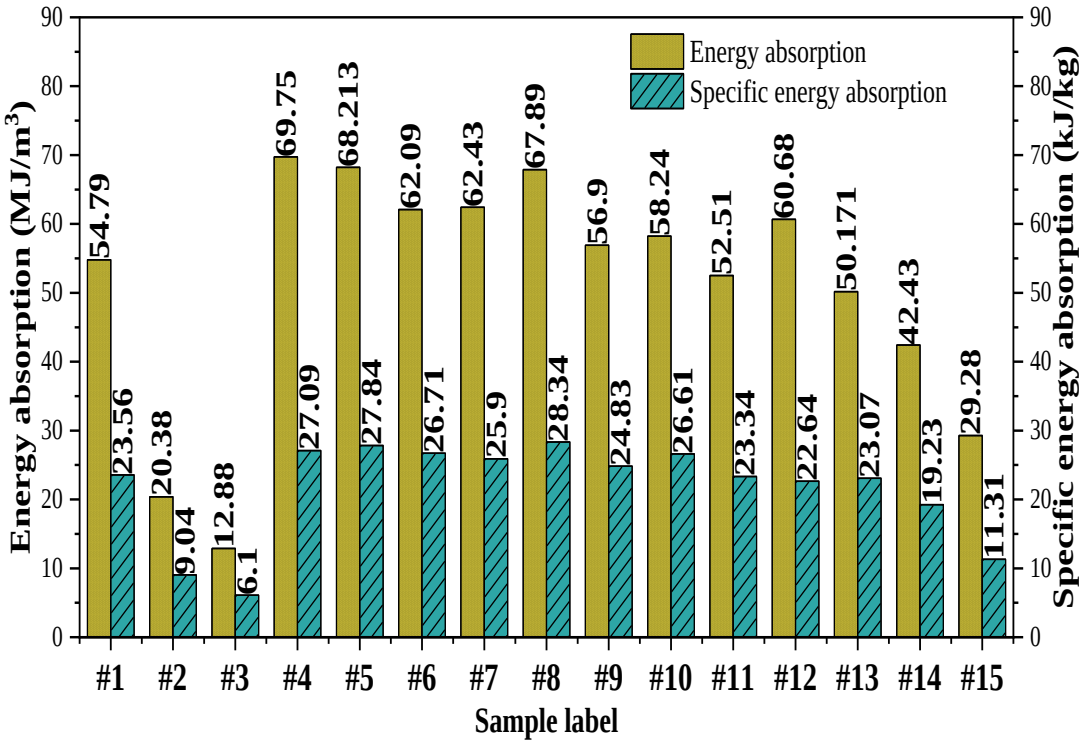

Figure 8.8: Energy absorption and Specific energy absorption of all the syntactic foams

Figure 8.9(a) - (d) shows the energy absorption efficiency (EAE) and ideal energy absorption efficiency (I-EAE) for alumina hollow spheres inscribed and hybrid syntactic foam materials [140]. These are essential in understanding the most suitable materials for energy absorption applications.

$$\eta = \frac{W}{\sigma} \tag{8.1}$$

$$\eta_{ideal} = \frac{W}{\sigma.\varepsilon} \tag{8.2}$$

Where η, η_{ideal} are energy absorption and ideal energy absorption efficiency, and σ & ε are corresponding stress-strain values.

The η curve for porous and cellular materials generally consists of two regions, such as a linear portion, until it reaches a maximum, which is also considered

densification, and then decreases concerning strain. This explains that the flow stress dominates more than the energy absorption beyond the maximum value. The densification strain is measured using the tangential line method that matches the values obtained from the η curves in **Figure 8.9,** as shown in **Table 8.2**.

Table 8. 2: Densification strain and Average ideal energy absorption efficiency of alumina hollow sphere and hybrid syntactic foam materials

Sample ID	Formula Based	Tangent method	Average η_{ideal}
#4	0.55	0.51	0.67±0.01
#5	0.58	0.58	0.69±0.015
#6	0.52	0.52	0.71±0.012
#7	0.55	0.54	0.67±0.015
#8	0.54	0.55	0.62±0.012
#9	0.52	0.51	0.68±0.015
#10	0.52	0.52	0.66±0.012
#11	0.51	0.51	0.44±0.012
#12	0.5	0.51	0.78±0.017
#13	0.46	0.46	0.83±0.015
#14	0.49	0.5	0.81±0.018
#15	0.58	0.56	0.89±0.019

The η_{ideal}- strain curves for different syntactic foam materials are shown in **Figure 8.9**. A typical stress-strain curve consists of a linear rise, a plateau region, and a fall concerning strain; the plateau region provides the maximum energy absorption efficiency by the materials. The alumina hollow sphere-based foams show a linear decline in efficiency after reaching maximum efficiency. The H-SF 13 - 14 has shown quite an amount of plateau region compared to the other conditions and the maximum

efficiency on the scale. This data contrasts with the other data presented in the earlier sections, as shown in **Figure 8.9(d)**. However, the high energy absorption alone is insufficient to judge the significance. Also, these curves need further investigation, which is covered in section 3.2.4.

The η_{ideal}, ideally raises to the plateau region during the elastic part of the stress-strain curve. Later, the plateau region is sustained up to the densification region and attenuated with increased strain. Nevertheless, in all **Figures 8.9 (a), (b) & (c)**, there is a gradual decline (almost linear) in the values as the strain increases. It is observed, based on the literature, that the slope of the stress-strain curve has a significant influence on not only the mechanical properties but also the energy-absorbing efficiency [108,141]. As suggested by Liang et al., the metal foams show heterogeneous behavior during plastic deformation. Different mechanisms are proposed to understand this behavior [142]. The current study observed that the alumina hollow sphere reinforced samples continuously hardened during the plastic region with different slopes (strain hardening coefficient). These slopes are identified by taking the stress-strain data between 0.1-0.5 strain values on a logarithmic scale and determining the individual slopes. At least three curves are taken to measure each value of the slope. The maximum and minimum values of *n* are identified as #7 - 0.67 and #14 - 0.18.

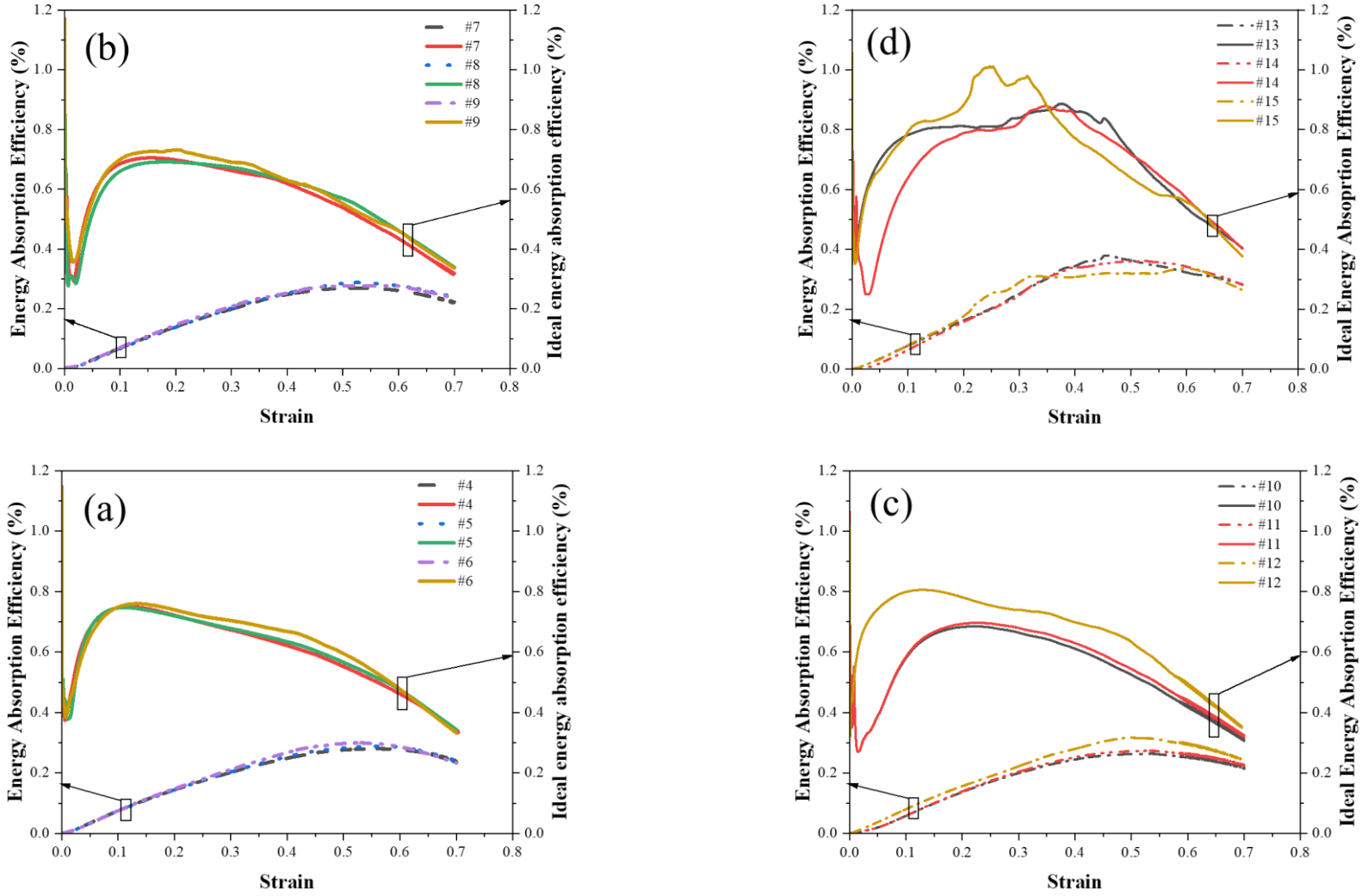

Figure 8.9: Energy absorption efficiency and ideal energy absorption efficiency of (a) alumina hollow sphere - 0.6 mm diameter spheres, (b) alumina hollow sphere - 1.7 mm diameter spheres, (c) & (d) hybrid combinations

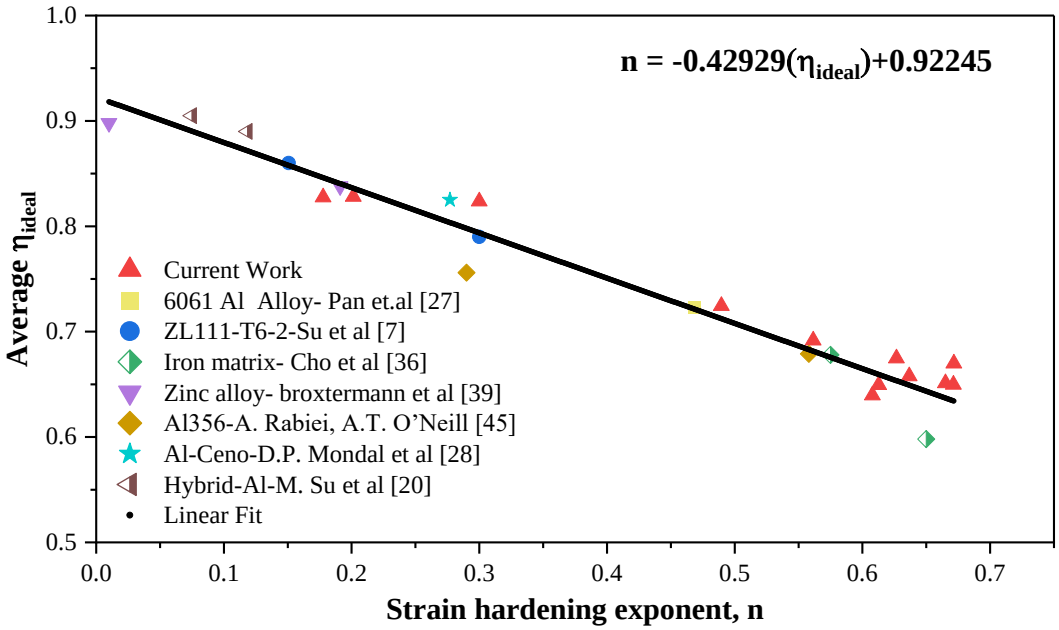

Figure 8.10: Strain hardening coefficient vs. energy absorption efficiency

Figure 8.10 shows a correlation between the slope of the plateau region of all the syntactic foams plotted against the average ideal absorption efficiency. The average ideal absorption efficiency for the plateau region is shown in **Figure 8.9**. Different slope data extracted from the literature are also plotted to predict the relation between the n and η_{ideal} [55,61,108,41,143,75,48]. All the data points follow a linear relation with a -0.42929 slope. This comparison provides the direct relation between the slope of plateau stress affected by different factors such as sphere diameter and volume fraction proposed in some of the earlier works [61,108] and energy absorption efficiency, which is the average value of the slope from the equation. It is also worth noticing that this relation is valid for hybrid syntactic foam studies in the current work and elsewhere [48].

8.4.2 Deformation mechanisms

The macroscopic deformation mechanism is observed using video recordings for the entire test. The macro photographs are captured before and after each compression test conducted for all the samples. The deformation pattern for cenosphere, alumina hollow sphere, and hybrid reinforced composites is presented in **Figures 8.11 (a) & (b)** at various strains. Unlike reported elsewhere, no significant oscillations are observed in all samples' stress-strain curves except for cenosphere-reinforced composites [61,142]. This steady failure behavior infers that the choice of particle size and synthesis technique can play a significant role in the deformation behavior of SFs. Some samples (#6, #10, & #13) exhibit a density gradient across the samples' length during deformation. Also, the samples exhibit near rigid behavior with minimum noticeable deformation up to 30 % of strain. This effect is prominently reflected in the syntactic foams' stress-strain behavior and EAEs'. Further, during densification, crack initiation and propagation are evident.

The cenospheres reinforced syntactic foams have failed before reaching the densification stage. The inflow strain is limited in these samples exhibiting minor plastic deformation immediately after the elastic region. This also suggests that particle strength contributes to the resistance offered against deformation. The alumina-based foams exhibit crack initiation during deformations' plateau region (35 % strain). This behavior confirms that the initial load is distributed among the ductile matrix and brittle particles up to the yield point. The possible reason for the surface cracks could be the poor surface of syntactic foams. During sample preparation, the absence of hollow spheres leaves dents that act as a source to stress concentration during deformation. Also, the brittle nature of alumina spheres may hardly contribute toward

plastic flow leading to the fracture of spheres and crack propagation when the local stress exceeds the crushing strength of the alumina.

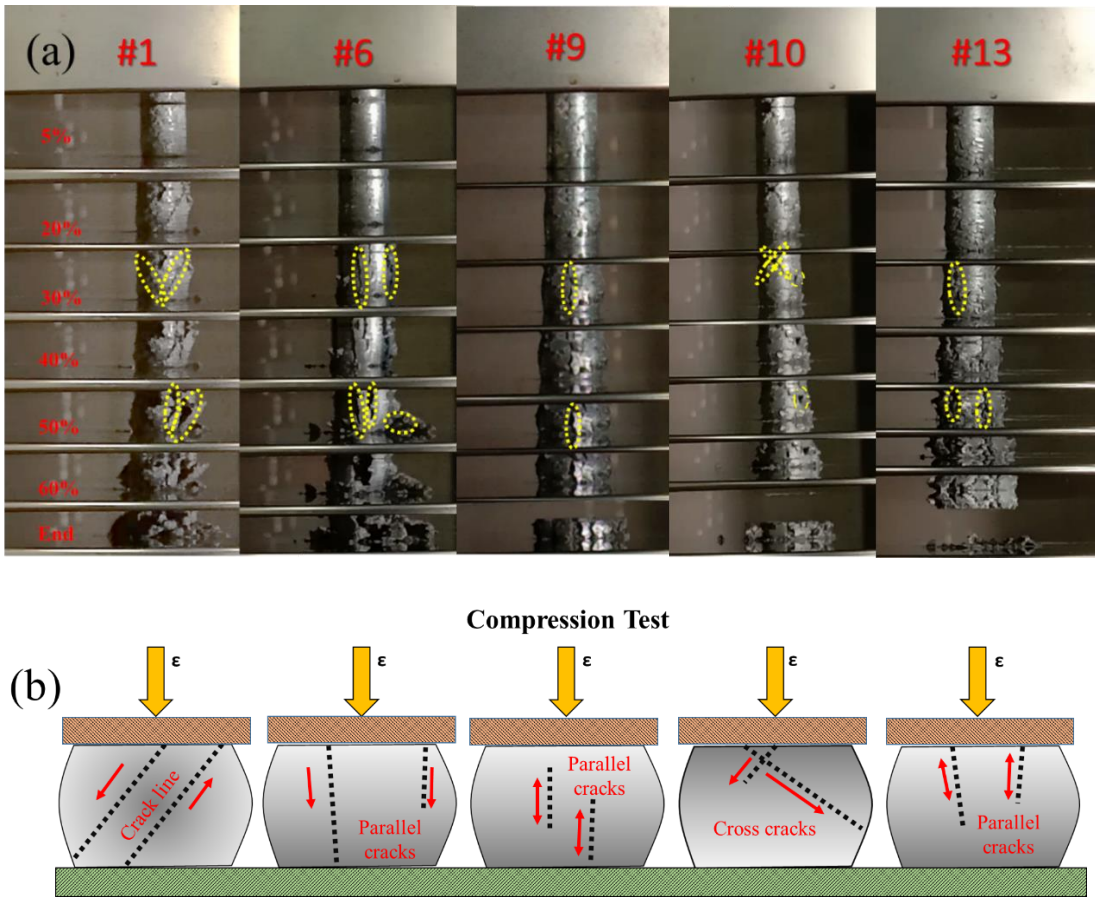

Figure 8.11: Deformation mechanism under compression (a) Macro fracture photographs collate (b) Failure patterns for the respective materials.

The combination of ductile matrix and soft reinforcement foams exhibits insufficient structural strength while testing. The cracks are evident even at lower strains (below 20 % strain) in cenosphere-based foams, thus leading to structural failure in pure shear failure before densification. The shear line formed on the surface of the sample is nearly 45°. A good agreement with the current study was reported by Al-Sahlani et al.[144]. In alumina-based foams, the initial surface cracks appeared parallel to the loading direction. Further, the gaps are apparent after crossing the elastic

region, as shown in **Figure 8.11(b)**. Later, a structural failure occurred with very minimum structure intact of the sample at the end of the test. Bulging and cracking occurred during this process, especially in the 30 % volume fraction for #6 and #9 conditions. Some previous studies have shown a similar failure of the structure and multiple wide cracks during the loading for higher volume fractions [23,48,61,144]. This behavior suggests that selecting higher volume fractions may enhance a few properties but can lead to catastrophic failure during the plastic deformation before it attains densification (>40 % strain).

As shown in **Figure 8.11(a)**, the deformation degree of hybrid composites is not very severe compared to the single-sphere samples. An evident recovery in the failure behavior can be observed compared to samples #6 and #9. The samples are deformed layer-by-layer in cenosphere and alumina-based foams. Whereas in the hybrid composites, more plastic flow is observed in the form of bulging. The cross shape cracks that appear initially during the deformation in sample #10 are closed at higher strains due to compressive forces, which are left with no crack later. Unlike single-sphere samples, the deformation pattern was altered due to the presence of cenospheres. The material has completely deformed with minimal surface cracks initiated during the plastic deformation. Based on the earlier discussions in section 3.2, the alumina-based samples have shown strain-hardening behavior at a lower volume fraction of the spheres. In contrast, the hybrid systems' overall energy absorption efficiency seems high (75%) from **Figure 8.9 (c & d)**, which matches the deformation pattern observed in **Figure 8.11**. The crack initiation and propagation are predominantly affected due to the presence of the secondary spheres.

8.5 HIGH STRAIN RATE

The stress-strain response follows the linear elastic, plateau, and densification regions shown in **Figure 8.12(a)**. The band region of each curve shows the deviation in the stress-strain response obtained through the repetition of each test. The strength of the foam (σ_y-0.02 strain) decreases with an increase in the V_f of the cenospheres to Al-Al_2O_3 SFs. The measured material properties are shown in **Table 8.3**. This behavior is attributed to an additional hollow particle in the matrix. Later, a gradual rise in the stress value without stress drop is observed concerning the strain. A strain-hardening behavior is observed in sample #1 due to the presence of hard alumina particles. However, the slope of the plateau region decreases with the addition of secondary particles. **Figure 8.12(a)** shows the ideal energy absorption efficiency (EAE) for the samples obtained.

Table 8. 3: Properties of SF and MPSFs

Sample ID	#6	#12	#15
EAE (%)	64.09	71.31	78.63
Energy absorption (MJ/m^3)	68.74	55.75	54.13
Log-log Slope of the plateau region	0.59	0.46	0.18
Plateau stress (MPa)	198.56	127.28	95.85
Elastic modulus (GPa)	4.2	2.25	2.05
Density (g/cm^3)	2.2354	2.1861	2.1091

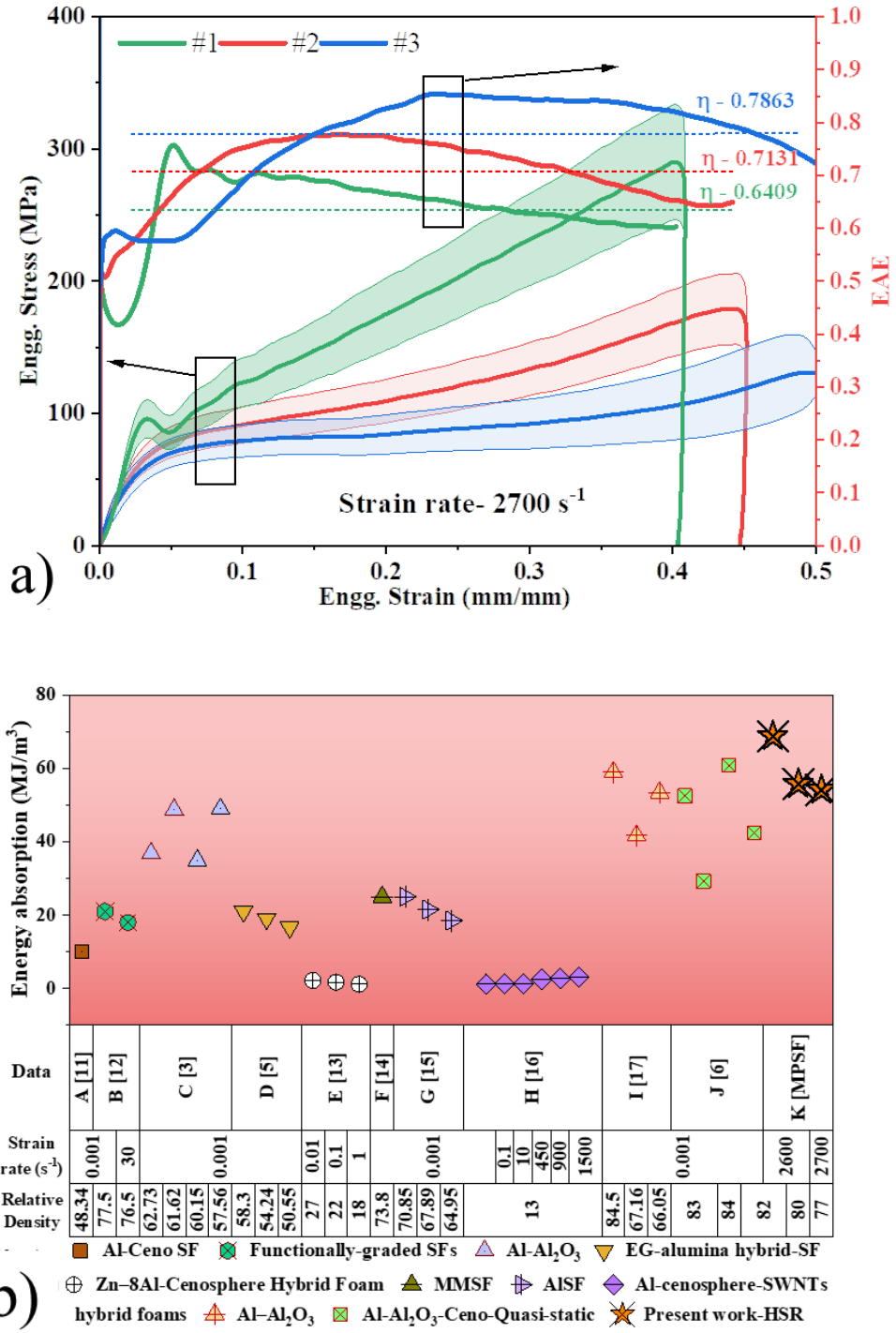

Figure 8.12: (a) Stress-strain plot and EAE of the Al_2O_3 and MPSFs at HSR, (b) Energy absorption properties of present work (K) compared against literature data tested at different RD and strain rates. (A- [145], B- [88], C- [55], D- [48], E- [146], F- [144], G- [61], H- [147], I- [35], J- [148]).

Figure 8.12(b) shows the energy absorption data against the literature, including the alumina-based, hybrid, and functionally graded SFs. It is evident from **Table 8.3** and **Figure 8.12** that the energy absorption properties of MPSFs are significantly high at HSRs compared to other foam materials. This implies that MPSF foams exhibit high strength and can withstand dynamic loading. Also, the influence of the RD and the strain rate on energy absorption is presented. In the present work, the density and the energy absorption of the MPSFs were decreased due to cenosphere addition and EAE increases.

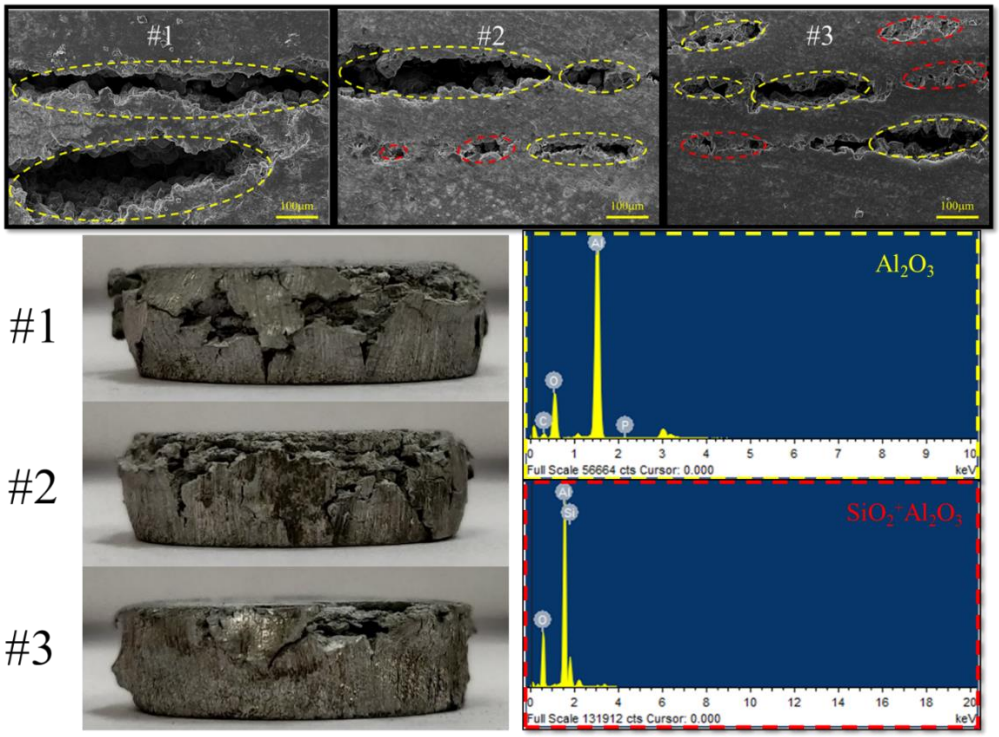

Figure 8.13: Fracture behavior, cross-sectional SEM micrographs, and EDX spectrum of MPSFs after deformation

The mechanical response of the MPSFs may not be sufficient to understand the influence of the secondary particle on the overall performance at HSRs. The tested samples are further systemically investigated. **Figure 8.13** shows the digital images of the samples and the cross-sectional SEM images of samples #6, #12, and #15, and the

corresponding EDX spectrum is shown as per the color code. The cracks initiated from the loading direction and propagated to the other face. The outer surface of the samples has shown a significant amount of damage control. Also, a residual amount of Al_2O_3 particles (sample #1) are present in the fractured region after the impact. The cenospheres were crushed utterly (Sample #12 and #15), contributing to the drop in the slope of the plateau region, elastic modulus, and energy absorption. This phenomenon significantly contributes to the high EAE (in samples #12 and #15).

8.6 SUMMARY

The synthesis, quasi-static, high strain rate compressive, and energy absorption behavior of Al_2O_3-Cenosphere-based MPSFs are presented. The presence of cenospheres has enhanced the overall energy absorption in contrast to the quasi-static and dynamic properties of different SF materials. The volume ratio of cenospheres has affected the slope of the plateau region, which contributes to the EAE. The fractured surface and the cross-sectional images confirm the role of the cenospheres in damage control. During high-velocity impact, this phenomenon makes them suitable for several structural applications. The next chapter presents the conclusions drawn based on studies conducted, results obtained, and discussions presented above on AMSFs and Hybrid syntactic foams.

Chapter 9: Conclusions and Future Scope

9.1 SUMMARY

The current work has effectively presented the synthesis and characterization of aluminum matrix syntactic foams and hybrid syntactic foams. The experimental and theoretical calculations are presented that show the excellent performance of the AMSFs. The quasi-static compression and the effect of temperature are studied for three different volume fractions of syntactic foams. The high strain rates studies showed the strain rate dependence at high strain rate testings. The energy absorption efficiency and densification strain at various temperatures are studied with varying particle sizes. The electrochemical studies using PDP and EIS on the AMSFs of different particle size was studied to understand the electrochemical response under various solutions (acidic, base, and neutral). Also, novel hybrid syntactic foams were produced using the powder metallurgy route to achieve enhanced properties with reduced densities. The microstructure, density, and mechanical studies have shown better results in contrast to the conventional syntactic foams. The following are the conclusions drawn from the proposed work on metal matrix syntactic foams produced using aluminum matrix and ceramic hollow particles. Chapter 1 provides a detailed introduction to the current research work, and Chapter 2 provides the literature survey conducted to execute the work.

9.2 CONCLUSIONS

Chapter 3 The AMSFs are produced using the powder metallurgy route successfully. A series of samples with different densities are produced by altering the particle's size and volume fraction. The relative density of these samples has shown minimum deviation from the theoretically measured values.

Chapter 4 In this chapter, the microstructure, density, and mechanical properties of the AMSFs are studied in detail. This chapter provides a basic understanding of the material properties studied in this work.

- The Microstructure of the AMSFs studied using the freeze-fracture method suggests that the matrix holds the hollow particles firmly, and the distribution is uniform.

- The theoretical and experimental densities have a close match. This suggests that the matrix is free from undesired porosity.

- The stress-strain response of different samples has shown a dependence on the size and volume fraction of the particle.

- A series of mechanical studies are performed at different strain rates. The AMSF shown a positive shift in the stress values with respect to the strain rate and a maximum strain range of 40-45% is obtained at 2700 s^{-1}.

Chapter 5 The energy absorption properties are discussed in this chapter. The following are the exciting observations drawn in this chapter.

- The sample tested at elevated temperatures showed a drop in yield stress values at a lower relative density of the AMSFs. A maximum value of 78.88 MPa is obtaind at 0.92 relative density tested at 250 ºC.

- The AMSF of relative density 0.86 has shown maximum energy absorption efficiency of 75.77 % tested at 250 ºC. The rise in the stress8 values of the stress-strain curve in the elastic region has contributed to retaining the maximum amount of energy even at high temperatures.

- The densification strain and energy absorption efficiency increases with decrease in relative density of AMSFs. This phenomenon is similar for different particle sizes.

- The deformation behavior of the samples broadly follows two modes of failure. It is observed that this behavior is proportional to the temperature at which the samples were tested.

- A significant deviation is observed in the hardening behavior of the AMSFs with different densities. Also, samples tested up to 1800 s^{-1}, shown no significant effect on hardening nature of the samples.

- There is no significant drop in the energy absorption properties of the AMSFs at high strain rates. The energy absorption efficiency of AMSFs has shown a maximum value of 72.34 % and 78.92 % for low and high strain rates, respectively.

- The fracture studies suggest a random crack growth during quasi-static deformation. During dynamic loading, the matrix interface suffers premature densification, contributing to the hardening AMSFs.

Chapter 6 The alumina hollow particles reinforced AMSF were produced and studied under quasi-static compression. Analytical and RVE models are used to evaluate the elastic constants of AMSF at different volume fractions. The RVE models are generated using the actual size of the particles used for experimental works. The RVE model and a few analytical models studied within the elastic limit failed to capture properties close to the experimental results. It is observed that the FE-based RVE results closely match the Mori-Tanaka and Differential self-consistent models

across the different volume fractions. The difference in the elastic moduli can be attributed to the manufacturing technique, micro-cracks, and the bond interface between the particles and matrix.

- The derivatives of the normalized elastic modulus data (sensitivity coefficients) show a significant deviation in models such as Rule of the Mixture, Halpin-Tsai, and Hashin-Shtrikman. However, there is a close agreement with Mori-Tanaka and Differential self-consistent models concerning the data from RVE models.

- In the experimental results, the peak strength of the SFs has shown a maximum of 350MPa at 60% strain. The stress-strain response of the RVE-based models matches the experimental results.

- The FE-model over-estimation the stress-strain response for 10% and 20% volume fractions. These models can be suitable for designing the materials for different matrix and reinforcement systems.

- The model accuracy may be improved by considering the cohesive region between the matrix and reinforcement. Also, these models may be tested for defects induced due to the selection of processing techniques, such as internal pores and defects, to capture the experimental data.

Chapter 7 Potentiodynamic polarization and impedance tests were performed on the Novel Al/ Al_2O_3 syntactic foam samples tested in various molar concentrations of acidic, neutral, and alkaline media. The corrosion rates of the Mg metal are as follows: acidic> neutral> alkaline solution.

- High degradation rates and more pits and cracks were noted in an acidic environment as the Cl- ion concentration increased from 0.01M to 1M. Furthermore, higher metal dissolution was found at 1M HCl concentration.

- All three Al/Al_2O_3 syntactic foam samples exhibited better corrosion resistance in all the solutions. #1 showed excellent corrosion resistance due to the high agglomeration percentage of the hallow particle distribution.

- High corrosion rates were observed in #3 syntactic foams in all molar concentrations of acidic, neutral, and alkaline media.

- Little degradation was observed in an alkaline media at pH 8 to pH 12. This is due to the Al_2O_3 passive layer, which reacts with the OH- ions in the alkaline media and forms $Al(OH)_3$.

Chapter 8 The conventional powder metallurgy route is a simple method for producing AMSFs using single and multi-sphere reinforcements. The hybrid syntactic foams prepared using cenosphere and alumina hollow sphere for a maximum 30% volume fraction are investigated.

- The freeze-fracture method confirms the particle distribution across the matrix, and the mechanical properties of all the samples are studied to understand the deformation behavior of the samples under compression loading.

- There is no significant impact of volume fraction and sphere size on the yield strength of the AMSFs. However, the peak stress values differ with respect to particle size and volume fraction of hollow spheres.

- The energy absorption and specific energy absorption of cenosphere, alumina hollow sphere reinforced syntactic foams can reduce with respect to the increase in the volume fraction of hollow spheres.

- The ideal energy absorption efficiency data obtained in the current study correlates with the literature data. A negative slope of -0.42929 is obtained for change in the slope of the stress-strain curve at the plateau region.

- The transverse strain increased in hybrid composites, which reduced the wide cracks observed during the deformation of single-sphere composites. The failure mode of different syntactic foams produced under axial compression load depends on reinforcements' types and volume fraction.

- Combining multiple hollow spheres at higher volume fractions can reduce the early rupture and damage observed in the single-sphere syntactic foams. The presence of cenospheres has enhanced the overall energy absorption in contrast to the quasi-static and dynamic properties of different SF materials.

- The volume ratio of cenospheres has affected the slope of the plateau region, which contributes to the EAE. The fractured surface and the cross-sectional images confirm the role of the cenospheres in damage control. During high-velocity impact, this phenomenon makes them suitable for several structural applications.

9.3 FUTURE SCOPE OF THIS WORK

The current work has effectively presented aluminum matrix syntactic foams and novel hybrid syntactic foams using the powder metallurgy route. The experimental studies have shown the excellent performance of the AMSFs and have a scope to fit different industrial applications where density is a crucial challenge. In order to scale up the process industrially, more studies with large volumes need to be studied further. In this regard, the following can be considered:

- The possibilities of scaling up the powder metallurgy route must be further explored for achieving a commercial product using AMSFs.

- Applying this powder metallurgy technique with different commercially available materials, such as Magnesium, Steel, Titanium, and others, would ease the manufacturing on a commercial scale. Studies in this direction would bridge the gap between the current research and manufacturing in the industry.

- Most of the studies in the literature and this work focus on ceramic-based hollow particles. There is scope to develop metal-based hollow particles with available advanced manufacturing techniques.

- The mechanical properties and deformation response of the AMSFs are conducted, facilitating the energy absorption properties. In addition, AMSFs show enhanced properties, stiffness, and stability during dynamic loadings, making them suitable for various applications in fields such as automotive, aerospace, and defensive engineering. However, this work has been limited to different strain rates at room temperatures. For future studies, the dynamic nature of the AMSFs at different temperatures and their energy absorption

properties need to understand. These studies are promising to explore the material response under different environmental conditions.

- Now that the FE-based computational material is established, the interface between the matrix and hollow particles may be the future interest of the researchers to understand the debonding and crack phenomenon of the hollow particle.

- The development of hybrid syntactic foams is an exciting field of research that can help reduce the overall weight of the material with enhanced strength. Introducing the novel components into the conventional syntactic foams may achieve this challenge.

References

[1] Afolabi LO, Ariff ZM, Hashim SFS, Alomayri T, Mahzan S, Kamarudin K-A, et al. Syntactic foams formulations, production techniques, and industry applications: a review. Journal of Materials Research and Technology 2020;9:10698–718. https://doi.org/10.1016/j.jmrt.2020.07.074.

[2] Anirudh S, Jayalakshmi CG, Anand A, Kandasubramanian B, Ismail SO. Epoxy/hollow glass microsphere syntactic foams for structural and functional application-A review. European Polymer Journal 2022;171:111163. https://doi.org/10.1016/j.eurpolymj.2022.111163.

[3] Yang M, Li J, Man Y, Peng Z, Zhang X, Luo X. A novel hollow alumina sphere-based ceramic bonded by in situ mullite whisker framework. Materials & Design 2020;186:108334. https://doi.org/10.1016/j.matdes.2019.108334.

[4] G. Papageorgiou D, Li Z, Liu M, A. Kinloch I, J. Young R. Mechanisms of mechanical reinforcement by graphene and carbon nanotubes in polymer nanocomposites. Nanoscale 2020;12:2228–67. https://doi.org/10.1039/C9NR06952F.

[5] (Rusty) Gray GT. High-Strain-Rate Deformation: Mechanical Behavior and Deformation Substructures Induced. Annual Review of Materials Research 2012;42:285–303. https://doi.org/10.1146/annurev-matsci-070511-155034.

[6] Marx J, Rabiei A. Study on the Microstructure and Compression of Composite Metal Foam Core Sandwich Panels. Metall Mater Trans A 2020;51:5187–97. https://doi.org/10.1007/s11661-020-05964-1.

[7] Cheng Y, Li Y, Chen X, Zhou X, Wang N. Compressive Properties and Energy Absorption of Aluminum Foams with a Wide Range of Relative Densities. Journal of Materials Engineering and Performance 2018;27:4016–24. https://doi.org/10.1007/s11665-018-3514-4.

[8] Bargmann S, Klusemann B, Markmann J, Schnabel JE, Schneider K, Soyarslan C, et al. Generation of 3D representative volume elements for heterogeneous

materials: A review. Progress in Materials Science 2018;96:322–84. https://doi.org/10.1016/j.pmatsci.2018.02.003.

[9] Li T, Grignon F, Benson DJ, Vecchio KS, Olevsky EA, Jiang F, et al. Modeling the elastic properties and damage evolution in Ti–Al3Ti metal–intermetallic laminate (MIL) composites. Materials Science and Engineering: A 2004;374:10–26. https://doi.org/10.1016/j.msea.2003.09.074.

[10] Matli PR, Shakoor RA, Mohamed AMA, Matli PR, Shakoor RA, Mohamed AMA. Development of Metal Matrix Composites Using Microwave Sintering Technique. IntechOpen; 2017. https://doi.org/10.5772/68081.

[11] Banhart J. Manufacture, characterisation and application of cellular metals and metal foams. Progress in Materials Science 2001;46:559–632. https://doi.org/10.1016/S0079-6425(00)00002-5.

[12] Kennedy A, Kennedy A. Porous Metals and Metal Foams Made from Powders. IntechOpen; 2012. https://doi.org/10.5772/33060.

[13] Bertoldi, Overvelde, Katia. Rational design of reconfigurable prismatic architected materials. APS March Meeting, vol. 2017, 2017, p. H18--011.

[14] Landrock AH. Handbook of Plastic Foams: Types, Properties, Manufacture and Applications. Elsevier; 1995.

[15] Bárczy T, Kaptay G. Modeling the Infiltration of Liquid Metals Into Porous Ceramics. Materials Science Forum 2005. https://doi.org/10.4028/www.scientific.net/MSF.473-474.297.

[16] Braszczyńska-Malik KN, Kamieniak J. AZ91 magnesium matrix foam composites with fly ash cenospheres fabricated by negative pressure infiltration technique. Materials Characterization 2017;128:209–16. https://doi.org/10.1016/j.matchar.2017.04.005.

[17] Fröhlich A, Sack R, Mott NF. Theory of the rheological properties of dispersions. Proceedings of the Royal Society of London Series A Mathematical

and Physical Sciences 1946;185:415–30. https://doi.org/10.1098/rspa.1946.0028.

[18] Neville BP, Rabiei A. Composite metal foams processed through powder metallurgy. Materials & Design 2008;29:388–96. https://doi.org/10.1016/j.matdes.2007.01.026.

[19] Bolat Ç, Bilge G, Gökşenli A. An Investigation on the Effect of Heat Treatment on the Compression Behavior of Aluminum Matrix Syntactic Foam Fabricated by Sandwich Infiltration Casting. Mat Res 2021;24. https://doi.org/10.1590/1980-5373-MR-2020-0381.

[20] Xiao Y, Yin J, Zhang X, An X, Xiong Y, Sun Y. Mechanical performance and cushioning energy absorption characteristics of rigid polyurethane foam at low and high strain rates. Polymer Testing 2022;109:107531. https://doi.org/10.1016/j.polymertesting.2022.107531.

[21] Gupta N, Rohatgi PK. Metal Matrix Syntactic Foams: Processing, Microstructure, Properties and Applications. DEStech Publications, Inc; 2014.

[22] Bálint A, Szlancsik A. Mechanical Properties of Iron Hollow Sphere Reinforced Metal Matrix Syntactic Foams. Materials Science Forum 2015;812:3–8. https://doi.org/10.4028/www.scientific.net/MSF.812.3.

[23] Birla S, Mondal DP, Das S, Prasanth N, Jha AK, Venkat ANCh. Compressive Deformation Behavior of Highly Porous AA2014-Cenosphere Closed Cell Hybrid Foam Prepared Using CaH2 as Foaming Agent: Comparison with Aluminum Foam and Syntactic Foam. Trans Indian Inst Met 2017;70:1827–40. https://doi.org/10.1007/s12666-016-0984-7.

[24] Cheneler D, Kennedy AR. A comparison of the manufacture and mechanical performance of porous aluminium and aluminium syntactic foams made by vacuum-assisted casting. Materials Science and Engineering: A 2020;789:139528. https://doi.org/10.1016/j.msea.2020.139528.

[25] Meng J, Liu T-W, Wang H-Y, Dai L-H. Ultra-high energy absorption high-entropy alloy syntactic foam. Composites Part B: Engineering 2021;207:108563. https://doi.org/10.1016/j.compositesb.2020.108563.

[26] Pulagara NV, Saini S, Dondapati RS. A Study of Manufacturing and Mechanical Properties of Mg-foam Using Dolomite as the Blowing Agent: A Review. Progress in Nanotechnology and Nanomaterials n.d.;4:7–10.

[27] Kaya AC, Zaslansky P, Ipekoglu M, Fleck C. Strain hardening reduces energy absorption efficiency of austenitic stainless steel foams while porosity does not. Materials & Design 2018;143:297–308. https://doi.org/10.1016/j.matdes.2018.02.009.

[28] Gupta N, Nagorny R. Tensile properties of glass microballoon-epoxy resin syntactic foams. Journal of Applied Polymer Science 2006;102:1254–61.

[29] Gupta N, Pinisetty D, Shunmugasamy VC. Reinforced Polymer Matrix Syntactic Foams: Effect of Nano and Micro-Scale Reinforcement. Springer International Publishing; 2013.

[30] Shams A, Panteghini A, Bardella L, Porfiri M. A micromechanical model to study failure of polymer-glass syntactic foams at high strain rates. Computational Materials Science 2017;135:189–204. https://doi.org/10.1016/j.commatsci.2017.04.007.

[31] Kubelka P, Kádár C, Jost N. Effect of the interface on the compressive properties of magnesium syntactic foams. Materials Letters 2021;287:129293. https://doi.org/10.1016/j.matlet.2020.129293.

[32] Yang Q, Yu B, Hu H, Hu G, Miao Z, Wei Y, et al. Melt flow and solidification during infiltration in making steel matrix syntactic foams. Materials Science and Technology 2019;35:1831–9. https://doi.org/10.1080/02670836.2019.1650444.

[33] Mondal DP, Datta Majumder J, Jha N, Badkul A, Das S, Patel A, et al. Titanium-cenosphere syntactic foam made through powder metallurgy route. Materials & Design 2012;34:82–9. https://doi.org/10.1016/j.matdes.2011.07.055.

[34] Orbulov IN. Compressive properties of aluminium matrix syntactic foams. Materials Science and Engineering: A 2012;555:52–6. https://doi.org/10.1016/j.msea.2012.06.032.

[35] Santa Maria JA, Schultz BF, Ferguson JB, Rohatgi PK. Al–Al2O3 syntactic foams – Part I: Effect of matrix strength and hollow sphere size on the quasi-static properties of Al-A206/Al2O3 syntactic foams. Materials Science and Engineering: A 2013;582:415–22. https://doi.org/10.1016/j.msea.2013.05.081.

[36] Ferguson JB, Santa Maria JA, Schultz BF, Rohatgi PK. Al–Al2O3 syntactic foams—Part II: Predicting mechanical properties of metal matrix syntactic foams reinforced with ceramic spheres. Materials Science and Engineering: A 2013;582:423–32. https://doi.org/10.1016/j.msea.2013.06.065.

[37] Rugele K, Lehmhus D, Hussainova I, Peculevica J, Lisnanskis M, Shishkin A. Effect of Fly-Ash Cenospheres on Properties of Clay-Ceramic Syntactic Foams. Materials 2017;10:828. https://doi.org/10.3390/ma10070828.

[38] Porfiri M, Gupta N. Effect of volume fraction and wall thickness on the elastic properties of hollow particle filled composites. Composites Part B: Engineering 2009;40:166–73. https://doi.org/10.1016/j.compositesb.2008.09.002.

[39] Jayavardhan ML, Bharath Kumar BR, Doddamani M, Singh AK, Zeltmann SE, Gupta N. Development of glass microballoon/HDPE syntactic foams by compression molding. Composites Part B: Engineering 2017;130:119–31. https://doi.org/10.1016/j.compositesb.2017.07.037.

[40] Szlancsik A, Katona B, Dombóvári Z, Orbulov IN. On the effective Young's modulus of metal matrix syntactic foams. Materials Science and Technology 2017;33:2283–9. https://doi.org/10.1080/02670836.2017.1374497.

[41] Broxtermann S, Vesenjak M, Krstulović-Opara L, Fiedler T. Quasi static and dynamic compression of zinc syntactic foams. Journal of Alloys and Compounds 2018;768:962–9. https://doi.org/10.1016/j.jallcom.2018.07.215.

[42] Kemény A, Leveles B, Károly D. Functional aluminium matrix syntactic foams filled with lightweight expanded clay aggregate particles. Materials Today: Proceedings 2021. https://doi.org/Effect of the interface.

[43] Linul E, Lell D, Movahedi N, Codrean C, Fiedler T. Compressive properties of zinc syntactic foams at elevated temperatures. Composites Part B: Engineering 2019;167:122–34. https://doi.org/10.1016/j.compositesb.2018.12.019.

[44] Gupta N, Kishore, Woldesenbet E, Sankaran S. Studies on compressive failure features in syntactic foam material. Journal of Materials Science 2001;36:4485–91. https://doi.org/10.1023/A:1017986820603.

[45] Zou LC, Zhang Q, Su H, Sun DL, Wu GH, Jiang LT. Compression deformation behaviour of aluminium matrix syntactic foams under quasistatic loading: in situ SEM compressive tests. Materials Research Innovations 2014;18:S4-536-S4-539. https://doi.org/10.1179/1432891714Z.000000000838.

[46] Taherishargh M, Belova IV, Murch GE, Fiedler T. On the mechanical properties of heat-treated expanded perlite–aluminium syntactic foam. Materials & Design 2014;63:375–83. https://doi.org/10.1016/j.matdes.2014.06.019.

[47] Ivañez I, Fernandez-Cañadas LM, Sanchez-Saez S. Compressive deformation and energy-absorption capability of aluminium honeycomb core. Composite Structures 2017;174:123–33. https://doi.org/10.1016/j.compstruct.2017.04.056.

[48] Su M, Wang H, Hao H, Fiedler T. Compressive properties of expanded glass and alumina hollow spheres hybrid reinforced aluminum matrix syntactic foams. Journal of Alloys and Compounds 2020;821:153233. https://doi.org/10.1016/j.jallcom.2019.153233.

[49] Wang L, Zhang B, Zhang J, Jiang Y, Wang W, Wu G. Deformation and energy absorption properties of cenosphere-aluminum syntactic foam-filled tubes under axial compression. Thin-Walled Structures 2021;160:107364. https://doi.org/10.1016/j.tws.2020.107364.

[50] Szlancsik A, Katona B, Bobor K, Májlinger K, Orbulov IN. Compressive behaviour of aluminium matrix syntactic foams reinforced by iron hollow

spheres. Materials & Design 2015;83:230–7. https://doi.org/10.1016/j.matdes.2015.06.011.

[51] Al-Sahlani K, Broxtermann S, Lell D, Fiedler T. Effects of particle size on the microstructure and mechanical properties of expanded glass-metal syntactic foams. Materials Science and Engineering: A 2018;728:80–7. https://doi.org/10.1016/j.msea.2018.04.103.

[52] Licitra L, Luong DD, Strbik OM, Gupta N. Dynamic properties of alumina hollow particle filled aluminum alloy A356 matrix syntactic foams. Materials & Design 2015;66:504–15. https://doi.org/10.1016/j.matdes.2014.03.041.

[53] Castro G, Nutt SR. Synthesis of syntactic steel foam using gravity-fed infiltration. Materials Science and Engineering: A 2012;553:89–95. https://doi.org/10.1016/j.msea.2012.05.097.

[54] Orbulov IN, Dobránszky J. Producing metal matrix syntactic foams by pressure infiltration. Periodica Polytechnica Engineering Mechanical Engineering 2008;52:35.

[55] Pan L, Rao D, Yang Y, Qiu J, Sun J, Gupta N, et al. Gravity casting of aluminum-Al2O3 hollow sphere syntactic foams for improved compressive properties. J Porous Mater 2020;27:1127–37. https://doi.org/10.1007/s10934-020-00889-x.

[56] Newsome DB, Schultz BF, Ferguson JB, Rohatgi PK. Synthesis and Quasi-Static Compressive Properties of Mg-AZ91D-Al2O3 Syntactic Foams. Materials 2015;8:6085–95. https://doi.org/10.3390/ma8095292.

[57] Baumeister E, Klaeger S. Advanced New Lightweight Materials: Hollow-Sphere Composites (HSCs) for Mechanical Engineering Applications. Advanced Engineering Materials 2003;5:673–7. https://doi.org/10.1002/adem.200320137.

[58] Zou HR, Yin WL, Cai CC, Yang Z, Li YB, He XD. Numerical Investigation on the Necessity of a Constant Strain Rate Condition According to Material's

Dynamic Response Behavior in the SHPB Test. Exp Mech 2019;59:427–37. https://doi.org/10.1007/s11340-018-00468-x.

[59] Movahedi N, Taherishargh M, Belova IV, Murch GE, Fiedler T. Mechanical and Microstructural Characterization of an AZ91–Activated Carbon Syntactic Foam. Materials 2019;12:3. https://doi.org/10.3390/ma12010003.

[60] Xie C, Li H, Yuan B, Gao Y, Luo Z, Zhu M. Ti3Sn–NiTi Syntactic Foams with Extremely High Specific Strength and Damping Capacity Fabricated by Pressure Melt Infiltration. ACS Appl Mater Interfaces 2019;11:28043–51. https://doi.org/10.1021/acsami.9b08145.

[61] Su M, Wang H, Hao H. Compressive Properties of Aluminum Matrix Syntactic Foams Prepared by Stir Casting Method. Advanced Engineering Materials 2019;21:1900183. https://doi.org/10.1002/adem.201900183.

[62] Daoud A. Synthesis and characterization of novel ZnAl22 syntactic foam composites via casting. Materials Science and Engineering: A 2008;488:281–95. https://doi.org/10.1016/j.msea.2007.11.020.

[63] Orbulov IN, Ginsztler J. Compressive characteristics of metal matrix syntactic foams. Composites Part A: Applied Science and Manufacturing 2012;43:553–61. https://doi.org/10.1016/j.compositesa.2012.01.008.

[64] Weise J, Lehmhus D, Baumeister J, Kun R, Bayoumi M, Busse M. Production and Properties of 316L Stainless Steel Cellular Materials and Syntactic Foams. Steel Research International 2014;85:486–97. https://doi.org/10.1002/srin.201300131.

[65] Movahedi N, Orbulov IN, Kemény A, Belova IV, Murch GE, Fiedler T. Fatigue characterization of functionally graded ZA27 alloy syntactic foams. Materials Science and Engineering: A 2020;798:140255. https://doi.org/10.1016/j.msea.2020.140255.

[66] Vogiatzis CA, Tsouknidas A, Kountouras DT, Skolianos S. Aluminum–ceramic cenospheres syntactic foams produced by powder metallurgy route. Materials & Design 2015;85:444–54. https://doi.org/10.1016/j.matdes.2015.06.154.

[67] Paturi UMR, Narala SKR, Pundir RS. Constitutive flow stress formulation, model validation and FE cutting simulation for AA7075-T6 aluminum alloy. Materials Science and Engineering: A 2014;605:176–85. https://doi.org/10.1016/j.msea.2014.03.033.

[68] Birla S, Mondal DP, Das S, Kashyap DK, Ch VAN. Effect of cenosphere content on the compressive deformation behaviour of aluminum-cenosphere hybrid foam. Materials Science and Engineering: A 2017;685:213–26. https://doi.org/10.1016/j.msea.2016.12.131.

[69] Kader MA, Hazell PJ, Islam MA, Ahmed S, Hossain MM, Escobedo JP, et al. Strain-rate dependency and impact dynamics of closed-cell aluminium foams. Materials Science and Engineering: A 2021;818:141379. https://doi.org/10.1016/j.msea.2021.141379.

[70] Josyula SK, Narala SKR. Study of TiC particle distribution in Al-MMCs using finite element modeling. International Journal of Mechanical Sciences 2018;141:341–58. https://doi.org/10.1016/j.ijmecsci.2018.04.004.

[71] Vogiatzis CA, Skolianos SM. On the sintering mechanisms and microstructure of aluminium–ceramic cenospheres syntactic foams produced by powder metallurgy route. Composites Part A: Applied Science and Manufacturing 2016;82:8–19. https://doi.org/10.1016/j.compositesa.2015.11.037.

[72] Son YG, Lee YC, Jung SS, Kwon HS, Lee W, Park Y. Synthesis and Characterization of Hollow Glass Sphere Containing Aluminum Syntactic Foam by Spark Plasma Sintering and Hot Pressing. Metals 2019;9:1266. https://doi.org/10.3390/met9121266.

[73] Mondal DP, Goel MD, Upadhyay V, Das S, Singh M, Barnwal AK. Comparative Study on Microstructural Characteristics and Compression Deformation Behaviour of Alumina and Cenosphere Reinforced Aluminum Syntactic Foam Made Through Stir Casting Technique. Trans Indian Inst Met 2018;71:567–77. https://doi.org/10.1007/s12666-017-1211-x.

[74] Price RD, Jiang F, Kulin RM, Vecchio KS. Effects of ductile phase volume fraction on the mechanical properties of Ti–Al3Ti metal-intermetallic laminate

(MIL) composites. Materials Science and Engineering: A 2011;528:3134–46. https://doi.org/10.1016/j.msea.2010.12.087.

[75] Mondal DP, Das S, Ramakrishnan N, Uday Bhasker K. Cenosphere filled aluminum syntactic foam made through stir-casting technique. Composites Part A: Applied Science and Manufacturing 2009;40:279–88. https://doi.org/10.1016/j.compositesa.2008.12.006.

[76] Maj J, Basista M, Węglewski W, Bochenek K, Strojny-Nędza A, Naplocha K, et al. Effect of microstructure on mechanical properties and residual stresses in interpenetrating aluminum-alumina composites fabricated by squeeze casting. Materials Science and Engineering: A 2018;715:154–62. https://doi.org/10.1016/j.msea.2017.12.091.

[77] Newsome DB, Schultz BF, Ferguson JB, Rohatgi PK. Synthesis and Quasi-Static Compressive Properties of Mg-AZ91D-Al2O3 Syntactic Foams. Materials 2015;8:6085–95. https://doi.org/10.3390/ma8095292.

[78] Sun Y, Li QM. Dynamic compressive behaviour of cellular materials: A review of phenomenon, mechanism and modelling. International Journal of Impact Engineering 2018;112:74–115. https://doi.org/10.1016/j.ijimpeng.2017.10.006.

[79] Mu Y, Ge Q, Zu G, He Y. New Insight into Predicting the Compression Flow Behavior of Metal Foam. Metall Mater Trans A 2020;51:6132–5. https://doi.org/10.1007/s11661-020-06018-2.

[80] Rajak DK, Kumaraswamidhas LA, Das S. Investigation and characterisation of aluminium alloy foams with TiH2 as a foaming agent. Materials Science and Technology 2016;32:1338–45. https://doi.org/10.1080/02670836.2015.1123846.

[81] Geramipour T, Oveisi H. Effects of foaming parameters on microstructure and compressive properties of aluminum foams produced by powder metallurgy method. Transactions of Nonferrous Metals Society of China 2017;27:1569–79. https://doi.org/10.1016/S1003-6326(17)60178-X.

[82] Mondal DP, Jha N, Badkul A, Das S, Khedle R. High temperature compressive deformation behaviour of aluminum syntactic foam. Materials Science and Engineering: A 2012;534:521–9. https://doi.org/10.1016/j.msea.2011.12.002.

[83] Li Z, Zheng Z, Yu J, Tang L. Effect of temperature on the indentation behavior of closed-cell aluminum foam. Materials Science and Engineering: A 2012;550:222–6. https://doi.org/10.1016/j.msea.2012.04.062.

[84] Yue X-Z, Fukazawa H, Kitazono K. Strain rate sensitivity of open-cell titanium foam at elevated temperature. Materials Science and Engineering: A 2016;673:83–9. https://doi.org/10.1016/j.msea.2016.06.080.

[85] Taherishargh M, Linul E, Broxtermann S, Fiedler T. The mechanical properties of expanded perlite-aluminium syntactic foam at elevated temperatures. Journal of Alloys and Compounds 2018;737:590–6. https://doi.org/10.1016/j.jallcom.2017.12.083.

[86] Balch DK, O'Dwyer JG, Davis GR, Cady CM, Gray GT, Dunand DC. Plasticity and damage in aluminum syntactic foams deformed under dynamic and quasi-static conditions. Materials Science and Engineering: A 2005;391:408–17. https://doi.org/10.1016/j.msea.2004.09.012.

[87] Luong DD, Strbik OM, Hammond VH, Gupta N, Cho K. Development of high performance lightweight aluminum alloy/SiC hollow sphere syntactic foams and compressive characterization at quasi-static and high strain rates. Journal of Alloys and Compounds 2013;550:412–22. https://doi.org/10.1016/j.jallcom.2012.10.171.

[88] Movahedi N, Vesenjak M, Krstulović-Opara L, Belova IV, Murch GE, Fiedler T. Dynamic compression of functionally-graded metal syntactic foams. Composite Structures 2021;261:113308. https://doi.org/10.1016/j.compstruct.2020.113308.

[89] Fischer SF. Energy absorption efficiency of open-cell pure aluminum foams. Materials Letters 2016;184:208–10. https://doi.org/10.1016/j.matlet.2016.08.061.

[90] Gibson LJ, Ashby MF. Cellular Solids: Structure and Properties. 2nd ed. Cambridge: Cambridge University Press; 1997. https://doi.org/10.1017/CBO9781139878326.

[91] Daoud A. Compressive response and energy absorption of foamed A359–Al2O3 particle composites. Journal of Alloys and Compounds 2009;486:597–605. https://doi.org/10.1016/j.jallcom.2009.07.013.

[92] Zhang B, Wang L, Zhang J, Jiang Y, Wang W, Wu G. Deformation and energy absorption properties of cenosphere/aluminum syntactic foam-filled circular tubes under lateral quasi-static compression. International Journal of Mechanical Sciences 2021;192:106126. https://doi.org/10.1016/j.ijmecsci.2020.106126.

[93] Lee KJ, Westmann RA. Elastic Properties of Hollow-Sphere-Reinforced Composites. Journal of Composite Materials 1970;4:242–52. https://doi.org/10.1177/002199837000400209.

[94] Huang JS, Gibson LJ. Elastic moduli of a composite of hollow spheres in a matrix. Journal of the Mechanics and Physics of Solids 1993;41:55–75. https://doi.org/10.1016/0022-5096(93)90063-L.

[95] Bardella L, Sfreddo A, Ventura C, Porfiri M, Gupta N. A critical evaluation of micromechanical models for syntactic foams. Mechanics of Materials 2012;50:53–69. https://doi.org/10.1016/j.mechmat.2012.02.008.

[96] Orbulov IN, Szlancsik A. On the Mechanical Properties of Aluminum Matrix Syntactic Foams. Advanced Engineering Materials 2018;20:1700980. https://doi.org/10.1002/adem.201700980.

[97] Bardella L, Malanca F, Ponzo P, Panteghini A, Porfiri M. A micromechanical model for quasi-brittle compressive failure of glass-microballoons/thermoset-matrix syntactic foams. Journal of the European Ceramic Society 2014;34:2605–16. https://doi.org/10.1016/j.jeurceramsoc.2013.11.045.

[98] Zhang Q, Lee PD, Singh R, Wu G, Lindley TC. Micro-CT characterization of structural features and deformation behavior of fly ash/aluminum syntactic

foam. Acta Materialia 2009;57:3003–11. https://doi.org/10.1016/j.actamat.2009.02.048.

[99] Huang R, Li P, Liu T. X-ray microtomography and finite element modelling of compressive failure mechanism in cenosphere epoxy syntactic foams. Composite Structures 2016;140:157–65. https://doi.org/10.1016/j.compstruct.2015.12.040.

[100] Lorgeril ED, Wyss F, Orbulov IN. Modelling of metal matrix syntactic foams - Description of the compressive stress-strain curves. Periodica Polytechnica Mechanical Engineering 2011;55:29–37. https://doi.org/10.3311/pp.me.2011-1.04.

[101] Orbulov IN, Májlinger K. Description of the compressive response of metal matrix syntactic foams. Materials & Design 2013;49:1–9. https://doi.org/10.1016/j.matdes.2013.02.007.

[102] Mandal DP, Majumdar DD, Bharti RK, Majumdar JD. Microstructural characterisation and property evaluation of titanium cenosphere syntactic foam developed by powder metallurgy route. Powder Metallurgy 2015;58:289–99. https://doi.org/10.1179/1743290115Y.0000000012.

[103] Qureshi W, Kannan S, Vincent S, Eddine NN, Muhammed A, Gupta M, et al. Influence of silica nanospheres on corrosion behavior of magnesium matrix syntactic foam. IOP Conf Ser: Mater Sci Eng 2018;346:012012. https://doi.org/10.1088/1757-899X/346/1/012012.

[104] Vogiatzis CA, Skolianos SM. Electrochemical evaluation of sintered aluminium – ceramic cenospheres composites. Corrosion Engineering, Science and Technology 2017;52:90–8. https://doi.org/10.1080/1478422X.2016.1211862.

[105] Akinwekomi AD. Microstructural characterisation and corrosion behaviour of microwave-sintered magnesium alloy AZ61/fly ash microspheres syntactic foams. Heliyon 2019;5:e01531. https://doi.org/10.1016/j.heliyon.2019.e01531.

[106] Aghion E, Perez Y. Effects of porosity on corrosion resistance of Mg alloy foam produced by powder metallurgy technology. Materials Characterization 2014;96:78–83. https://doi.org/10.1016/j.matchar.2014.07.012.

[107] Sonti KSM, Vincent S, Narala SKR. Effect of single and hybrid hollow sphere reinforcement on the deformation mechanism of aluminum matrix syntactic foam at a low strain rate. Journal of Alloys and Compounds 2022;901:163573. https://doi.org/10.1016/j.jallcom.2021.163573.

[108] Cho YJ, Lee TS, Lee W, Lee YC, Park YH. Preparation and Characterization of Iron Matrix Syntactic Foams with Glass Microspheres via Powder Metallurgy. Met Mater Int 2019;25:794–804. https://doi.org/10.1007/s12540-018-00215-w.

[109] Wang Z, Li P. Characterisation of dynamic behaviour of alumina ceramics: evaluation of stress uniformity. AIP Advances 2015;5:107224. https://doi.org/10.1063/1.4934793.

[110] Marc A. Meyers. Dynamic Behavior of Materials. John Wiley & Sons; 1994.

[111] Li QM, Magkiriadis I, Harrigan JJ. Compressive Strain at the Onset of Densification of Cellular Solids. Journal of Cellular Plastics 2006;42:371–92. https://doi.org/10.1177/0021955X06063519.

[112] Vazquez-Fernandez NI, Soares GC, Smith JL, Seidt JD, Isakov M, Gilat A, et al. Adiabatic Heating of Austenitic Stainless Steels at Different Strain Rates. J Dynamic Behavior Mater 2019;5:221–9. https://doi.org/10.1007/s40870-019-00204-z.

[113] Xia Y, Shi J, Mu Y. Compressive behaviour of open-cell Al–Si alloy foam produced by infiltration casting. Materials Science and Technology 2023;0:1–13. https://doi.org/10.1080/02670836.2023.2202496.

[114] Gvk SS, Tan MJ, Liu Z. Analysis of Strain Rate Sensitivity and Strain Rate Hardening in Co–Cr–Ni–Mo Wires Drawn with Different Drawing Practices. Met Mater Int 2019;25:1047–62. https://doi.org/10.1007/s12540-019-00239-w.

[115] Wang J, Liu A, Ao Q, Wu C, Ma J, Cao P. Energy absorption characteristics and preparation of porous titanium with high porosity. Materials Today Communications 2023;34:105003. https://doi.org/10.1016/j.mtcomm. 2022.105003.

[116] Zhang H, Zhou H, Zhou Z, Zeng H, Zhang X, Yang J, et al. Energy absorption diagram characteristic of metallic self-supporting 3D lattices fabricated by additive manufacturing and design method of energy absorption structure. International Journal of Solids and Structures 2021;226–227:111082. https://doi.org/10.1016/j.ijsolstr.2021.111082.

[117] Raju B, Hiremath SR, Roy Mahapatra D. A review of micromechanics based models for effective elastic properties of reinforced polymer matrix composites. Composite Structures 2018;204:607–19. https://doi.org/10.1016/j.compstruct .2018.07.125.

[118] Marur PR. Numerical estimation of effective elastic moduli of syntactic foams. Finite Elements in Analysis and Design 2010;46:1001–7. https://doi.org/10. 1016/j.finel.2010.07.006.

[119] Nian G, Shan Y, Xu Q, Qu S. Effects of hollow particle shape and distribution on the elastic properties of syntactic foams: 3D computational modeling. Computational Materials Science 2014;95:106–12. https://doi.org/10.1016/ j.commatsci.2014.07.012.

[120] Marur PR. Effective elastic moduli of syntactic foams. Materials Letters 2005;59:1954–7. https://doi.org/10.1016/j.matlet.2005.02.034.

[121] Okereke M, Keates S. Finite Element Applications: A Practical Guide to the FEM Process. Springer; 2018.

[122] Alfonso I, Figueroa IA, Rodriguez-Iglesias V, Patiño-Carachure C, Medina-Flores A, Bejar L, et al. Estimation of elastic moduli of particulate-reinforced composites using finite element and modified Halpin–Tsai models. J Braz Soc Mech Sci Eng 2016;38:1317–24. https://doi.org/10.1007/s40430-015-0429-y.

[123] Cho YJ, Lee W, Park YH. Finite Element Modeling of Tensile Deformation Behaviors of Iron Syntactic Foam with Hollow Glass Microspheres. Materials 2017;10:1201. https://doi.org/10.3390/ma10101201.

[124] Omairey SL, Dunning PD, Sriramula S. Development of an ABAQUS plugin tool for periodic RVE homogenisation. Engineering with Computers 2019;35:567–77. https://doi.org/10.1007/s00366-018-0616-4.

[125] Zhang Z-F, Brunner D, Scheu C, Rühle M. Deformation and fracture mechanisms of Al2O3/Nb/Al2O3 composites under compression. International Journal of Materials Research 2005;96:62–70. https://doi.org/10.3139/ijmr-2005-0009.

[126] Noor AK, Shah RS. Effective thermoelastic and thermal properties of unidirectional fiber-reinforced composites and their sensitivity coefficients. Composite Structures 1993;26:7–23. https://doi.org/10.1016/0263-8223(93)90040-W.

[127] Kamiński M. Sensitivity analysis of homogenized characteristics for some elastic composites. Computer Methods in Applied Mechanics and Engineering 2003;192:1973–2005. https://doi.org/10.1016/S0045-7825(03)00214-7.

[128] Goel MD, Parameswaran V, Mondal DP. High Strain Rate Response of Cenosphere-Filled Aluminum Alloy Syntactic Foam. J of Materi Eng and Perform 2019;28:4731–9. https://doi.org/10.1007/s11665-019-04237-2.

[129] Yu L, Zhang C, Liu Y, Yan Y, Xu P, Jiang Y, et al. Comparing the Corrosion Resistance of 5083 Al and Al2O33D/5083 Al Composite in a Chloride Environment. Materials 2023;16:86. https://doi.org/10.3390/ma16010086.

[130] Singh IB, Mondal DP, Singh M, Bhadkul A, Jha N. Corrosion behaviour of AA2014 aluminium alloy-cenospheres syntactic foam in 3.5% NaCl solution. IJCT Vol21(3) [May 2014] 2014.

[131] Amirjan M, Bozorg M. Properties and corrosion behavior of Al based nanocomposite foams produced by the sintering-dissolution process. Int J Miner Metall Mater 2018;25:94–101. https://doi.org/10.1007/s12613-018-1551-5.

[132] Hamza HM, Deen KM, Haider W. Microstructural examination and corrosion behavior of selective laser melted and conventionally manufactured Ti6Al4V for dental applications. Materials Science and Engineering: C 2020;113:110980. https://doi.org/10.1016/j.msec.2020.110980.

[133] Chen Y, Hong T, Gopal M, Jepson WP. EIS studies of a corrosion inhibitor behavior under multiphase flow conditions. Corrosion Science 2000;42:979–90. https://doi.org/10.1016/S0010-938X(99)00127-4.

[134] Sudha P, Tun KS, Gupta M, Mourad A-HI, Vincent S. Electrochemical characterization of a novel multicomponent Al75Mg5Li10Zn5Cu5 low entropy alloy in different pH environments. Materials and Corrosion 2022;73:2071–83. https://doi.org/10.1002/maco.202213103.

[135] Korchef A, Kahoul A. Corrosion Behavior of Commercial Aluminum Alloy Processed by Equal Channel Angular Pressing. International Journal of Corrosion 2013;2013:e983261. https://doi.org/10.1155/2013/983261.

[136] Zhang Z, Liu F, Han E-H, Xu L. Mechanical and corrosion properties in 3.5% NaCl solution of cold sprayed Al-based coatings. Surface and Coatings Technology 2020;385:125372. https://doi.org/10.1016/j.surfcoat.2020.125372.

[137] Birla S, Mondal DP, Das S, Kulshrestha A, Ahirwar SL, Venkat ANCh, et al. Influence of Cell Anisotropy and Relative Density on Compressive Deformation Responses of LM13-Cenosphere Hybrid Foam. J of Materi Eng and Perform 2019;28:1–11. https://doi.org/10.1007/s11665-018-3731-x.

[138] Sahu S, Ansari MZ, Mondal DP, Cho C. Quasi-static compressive behaviour of aluminium cenosphere syntactic foams. Materials Science and Technology 2019;35:856–64. https://doi.org/10.1080/02670836.2019.1593670.

[139] Basit MM, Cheon SS. Time-dependent crashworthiness of polyurethane foam. Mech Time-Depend Mater 2019;23:207–21. https://doi.org/10.1007/s11043-018-9391-2.

[140] Xia XC, Chen XW, Zhang Z, Chen X, Zhao WM, Liao B, et al. Effects of porosity and pore size on the compressive properties of closed-cell Mg alloy

foam. Journal of Magnesium and Alloys 2013;1:330–5. https://doi.org/10.1016/j.jma.2013.11.006.

[141] Harris JA, McShane GJ. Metallic stacked origami cellular materials: Additive manufacturing, properties, and modelling. International Journal of Solids and Structures 2020;185–186:448–66. https://doi.org/10.1016/j.ijsolstr.2019.09.007.

[142] Liang X, Luo H, Mu Y, Chen M, Ye J, Chi D. Quasi-static and Dynamic Compression of Aluminum Foam at Different Temperatures. J of Materi Eng and Perform 2019;28:4952–63. https://doi.org/10.1007/s11665-019-04207-8.

[143] Rabiei A, O'Neill AT. A study on processing of a composite metal foam via casting. Materials Science and Engineering: A 2005;404:159–64. https://doi.org/10.1016/j.msea.2005.05.089.

[144] Al-Sahlani K, Kisi E, Fiedler T. Impact of particle strength and matrix ductility on the deformation mechanism of metallic syntactic foam. Journal of Alloys and Compounds 2019;786:292–9. https://doi.org/10.1016/j.jallcom.2019.01.283.

[145] Leveles B, Kemény A, Szijártó A. Mechanical investigation of in-situ produced aluminium matrix syntactic foam-filled tubes. Materials Today: Proceedings 2021. https://doi.org/10.1016/j.matpr.2020.12.161.

[146] Mohbe M, Afzal Khan DM, Mondal DP. Microstructural Characterization and Deformation Behavior of Zn–8Al-Cenosphere Hybrid Foam. Trans Indian Inst Met 2019;72:2477–86. https://doi.org/10.1007/s12666-019-01701-4.

[147] Muchhala D, Yadav BN, Pandey A, Chilla V, Md. Shafeeq M, Gupta G, et al. Influences of relative density and strain rate on the mechanical properties of Al-cenosphere-SWNTs hybrid foams. International Journal of Mechanical Sciences 2021;198:106388. https://doi.org/10.1016/j.ijmecsci.2021.106388.

[148] S.M. Sonti K, Vincent S, Narala SKR. Effect of single and hybrid hollow sphere reinforcement on the deformation mechanism of aluminum matrix syntactic foam at a low strain rate. Journal of Alloys and Compounds 2022;901:163573. https://doi.org/10.1016/j.jallcom.2021.163573.

List of Publications

International Journals Published:

1. **Kartheek. S.M. Sonti**, Pavan Kumar Penumakala, Suresh Kumar Reddy Narala, S. Vincent, Experimental and numerical analysis of the compression behavior of aluminum syntactic foams reinforced with alumina hollow particles. **Engineering Structures- (Elsevier) 300 (2024) 117144 (IF: 5.5, SCI Indexed, Q1 Journal)**, https://doi.org/10.1016/j.engstruct.2023.117144.

2. **Kartheek. S.M. Sonti**, S. Vincent, S.K.R. Narala, Quasi-static compressive response and energy absorption properties of aluminum matrix syntactic foams: Room temperature and elevated temperature conditions, **Materials Today Communications (Elsevier) 35 (2023) 105580. (IF: 3.8, SCI Indexed, Q2 Journal)**. https://doi.org/10.1016/j.mtcomm.2023.105580.

3. **Kartheek. S. M. Sonti**, S. Vincent, Suresh Kumar Reddy Narala, Effect of single and hybrid hollow sphere reinforcement on the deformation mechanism of aluminum matrix syntactic foamat a low strain rate. **Journal of Alloys and Compounds (Elsevier) 901 (2022) 163573 (IF: 6.2, SCI Indexed, Q1 Journal).** https://doi.org/10.1016/j.jallcom.2021.163573.

International Journals Under Revision:

1. **Kartheek. S. M. Sonti**, S. Vincent, Suresh Kumar Reddy Narala, Enhancement in the mechanical properties of newly developed ceramic reinforced Al-based syntactic foams: Analysis of microstructure, mechanical response, and energy absorption properties- **Journal of Materials Engineering and Performance (Springer) (IF: 2.3, SCI Indexed, Q2 Journal)**.

International Journals Under Review:

1. **Kartheek. S. M. Sonti**, Priya Sudha, S. Vincent, Suresh Kumar Reddy Narala, Electrochemical impedance spectroscopy and corrosion behavior of Al-Al_2O_3 syntactic foam composite materials- **Corrosion Engineering, Science and Technology– Taylor and Francis**

Book Chapter Under Review:

1. **Kartheek. S.M. Sonti,** S. Vincent, Suresh Kumar Reddy Narala "Lightweight ceramic composites for structural applications"- **ISBN: 9780443188527**, **Elsevier Publications.**

Bibliography of the Candidate

S S M Kartheek is a Ph.D. candidate in the Department of Mechanical Engineering, Birla Institute of Technology and Science, Pilani (BITS Pilani), Hyderabad Campus. He received his bachelor's degree in the Department of mechanical engineering at Pondicherry University in 2009. Later he received his master's degree in Metallurgical and Materials Engineering from the National Institute of Technology, Trichy, Tamilnadu, in 2014. Further, he served as an Assistant professor for over 4 years at various deemed institutions such as GITAM and Symbiosis Universities. Also, he was involved in research projects and served as a junior and senior research fellow at NIT Trichy, IIT Bombay and BITS Pilani, Hyderabad Campus. He received the prestigious CSIR Direct SRF fellowship in the year 2019 before he joined Ph.D. in BITS Pilani. His research focuses primarily on processing aluminum matrix syntactic foams and their mechanical characterization.

Bibliography of the Supervisor

Prof. Suresh Kumar Reddy Narala, Professor and Head in the Department of Mechanical Engineering at Birla Institute of Technology and Science, Pilani (BITS Pilani), Hyderabad Campus. He received his Ph.D. in Mechanical Engineering from IIT Delhi in 2006. He has vast teaching, research experience, and administrative roles. Before joining BITS Pilani, Hyderabad Campus in 2008, he was a Post-Doctoral Fellow in Mechanical Engineering at KAIST, South Korea. Subsequently, he did another Post-Doctoral research at InSIC, France, in 2010. Later, he served as visiting faculty at UOIT (University of Ontario Institute of Technology) Canada in the years 2012, 2013, 2015, and UFU (Federal University of Uberlandia), Brazil in the year 2014. His research interests include High-speed machining, FE-modeling, optimization of machining processes, Tribology, Environmentally conscious machining processes, Micro/Nano machining, Experimental characterization of materials, machining of difficult-to-cut materials, Dynamics of machine tools, and study of functional materials such as syntactic foams and TPMS structures. He was invited to various research organizations, academic institutions, and national/international conferences to deliver guest lectures on various advanced topics. During his 22 years of career in research and academics, he has published 64 international journal papers and taught multiple courses to undergraduates and post-graduates. To his credit, he has 25 international and 16 national conference publications. Besides, he has completed six research-sponsored projects funded by agencies like DST-SERB, CSIR, and DRDL. Also, he successfully supervised 6 Ph.D. students while 8 are currently pursuing.

Bibliography of the Co-Supervisor

Dr. Vincent Shantha Kumar, Associate Professor in the Department of Mechanical Engineering, has been associated with Birla Institute of Technology & Science, Pilani - Dubai Campus since September 2015. During this tenure, he has also served as visiting faculty/scholar in the University of North Texas, Denton, USA (Jun - Jul 2021), National University of Singapore, Singapore (Jun-Aug 2019) & Seoul National University, South Korea (Jan - Feb 2017). He holds a Doctorate in materials science from VNIT, Nagpur, India. He was awarded the prestigious Binani Gold Medal in 2013 by the Indian Institute of Metals and was chosen as the best researcher from VNIT to meet the then Hon'ble President of India, Shri. Pranab Mukherjee to attend NITs Scholar-In-Residence Programme at Rashtrapati Bhavan, New Delhi, in 2015. He also received travel grants from DST and CSIR to present his research work at International conferences. He is a core project member of a joint research collaboration between KTH Sweden and BITS Pilani, funded by The Swedish Foundation for International Cooperation in Research and Higher Education (STINT). Dr. Vincent's research interests are the design and synthesis of novel advanced materials such as metallic glasses and entropy alloys. To his credit, he has several publications in reputed journals and guiding PhDs in biocorrosion, cytotoxicity, and mechanical behavior of advanced materials.